Towards a new test of time dilation

Laser spectroscopy on lithium ions stored at a velocity of 33.8 % of the speed of light

Dissertation
for the degree of
Doctor of Natural Sciences

submitted to the
Department of Physics, Mathematics and Computer Science
of the Johannes Gutenberg-Universität in Mainz

presented by
Dipl.-Ing. (FH) Christian Novotny
born in Hanau

Date: 29.08.2008

Date of oral examination:

27.11.2008

ABSTRACT

In this thesis results towards a new test of time dilation given by the theory of special relativity (SR) are presented. The performed experiment follows the measurement principle of Ives and Stilwell which states: time dilation can be accurately tested by the simultaneous measurement of the Doppler-shifts of a clock transition both with and against the clock's motion. The clocks are $^7Li^+$ ions which were stored at a velocity (υ) of 33.8 % of the speed of light (c) in the experimental storage ring (ESR) at the Gesellschaft für Schwerionenforschung, Darmstadt. The used Li^+ ions were in the metastable ground state where they exhibit a strong electric dipole transition in the optical region ($548.5\ \text{nm}$) and the hyperfine-structure allows optical double resonance spectroscopy. By means of such a spectroscopy scheme the Doppler-shifts can be measured without limitations from Doppler-broadening, caused by the velocity distribution of the ions in a storage ring. Consequently, both time dilation as well as the ion velocity can be extracted with high accuracy for a test of the predictions of SR.

A fluorescence detection system with two counter propagating laser beams (at $\lambda_1 = 780\ \text{nm}$, $\lambda_2 = 386\ \text{nm}$) which are aligned collinearly to the ion beam was set up. To achieve a robust control of the laser frequencies required for the beam times, a redundant system of frequency standards consisting of rubidium spectrometer, an iodine spectrometer, and a frequency comb was developed. The laser setup includes adequate frequency references for each laser and allows resonant (laser) excitation with and against the flight direction of the ions. At the experimental section of the ESR, an automated laser beam guiding system for exact control of polarisation, beam profile, and overlap with the ion beam, as well as a fluorescence detection system were build up.

During the first experiments, the generation, the acceleration and the lifetime of the metastable ions were investigated at the GSI facility. Further the velocity of the stored ion beam has been measured directly, for the first time, via the Doppler effect, and thus the effective voltage of the electron cooler.

In the following step the first sub-Doppler spectroscopy signals from an ion beam at 33.8 %c could be recorded. Here, the excitation frequencies $\nu_{\text{p,a}}$ in the laboratory frame are shifted with respect to the rest frequencies of the ions $\nu_{1,2}$ by $\nu_{\text{p,a}} = \nu_{1,2} \cdot \gamma \cdot (1 \pm \beta)$ when moving with $\beta = \upsilon / c$. If special relativity holds $\nu_1 \cdot \nu_2 = \nu_{\text{a}} \cdot \nu_{\text{p}}$, i.e. $\gamma^2 = 1/(1-\beta^2)$. In test theories hypothetical deviations from special relativity are described by a series of parameters (α, α_2, …) which are weighted by even powers of β. These Lorentz violations can be identified by a slightly modified time dilation factor $\gamma_{\text{MS}} = \gamma \cdot (1 + 2 \cdot \alpha \cdot \beta^2 + (\alpha + 2 \cdot \alpha_2) \cdot \beta^4 + ...)$.

Previous time dilation experiments were either restricted to comparably low velocities and thus limited to first-order deviations described by α; or, if the particle velocity allows for higher-order tests, the experiments suffered from poor frequency accuracy. In this thesis measurements are presented that combine high particle velocities with precision spectroscopy. The unprecedented accuracy in this experiment allowed to derive a new upper bound for possible higher-order deviations from SR. Consequently, in the measurements time dilation was found to be consistent to an upper bound of $|\alpha_2| < 9.8 \times 10^{-6}$ for deviations to the order β^4. This means an improvement by a factor of 28 compared to previous experiments.

Moreover, future measurements with the experimental setup developed in this thesis have the potential to improve the sensitivity to low-order deviations by at least one order of magnitude compared to previous experiments; and will thus lead to a further contribution to the test of standard model of particles.

ZUSAMMENFASSUNG

Im Rahmen dieser Arbeit werden Ergebnisse zum Test der Speziellen Relativitätstheorie durch Messung der Zeitdilatation präsentiert. Die Experimente wurden nach dem Messprinzip von Ives und Stilwell durchgeführt, welches besagt, dass die Zeitdilatation durch Messung der Dopplerverschiebungen eines geeigneten Uhrenübergangs in und entgegen der Bewegungsrichtung der Uhr präzise getestet werden kann. Als Uhren wurden $^7Li^+$ Ionen verwendet, welche mit einer Geschwindigkeit (υ) von 33,8 % der Lichtgeschwindigkeit (c) im Experimentierspeicherring (ESR) der Gesellschaft für Schwerionenforschung in Darmstadt gespeichert werden können. In seinem metastabilen Spektrum hat das Lithiumion einen starken Dipolübergang im Optischen (548,5 nm) und seine Hyperfeinstrukturaufspaltung ermöglicht eine optische Doppelresonanzspektroskopie (Λ-Spektroskopie). Dieses erlaubt die Bestimmung der Dopplerverschiebungen ohne eine Limitierung aufgrund der Signalverbreiterung, welche durch die Geschwindigkeitsverteilung der Ionen im Speicherring verursacht wird. Hieraus lassen sich sowohl die die Zeitdilatation als auch die Geschwindigkeit der Ionen mit hoher Genauigkeit bestimmen und so die Vorhersage der Speziellen Relativitätstheorie überprüfen.

Dazu wurde ein Fluoreszenznachweis mit zwei exakt gegenläufigen Laseranregungen aufgebaut (mit $\lambda_1 = 780$ nm, $\lambda_2 = 386$ nm), die mit diesem Ionenstrahl parallel überlagert sind. Für die robuste Frequenzkontrolle dieser Laser während der Strahlzeiten am ESR wurde ein redundantes System von Frequenzstandards bestehend aus einem Rubidium- und einem Iodspektrometer sowie einem optischen Frequenzkamm entwickelt. An der ESR Experimentiersektion erfolgte der Aufbau einer automatisierten Laserstrahlführung zur exakten Kontrolle von Strahlprofil, Polarisation und Überlapp mit dem Ionenstrahl, sowie eines Detektorsystems für den Fluoreszenznachweis.

In den ersten Experimenten wurden zunächst die Produktion, Beschleunigung und Lebensdauer der metastabilen Ionen am GSI Beschleunigersystem und im ESR erstmals vermessen. Weiterhin wurde, neben der Charakterisierung des Strahls, erstmalig die Geschwindigkeit eines gespeicherten Ionenstrahls im ESR über den Dopplereffekt direkt gemessen, und damit die effektive Spannung des Elektronenkühlers bestimmt.

Anschließend konnten mit der Doppelresonanzspektroskopie Signale für den Test der Speziellen Relativitätstheorie aufgenommen werden. Bei diesen Messungen wurden die Laseranregungsfrequenzen so gewählt, dass diese resonant mit jeweils einem Übergang des Λ-Systems sind. Die Transformation der Laserfrequenzen $\nu_{p,a}$ aus dem Laborsystem in die Anregungsfrequenzen $\nu_{1,2}$ im Ruhesystem der Ionen erfolgt mittels der Dopplerformel $\nu_{p,a} = \nu_{1,2} \cdot \gamma \cdot (1 \pm \beta)$ wobei $\beta = \upsilon / c$. Unter Annahme der Gültigkeit

der Speziellen Relativitätstheorie (d.h. $\gamma = 1/\sqrt{1-\beta^2}$), ergibt das Multiplizieren der beiden Gleichungen $\nu_1 \cdot \nu_2 = \nu_a \cdot \nu_p$. Abweichungen hiervon werden in kinematischen Testtheorien mit einem Satz Testparametern (α, α_2, …) beschrieben, welche sich nach Ordnungen von β^2 entwickeln lassen. Mit diesen Parametern können hypothetische Verletzungen der Speziellen Relativitätstheorie mit einem veränderten Lorentzfaktor $\gamma = \gamma_{SR} \cdot \left(1 + 2 \cdot \alpha \cdot \beta^2 + \left(\alpha + 2 \cdot \alpha_2\right) \cdot \beta^4 + ...\right)$ quantifiziert werden.

Bisherige Experimente zum Test der Zeitdilatation wurden entweder bei vergleichsweise niedrigen Teilchengeschwindigkeiten durchgeführt und waren somit nur auf Abweichungen erster Ordnung empfindlich oder, wenn durch eine hohe Teilchengeschwindigkeit die Empfindlichkeit auf höhere Ordnungen gegeben war, war die Genauigkeit dieser Experimente vergleichsweise gering. In dieser Arbeit wird ein Experiment vorgestellt, dass hohe Teilchengeschwindigkeiten mit hochauflösender Präzisionsspektroskopie kombiniert und so eine Bestimmung einer neuen Obergrenze für hypothetische Abweichungen höherer Ordnungen von der Speziellen Relativitätstheorie erlaubt. Aus den durchgeführten Messungen konnte eine neue Obergrenze von $|\alpha_2| < 9.8 \times 10^{-6}$, für Abweichungen in β^4-Ordnung, ermittelt werden. Dies stellt eine Verbesserung um den Faktor 28 gegenüber früheren Experimenten dar.

Damit wurden die Voraussetzungen geschaffen, um in weiteren Experimenten die bisherigen Grenzen in niedrigster Ordnung ebenfalls um mindestens eine Größenordnung zu verbessern und damit einen weiteren Beitrag zum Test des Standardmodells zu liefern.

CONTENTS

1 THEORETICAL FOUNDATIONS

Our understanding of physics is described by four fundamental interactions and their massive constitution of matter, hadrons and leptons: the electromagnetic force, the nuclear weak force, the nuclear strong force and gravity. The electromagnetic and the weak forces are merged in the electroweak theory that builds, together with quantum chromodynamics (description of the strong force), the basics for the standard model (SM). The SM consists of quantum field theories formulated in the early seventies which are consistent with both the theory of quantum mechanics and special relativity (SR). This model allows to reproduce all experimental observations even though it cannot reveal the origin of the different strength of the interaction e.g. the masses of bosons (and fermions). In sum, the SM consists of 17 particles of which twelve are fermions: 6 quarks and 6 leptons. The remaining five particles are bosons, four of which are physical manifestations of the forces through which particles interact (at high energies the weak nuclear force merges with electromagnetic force). The fifth boson is the (up to present not detected) Higgs boson which would give particles their masses. The mass of the Higgs boson is expected to be in the range of 114-153 GeV[1], which is out of reach for hitherto existing facilities. A new accelerator the Large Hadron Collider at CERN[2] (scheduled start 2008), is expected to disentangle the Higgs puzzle. Although the SM is a very successful theory it is still a local description of the world since general relativity is not included. Nevertheless, a basic constituent of both the SM and the theory of general relativity is the Lorentz invariance which is allowed to be violated at certain scales in unifying models (e.g. string theory). This means, looking for Lorentz violating signatures could lead to a dramatic indication for new physics. Beside in unifying theories, Lorentz violating parameters are introduced in several test theories that compare and quantify experimental results and deduce limits for hypothetical deviations to the predictions of the SM and general relativity. A model describing Lorentz violations is the standard model extension (SME) developed by Kostelecký and coworkers [Kostelecký89[s]]. The SME is a dynamical test theory which starts with a Langrangian including parameterised Lorentz- and CPT[3]-violating terms that can be

---

[1] Measurements at the Large Electron-Positron collider ruled out masses of up to 144.4 GeV and the upper limit is set by a measurement of the mass of the W boson to 80.413 GeV [Hogan07].

[2] CERN: Conseil Européen pour la Recherche Nucléaire, which is French for European Council for Nuclear Research.

[3] CPT: Charge, Parity, Time.

formed with known fields. This can be considered as a generalisation of the test theory, developed by Robertson and extended by Mansouri-Sexl (MS) to parameterise hypothetical Lorentz violations [Robertson49, MS77a-c]. In contrast to the SME, these kinematical test theories postulate a preferred reference frame and assume generalised Lorentz transformations between this frame and moving inertial frames.

Before these test theories are introduced (chapter 1.3.1 and 1.3.3) a review on the relevant constituents of special relativity for performing precision spectroscopy on fast ions in a storage ring is given.

1.1 THEORY OF SPECIAL RELATIVITY

In 1905, Einstein published the theory of special relativity in his famous paper *Zur Elektrodynamik bewegter Körper* [Einstein05]. It generalises Galileo's principle of relativity that all uniform motion is relative and therefore abolishes the Newtonian notion of absolute space and time. It states that space and time are perceived differently by observers in different states of motion. Special relativity is restricted to inertial frames and does not include e.g. gravitational fields. In general relativity as formulated, again by Einstein, accelerated frames are included as distortion of space and time [Einstein15&16]. Nevertheless, in the formalism of general relativity, SR is embedded as the description of local space-time with negligible gravity. This results in the fact that it is possible to find local coordinates on a four-dimensional manifold such that a worldline element ds is described by $\mathrm{d}s^2 = c^2 \cdot \mathrm{d}t^2 - \mathrm{d}x^2 - \mathrm{d}y^2 - \mathrm{d}z^2$.

Since the experiment, presented in this thesis, is performed on particles with velocities approaching the speed of light, in negligible gravitational fields, the Einstein-Minkowski space-time is needed to describe the physics. Here the Lorentz transformations play an important role for the description of kinematics. In general the transformation equations can be deduced considering only the properties of space:

- the isotropy of space (all directions in space are equal),
- the uniformity of space-time (viz, no point in space or time is preferred compared to another),

and Einstein's principle of relativity:

- all inertial frames are equal (the laws of physics are the same in each inertial frame; there is no possibility to detect absolute motion and no preferred frame exists).

In these equations an invariant constant remains which can be identified with the speed of light in vacuum. Vice versa, it is possible to postulate the constancy of the speed of light from the beginning which leads to the same transformation equations (only the way of mathematical argumentation is shorter) [Schröder94].

The Lorentz transformations, valid for an inertial system S′ with the Cartesian coordinates (x', y', z', t'), which is moving with a constant velocity υ along the x-axis, relative to a second inertial system S with (x, y, z, t), are

$$\begin{aligned} x' &= \gamma \cdot (x - \upsilon \cdot t) \\ y' &= y \\ z' &= z \\ t' &= \gamma \cdot \left(t - \frac{\upsilon \cdot x}{c^2} \right) \end{aligned} \qquad \text{(1.1a-d)}$$

where γ labels the Lorentz factor of the special relativity

$$\gamma = \frac{1}{\sqrt{1-\beta^2}} \qquad (1.2)$$

and the velocity is expressed by $\beta = \upsilon / c$. Consequences of the Lorentz transformations are length contractions of rods along their moving direction and time dilation of moving clocks by the factor $\sqrt{1-\beta^2}$.

Considering a monochromatic plane wave in S the electric field $\vec{E}(\vec{r},t)$ is described by

$$\vec{E}(\vec{r},t) = A_0 \cdot \mathrm{e}^{i(\omega \cdot t - \vec{k} \cdot \vec{r})} \qquad (1.3)$$

with the angular frequency ω, the amplitude A_0 and the wave number vector $\vec{k}$ which indicates the propagation direction of the wave and has an absolute value of $|\vec{k}| = \omega / c$. The exponential term in the wave function is the Lorentz invariant phase φ. If one considers a point in space-time where the wave function has a maximum value this point has to remain independent of the inertial frame. This is due to the uniformity of space-time and is expressed by

$$\varphi = \omega \cdot t - \vec{k} \cdot \vec{r} = \omega' \cdot t' - \vec{k}' \cdot \vec{r}' . \qquad (1.4)$$

Assuming the wave number vector is given by $\vec{k} = |\vec{k}| \cdot (\cos\theta, \sin\theta, 0)$ in S, where θ is the angle between the propagation direction of the wave and the moving direction of S′ measured in S and applying the Lorentz transformations to (1.4), one obtains the Doppler formula

$$\omega' = \omega \cdot \gamma \cdot \left(1 - \frac{\upsilon}{c} \cdot \cos\theta\right) = \omega \cdot D^{-1} \tag{1.5}$$

where D is called Doppler factor. Consequently, the conversion of the angles from the frame at rest to a moving system is described by

$$\cos\theta' = \frac{\cos\theta - \beta}{1 - \beta \cdot \cos\theta} \quad \text{and} \quad \sin\theta' = \frac{\sqrt{1-\beta^2}\,\sin\theta}{1 - \beta \cdot \cos\theta}. \tag{1.6a, b}$$

1.2 TEST OF TIME DILATION

Shortly after the formulation of special relativity, Einstein proposed experimental tests of time dilation, based on the observation of the transverse Doppler effect in fast canal rays [Einstein07]. He assumed to measure the frequency emitted by a source that is moving perpendicular to the detector ($\theta = 90°$). If special relativity holds the frequency $\nu_\perp$ measured in the laboratory has to be shifted by

$$\nu' = \gamma \cdot \nu_\perp \tag{1.7}$$

compared to ν' which indicates the rest frequency of the moving emitter. The first-order (classical) Doppler effect vanishes for a frequency detection perpendicular to the moving direction of the particle. However, to perform such a test one has to verify carefully that the measured frequency is emitted perpendicular and not under a small angle from the source. Indeed, this technical challenge was overcame only 1979 by Hasselkamp et al. They observed the Hα-line of linearly moving hydrogen atoms and could verify the predictions of special relativity to be better than 3×10^{-2} [Hasselkamp79].

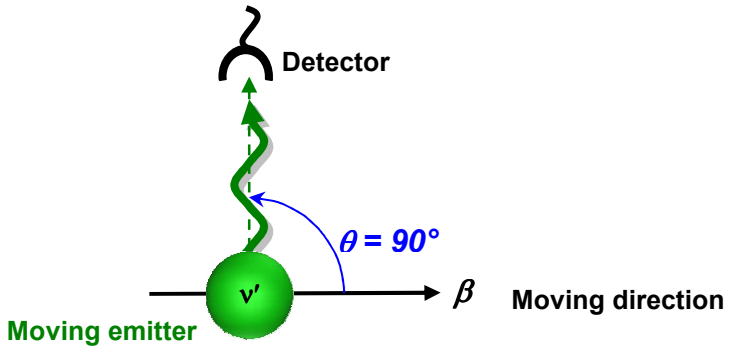

Figure 1.1: Principle sketch of Einstein's idea to measure the transverse Doppler effect directly: A detector is used to measure the frequency emitted by a source that is moving perpendicular to the detector with the velocity β. Only the radiation emitted at $\theta = 90°$ has to be measured.

Another possibility to test time dilation is to measure the frequency of a moving emitter in and against the flight direction of the source. This experiment was originally performed by Ives and Stilwell in 1938 and gives the whole class of measurements the name Ives-Stilwell (IS-) type experiments (see chapter 3). Following equation (1.5) this leads to

$$\nu' = \nu_p \cdot \gamma \cdot (1 - \beta) \tag{1.8}$$

for the frequency of a wave that is emitted parallel to the moving direction of the particle ($\theta = 0°$) and to

$$\nu' = \nu_a \cdot \gamma \cdot (1 + \beta) \tag{1.9}$$

for a wave that is propagating in the other direction ($\theta = 180°$). Combining equations (1.8) and (1.9) by multiplication, one yields

$$\nu'^2 = \nu_a \cdot \nu_p , \tag{1.10}$$

where only three frequencies are left. A simultaneous measurement of both shifted frequencies and the precise knowledge of the rest frequency leads to a further test of the prediction of special relativity. Such a measurement is feasible without the necessity of having precise knowledge of the particle velocity. It is remarkable that this is only true for the measurement in and against the moving direction of the particle. For all other configurations the particle velocity remains in the equation and contributes to the measurement uncertainties.

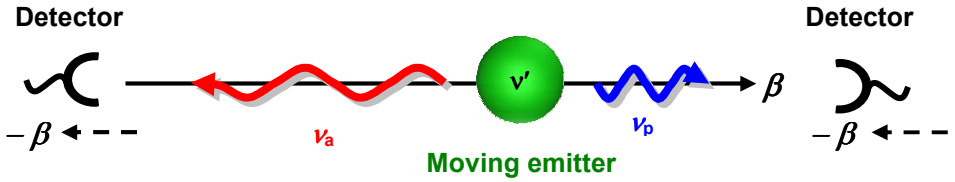

Figure 1.2: Principle of the original Ives-Stilwell type experiments. The frequency which is emitted in and against the flight direction of a moving source is analysed and compared with the known rest frequency. This allows a test of the predictions of special relativity. The solid arrow indicates the moving direction of the emitter as appears in the laboratory frame, the dashed arrows sketch the situation in the emitter's frame.

In modern versions of IS-type experiments fast moving absorbers (e.g. atoms, ions) are excited by lasers. Laser beams are aligned parallel and antiparallel to the flight direction of the particle and the emitted fluorescence light is detected as a function of the laser frequencies (see Figure 1.3). In the inertial system of the absorber these lasers appear moving (with the velocity $-\beta$), so in the laboratory frame their frequencies have to be shifted in relation to the Doppler formula to be in resonance with the absorber. For the

frequency of laser 1 ν_p (the laser which is moving apart from the absorber) one has to obey relation

$$\nu_p = \frac{\nu'}{\gamma \cdot (1-\beta)} \tag{1.11}$$

which leads to a blue shift of the frequency. The frequency of laser 2 (moving towards the absorber) has to be red shifted

$$\nu_a = \frac{\nu'}{\gamma \cdot (1+\beta)} . \tag{1.12}$$

Although the modern IS-type experiments seem to be performed in a different way the principles are the same and equation (1.10) is still valid. The laser frequencies in the laboratory frame are transformed into the rest frame of the moving absorber, where they have to fulfil the resonance condition for excitation. Measuring the fluorescence of excited particles by the help of spectroscopy techniques, correlating this signal with the laser frequencies in the laboratory and comparing this with the rest frequency of the absorber leads to a test of the predictions of special relativity.

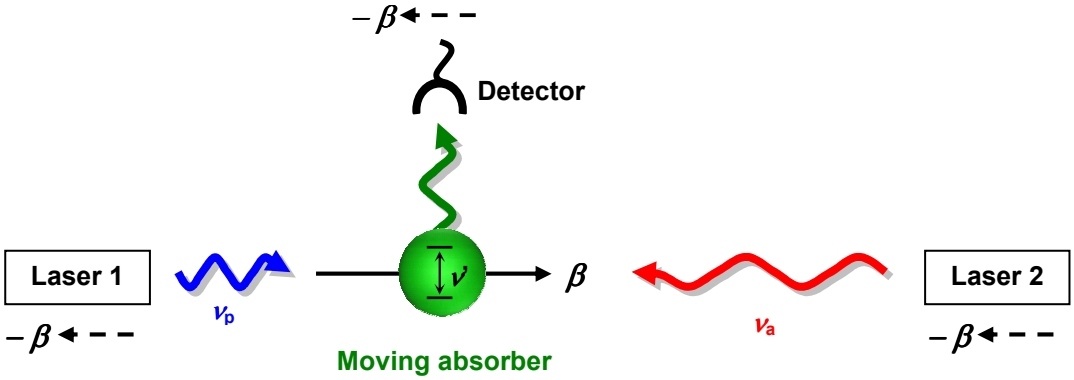

Figure 1.3: The red detuned antiparallel laser beam ν_a and the blue detuned parallel laser beam ν_p interact simultaneous with the moving particle. The laser frequencies are chosen to be resonant with the same transition in the absorbers` rest frame. So, in this frame the laser frequencies are equal. The emitted fluorescence light is recorded by a detector e.g. as a function of the angle of the parallel laser beam with respect to the particles movement. This spectrum can give a statement on hypothetical violation of Lorentz invariance. The solid arrow indicates the moving direction of the absorber in the laboratory frame; the dashed arrows sketch the situation in the emitter's frame.

Moreover, the laser frequencies and the laser beam alignment are parameter that can be controlled and changed with high accuracy in the laboratory frame and allow for precise measurements of time dilation. In the original IS-type experiment the emission frequency and its direction are measurement parameters and one remains with their uncertainties.

1.3 TEST THEORIES

In order to describe hypothetical violations of Lorentz invariance, various different test theories were developed. The aim of such theories is to parameterise and quantify possible deviations from standard theories. Furthermore, they allow for comparing results of different types of Lorentz tests (e.g. experiments that probe the constancy of the speed of light with those testing time dilation) by introducing test parameters. In principle test theories can be subdivided in two classes: kinematical test theories and dynamical test theories. The properties of the kinematic theories are: independence from any particle model, dealing with a little number of test parameters (e.g. at MS test theory three) and requiring a preferred frame. The dynamical test theories imply many test parameters (e.g. the SME more than one hundred) and can describe particular violations (e.g. birefringence in vacuum) [Mattingly05, Lämmerzahl06].

In this thesis, both currently prevalent theories are introduced and described in relation to the performed experiment. The first is the kinematical test theory formulated by Robertson in 1949 [Robertson49] and extended by Mansouri and Sexl 1976 [MS77a-c] (see chapter 1.3.1). The second is the dynamical theory of the standard model extension, formulated and further developed by Kostelecký and coworkers [e.g. Kostelecký89[s] and Colladay97[s]] (see chapter 1.3.3).

1.3.1 ROBERTSON-MANSOURI-SEXL TEST THEORY

In 1949 Robertson formulated a test theory, which postulates a preferred reference frame Σ (Einstein's "rest-system", with the coordinates X, Y, Z, T), where the velocity of light is assumed to be isotropic and constant. Usually the cosmic microwave background (CMB) is identified with this reference frame. Furthermore, a second frame S (Einstein's "moving frame", with the coordinates x, y, z, t) that is moving with velocity υ in relation to Σ, is assumed. For the transformation the only vector of intrinsic significance is the velocity vector and in all frames Einstein's clock synchronisation[4] is used. The x-axis of S is parallel to the X-axis in Σ, the x-z-plane coincides with the X-Z-plane and the origin of S moves along the X-axis with the velocity υ. In this framework the conversion from one frame into the other is done by a generalised

[4] Einstein's clock synchronisation is defined as follows: Consider two clocks, A and B, at rest with respect to each other. At $t = 0$, a light signal is sent from A to B. At $t = t_1$, the signal arrives at B, and a signal is immediately sent back to A, where it arrives at $t = t_2$. Einstein clock synchronisation demands that $t_2 = 2 \cdot t_1$ [MacArthur86a]. Here the isotropy of space is already assumed. A further discussion of synchronisation procedures is given in [MS77a].

transformation where three irreducible parameter functions $a_0(\upsilon)$, $a_1(\upsilon)$ and $a_2(\upsilon)$ remain (equations 1.13a-d).

$$\begin{aligned} T &= a_0(\upsilon)\cdot t + \left(\frac{\upsilon}{c^2}\right)\cdot a_1(\upsilon)\cdot x \\ X &= a_0(\upsilon)\cdot \upsilon\cdot t + a_1(\upsilon)\cdot x \\ Y &= a_2(\upsilon)\cdot y \\ Z &= a_2(\upsilon)\cdot z \end{aligned} \qquad (1.13a\text{-}d)$$

These test parameters are velocity dependent and can be determined by the result of three different experiment-types [Robertson49]:

1. Michelson-Morley (MM) experiments: *The total time required for light to traverse, in free space, a distance l and to return is independent of its direction.*

2. Kennedy-Thorndike (KT) experiments: *The total time required for light to traverse a closed path in S is independent of the velocity υ of S relative to Σ.*

3. Ives-Stilwell (IS) experiments: *The frequency of a moving atomic source is altered by the factor $(1 - \upsilon^2/c^2)^{1/2}$, where υ is the velocity of the source with respect to the observer.*

In the year 1976 Mansouri and Sexl (MS) formulated a more general[5] approach to describe Lorentz violation, based on Robertson's test theory (equations (1.14a-d)). They used only Robertson's assumption of the isotropy of a preferred frame and the significance of the velocity vector. No restrictions on the clock synchronisation were made. For this reason three additional parameters $\vec{\varepsilon} = \varepsilon_n$ (n = 1, 2, 3) that can not be tested by experiment remain. They have to be defined by the synchronisation procedure. Hence, using Einstein synchronisation (equation (1.15a, b)) to define $\vec{\varepsilon}$, the formulation of MS becomes equivalent to the one of Robertson, again, with three test parameters ($a(\upsilon)$, $b(\upsilon)$, $d(\upsilon)$). Due to the similarity of both theories, this approach to explain Lorentz violations is often combined to the Robertson-Mansouri-Sexl test theory. A comparison of both theories is given in [MacArthur86a].

[5] MS formulated their test theory without any assumptions for clock synchronisation.

$$\begin{aligned} t &= a(\upsilon)\cdot T + \varepsilon_1 \cdot x + \varepsilon_2 \cdot y + \varepsilon_3 \cdot z \\ x &= b(\upsilon)\cdot (X - \upsilon \cdot T) \\ y &= d(\upsilon)\cdot Y \\ z &= d(\upsilon)\cdot z \end{aligned} \qquad \text{(1.14a-d)}$$

$$\varepsilon_1 = -\frac{a}{b}\cdot\frac{\upsilon}{c^2-\upsilon^2}, \quad \varepsilon_2 = \varepsilon_3 = 0 \qquad \text{(1.15a, b)}$$

As we restrict ourselves to the case of Einstein synchronisation, which uses the back and forth movement of a light signal and is therefore insensitive to the one-way speed of light, $a(\upsilon)$, $b(\upsilon)$, $d(\upsilon)$ and $a_0(\upsilon)$, $a_1(\upsilon)$, $a_2(\upsilon)$ can only depend on υ^2. Since most laboratory experiments were performed at velocities relatively small compared to the speed of light it is useful to expand the three parameters of MS in powers of υ^2 [Will92].

$$a(\upsilon) = 1 + \left(\alpha - \frac{1}{2}\right)\cdot\frac{\upsilon^2}{c^2} + \left(\alpha_2 - \frac{1}{8}\right)\cdot\frac{\upsilon^4}{c^2} + \ldots \qquad \text{(1.16)}$$

$$b(\upsilon) = 1 + \left(\hat{\beta}_1 + \frac{1}{2}\right)\cdot\frac{\upsilon^2}{c^2} + \left(\hat{\beta}_2 + \frac{3}{8}\right)\cdot\frac{\upsilon^4}{c^2} + \ldots \qquad \text{(1.17)}$$

$$d(\upsilon) = 1 + \hat{\delta}\cdot\frac{\upsilon^2}{c^2} + \hat{\delta}_2\cdot\frac{\upsilon^4}{c^2} + \ldots \qquad \text{(1.18)}$$

The Greek-lettered, velocity independent coefficients are defined in such a way that they vanish when special relativity is valid[6]. Than the test functions $a(\upsilon)$, $b(\upsilon)$ and $d(\upsilon)$ can be identified with

$$a(\upsilon) = \sqrt{1 - \frac{\upsilon^2}{c^2}}, \qquad \text{(1.19)}$$

$$b(\upsilon) = \frac{1}{\sqrt{1 - \frac{\upsilon^2}{c^2}}}, \qquad \text{(1.20)}$$

$$d(\upsilon) = 1. \qquad \text{(1.21)}$$

[6] In the original work of MS the test parameter are introduced to be $\alpha = -\frac{1}{2}$, $\hat{\beta}_1 = \frac{1}{2}$ and $\hat{\delta} = 0$, if special relativity is valid. We follow the analysis of [Kretzschmar92] and [Will92] where the test parameters are defined to be $\alpha = \hat{\beta}_1 = \hat{\delta} = 0$ for special relativity.

In the notation of the Robertson test theory no expansion to powers of υ is done (although it could be done in a similar way [Lämmerzahl06]). The parameters are usually expressed in terms of g_0, g_1 and g_2 as $a_0 = \gamma \cdot g_0$, $a_1 = \gamma \cdot g_0$ and $a_2 = g_2$. Special relativity represents the limit where $g_0 = g_1 = g_2 = 1$. Again, it should be emphasised that g_0, g_1 and g_2 are all functions of υ rather than constants, so the g's should be measured at many different velocities [MacArthur86a]. This leads to the necessity to control the velocity of the clock very carefully. Charged particles (e.g. ions) in electric and magnetic fields allow this.

From the assumption of a preferred reference frame, it turns out that the velocity of light is in general dependent on both, the direction and the absolute value of $\vec{\upsilon}$. According to [MS77a] and equations (1.14a-d), the speed of light c can be deduced from the generalised Lorentz transformation and is given, up to second-order in υ

$$\frac{c}{c_\theta} = 1 + \underbrace{\left(\hat{\beta}_1 + \hat{\delta}\right) \cdot \frac{\upsilon^2}{c^2} \cdot \sin^2\theta}_{\text{MM-type experiments}} + \underbrace{\left(\alpha - \hat{\beta}_1\right) \cdot \frac{\upsilon^2}{c^2}}_{\text{KT-type experiments}} . \tag{1.22}$$

θ denotes the angle of the propagation direction of the light wave with respect to υ.

The three parameters of the MS theory can be correlated to three experiments: MM-type experiments are probing $(\hat{\beta}_1 + \hat{\delta})$, KT-type experiments are sensitive for $(\alpha - \hat{\beta}_1)$ and the IS-type tests can measure solely α. Further, the IS-type experiments manifest a positive effect in time dilation instead of measuring a null-result in the MM- and KT-type experiments.

In the past experiments testing $(\hat{\beta}_1 + \hat{\delta})$ and $(\alpha - \hat{\beta}_1)$, respectively, were performed with Michelson-interferometers to reveal anisotropy of the speed of light due to Earth's motion through an aether medium. Modern experiments have been realised using cryogenic optical [Antonini05] or microwave resonators [Stanwix05] that are mounted in an actively rotating setup and thus independent of the Earth's rotation. An overview of experiments that probe the anisotropy of the speed of light is given in [Herrmann06]. Experiments measuring time dilation are sensitive to the parameter α and g_0, respectively. These will be described in detail in chapter 3. An overview on the current boundaries in terms of MS formalism is given in chapter 7.8.

1.3.2 IVES-STILWELL-TYPE EXPERIMENTS IN THE MANSOURI-SEXL FRAMEWORK

The results of IS-type experiments can be used to derive a limit on the test parameter α of the MS test theory. For this, both inertial frames of the experiments have to be related to a preferred reference frame [Kretzschmar92,Will92]. The three frames are: the reference frame Σ with the coordinates (X, Y, Z, T). Only there the light propagation is isotropic and the speed of light is constant. The second system is the laboratory frame S with (x, y, z, t) where the lasers are at rest and the third system is the rest frame of the particle S′ with the coordinates (x', y', z', t'). The general transformations from the preferred rest frame Σ to the laboratory frame are given by equations (1.23) & (1.24) with the relative motion $\vec{w}$ between both frames[7]. To transform from the frame S′ to Σ the equations (1.25) & (1.26) have to be used, where $\vec{u}$ denotes the relative velocity of both frames. An overview of the three frames with their coordinates is shown in Figure 1.4.

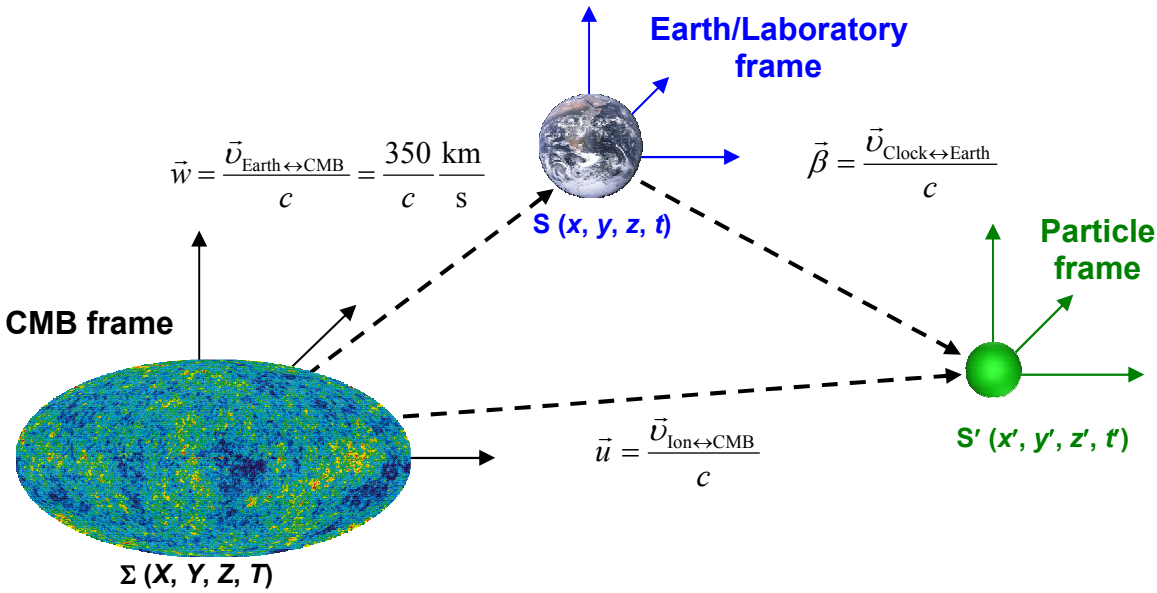

Figure 1.4: Movement of the laboratory frame (which is equal to the Earths' frame, when its rotation is neglected) and the particles rest frame with respect to the preferred frame Σ (that is assumed to be the cosmic microwave background (CMB) [NASA08, NASA72].

For the description of the three frames one uses the generalised Lorentz transformations

$$t = a \cdot T + \vec{\varepsilon} \cdot \vec{x} \tag{1.23}$$

$$\vec{x} = -b \cdot T \cdot \vec{w} + b \cdot \hat{\vec{n}} \cdot \left(\hat{\vec{n}} \cdot \vec{X}\right) + d \cdot \left(\vec{X} - \hat{\vec{n}} \cdot \left(\hat{\vec{n}} \cdot \vec{X}\right)\right) \tag{1.24}$$

[7] Note, all velocities are given in units of the speed of light in Σ. Only there the speed of light is constant.

and

$$T = \frac{1}{a'} \cdot \left(t' - \vec{\varepsilon}' \cdot \vec{x}'\right) \tag{1.25}$$

$$\vec{X} = \frac{1}{d'} \cdot \vec{x}' + \left(\frac{1}{b'} - \frac{1}{d'}\right) \cdot \left(\hat{\vec{n}}' \cdot \vec{x}'\right) \cdot \hat{\vec{n}}' + T \cdot \vec{u} \tag{1.26}$$

where $\hat{\vec{n}}$ (and $\hat{\vec{n}}'$, respectively) is the unity vector in the direction of $\vec{w}$ (and $\vec{u}$, respectively). Combining equations (1.23)-(1.26), one can connect the coordinates of the particle frame S′ with the one's of the laboratory frame S. Comparing a clock at rest in S′ with clocks that are at rest in S one obtains

$$\Delta t = \Gamma\left(\vec{u}, \vec{w}\right) \cdot \Delta t' \,. \tag{1.27}$$

$\Gamma(u, w)$ plays the role of a generalised time dilation factor relating S′ and S

$$\Gamma\left(\vec{u}, \vec{w}\right) = \frac{a}{a'} + \frac{b}{a'}\left(\vec{\varepsilon} \cdot \left[\hat{\vec{n}} \cdot \left(\hat{\vec{n}} \cdot \vec{u}\right) - \vec{w}\right]\right) + \frac{d}{a'}\left(\vec{\varepsilon} \cdot \left[\vec{u} - \hat{\vec{n}} \cdot \left(\hat{\vec{n}} \cdot \vec{u}\right)\right]\right) \tag{1.28}$$

and reduces, when special relativity holds, to

$$\Gamma\left(\vec{u}, \vec{w}\right) = \frac{1 - \vec{u} \cdot \vec{w}}{\sqrt{\left(1 - \vec{w}^2\right) \cdot \left(1 - \vec{u}^2\right)}} = \frac{1}{\sqrt{1 - \beta_{SR}^2}} \tag{1.29}$$

with

$$\beta_{SR} = \frac{1}{1 - \vec{u} \cdot \vec{w}} \cdot \sqrt{\left(\vec{u} - \vec{w}\right)^2 - \left(\vec{w}^2 \times \vec{u}^2\right)} \,. \tag{1.30}$$

The parameter β_{SR} stands for the velocity of the particle's frame relative to the laboratory frame in the case special relativity holds. Furthermore the general Doppler-shift formula can be derived. Consider a particle at rest in the reference frame S′ to absorb light with a frequency ν_0. The laser beams are aligned parallel and antiparallel with respect to the flight direction of the particle and at rest in the laboratory frame S. Here the lasers need to have the frequency $\nu^{\pm}$ in S to be resonant with the particle's transition at ν_0. Thereby, the relations of $\nu^{\pm}/\nu_0$ have to obey the Doppler formula

$$\frac{\nu^{\pm}}{\nu_0} = \left[\frac{a\left(\vec{u}^2\right)}{\sqrt{1 - \vec{u}^2}} \cdot \frac{\sqrt{1 - \vec{w}^2}}{a\left(\vec{w}^2\right)}\right] \cdot \frac{1 \pm \beta_{SR}}{\sqrt{1 - \beta_{SR}^2}} = \left[\frac{\alpha\left(\vec{u}^2\right)}{\alpha\left(\vec{w}^2\right)}\right] \cdot \frac{1 \pm \beta_{SR}}{\sqrt{1 - \beta_{SR}^2}} \,. \tag{1.31}$$

It turns out that all terms containing the parameters b, d, ε and b', d', ε' cancel out. Except for the multiplication factor $\alpha\left(\vec{w}^2\right)/\alpha\left(\vec{u}^2\right)$ the Mansouri-Sexl test theory yields the same Doppler-shift formula as the special relativity. This result depends neither on clock synchronisation procedures, nor on the one-way velocity of light. The factor $\alpha\left(\vec{w}^2\right)/\alpha\left(\vec{u}^2\right)$ is a function of only the magnitudes, but not the directions of $\vec{w}$ and $\vec{u}$,

thus reflecting the assumed isotropy of space from the viewpoint of the preferred aether frame Σ. If the factor differs from unity, special relativity is violated [Kretzschmar92].

Furthermore, in equation (1.31) a generalised Lorentz factor can be identified to

$$\gamma = \frac{\alpha\left(\vec{u}^2\right)}{\alpha\left(\vec{w}^2\right)} \cdot \frac{1}{\sqrt{1-\beta_{SR}^2}} = \frac{\alpha\left(\vec{u}^2\right)}{\alpha\left(\vec{w}^2\right)} \cdot \gamma_{SR} \,. \tag{1.32}$$

From the derived formula the test parameters can be related to the frequencies measured in time dilation experiments. For the laser beam aligned parallel to the ion beam equation (1.33) describes the resonance condition. The antiparallel regime is given in equation (1.34)

$$\frac{\nu_p}{\nu_0} = \frac{\alpha\left(\vec{u}^2\right)}{\alpha\left(\vec{w}^2\right)} \cdot \frac{1+\beta_{SR}}{\sqrt{1-\beta_{SR}^2}} = \frac{\alpha\left(\vec{u}^2\right)}{\alpha\left(\vec{w}^2\right)} \cdot \gamma_{SR} \cdot \left(1+\beta_{SR}\right), \tag{1.33}$$

$$\frac{\nu_a}{\nu_0} = \frac{\alpha\left(\vec{u}^2\right)}{\alpha\left(\vec{w}^2\right)} \cdot \frac{1-\beta_{SR}}{\sqrt{1-\beta_{SR}^2}} = \frac{\alpha\left(\vec{u}^2\right)}{\alpha\left(\vec{w}^2\right)} \cdot \gamma_{SR} \cdot \left(1-\beta_{SR}\right). \tag{1.34}$$

By multiplication of both one yields

$$\nu_{\mathrm{a}} \cdot \nu_{\mathrm{p}} = \left[\frac{\alpha\left(\vec{u}^2\right)}{\alpha\left(\vec{w}^2\right)}\right]^2 \cdot \nu_0^2 \,. \tag{1.35}$$

This is equivalent to equation (1.10) except the Lorentz violating factor $\alpha\left(\vec{w}^2\right)/\alpha\left(\vec{u}^2\right)$. Hypothetical deviations from the theory of special relativity can be expressed in even powers of the velocity

$$\left[\frac{\alpha\left(\vec{u}^2\right)}{\alpha\left(\vec{w}^2\right)}\right]^2 = \left[\frac{1+\alpha\cdot\vec{u}^2+\alpha_2\cdot\vec{u}^4+\ldots}{1+\alpha\cdot\vec{w}^2+\alpha_2\cdot\vec{w}^4+\ldots}\right]^2 . \tag{1.36}$$

Developing this in $\vec{w}$ and neglecting all terms that contain a velocity-order higher than two one obtains

$$\left[\frac{\alpha\left(\vec{u}^2\right)}{\alpha\left(\vec{w}^2\right)}\right]^2 \approx 1+2\cdot\alpha\cdot\left(\vec{u}^2-\vec{w}^2\right). \tag{1.37}$$

The velocity of the CMB, that is assumed to be the preferred frame Σ, is measured to $\vec{w}$ = 350 km/s in relation to the laboratory frame S. The particle's velocity $\vec{u}$ with respect to the CMB can not be measured directly, but it is known in relation to the

laboratory frame ($\vec{\beta}$). These three velocities, ($\vec{u}^2 - \vec{w}^2$) and $\vec{\beta}$ can be expressed to second-order approximation by its special relativistic limit

$$\begin{aligned}\left(\vec{u}^2 - \vec{w}^2\right)_{SR} &= 1 - \vec{w}^2 - \frac{\left(1-\vec{w}^2\right)\cdot\left(1-\beta^2\right)}{\left(1+\vec{w}\cdot\vec{\beta}\right)} \\ &\approx \beta^2 + 2\cdot\vec{w}\cdot\vec{\beta}\,.\end{aligned} \tag{1.38}$$

In IS-type experiments with particle velocities of several percentages of the speed of light with respect to the laboratory frame, the contribution of the laboratory velocity (viz. the Earth) with respect to the CMB is considerably small (e.g. TSR experiment $w/\beta = 0.004$) and thus can be neglected. Experiments that are sensitive to the sidereal term $\left(2\cdot\alpha\cdot\vec{w}\cdot\vec{\beta}\right)$ are for instance the Mössbauer rotor experiment [Champeney63], the Gravity Probe A mission [Vessot79] and the TPA by [McGowan93]. The comparison of ground-based hydrogen maser clocks with atomic clocks on GPS satellites leads to the current upper bound of $\alpha < 10^{-6}$ for sidereal effects [Wolf97]. An overview of these experiments is given in appendix A.

On the other hand, if time dilation is probed with particles velocities of several tens of the speed of light (e.g. the present ESR experiment at $\beta = 0.338$), equation (1.36) has to be analysed to higher-order. This is done, till the fourth-order of the velocity, in [Will92] and results in

$$\frac{\nu_a \cdot \nu_p}{\nu_0^2} = 1 + 2\cdot\alpha\cdot\beta^2 + \left(\alpha + 2\cdot\alpha_2\right)\cdot\beta^4\,, \tag{1.39}$$

still neglecting all terms containing $\vec{w}$. From this one finds that the sensitivity on hypothetical deviations of the predictions of special relativity scales with β^2 and β^4, respectively (see Figure 1.5). Nevertheless, one has to be aware that the expansion of the test function in terms of β^2 is appropriate only for reasonably low velocities, compared to the speed of light. For $\beta \to c$ higher-order contributions can not be neglected any more. So this expansion can not be used. In Figure 1.5 the contribution of second-order test parameter α_2, relative to α, is shown as a function of the particle velocity. In experiments performed below $\beta = 0.1$ the α_2 contributions are below 1 % (e.g. at the storage ring experiments in Heidelberg, see chapter 3.5). In contrast, second-order contributions, larger than 10 %, are expected at experiments dealing with particle velocities of more than 50 % of the speed of light. At the present test of time dilation at ESR, particles stored at a speed of $\beta = 0.338$ are used. This leads to a contribution of 5.6 % for the second terms in the MS test theory and a reasonable good sensitivity.

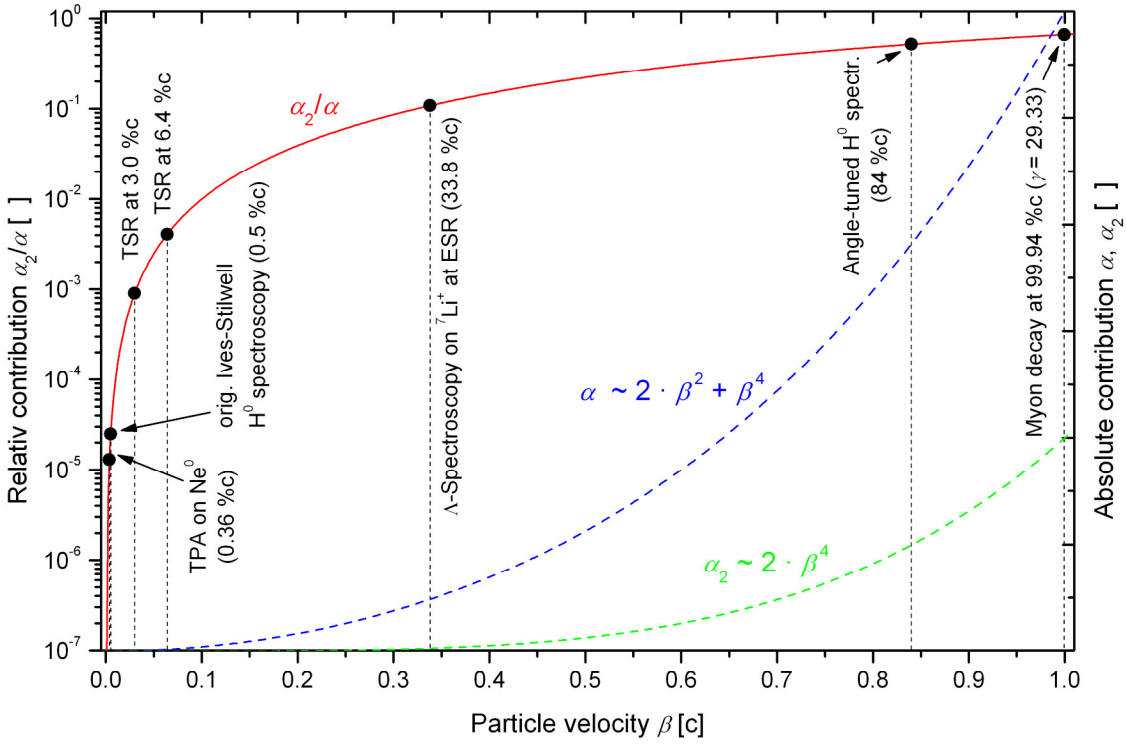

Figure 1.5: Relative and absolute contributions of the MS test parameter α and α_2. The dashed lines give the absolute contribution of the test parameters at different velocities (linear y-scale on the right side). The red curve indicates the relative contribution of α_2 to α (log y-scale on the left side). Only experiments that are not sensitive to sidereal changes ($\vec{\beta} >> \vec{w}$) are inserted. The marked experiments are described in chapter 3.

1.3.3 STANDARD MODEL EXTENSION

The standard model extension (SME) provides the most general observer independent field theoretical framework for investigations of Lorentz and/or CPT violation. The SME-Langrangian by definition contains all Lorentz violating interaction terms that can be written as observer scalars and that involve particle fields in the standard model and gravitational fields in a generalised theory of gravity. This includes all possible terms that could arise from a process of spontaneous Lorentz violation in the context of a more fundamental theory, as well as terms that explicitly break Lorentz symmetry. The SME can be sub-divided into different sectors where a set of parameters quantify hypothetical deviations from the standard model. Each sector has a different number of test parameters (e.g. 19 for photons or n·48 for every particle[8]) which can be quantified by experiment, individually or in combination. Altogether more than hundred test

[8] n is the number of different elementary particles like electrons, protons, neutrons, etc.

parameters are present in the SME. In the following examples of experiments that test certain parameters of the SME are listed (the ESR time dilation experiment is described in the next chapter). For instance, measurements of the Lamor precession frequency of polarised noble gas atoms (^{3}He, ^{129}Xe) during a sidereal day are sensitive to linear combinations of test parameter in the fermion sector. Those experiments look for a coupling of the atomic spins to a hypothetical background field [Gemmel06]. In astronomical measurements (e.g. spectropolarimetry of cosmological sources) the vacuum is tested of being birefringent [Lehnert08]. Or, Penning traps are used for measurements of the anomalous magnetic moment, the charge-to-mass ratio, the cyclotron frequency of different elements or comparing hyperfine Zeeman transitions in hydrogen and antihydrogen which lead to tests of the CPT and Lorentz symmetry [Bluhm98/99]. An overview of other experiments testing the SME and a summary of recent upper limits on the SME the test parameters can be found in [Kostelecký08].

1.3.4 STORAGE RING EXPERIMENTS IN THE SME FRAMEWORK

The standard reference frame in the SME test theory is the non-rotating sun-centred celestial equatorial system. To this frame the earth bound laboratory frame, as well as the rest frame of the ion beam, is related (similar to the MS test theory). The contribution of the time dilation experiments at storage rings in the SME framework was analysed for the photon sector by Tobar et al. [Tobar05] and for the fermion sector by Lane [Lane05]. Later Hohensee et al. reanalysed the photon sector [Hohensee07].

PHOTON SECTOR

One starts with the "normal" QED-Langrangian of the SM

$$L = -\frac{1}{4} \cdot F^{\mu\nu} \cdot F_{\mu\nu} \tag{1.40}$$

where $F_{\mu\nu} \equiv \partial_\mu A_\nu - \partial_\nu A_\mu$, the electromagnetic tensor. In the formalism of the standard model extension L is modified to

$$L = -\frac{1}{4} \cdot F^{\mu\nu} \cdot F_{\mu\nu} - \frac{1}{4} \cdot (k_F)_{\kappa\lambda\mu\nu} \cdot F^{\kappa\lambda} \cdot F^{\mu\nu} + \frac{1}{2} \cdot (k_{AF})^{\kappa} \cdot \varepsilon_{\kappa\lambda\mu\nu} \cdot A^{\lambda} \cdot F^{\mu\nu} \tag{1.41}$$

where A^λ is the 4-potential, $\varepsilon_{\kappa\lambda\mu\nu}$ is the Levi-Civita (permutation) symbol, the $(k_{AF})^\kappa$ terms have the dimension of mass and are CPT odd, the $(k_F)_{\kappa\lambda\mu\nu}$ terms are CPT even and dimensionless [Colladay97^s].

The CPT odd term provides negative contributions to the canonical energy and therefore is a potential source of instability. In good agreement to theory [Colladay97^s]

and consistent with astronomical measurements [Carroll90] the $(k_{AF})^{\kappa}$ terms can be set to zero. Out of the 256 possible combinations of κ, λ, μ and ν for the CPT even parameters, only 19 are independent and remain.

The equations of motion from the modified Langrangian (equation (1.41)) are

$$\partial_\alpha F_\mu^\alpha + \left(k_F\right)_{\mu\alpha\beta\gamma} \partial^\alpha F^{\beta\gamma} = 0\,. \tag{1.42}$$

These equations can be identified as modified Maxwell equations that describe electrodynamics in an anisotropic media instead of a vacuum

$$\begin{pmatrix} D \\ H \end{pmatrix} = \begin{pmatrix} \varepsilon_0 \cdot \left(\widetilde{\varepsilon}_r + \kappa_{DE}\right) & \sqrt{\frac{\varepsilon_0}{\mu_0}} \cdot \kappa_{DE} \\ \sqrt{\frac{\varepsilon_0}{\mu_0}} \cdot \kappa_{HE} & \mu_0^{-1} \cdot \left(\widetilde{\mu}_r^{-1} + \kappa_{HB}\right) \end{pmatrix} \cdot \begin{pmatrix} E \\ B \end{pmatrix} \tag{1.43}$$

where the κ-matrices are rank 3 and derived by linear combinations of the CPT even terms [Colladay97[s]]. $\widetilde{\varepsilon}_r$ and $\widetilde{\mu}_r$ are 3×3 matrices if the medium of interest has general magnetic dielectric properties. In vacuum $\widetilde{\varepsilon}_r$ and $\widetilde{\mu}_r$ are identity matrices. The rank of the modified Maxwell equations is 6 and converges to the standard Maxwell equations in vacuum when the κ-matrices are set to zero. Thus the effect of the SME in the photon sector can be interpreted as introducing medium-like properties to the vacuum. The κ-matrices are all position dependent and can be combined to birefringent and non-birefringent terms [Colladay97[s]].

For the interpretation of storage ring experiments, Tobar et al. assumed that Lorentz transformation is still valid for matter and $\widetilde{\varepsilon}_r$ and $\widetilde{\mu}_r$ are identity matrices. Or in other words, the transition frequency is affected only by violations in the photon sector via radiative corrections (e.g., Lamb shift). The matter sector is kept Lorentz invariant (for violations in this sector see next paragraph). They found that in principle

$$\frac{\nu_\mathrm{a} \cdot \nu_\mathrm{p}}{\nu_0^2} = 1 + \varepsilon_{LV}(t) \tag{1.44}$$

where $\varepsilon_{LV}(t)$ is (in general) a time varying term, which characterises hypothetical Lorentz violations in the SME framework. Using standard Lorentz transformation and requiring that both laser frequencies $(\nu_\mathrm{a}, \nu_\mathrm{p})$ are in resonance with the same transition one obtains

$$\nu_\mathrm{a} = \nu_0 \cdot \frac{\sqrt{1-\beta^2}}{1+\beta\cdot\left(c/c_\mathrm{a}\right)} \text{ and } \nu_\mathrm{p} = \nu_0 \cdot \frac{\sqrt{1-\beta^2}}{1-\beta\cdot\left(c/c_\mathrm{p}\right)} \tag{1.45}$$

where $c_{a,p}$ are the phase velocities from the parallel and the antiparallel laser beams. These are related to the trace of the κ_{DE}-tensor divided by 3 (κ_{tr}). After some calculation [Tobar05, Hohensee07] one finds, for the lowest-order in κ_{tr}, that

$$\frac{\nu_a \cdot \nu_p}{\nu_0^2} = 1 + 2 \cdot \kappa_{tr} \cdot \left[\beta^2 + 2 \cdot \vec{\beta} \cdot \vec{\beta}_\oplus(t)\right] + O\left(\kappa_{tr}^2\right) \tag{1.46}$$

where $\vec{\beta}_\oplus(t)$ represents the sinusoidal varying velocity vector of the Earth's motion in the Sun-centred frame. Hence, $\beta >> \vec{\beta}_\oplus(t)$ the time-dependent sidereal term can be neglected, which leads to the fact that the bound on κ_{tr} is equivalent to a bound on α of the MS test theory.

FERMION SECTOR

Charles D. Lane analysed the storage ring experiment in the fermion sector of the SME. Such a test of time dilation is sensitive to various combinations of Lorentz violating parameters that are related to the proton an electron sector. A detailed description and calculation of all parameters is given in [Lane05]. In general, influences in the fermion sector of the SME, for spectroscopy experiments at storage rings, can be described by

$$\frac{\bar{\nu}_{beam}^2}{\nu_0^2} = 1 + \frac{2}{\nu_{SM}} \cdot \left(\delta\bar{\nu}_{beam} - \delta\nu_0\right) \tag{1.47}$$

where $\bar{\nu}_{beam}^2 = \nu_a \cdot \nu_p$ viz. the product of both laser frequencies measured in the laboratory frame, ν_0 is the rest frequency of the excited transition, ν_{SM} is the conventional frequency (according to the standard model), and $\delta\bar{\nu}_{beam}$ and $\delta\nu_0$ are shifts induced by the SME. The experimental quantities for the TSR experiment[9] can be summarised to

$$\frac{\bar{\nu}_{beam}^2}{\nu_0^2} \approx 1 - \frac{1}{3 \cdot \pi \cdot \nu_{SM}} \times \sum_{w=p,e} \gamma_w \cdot \left[\frac{1}{6} \cdot \beta^2 \cdot C_Q^w + \beta^2 \cdot \beta_\oplus \cdot \left(\frac{3}{2} \cdot C_{TX}^w - \frac{3}{2} \cdot C_{TY}^w - C_{TZ}^w\right)\right] \tag{1.48}$$

where $C_Q^w = m^w\left(c_{XX}^w + c_{YY}^w + 2 \cdot c_{ZZ}^w\right)$ and $C_{TJ}^w = m^w\left(c_{TJ}^w + c_{JT}^w\right)$; $(J = X, Y, Z)$.

w is p for the proton and e for the electron, m^w is the mass and c_{tj}^w is the quadrupole parameter of the corresponding particle. γ_w is given by the nuclear Schmidt model for protons and standard atomic calculations for electrons, respectively.

[9] TSR = test storage ring at the Max Planck Institute in Heidelberg, see chapter 3.5.

2 THE LITHIUM ION

To attain high sensitivity on the test-parameters $\left(\text{e.g. } \alpha, \alpha_2, \kappa_{tr}\right)$, high velocities are favourable. Therefore charged particles i.e. ions are used which can be easily accelerated by electric and captured by magnetic fields. To apply precision spectroscopy on fast particles some technical conditions have to be fulfilled: The particles should have a strong electric dipole transition (E1) within the optical frequency range that can be excited by lasers. The linewidth of this transition should be sufficiently narrow to allow for an accurate determination of the line centre.

2.1 PROPERTIES OF $^7Li^+$

For the time dilation experiment at the ESR as well as at the TSR the helium-like lithium ion in the metastable triplet state $2s^3S_1$ is the best choice. The small mass-over-charge ratio allows for highest ion velocities, the hyperfine-structure splitting (hfs) is much larger than the Doppler-width of the cooled ion beam (as will be shown later) and the transition frequencies are well measured. Both lithium isotopes ($^6Li^+$, and $^7Li^+$) were used in previous experiments, testing special relativity at the TSR. Due to the larger hfs[10] and the higher natural abundance (97 %), the latest measurements, at an ion velocity of 3.0 %c or 6.4 %c were done with $^7Li^+$ at the $2s^3S_1 \rightarrow 2p^3P_2$ transition. The lifetime of the upper $2p^3P_2$ state is τ_{3P2} = 43 ns. This corresponds to a reasonably narrow natural linewidth of $\Delta\nu_{3P2}$ = 3.7 MHz[11]. At the ESR half of the excited ions decay within a flight distance of 4.3 m (after excitation) what is well inside the field-free experimental section (20 m). For the experiment, the lithium ions need to be excited into the metastable triplet state which lies 59.02 eV above the singlet ground state $1s^1S_0$ and has a lifetime of (52.2 ± 5.0) s in vacuum [Saghiri99], determined by the M1 decay channel (see Figure 2.1). A second very weak loss-mechanism is the two-photon decay (four orders of magnitude weaker than the M1 channel). However, at finite pressures the lifetime in storage rings is decreased by interactions of the ions with residual gas and the cooling-electrons. At excellent ESR vacuum conditions of < 10^{-11} mbar a storage time of 50 s was measured. This value drops to insufficient 2 s if the residual gas pressure increases to ~ 10^{-9} mbar.

---

[10] Hfs in $^6Li^+$ = 1-6 GHz; hfs and in $^7Li^+$ = 6-20 GHz.

[11] All linewidths are given in full-width half-maximum (FWHM) values.

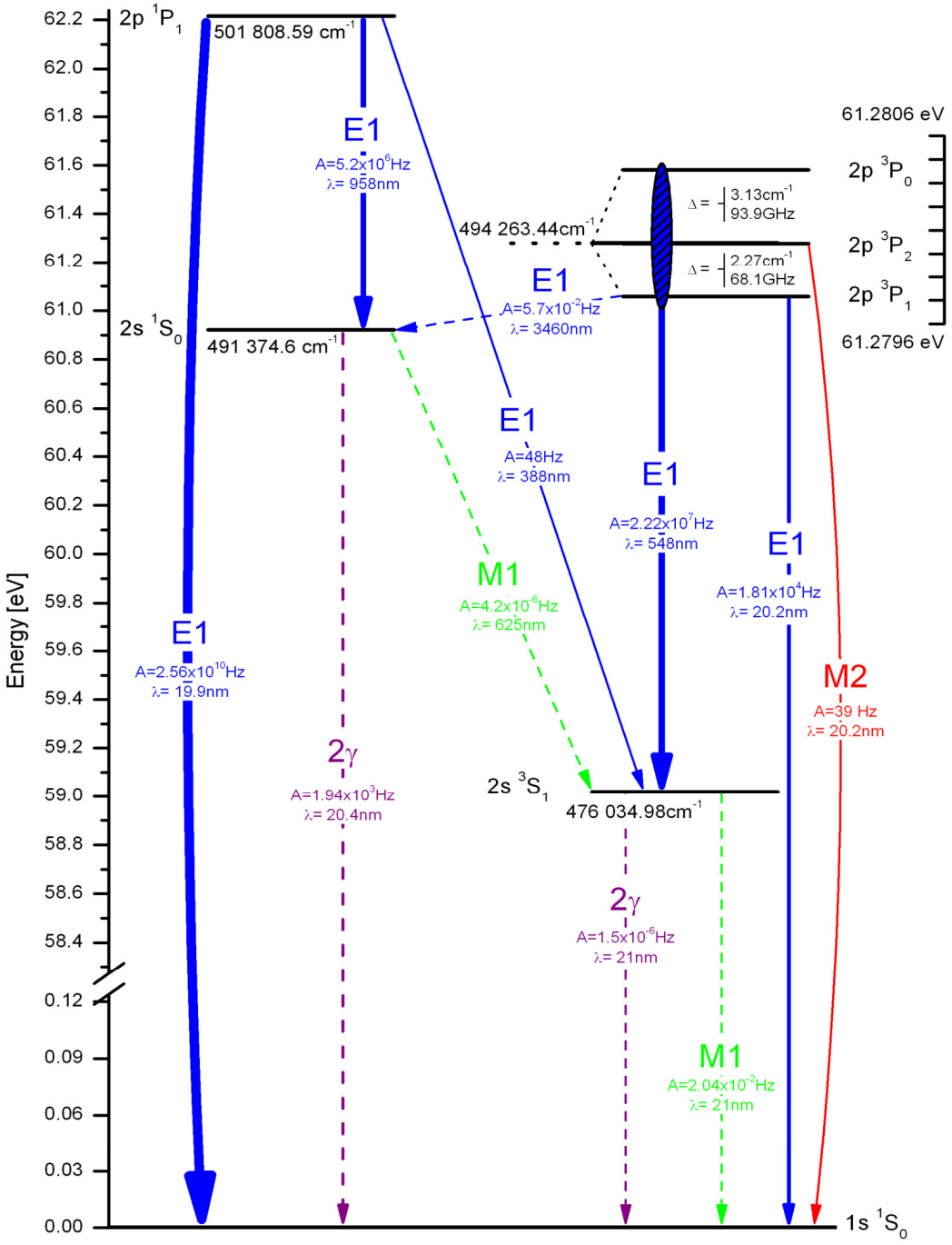

Figure 2.1: Possible radiative and non-radiative transitions in a $^7Li^+$ ion, including strongly suppressed inter-combination lines from a singlet to a triplet state. The wave numbers quantify the distance of the states from the $1s^1S_0$ ground state. (E1: electric dipole transition, M1: magnetic dipole transition, M2: magnetic quadrupole transition, 2γ: two photon transition.)

The $2s^3S_1$ is connected to the $2p^3P_{1,2,3}$ state via the required strong E1 transition ($A = 2.22 \times 10^7$ Hz)[12] at a wavelength of 548.5 nm. The fine-structure of this excited state splits into three levels which are separated by $\Delta\nu_{12} = 68$ GHz and $\Delta\nu_{23} = 94$ GHz, respectively[13]. Further, the hyperfine states are separated by a gap of 6-11 GHz. Three different kinds of spectroscopy techniques that gain signals with sub-Doppler linewidths are allowed by electron-excitation from the $2s^3S_1$ ground state to the $2p^3P_2$ state by the hyperfine-structure splitting (see Figure 2.2). A closed two level system ($F = {}^5/_2$) → ($F = {}^7/_2$) can be used for saturation spectroscopy. Λ-spectroscopy can be applied on two different closed three level systems that are coupled by the excited state:

1. $2s^3S_1$ ($F = {}^5/_2$) → $2p^3P_2$ ($F = {}^5/_2$) and $2s^3S_1$ ($F = {}^3/_2$) → $2p^3P_2$ ($F = {}^5/_2$)
2. $2s^3S_1$ ($F = {}^1/_2$) → $2p^3P_2$ ($F = {}^1/_2$) and $2s^3S_1$ ($F = {}^3/_2$) → $2p^3P_2$ ($F = {}^1/_2$)

The third technique uses a closed three level V-system, where two excited states are coupled via the ground state $2s^3S_1$ ($F = {}^5/_2$) → $2p^3P_2$ ($F = {}^5/_2$) and $2s^3S_1$ ($F = {}^5/_2$) → $2p^3P_2$ ($F = {}^7/_2$).

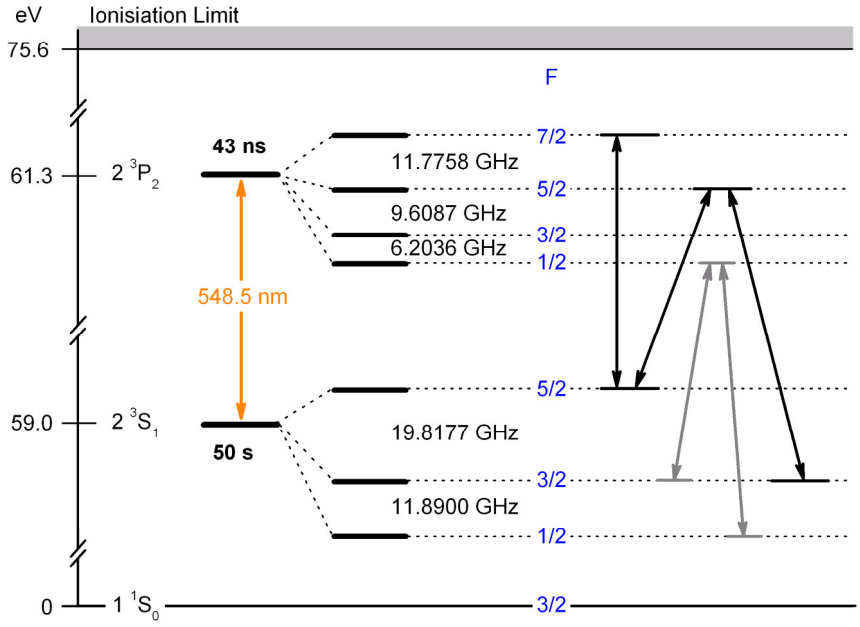

Figure 2.2: Level-scheme of the triplet system in $^7Li^+$. It contains two closed Λ-type systems, which can be used for first-order Doppler-free spectroscopy. Further the closed two-level system is suitable for both, ion beam diagnosis and first-order Doppler-free saturation spectroscopy.

[12] A = Einstein-coefficient for spontaneous emission in [Hz].

[13] The indices at $\Delta\nu$ indicate the fine-structure quantum numbers of the two $2p^3P_2$ levels.

Beside the mentioned strong E1 transition, another weak M2 decay channel from the excited $2p^3P_2$ to the $1s^1S_0$ ground state exists. However, this is a factor 10^7 less efficient than the dominant E1 process. The saturation intensity for lithium, using a laser with a linewidth of $\Delta\nu_{\text{Laser}} \approx 1$ MHz, is 6.7 mW/cm^2 [Wanner98].

For the time dilation experiment the absolute frequency of the lithium at rest has to be known very accurately. Over several years, different experiments have reported strongly disagreeing results [Riis94, Rong98]. In 2003 Clarke et al. remeasured the fine-structure and hyperfine-structure splitting of both lithium isotopes. Their results are in good accordance to the measurements of Riis et al. and therefore give a clear statement for the correctness of the experiment. Furthermore, their measurements are in excellent agreement with theoretical calculations [Clarke03]. In 2007, a new value for the absolute rest frequency of the $2s^3S_1$ ($F = {}^5/_2$) $\rightarrow$ $2p^3P_2$ ($F = {}^7/_2$) transition in $^7Li^+$ of (546 466 918.531 ± 73) kHz was presented [Reinhardt07a]. It was derived from the TSR measurements at two different ion velocities (assuming Lorentz invariance is not violated), and is in well agreement with [Riis94], but five times more precise. In Table 2.1 used the frequencies are listed.

Table 2.1: Transition frequencies of the $^7Li^+$ ion which are relevant for the experiment, testing time dilation in storage rings

Transition	Frequency [MHz]	Reference
electronic transition		
$2s^3S_1$ ($F = {}^5/_2$) → $2p^3P_2$ ($F = {}^7/_2$)	546 466 918.531(73) 546 466 918.79(40)	Reinhardt07a Riis94
hyperfine-structure splitting		
$2s^3S_1$ ($F = {}^3/_2$) → $2s^3S_1$ ($F = {}^5/_2$)	19 817.673(13) 19 817.90(24) 19 817.680(25)	Kowalski83 Clarke03 Riis94 (theory)
$2p^3P_2$ ($F = {}^5/_2$) → $2p^3P_2$ ($F = {}^7/_2$)	11 775.8(2) 11 774.04(31) 11 773.05(18)	Kowalski83 Clarke03 Riis94 (theory)

2.2 LINEWIDTH TRANSFORMATION

Usually linewidths are given in the rest system of the considered particle. Hence, the linewidths that are measured in the storage ring experiments have to be transformed from the laboratory system to the rest frame of the ion. For a transition in an ion that is moving with a relativistic velocity we have in general

$$\nu_1 = \nu_a \cdot \gamma \cdot (1+\beta) \tag{2.1}$$

and

$$\nu_2 = \nu_p \cdot \gamma \cdot (1-\beta). \tag{2.2}$$

ν_1 and ν_2 are the rest frame frequencies, ν_a and ν_p denote the laser frequencies in the laboratory frame. The lasers are assumed to be in the antiparallel and collinear alignment scheme (compare Figure 5.1c) that allows for a test of special relativity. Adding these equations one yields

$$\nu_1 + \nu_2 = \nu_a \cdot \gamma \cdot (1+\beta) + \nu_p \cdot \gamma \cdot (1-\beta). \tag{2.3}$$

Let ν_a be the frequency of the tunable laser and ν_p be fixed. In spectroscopy experiments at storage rings the linewidth $\Delta\nu_a$ is observed as a function of the linewidths $\Delta\nu_1$ and $\Delta\nu_2$, in terms of the laboratory frame. Solving equation (2.3) for ν_a results in

$$\nu_a = \frac{\nu_1 + \nu_2 - \nu_p \cdot \gamma \cdot (1-\beta)}{\gamma \cdot (1+\beta)}. \tag{2.4}$$

To find $\Delta\nu_a$ error progression is used. Here, $\Delta\nu_p$ can be neglected since ν_p is fixed and the linewidth of the laser for parallel excitation is considerably narrower than $\Delta\nu_2$. One gets

$$\Delta\nu_a = \frac{\Delta\nu_1 + \Delta\nu_2}{\gamma \cdot (1+\beta)} \tag{2.5}$$

in the case of V- and Λ-type spectroscopy. In the case of saturation spectroscopy, where $\nu_1 = \nu_2 = \nu_0$ and therefore $\Delta\nu_1 = \Delta\nu_2 = \Delta\nu_0$ one finds

$$\Delta\nu_a = \frac{2 \cdot \Delta\nu_0}{\gamma \cdot (1+\beta)}. \tag{2.6}$$

3 TIME DILATION EXPERIMENTS

This chapter gives an overview of different experiments probing the predictions of special relativity for time dilation. The described experiments are sensitive only to non-sidereal effects. Experiments sensitive to sidereal fluctuations are discussed in appendix A. This list is not exhaustive but shows the history of time dilation tests from the original Ives-Stilwell experiment to the recent measurements at storage rings. Further comparisons of time dilation experiments can be found in [MacArthur86a] or [Zhang97] (for instance, measurements performed on rotating disks using the Mössbauer-effect [Champeney63] or satellite based experiments [Wolf97]). A detailed discussion of those experiments in terms of the MS test theory is reported in [Will92, Gwinner05].

3.1 THE ORIGINAL IVES STILWELL EXPERIMENT

Already in 1938, Ives and Stilwell carried out a measurement on fast hydrogen atoms in canal rays [IS38 and IS41]. This was the first experiment that measured the time dilation directly. They observed the emission of the Hβ-line (λ_0 = 486.1 nm) in and against the direction of motion of the hydrogen with a spectrograph (Figure 3.1). The velocity of the hydrogen atoms was $\upsilon = 0.005\ c$. So, the observed wavelengths should obey the relations $\lambda_- = \lambda_0 \cdot \gamma \cdot (1-\beta)$ for light emitted in flight direction and $\lambda_+ = \lambda_0 \cdot \gamma \cdot (1+\beta)$ for light that is emitted against the direction of motion. Whit these relations the effect of the transversal and of the longitudinal Doppler effect can be measured. By calculating the mean value of both measured wavelengths one finds the contribution of time dilation

$$\lambda_{\text{mean}} = \frac{\lambda_+ + \lambda_-}{2} = \gamma \cdot \lambda_0 \tag{3.1}$$

which leads to the transversal Doppler-shift

$$\Delta\lambda_{\text{tr}} = \lambda_{\text{mean}} - \lambda_0 = \frac{\lambda_0}{\sqrt{1-\beta^2}} - \lambda_0 \approx \frac{1}{2} \cdot \lambda_0 \cdot \beta^2 . \tag{3.2}$$

The velocity of the atoms was determined by the measurement of the longitudinal Doppler-shift (viz measuring the separation of the lines $\Delta\lambda_{\text{long}} = \lambda_0 - \lambda_+ \approx \lambda_0 \cdot \beta$, assuming $\gamma \approx 1$). With this experiment time dilation could be confirmed, expressed in terms of the MS test parameter [MS77c], to $|\alpha| < 10^{-2}$.

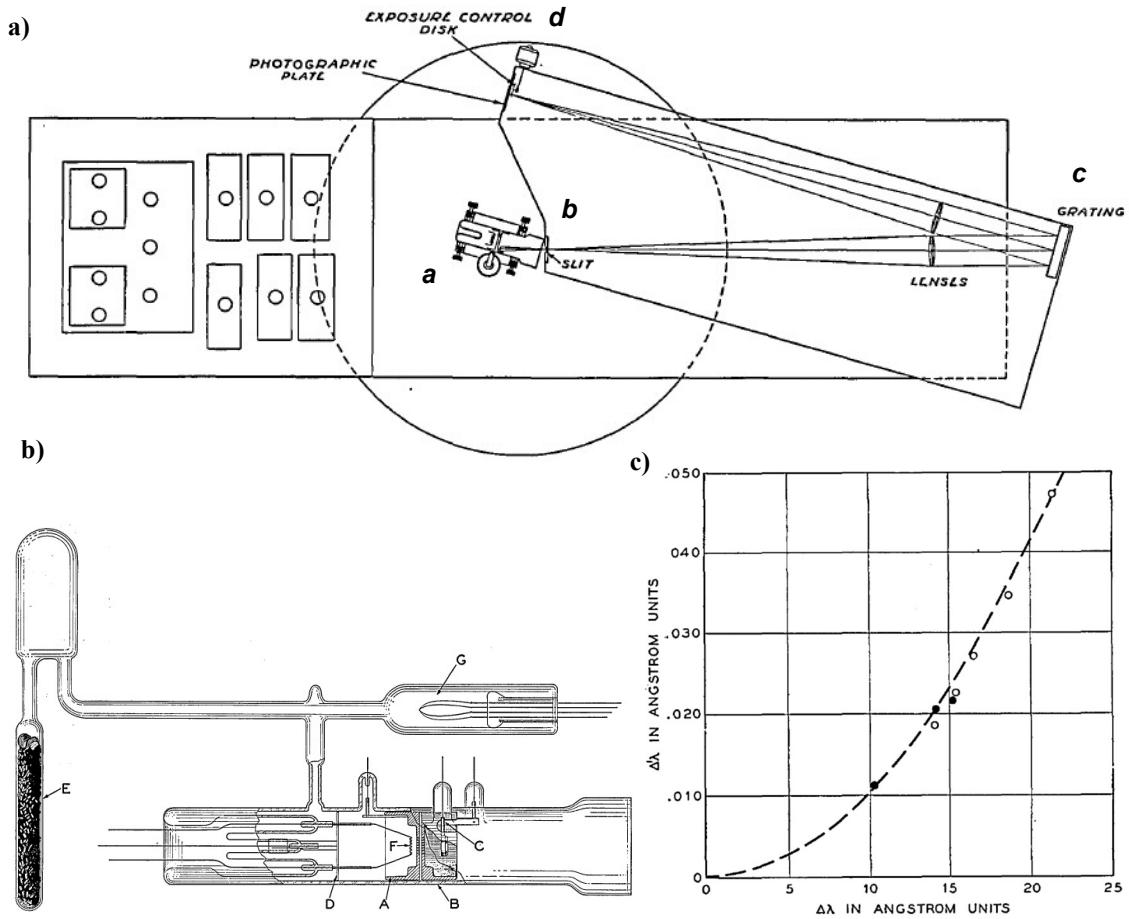

Figure 3.1: a) Top view on the experiment setup with the canal ray tube *a*, the entrance slit to the spectrograph *b* and the metal grating *c* to bring the Hβ lines on the photographic plate *d*. b) The canal ray tube: positive particles were produced in a hydrogen arc between the oxide coated filaments F and the grounded element of the double electrode A and B, the discharge being constricted to the desired region by the shielding electrode D. In the double electrode between which the accelerating field is applied, 1 mm diameter holes are drilled to provide a positive canal ray beam approximately 1 cm square. In front of electrode B an aluminium coated spectacle lens is placed, which images the slit of the spectrograph (placed 2 cm in front of the observation window) upon itself. The hydrogen was stored in the side tube E and the relative gas pressure was measured by a thermocouple gauge G. c) Computed (dashed line) and observed second-order shifts (at different electrode voltages) plotted against first-order Doppler-shifts of H_2 (white circles) and H_3 (black circles). The agreement is within the probable errors of the measurements [IS38].

3.2 MUON DECAY

At the CERN muon storage ring an experimental series with highly relativistic muons was performed in the late 70ies by Bailey et al. [Bailey77, Bailey79]. An overview of the setup and a plot of the muon data is given in Figure 3.2. The lifetime of positively charged muons which are stored at a maximum velocity of $\beta = 0.9994$ (or $\gamma \approx 29.3$), was measured and compared to the prediction of special relativity. They found an agreement between the observed and expected time dilation factor at the 0.1 % level. Naively, this corresponds to an upper bound for deviations of α from zero of $|\alpha| < 5 \times 10^{-4}$, a value not competitive with modern low-velocity experiments. However, one has to remember, that the expansion in terms of β^2 for the test parameter is not appropriate for such particle velocities. Although the muon lifetime result is not comparable to other experiments in a straightforward way, it offers the possibility to test the validity of special relativity under extreme conditions (e.g. continuous acceleration of the muons by $10^{16}\, g$)[14].

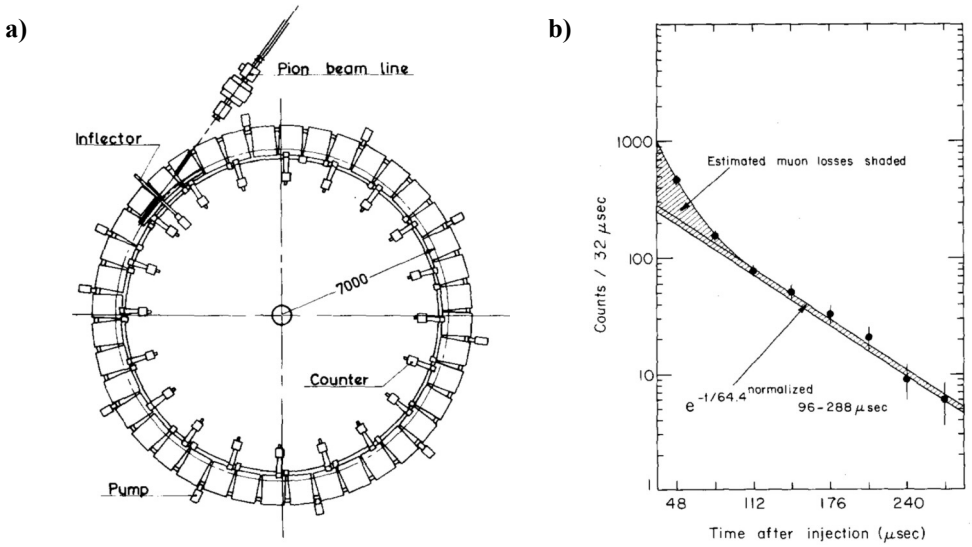

Figure 3.2: a) Plan view of the muon storage ring (radius = 7 m, 40 bending magnets producing a field of 1.47 T and 22 electron detectors are nearly uniform distributed around the ring). The muons were generated by shooting bunched protons on a copper target (which is placed at the injection to the storage ring) to produce pions which enter the storage ring and decay in flight into muons. The produced muons had a momentum of 3.1 GeV/c and a velocity of $\gamma = 29.3$ which lead to a dilated lifetime of 64 μs (2.2 μs in the muons' frame). The lifetime was measured by detecting the decay electrons. b) Raw spectrum of the muon counts. The total estimated muon loss is shaded, the remainder of the spectrum due to misidentified decay electrons [Bailey79].

[14] The authors of [Bailey77] stated that the muons are accelerated by 10^{18}g. This value results from an improper transformation of the muon velocity into terms of the gravitational acceleration *g*. Indeed it is $10^{16}\, g$.

3.3 ANGLE-TUNED SPECTROSCOPY ON HYDROGEN

MacArthur et al. used a beam of atomic hydrogen at β = 0.84 to test time dilation [MacArther86b]. They excited the hydrogen from the well known 1s ground state to different np levels, by the use of the 4th harmonic of a Nd:YAG laser (E_0 = 4.66 eV). The photon energy, seen by the hydrogen atoms, is varied by changing the angle between the laser beam and the atomic beam. The energy E in the rest frame of the hydrogen, written in the generalised transformation of Robertson, is

$$E = \frac{E_0}{g_0} \cdot \gamma \cdot (1 + \beta \cdot \cos\phi) \tag{3.3}$$

where ϕ is the angle between the hydrogen beam and the laser beam. A sketch of the setup and the typical spectrum is shown in Figure 3.3. With this experiment the test parameter g_0 is determined and verified to be equal to unity with an accuracy of 2.7×10^{-4}. This leads to an upper limit for α of $|\alpha| < 2.0 \times 10^{-4}$.

However, using more accurate low-velocity bounds for α, this experiment can set a strong limit for the second-order test parameter α_2. Regarding equation (1.39) where only $\vec{w}$-independent terms are considered one gets

$$\alpha + \left(\frac{1}{2} \cdot \alpha + \alpha_2\right) \cdot \beta^2 < 2.0 \times 10^{-4}. \tag{3.4}$$

Using the recent upper limit for $|\alpha| < 8.4 \times 10^{-8}$ [Reinhardt07a] a limit for α_2 can be derived to $|\alpha_2| < 2.8 \times 10^{-4}$.

a)

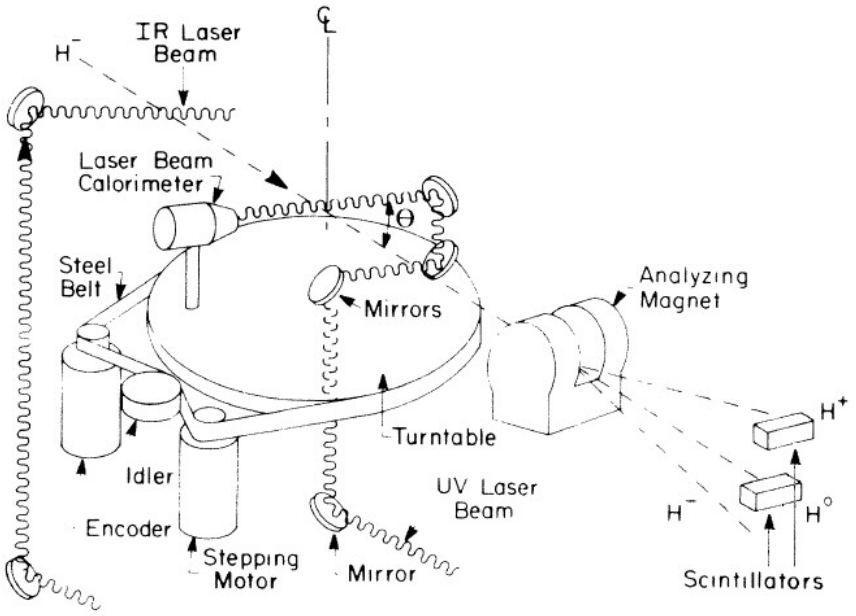

b)

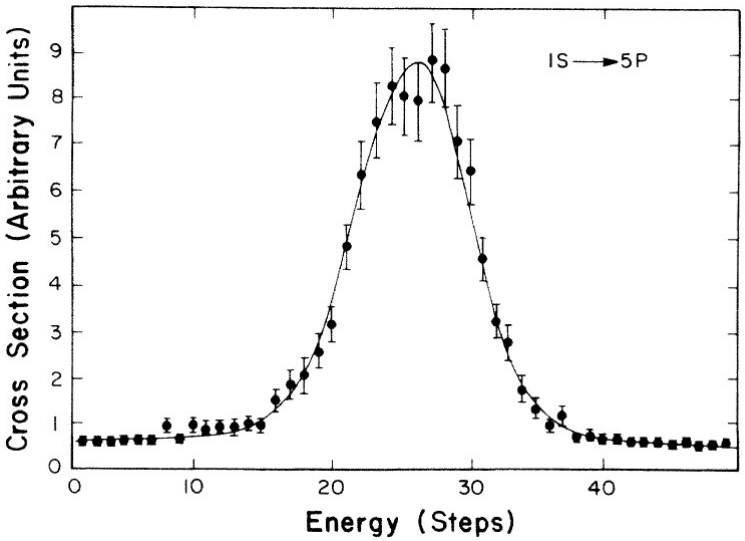

Figure 3.3: a) Schematic of the photodetachment apparatus. The upstream infrared laser beam creates H^0 atoms from the H^- ions in the LAMPF[15] beam by photodetachment (kinetic energy of the H^- beam: 800 MeV). The UV laser beam crosses the relativistic H^0 beam at the centre of the chamber; the pulsed laser beam is aligned to enter the chamber along the vertical axis of the rotating optical bench and is directed across the interaction region by mirrors mounted on the optical bench. A calorimeter monitors the laser beam intensity. The downstream analysing magnet's motional electric field ionises hydrogen atoms excited to states of $n > 3$ and then directs the resulting H^+ ions into a detector; the H^+ scintillation signals are observed in coincidence with the laser pulses. A stepping motor turns the rotating optical bench 360° with a minimum increment of 30.2 μrad. The angle θ between the particle beam and the UV laser beam is measured by an optical shaft-angle encoder. b) Data points and a fit of Gaussian line shape for a 1s to 5p resonance line. The energy scale corresponds to 0.85 MeV per step [MacArther86b].

[15] LAMPF = Los Alamos meson physics facility.

3.4 TWO-PHOTON ABSORPTION IN NEON

Several experiments were carried out using two photon absorption (TPA) on a neon beam. The original experiment in 1985 from Kaivola et al. measured the frequency difference between the transition in the (fast) neon beam (at $\beta = 0.0036$) and a cell filled with neon gas at thermal conditions (see Figure 3.4 and [Kaivola85]). They applied counter-propagating laser beams of equal frequency ν_L for TPA and cancelled out the first-order Doppler effect. The atoms were excited from an initial level to an excited state via an intermediate level. The laser frequency was controlled so that the two photons could accomplish the required two-photon transition, whereas the atomic beam velocity was controlled for the intermediate transition to occur. Will et al. analysed this experiment in the framework of the MS test theory in [Will92] to

$$\nu_L = \sqrt{\nu_1 \cdot \nu_2} \cdot \left(1 + \alpha \cdot \beta^2 + 2 \cdot \alpha \cdot \vec{\beta} \cdot \vec{w} + \ldots\right). \tag{3.5}$$

$\vec{w}$ is the velocity of the laboratory with respect to the preferred frame, ν_1 and ν_2 are the transition frequencies of the two-photon transition in the rest frame of the neon beam.

The non-sidereal term $\alpha \cdot \beta^2$ was investigated in [Kaivola85] and gave an upper limit of $|\alpha| < 4 \times 10^{-5}$. In 1988, the sidereal part $2 \cdot \alpha \cdot \vec{\beta} \cdot \vec{w}$ was investigated by Riis et al. and resulted in an upper limit of $|\alpha| < 1.4 \times 10^{-6}$ [Riis88]. In 1992, McGowan et al. improved the limit to $|\alpha| < 2.3 \times 10^{-6}$ in the non sidereal term by remeasuring with more accurate references [McGowan93].

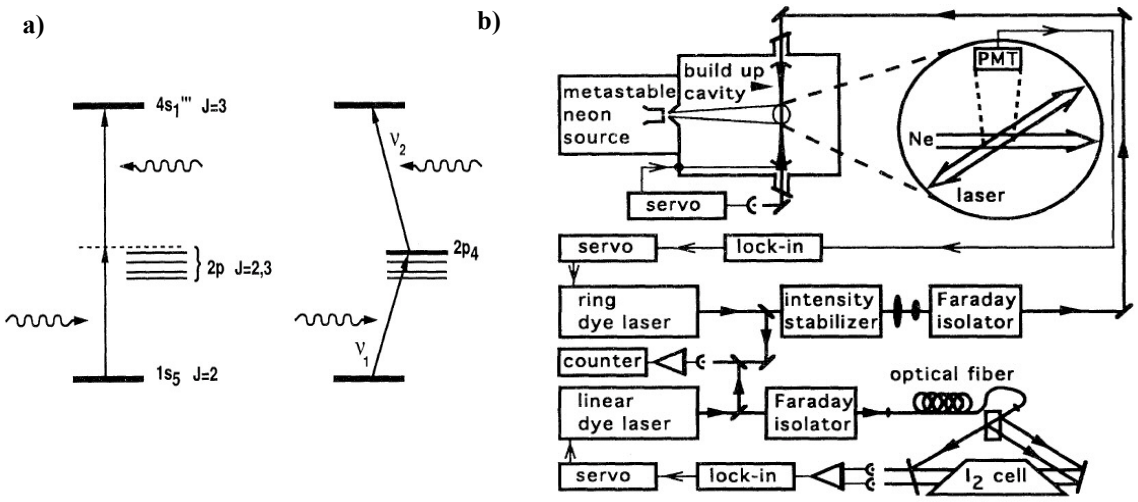

Figure 3.4: a) Partial level diagram of neon. Left: two-photon transition in a thermal neon gas is an off resonant process. Right: In the fast ion beam, an intermediate level is Doppler tuned into resonance. b) Schematic of the thermal neon gas cell experiment. The apparatus includes a two-photon spectrometer consisting of a metastable beam excited by a ring dye laser, a saturation spectrometer consisting of an I_2 cell excited by a linear dye laser, and a heterodyne setup for measuring the frequency difference of the two lasers. PMT: photomultiplier tube. [McGowan93]. The setup for excitation of a fast ion beam is comparable to the setup for the thermal neon experiment and described in [Riis88].

3.5 STORAGE RING EXPERIMENTS ON LITHIUM

The advent of heavy-ion storage rings equipped with electron cooler devices in the late 1980s opened up the possibility of performing precision laser spectroscopy on ion beams at $\beta >> 0.01$. In 1988, Huber et al. proposed an experiment providing the potential to improve all performed tests of time dilation [Huber88]. Hereupon a measurement program at the TSR heavy-ion storage ring was started with lithium ions at a velocity of $\beta = 0.064$ (the highest velocity at which $^7Li^+$ can be stored in the TSR) [Klein91]. They used the same closed three-level system with a common upper level and two different ground levels for Λ-type spectroscopy as in the present work ($2s^3S_1$ ($F = {}^5/_2$) → $2p^3P_2$ ($F = {}^5/_2$) and $2s^3S_1$ ($F = {}^3/_2$) → $2p^3P_2$ ($F = {}^5/_2$)). In the experiment two laser beams were aligned in and against the flight direction of the ions. Each laser frequency had to fulfil the resonance condition for one leg of the Λ-system in its corresponding alignment (see Figure 3.5). The laser frequencies were maintained by comparing these with transitions in molecular iodine. In the notation of the MS test theory this leads to a sensitivity to α of

$$\frac{\nu_a \cdot \nu_p}{\nu_1 \cdot \nu_2} = 1 + 2 \cdot \alpha \cdot \beta^2 \tag{3.6}$$

where ν_a and ν_p are the laser frequencies antiparallel and parallel to the ion beam. ν_1 and ν_2 are the transition frequencies between the two ground states and the upper state. From this, an upper bound for deviations of α from zero of $|\alpha| < 1.5 \times 10^{-5}$ was obtained. In 1994, Grieser et al. improved this value by introducing more accurate frequency references and reducing systematic uncertainties to $|\alpha| < 8 \times 10^{-7}$ [Grieser94]. A typical spectrum of the Λ-type spectroscopy compared to molecular iodine references is shown in Figure 3.5b. This result was limited by the fact that mechanisms in the storage ring are present (e.g. electron cooling, intra-beam scattering) which change the velocity class of an ion during several circulations in the ring and therefore shift it in- or off-resonance with the lasers. This causes a line-broadening and lowers the accuracy in frequency determination.

In 2003, Saathoff et al. obtained a new upper limit, by changing the spectroscopy scheme from the Λ-type to a closed two-level saturation regime ($2s^3S_1$ ($F = {}^5/_2$) → $2p^3P_2$ ($F = {}^7/_2$)) [Saathoff03]. In contrast to the previous, this saturation-type spectroscopy is less sensitive to velocity-changing collisions because both lasers interact always simultaneously with the ions and therefore does not suffer from this line-broadening mechanism. However, the laser setup remains comparable (see Figure 3.6a) while the fluorescence signal turns from a peak into a narrow dip (compare Figure 3.6b and chapter 5). In this case, the resonance condition within the theory of special relativity is

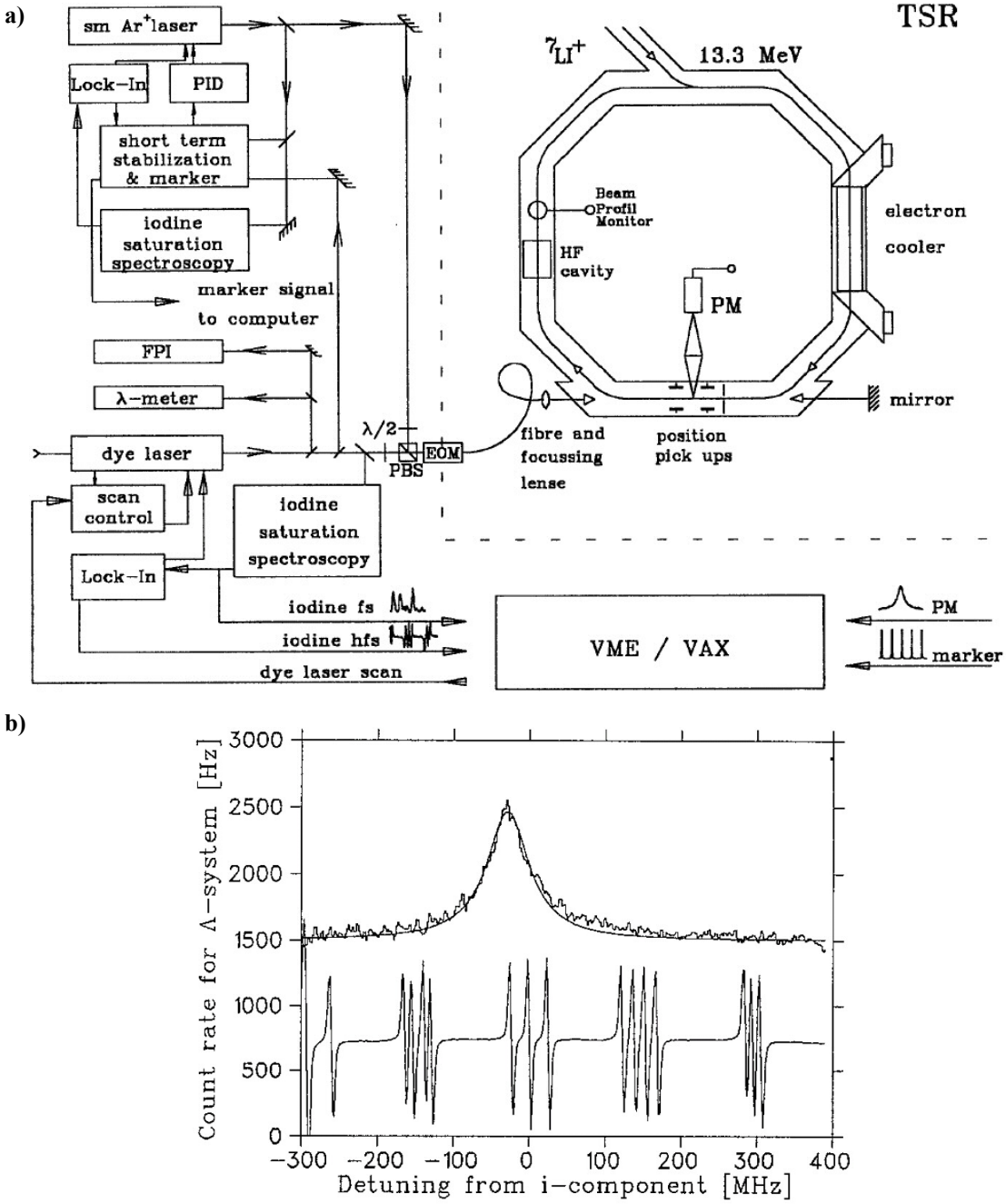

Figure 3.5: a) Schematic of the setup used in [Klein91] and [Grieser94] for a test of time dilation at the TSR. An argon ion laser is frequency locked to an $^{127}I_2$ hfs component and a tunable dye laser is frequency controlled by comparing to some $^{127}I_2$ hfs lines. The laser beams are combined in a polarisation beam splitter (PBS) and fed into one single mode fiber, overlapped with the ion beam and retro reflected by a mirror after one pass through the storage ring section. A $\lambda/4$ plate is used to match the polarisation of the counterlinearly exciting dye laser beam and the collinearly exciting Ar^+ laser beam. The induced fluorescence is monitored by photomultipliers (PM). b) Typical fluorescence signal from a multiple scan of the Λ resonance compared to some $^{127}I_2$ hfs lines.

$$\nu_a \cdot \nu_p = \nu_0^2, \tag{3.7}$$

where ν_0 is the frequency of the closed two-level transition at rest and ν_p and ν_a are the resonance frequencies in and against the flight direction of the ion. In the MS formalism this reads

$$\frac{\nu_a \cdot \nu_p}{\nu_0^2} = 1 + 2 \cdot \alpha \cdot \beta^2 . \tag{3.8}$$

The resonance frequencies, obtained in this experiment, were compared to transitions in molecular iodine that were known to an accuracy of better than 200 kHz. This means a relative frequency accuracy of $\Delta\nu/\nu = 1 \times 10^{-9}$ and yields a new upper limit for α of $|\alpha| < 2.2 \times 10^{-7}$ [Saathoff03].

The leading uncertainty in the measurement was a relatively weak accuracy of the rest frequency ($\Delta\nu_0$ = 400 kHz, [Riis94]) of the lithium ion, compared to other errors. Moreover, a second rest frequency measurement exists [Rong98] that differs by more than two standard deviations. To overcome this limitation the same spectroscopy experiment was set up at a second ion velocity β = 0.030 (the lowest velocity $^7Li^+$ can be stored in the TSR). Combining both measurements, one derives in terms of MS

$$\frac{\nu_a^{(2)} \cdot \nu_p^{(2)}}{\nu_a^{(1)} \cdot \nu_p^{(1)}} = \frac{1 + 2 \cdot \alpha \cdot \beta_2^2}{1 + 2 \cdot \alpha \cdot \beta_1^2} \approx 1 + 2 \cdot \alpha \cdot \left(\beta_2^2 - \beta_1^2\right). \tag{3.9}$$

$\nu_a^{(1,2)}$ and $\nu_p^{(1,2)}$ are the Doppler-shifted frequencies, measured at the velocities β_1 and β_2. This relation is independent of the rest frame frequency and as $\beta_2^2 - \beta_1^2 \approx 0.8 \cdot \beta_2^2$, the sensitivity is not significantly diminished. Furthermore, the iodine transitions the lasers, for antiparallel ion excitation, are referenced to have been calibrated by the use of a frequency comb to an absolute accuracy of better than 75 kHz [Reinhardt06]. Hence, a relative frequency accuracy of $\Delta\nu/\nu = 2 \times 10^{-10}$ is achieved and the limit for α was pushed in 2007 by [Reinhardt07a] et al. to

$$|\alpha| \leq 8.4 \times 10^{-8} .$$

A schematic sketch of the used setup is given in Figure 3.7.

This value is the current best upper bound for the α parameter of the MS formalism. A further improvement of the experiment on the TSR would require a better understanding of several experiment parameters whose uncertainties are all in the same range and thus limit the sensitivity (e.g. influences of velocity changes, light forces, magnetic fields in the experimental section on the line shape and position).

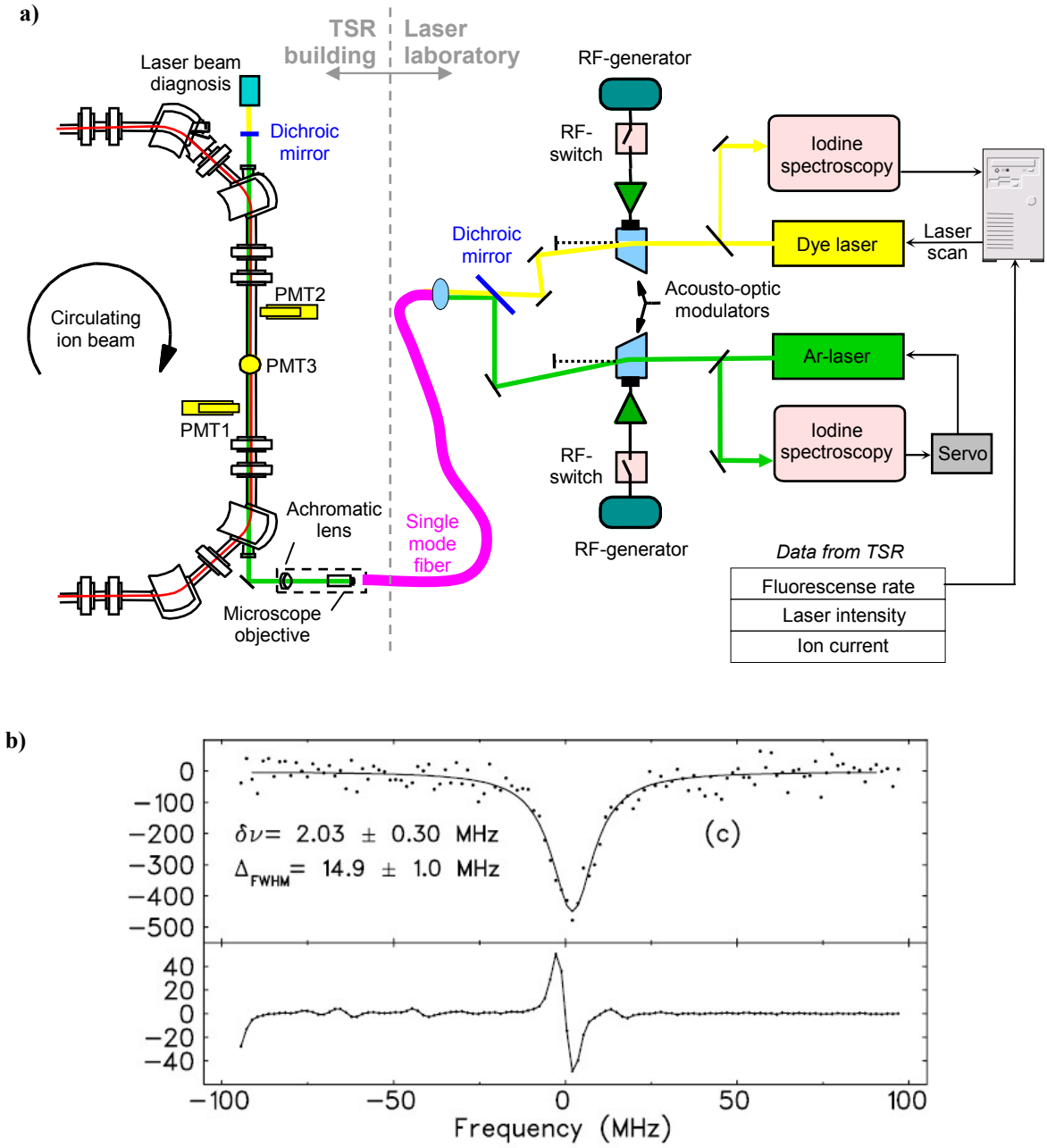

Figure 3.6: a) Overview of the experimental setup used in [Saathoff03]. Co- and anticollinear laser beams are used to perform saturation spectroscopy on $^{7}Li^{+}$ in the metastable state at a velocity of 6.4 %*c*. The laser light is generated by an argon ion laser (which is locked to on an $^{127}I_2$ hfs component) and a tunable dye laser. In order to determine the frequency of the scanning dye laser a suitable $^{127}I_2$ hfs line is recorded simultaneously with the fluorescence measurement. Both lasers pass acousto-optic modulators that allow for a fast on/off-switching of the laser beam at the TSR. The laser beams are overlapped with a dichroitic mirror, transmitting the dye laser light and reflecting the argon ion laser light, and then sent to TSR through a polarisation maintaining single-mode fibre. At the TSR the bichromatic laser light is collimated, overlapped with the ion beam and retro reflected by a mirror. The fluorescence of the lithium ions is monitored by photomultipliers (PMT). b) Upper panel: Lamb-dip signal of the saturation spectroscopy with a linewidth of ~ 15 MHz. The scanning range was ± 100 MHz. Lower panel: simultaneously recorded iodine line to determine the frequency of the dye laser [Saathoff03].

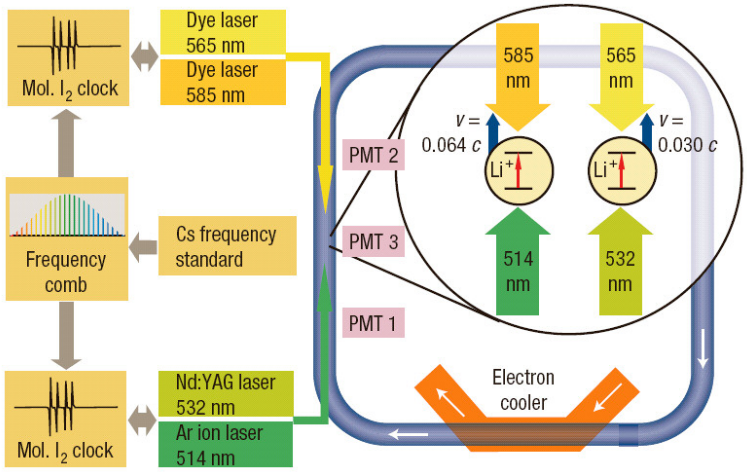

Figure 3.7: Schematic of the time dilation experiment performed at two different ion velocities (3.0%*c* and 6.4%*c*) at the TSR. An argon ion laser or a Nd:YAG laser was stabilised to a calibrated iodine line and provided the light for parallel excitation of the $^7Li^+$ ions in the metastable state. The light for antiparallel ion excitation was generated by a dye laser, which was frequency controlled by a frequency offset-lock relative to a second dye laser (for simplicity not sketched), which was locked to a calibrated iodine line. Both laser beams pass through acousto-optic modulators, are then merged via a dichroitic mirror and guided to the TSR by a polarisation maintaining single-mode fibre. The fluorescence signal of the lithium ions which is induced by saturation spectroscopy is monitored by photomultipliers [Reinhardt07a].

The storage ring experiments were analysed in the formalism of the standard model extension by Tobar et al. and Hohensee et al. in the photon sector and by Lane at al. for the fermion sector (chapter 1.3.4). In the photon sector the recent upper bound for κ_{tr} (the isotropic part of κ_{DE} and κ_{HB}) is given by [Hohensee07] to $\kappa_{tr} < 8.4 \times 10^{-8}$. In the fermion sector a limit on combinations of the quadrupole parameter of the proton and the electron, respectively is calculated by [Lane05] to

$$\left| c^{p}_{XX} + c^{p}_{YY} + 2 \cdot c^{p}_{ZZ} \right| \leq 10^{-11},$$
$$\left| c^{p}_{TJ} + c^{p}_{JT} \right| \leq 10^{-8}; \qquad (J = X, Y, Z).$$
$$\left| c^{e}_{XX} + c^{e}_{YY} + 2 \cdot c^{e}_{ZZ} \right| \leq 10^{-5},$$
$$\left| c^{e}_{TJ} + c^{e}_{JT} \right| \leq 10^{-2}; \qquad (J = X, Y, Z).$$

4 THE GSI FACILITY

In 1988, Huber et al. proposed an experiment with lithium ions at the experimental storage ring (ESR) at the Gesellschaft für Schwerionenforschung mbH (GSI) in Darmstadt, providing the potential to improve all performed tests of time dilation [Huber88]. For such a modern Ives-Stilwell type experiment, sensitive to hypothetical deviations in the predictions of special relativity, particles with high velocities are needed. Beside fast particles, precision spectroscopy requires an ion beam of highest quality (e.g. small momentum spread ~ 10^{-4}) like it is offered in storage ring facilities (MPIK[16], GSI). Since the ESR was put into operation only 1990, a measurement program at the TSR in Heidelberg was initiated in 1988. In 2005, the time dilation experiments at the TSR were finished successfully and the tests at the ESR started. In this chapter, the GSI facility with the used experiment areas is introduced (chapter 3.5).

In principle the facility consists of three platforms for ion sources, a linear accelerator, two ring accelerators, a fragment separator and experimental caves in the low and the high energy area (Figure 4.1). With these devices a particle range from protons to bare uranium can be accelerated. Typically low-charged ions are produced by an ion source[17], pre-accelerated to 1.4 MeV/u by a radio-frequency quadrupole structure (RFQ) and further accelerated by the universal linear accelerator (UNILAC) to an energy of typically 11.4 MeV/u for heavy ions. With this energy the ions can be injected into the Schwerionensynchrotron (SIS) and reach an energy of 30 MeV/u to 2 GeV/u for Ne^{10+} and to nearly 1 GeV/u for U^{92+} [Frantzke87]. To produce these highly charged ions, several targets along the acceleration line and in the SIS, are available where electrons can be stripped off the low-charged ion beam. From the SIS the ions can be extracted either to the high energy target area or into the fragment separator (FRS). The latter allows for production and separation of exotic radioactive ion beams that can be further analysed in the ESR or reinjected into the SIS [Geissel92].

One can conclude that: *"The research program of GSI spans over 17 decimal powers: it ranges from the modification of materials to the destruction of cancer cells, to the investigation of atoms, to the investigation of atomic nuclei as well as the Quark-gluon plasma"* [GSI08].

---

[16] MPIK = Max Planck-Institut für Kernphysik in Heidelberg.

[17] Available ion sources are for instance: a MEVVA (Metal Vapour Vacuum Arc), a Penning or a ECR (Electron Cyclotron Resonance).

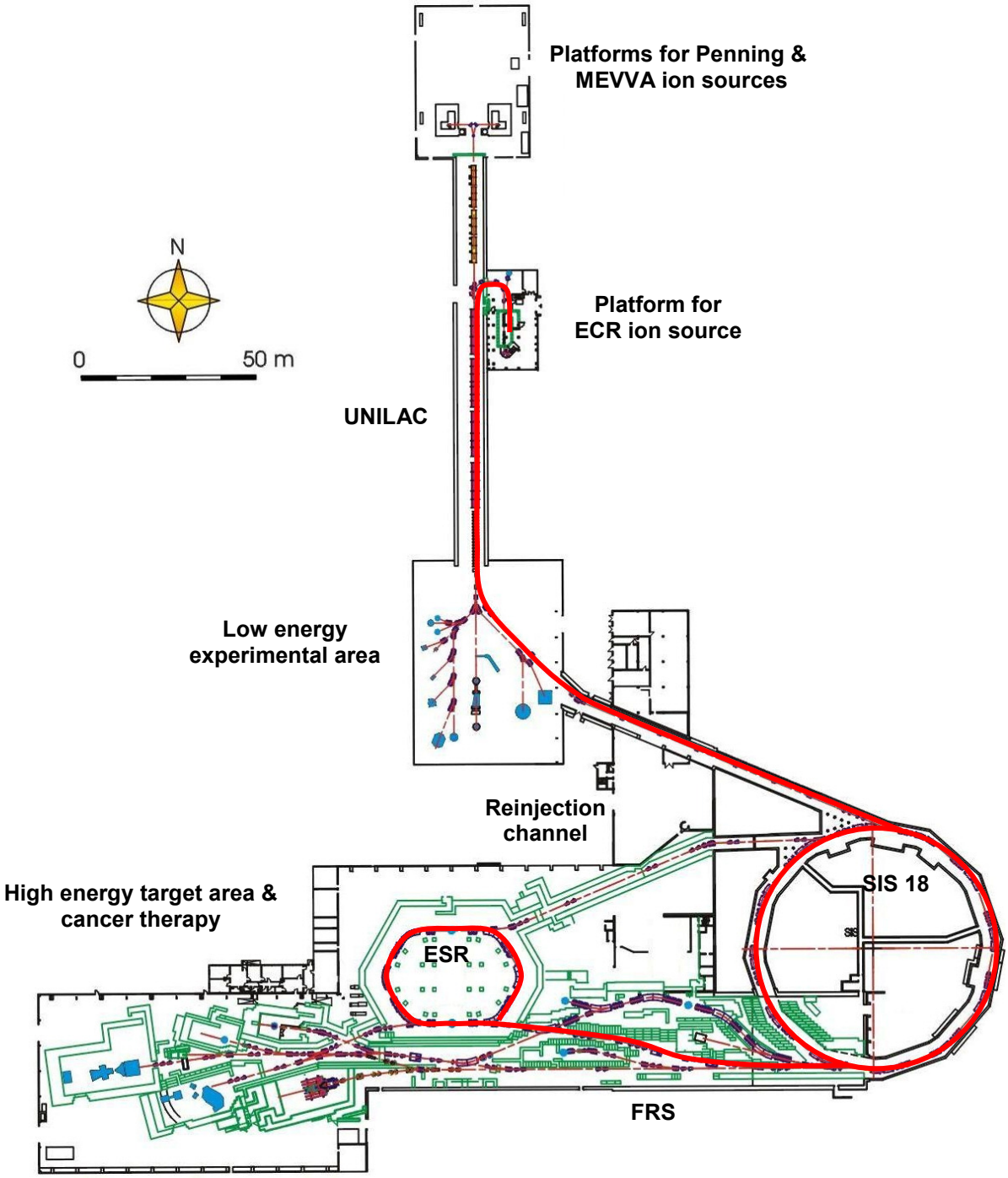

Figure 4.1: Schematic view of the GSI facility. Three platforms for different type of ion sources are available. From the universal linear accelerator (UNILAC) the ions can gain a maximum kinetic energy of 11.4 MeV/u for injection into the Schwerionensynchrotron (SIS) or analyses in the low energy experimental area. The SIS provides e.g. bare uranium ion beams up to 1 GeV/u that can be fed into the fragment separator (FRS), the experimental storage ring (ESR) or to the high energy experimental area. The path of the lithium ion from the ECR source to the ESR is highlighted in red.

4.1 PRODUCTION AND ACCELERATION OF $^7Li^+$ IONS

At the GSI the ion acceleration is accomplished by radiofrequency (rf) accelerators which do not involve electron stripping processes. Thus the production method for $^7Li^+$ in the metastable $1^1S_0 2^3S_1$ ground state can be done in two ways: either by electron capture with $^7Li^{2+}$ or excitation with $^7Li^+$ from the 1^1S_0 state. Indeed a common process for the metastable production is electron capture at energies in the range of 50 keV [Hvelplund76]. Unfortunately no foil or gas stripper is available at those energies and due to the compact design of the beam line, in the area from the ion source to the linear accelerator, there is no possibility of integrating such devices. Hence, the production has to be performed through excitation processes directly in the source. Here a type of ion source is preferred that produces simultaneously all possible charge states (from +1 to +3) of lithium ions because in equilibrium condition there should be a distribution over all charges including a population of the metastable ground states. The 14.5 GHz ECR ion source offers such a possibility and even some experience with lithium exists at GSI [Tinschert08]. A principle sketch of the ECR source is shown in Figure 4.2a. In this source the raw material is evaporated, ionised by the electrons in the plasma chamber and extracted by a voltage of 15 kV. A typical mass-to-charge spectrum of the extracted ions, using LiF as source material, is shown in Figure 4.2b. A significant fraction of the accelerated ion cloud consists of fluoride ions (with different charge configurations) and ions from residual gas that remains from filling the oven of the ECR source or inclusions of the source material. Moreover the fraction of singly charged $^7Li^+$ ions can not be distinguished from doubly charged nitrogen $^{14}N^{2+}$ in this spectrum. Indeed the ratio of both fractions can not be determined until the ions are injected in the ESR[18].

After the ionisation of the source material the cloud of ions is extracted and pre-accelerated to 15 keV. Out of this cloud the desired ions with a mass-to-charge ratio of seven are selected by an analyser magnet and further accelerated to an energy of 1.4 MeV/u by the RFQ and the high-current injector. From there the ion beam is injected in the UNILAC. Along these 120 m the ions gain energy of 8 MeV/u and are injected in the SIS at the end. This synchrotron has a circumference of 216 m, which is exactly twice the circumference of the ESR. Further an electron cooler is installed that allows for cooling the ion beam before extraction. In the SIS the kinetic energy of the ions is ramped up in two hf-accelerator sections to the desired particle velocity. For the

[18] In appendix B tests with different source materials are described that were performed to optimise the yield of metastable lithium ions in the ion beam.

$^{7}Li^{+}$ ions this means an energy of 58 MeV/u or $\upsilon = 33.8\ \%c$[19]. At this velocity, the beam pulses are extracted into the ESR with an efficiency of 10 %. The whole process from the acceleration till extraction into the ESR takes place in 2-3 s (mostly in the SIS in an atmosphere of 10^{-10} mbar where they are continuously affected by acceleration forces of the order of 10^{13} g). Losses in the ion beam due to collisions with residual gas are negligible. Till the extraction the ions passed already a distance of about 2×10^{8} m; what is comparable to the half of the distance Earth to Moon. In the ESR the lifetime of the ion beam can reach two minutes (compare chapter 4.2.4) what means the ions can travel a distance of 10^{10} m in the ESR.

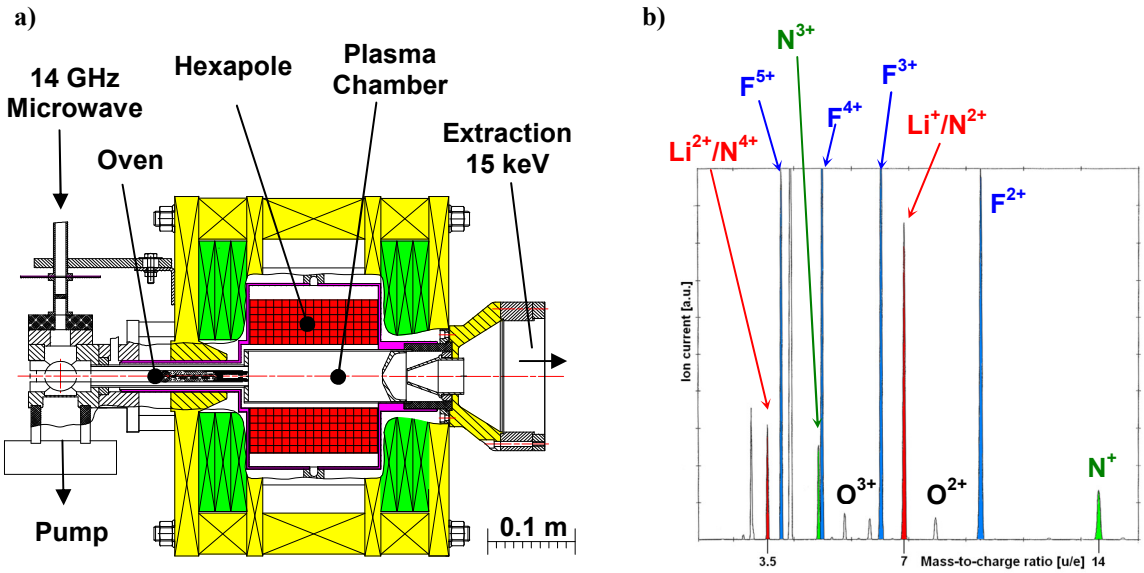

Figure 4.2: a) Schematic of the electron cyclotron resonance (ECR) source at the GSI. For explanation see text. b) A typical mass-to-charge spectrum of the ECR ion source using LiF for source material is shown. The spectrum was taken directly behind ion source. Beside the expected lithium (green and red signals) and fluorine (blue signals) ions, a considerable amount of residual gases (e.g. oxygen and nitrogen) are found.

4.2 STORING IONS IN A RING

To store or accelerate an ion beam in the ESR, the SIS or in any ring structure, two forces have to be taken into account: the centripetal force, to bend the beam along the circumference of the ring and the repelling forces of the ion-ion interaction. In the ESR six 60 ° dipole magnets with a maximal magnetic field of 1.6 Tesla are distributed over the ring, keeping the particles on a closed orbit. Additionally, twenty multipole magnets

[19] A particle speed of 33.8 %*c* was chosen (instead of the maximal possible storage velocity of 41.7 %*c*) because of the commercial availability of laser sources and respective frequency references for the excitation of the $^{7}Li^{+}$ ions.

focus the ions in both transversal directions. The ring has a circumference of 108 m and a shape of a drawn-out hexagon with two long sections. In one of these two straight sections, the electron cooler is placed and in the other the spectroscopy experiment is situated (see Figure 4.3).

The kinetic energy of ions stored in a ring has to obey

$$q \cdot B \cdot \upsilon = \frac{\gamma \cdot m \cdot \upsilon^2}{\rho} \quad \leftrightarrow \quad B \cdot \rho = \frac{\gamma \cdot m \cdot \upsilon}{q} \tag{4.1}$$

where the Lorentz force must be equal to the centripetal force. The product $B \cdot \rho$ is the magnetic rigidity, the characteristic value for storage rings because it determines the maximum energy ions can be stored at. For the ESR a value of 10 Tm is possible and therefore a maximum velocity of β = 41.7 % for $^7Li^+$ ions. More precisely B is the magnetic field of the dipole magnets (at the ESR: B_{max} = 1.6 T) and ρ their bending radius. m is the mass and q is the charge state of the ions, γ is the Lorentz factor of special relativity.

The ions perform an oscillatory motion around the central orbit. These betatron oscillations are determined by the focussing strength of the quadrupole magnets $K(s)$ and the bending radius ρ of the dipole magnets and can be described by a Hill's type differential equation

$$\frac{d^2x(s)}{dx^2} + K(s) \cdot x(s) = \frac{1}{\rho} \cdot \frac{\Delta p}{p_0} \tag{4.2}$$

where $x(s)$ is the transversal displacement from the central orbit, s is the longitudinal beam parameter and Δp is the deviation from the design momentum p_0. A solution of the homogenous equation ($\Delta p/p = 0$) reads

$$x(s) = x_0(s) \cdot \cos[\psi(s) + \delta] \tag{4.3}$$

where $\psi(s)$ is the betatron phase[20] and δ is an arbitrary phase which can be neglected in the following discussion. The transversal ion movement along the central orbit has a s-dependent amplitude $x_0(s) = 1/\sqrt{\varepsilon \cdot \beta(s)}$ that contains the beta function $\beta(s)$ which is an intrinsic property of the storage ring lattice (see Figure 4.4). ε is the emittance of the beam. $x(s)$ and $dx(s)/ds$ form an ellipse with the area $F = \pi \cdot \varepsilon$, centred at the

[20] $\psi(s) = \int ds/\beta(s)$

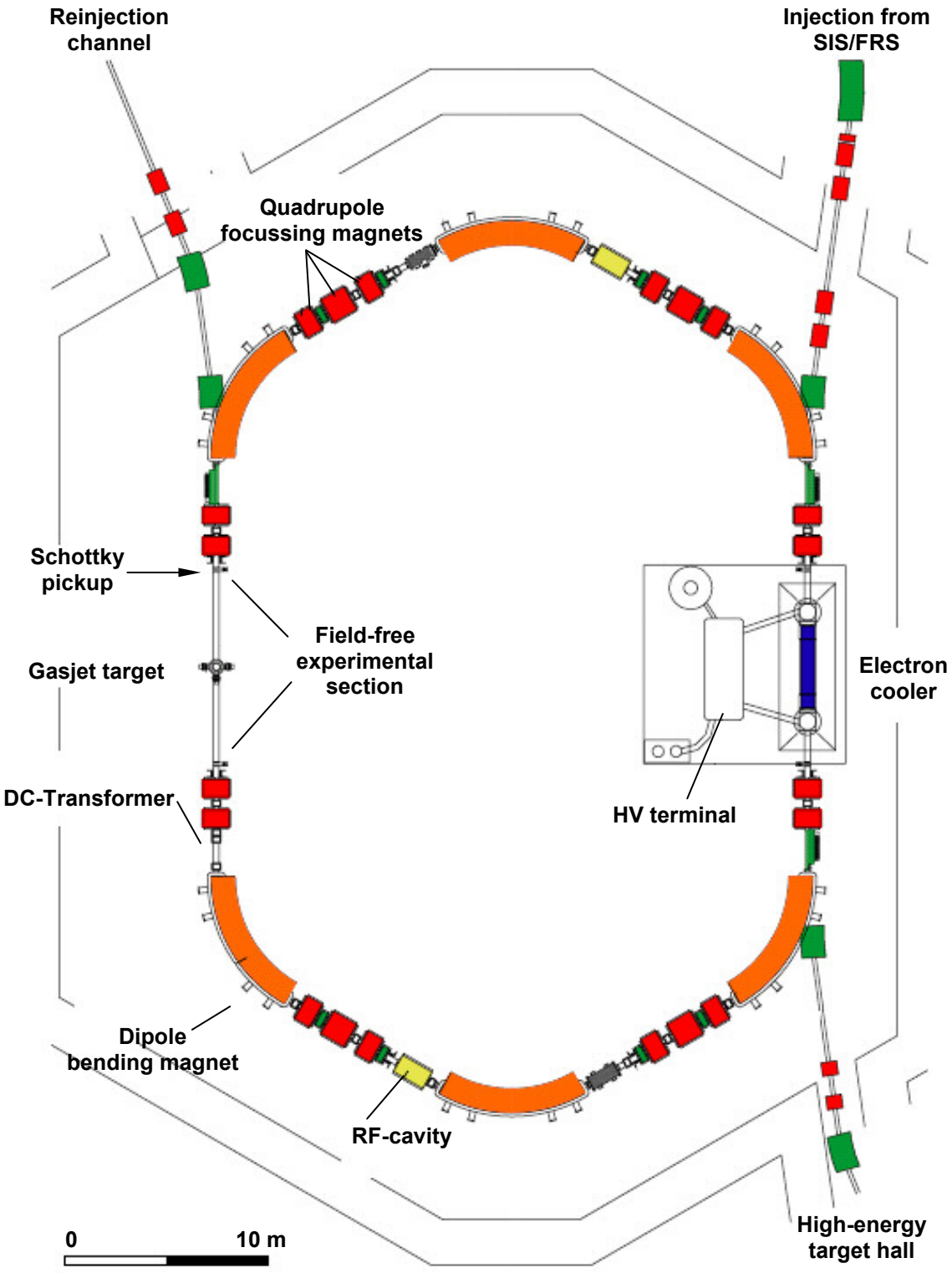

Figure 4.3: Schematic view of the experimental storage ring. It consists of 6 dipole magnets to bend the ion beam and overall 22 multipole magnets to focus the beam. The laser spectroscopy experiment takes place in the straight and field-free experimental section which is on the opposite side to the electron cooler.

sollbahn. According to Liouville's theorem this area stays constant if the ions are subjected to conservative forces only. Therefore if the amplitude of the ion beam at a certain position is known, the emittance as well as the resulting amplitude at each position can be calculated using the beta function. Concerning the maximal deviation from the sollbahn of a particle that is still stored in the ring, the envelope $E(s)$ and the divergence $\hat{E}(s)$ can be calculated by

$$E(s) = x_{\max}(s) = \sqrt{\varepsilon \cdot \beta(s)} \tag{4.4}$$

and

$$\hat{E}(s) = \frac{\mathrm{d}x_{\max}(s)}{\mathrm{d}s} = \sqrt{\varepsilon} \cdot \sqrt{\frac{1 + [\beta'(s)/2]^2}{\beta(s)}} \,. \tag{4.5}$$

Up to now only particles with the design momentum p_0 have been considered. But in a storage ring an ion beam consists of an ensemble of particles with a momentum spread $\Delta p \neq 0$ and therefore each particle experiences a different bending radius in the dipole magnets due to the velocity dependence of the Lorentz force. This leads to a horizontal displacement that obeys

$$\Delta x(s) = \frac{\Delta p}{p_0} \cdot D(s) \tag{4.6}$$

where $D(s)$ is the dispersion function, which is an intrinsic property of the storage ring lattice and shown in Figure 4.5 for ESR. The change of the momentum together with a change of the length of the central orbit involved in the dispersion leads to a corresponding change of the revolution frequency [Wille96]

$$\frac{\Delta f}{f} = \eta \frac{\Delta p}{p_0} \,. \tag{4.7}$$

η is the slip-factor[21] and has a value of $\eta = 0.706$ for the lithium experiment.

[21] The slip-factor is defined by $\eta = \gamma^{-2} - \Gamma^{-2}$ where γ is the Lorentz factor and Γ the transition energy that describes a point where a bunched beam runs into instabilities due to the transversal focussing of the magnets. Ion beams at the ESR are typically tuned to a value of $\Gamma = 2.35$.

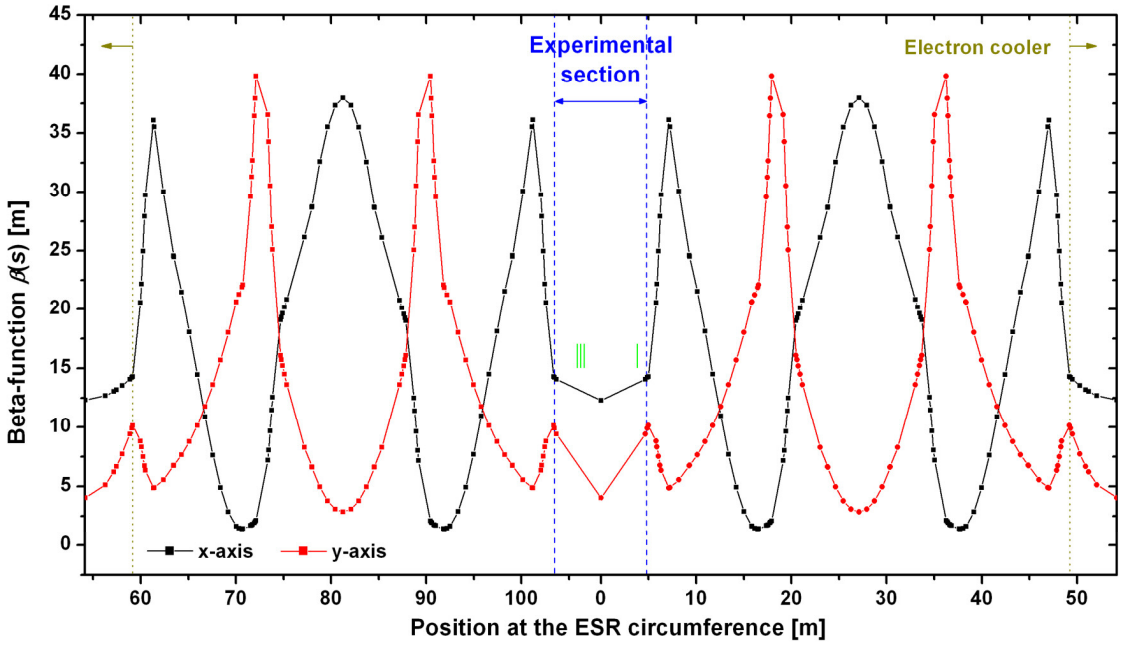

Figure 4.4: Beta function $\beta(s)$ of the ESR for the x- (black curve) and the y-axis (red curve) in meters. The zero-point is at the gasjet target in the experimental section. The green lines indicate the PMT positions.

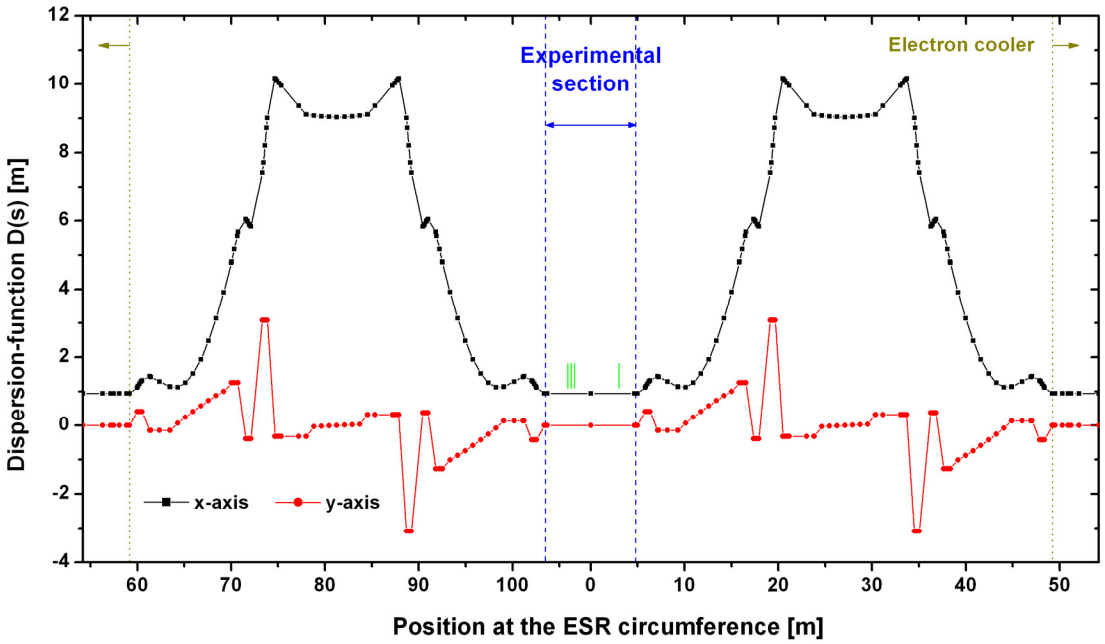

Figure 4.5: Dispersion function $D(s)$ of the x- (black curve) and the y-axis (red curve) for the ESR. The zero-point is at the gasjet target in the experimental section. The green lines indicate the PMT positions.

4.2.1 ELECTRON COOLING

Now that the ions are kept on a stable orbit in the storage ring, one has to investigate the quality of the beam because for precision experiments an ion beam with superb quality is necessary. Since the ions are extracted from the SIS with a large momentum spread and strong beam divergence, which severely limits the frequency accuracy of laser spectroscopy experiments, a cooling of the beam is indispensable[22]. To reduce these parameters the betatron oscillations must be damped. This is done with the help of the electron cooler. A cold electron beam is overlapped with the hot ion beam in a certain region of the storage ring. Due to coulomb forces between the ions and the continuously renewed cold electrons the ion beam is cooled. For example, if an ion has a velocity that is smaller than that of the electron beam it gets kicked by the electrons and therefore gains kinetic energy. If it is faster, it hits the electron and loses energy. The electrons are always renewed and therefore the net effect for the ion beam is cooling in all dimensions. Electron cooling was first described in 1966 by I.G. Budker and realised 1974 for cooling protons at the storage ring in Novosibirsk [Budker76]. An extended description of electron cooling can be found in [Poth90].

The electron cooler of the ESR is installed on the opposite long straight section of the target section, directly behind the injection (Figure 4.3). The effective length, where the electron beam is merged with the ion beam, is 2.5 m, while the whole system has a length of 6 m. The electrons are generated from a 50.8 mm diameter cathode (T = 1100 °C), immersed in a longitudinal magnetic field (Figure 4.6). This field guides the electron beam from the gun, to the cooling section and in the end to the electron collector, with constant field strength. In the lithium experiment the magnetic guiding field intensity is 0.1 T. This is in the normal operation regime (0.015-0.18 T) of the cooler [Steck04]. The velocity distribution of the electrons, that emerge from the cathode, is $k_B \cdot T_\perp \approx 0.1$ eV for the transverse direction and $k_B \cdot T_{||} \approx 0.1$ meV in the longitudinal direction (due to the acceleration)[23].

[22] A pre-cooling of the ion beam is possible by the SIS electron cooler before the ions are accelerated by the SIS. However, no significant increase in the transfer efficiency or the ion beam quality was found by performing a pre-cooling (see chapter 4.2.3).

[23] k_B = Boltzmann constant.

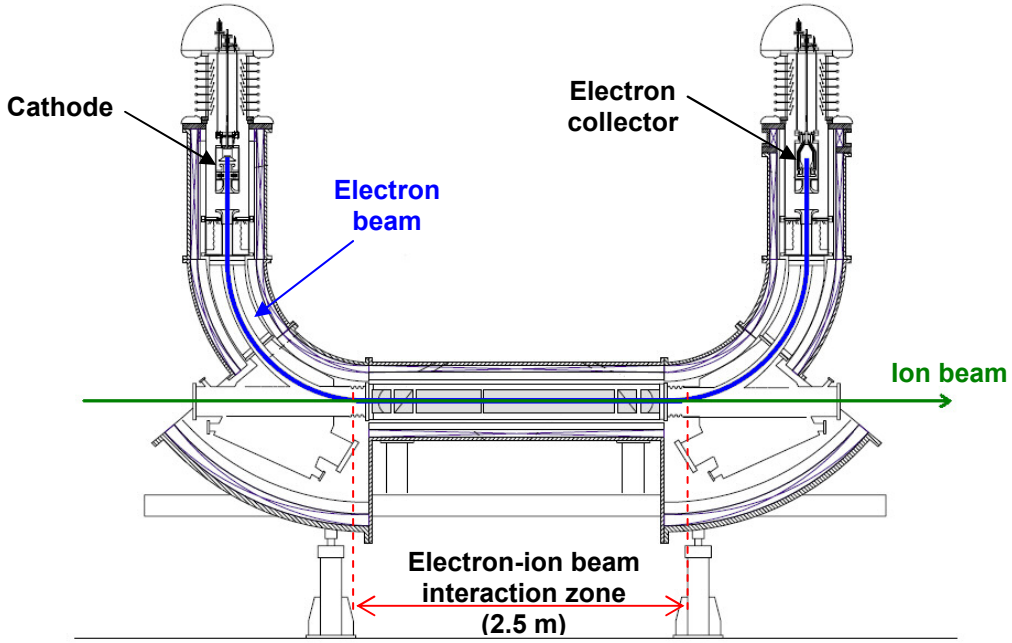

Figure 4.6: Technical drawing of the electron cooler of the ESR. The electrons are generated at the upper left side by a heated cathode, guided into the 2.5 m long interaction zone where the ion beam is cooled. The hot electrons are removed from the ion beam and collected in the upper right electron collector [Steck04].

For the $^{7}Li^{+}$ ion beam a time of at least 10 s of electron cooling is necessary to achieve an ion beam that can be used for spectroscopic purposes (see Figure 4.7). After the injection from SIS both ion species, singly charged lithium ions (red fit) and doubly charged nitrogen ions (green fit), can be only barley distinguished. However, a Gaussian distribution can be fitted to the each fraction that indicates a momentum spread of $\Delta p/p \sim 5\times10^{-4}$. Ten seconds later, both ion fractions are separated by the electron cooler and their velocity distribution changes from a Gaussian shape to a Lorentzian. After 20 s of electron cooling the ion distribution is in a Lorentzian shape with a momentum spread of $\Delta p/p \sim 10^{-5}$ for both fractions.

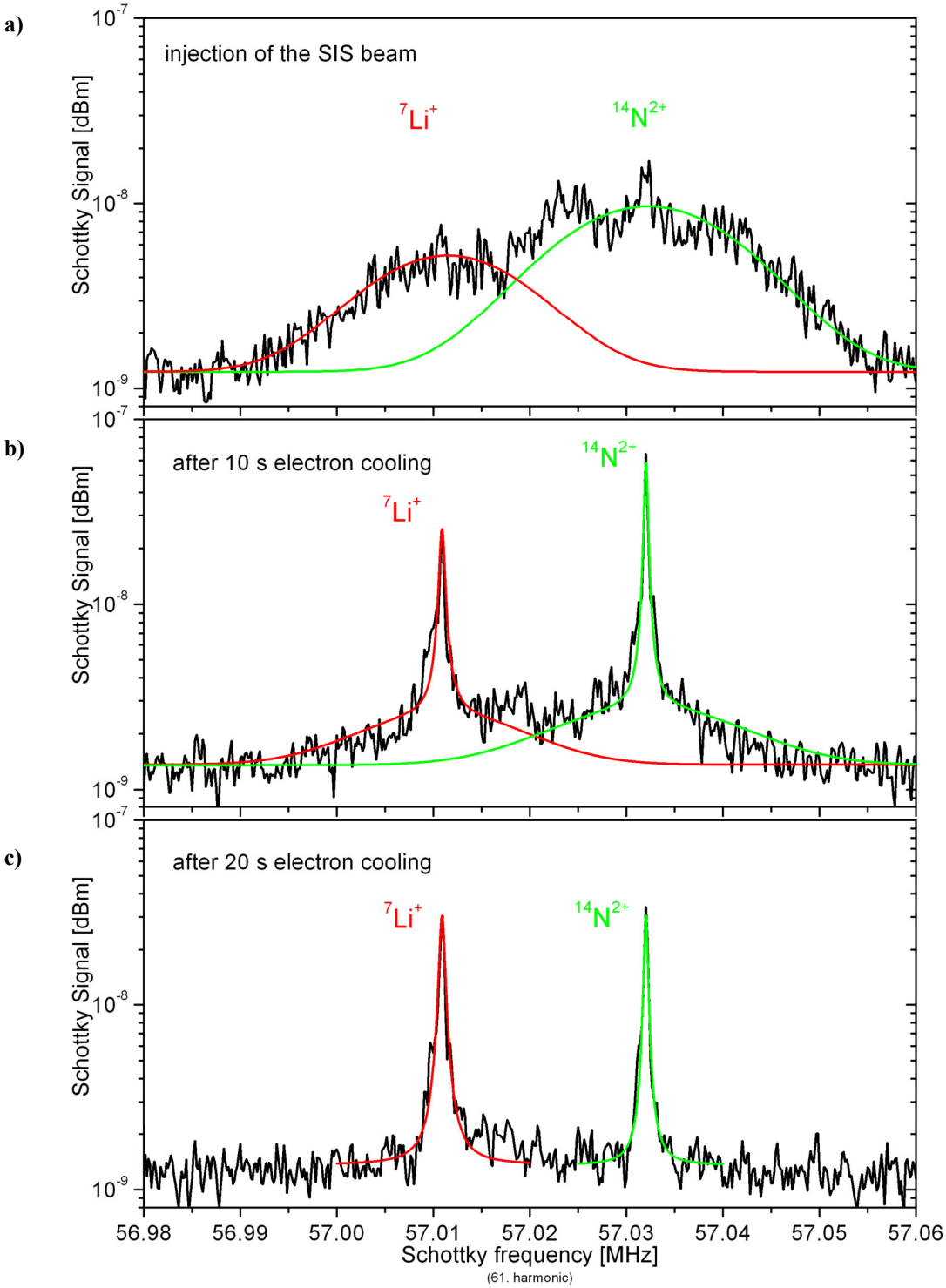

Figure 4.7: Schottky spectrum (a description of the Schottky analysis is given in chapter 4.2.2) of the progress of electron cooling in the ESR. The left signal is generated by the fraction of singly charged lithium ions, the right by doubly charged nitrogen ions. a) Spectrum taken directly after injection from the SIS. The ion beam has a broad Gaussian velocity distribution where a differentiation between the lithium and the nitrogen fraction is barley possible. b) After 10 s of electron cooling two separated Lorentzian-shaped peaks emerge on the Gaussian background. c) After 20 s of electron cooling both ion fractions are separated completely. The red/green lines are Gaussian and/or Lorentzian fits to the spectra (see text).

4.2.2 ION BEAM ANALYSIS

The momentum spread and the lifetime of the ions in the ESR are crucial parameter for the test of time dilation. A large momentum spread causes a large velocity distribution in the ion beam and the fluorescence signal is smeared out. Applying techniques of electron cooling and beam bunching keep the momentum spread in the order of 10^{-5}-10^{-6}, which is sufficient for precision spectroscopy. To determine this value, Doppler-broadened fluorescence spectroscopy as well as Schottky analysis of the ion beam can be used. The lifetime of the ion beam in the ESR is strongly dependent on the vacuum conditions and can by measured with a DC-Transformer which measures the DC-current of the circulating ions with pick up electrodes. However, a determination of the lifetime of the metastable fraction of the ion beam is only feasible by fluorescence measurements.

SCHOTTKY ANALYSIS

Schottky analysis is a non-destructive method to determine the revolution frequency of a single ion or an ion beam [Boussard85]. The induced current signals (noise) from the circulating ions are detected by capacitive pickup electrodes. A single ion leads to an infinite series of equally spaced delta spikes that are related to the revolution frequency $f_n = n \cdot f_0$ (n is the order of the harmonic of the revolution frequency f_0). A Fourier transformation of this signal generates a line spectrum at each harmonic of f_0. For ions in a beam with a momentum spread $\Delta p/p$, the lines of the spectrum change to a frequency band Δf around f_0 with a frequency distribution

$$\Delta f = f_n \cdot \eta \cdot \frac{\Delta p}{p}. \tag{4.8}$$

From the Schottky spectrum only the relative momentum $\Delta p/p$ can be determined, whereas the absolute momentum is dependent on the orbit length which is not known to a sufficient accuracy for the experiment. An example of early Schottky spectra from the ESR of U^{92+} at 320 MeV/u is given in Figure 4.8. The electron cooled ion beam is given by the red spectra, the “hot” ion beam by the green.

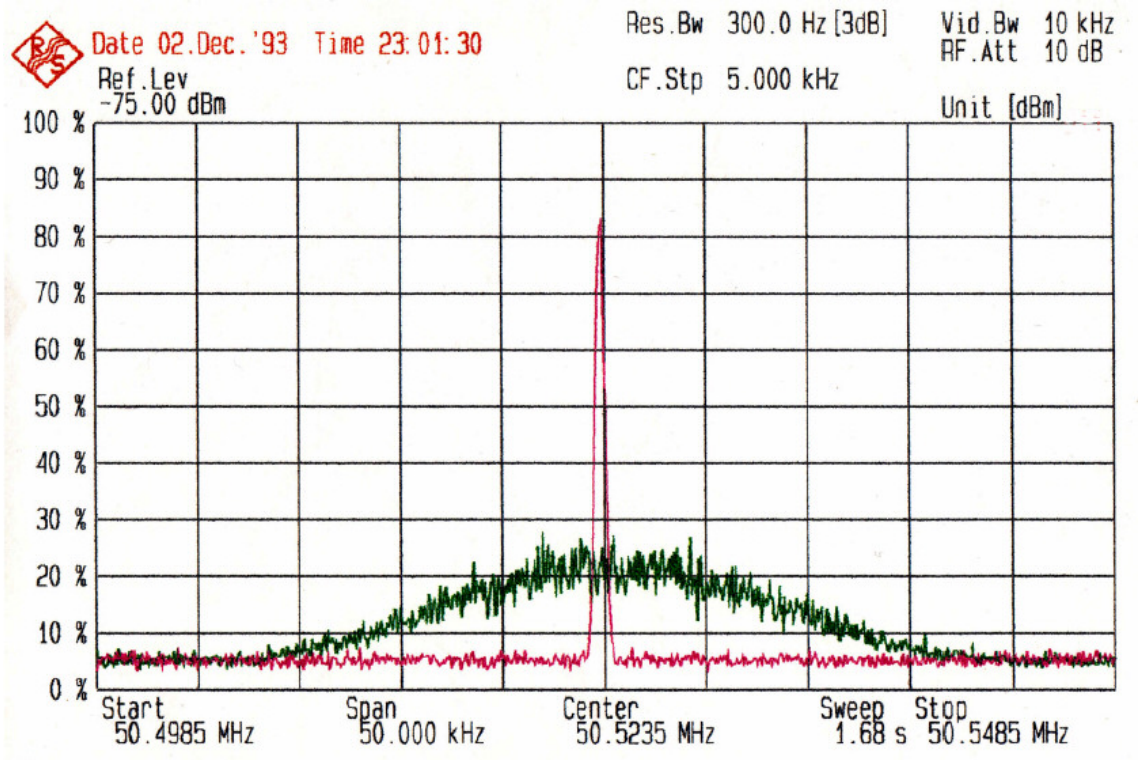

Figure 4.8: Example of an early (1993) Schottky spectra from the ESR before (green) and after (red with $\Delta p/p = 2 \times 10^{-5}$) electron cooling of U^{92+} at 320 MeV/u [Steck06].

FLUORESCENCE MEASUREMENT

A second method to determine the relative momentum spread is Doppler-broadened spectroscopy. Here, laser light is frequency tuned across the $2s^3S_1$ ($F = {}^5/_2$) $\rightarrow$ $2p^3P_2$ ($F = {}^7/_2$) transition of the lithium ion and the fluorescence light is measured as a function of the laser frequency. If the laser beam is aligned exactly anti-collinear with respect to the ion beam, the momentum spread and the spread in frequency are connected via the Doppler formula $\nu_a = \nu_0 \cdot \gamma \cdot (1 - \beta)$ and the momentum $p = m_0 \cdot c \cdot \gamma \cdot \beta$ to

$$\frac{\Delta p}{p} = -\frac{1}{\beta} \cdot \frac{\Delta \nu_a}{\nu_a} . \tag{4.9}$$

A typical spectrum generated with $^7Li^+$ ions at $\beta = 0.338$ is shown in Figure 7.19.

Further the lifetime of the metastable ion fraction of the beam can be determined with laser spectroscopy. Here the laser is fix in frequency and in resonance with $2s^3S_1$ ($F = {}^5/_2$) $\rightarrow$ $2p^3P_2$ ($F = {}^7/_2$) transition. The fluorescence signal is recorded as a function of time (Figure 4.12).

4.2.3 ION BEAM PROPERTIES IN THE SIS

An average amount of 3×10^9 ions ($I_{DC} \approx 200$ µA) is kept on the orbit of the SIS and accelerated to 58 MeV/u ($\beta = 0.338$). Before this last acceleration step, a pre-cooling of the ions can be applied to narrow the momentum spread and the emittance of the ion beam in the SIS. For this purpose the SIS electron cooler is used that allows to reduce the emittance of the ion beam from 30 mm·mrad to 5 mm·mrad. Nevertheless, the beam has to be further electron cooled in the ESR. The pre-cooling in the SIS offers the possibility to increase the transfer efficiency from the SIS to the ESR and/or to reduce the cooling time in the ESR.

The effect of the pre-cooling was investigated for SIS cooling times from 1-8 s (Figure 4.9). The total amount of ions was measured with the DC-Transformer signal and the distribution of the metastable fraction, after 8 s additional electron cooling in the ESR, was recorded with the Doppler-broadened spectroscopy technique[24]. Changing the SIS cooling time from one second to 3 s a small increase in the signal was measured while the total transmission efficiency stays constant at ~ 5 %. Using higher cooling times (5-8 s) the spectroscopic signal of metastable ions drops due to the lifetime of the metastable fraction. Further it turned out, that no significant worsening of the ion beam properties occurs if the SIS electron cooler is not used at all. Consequently, a pre-cooling for a $^7Li^+$ ion beam is not required.

[24] The Doppler-broadened measurements are described in detail in chapter 7.6

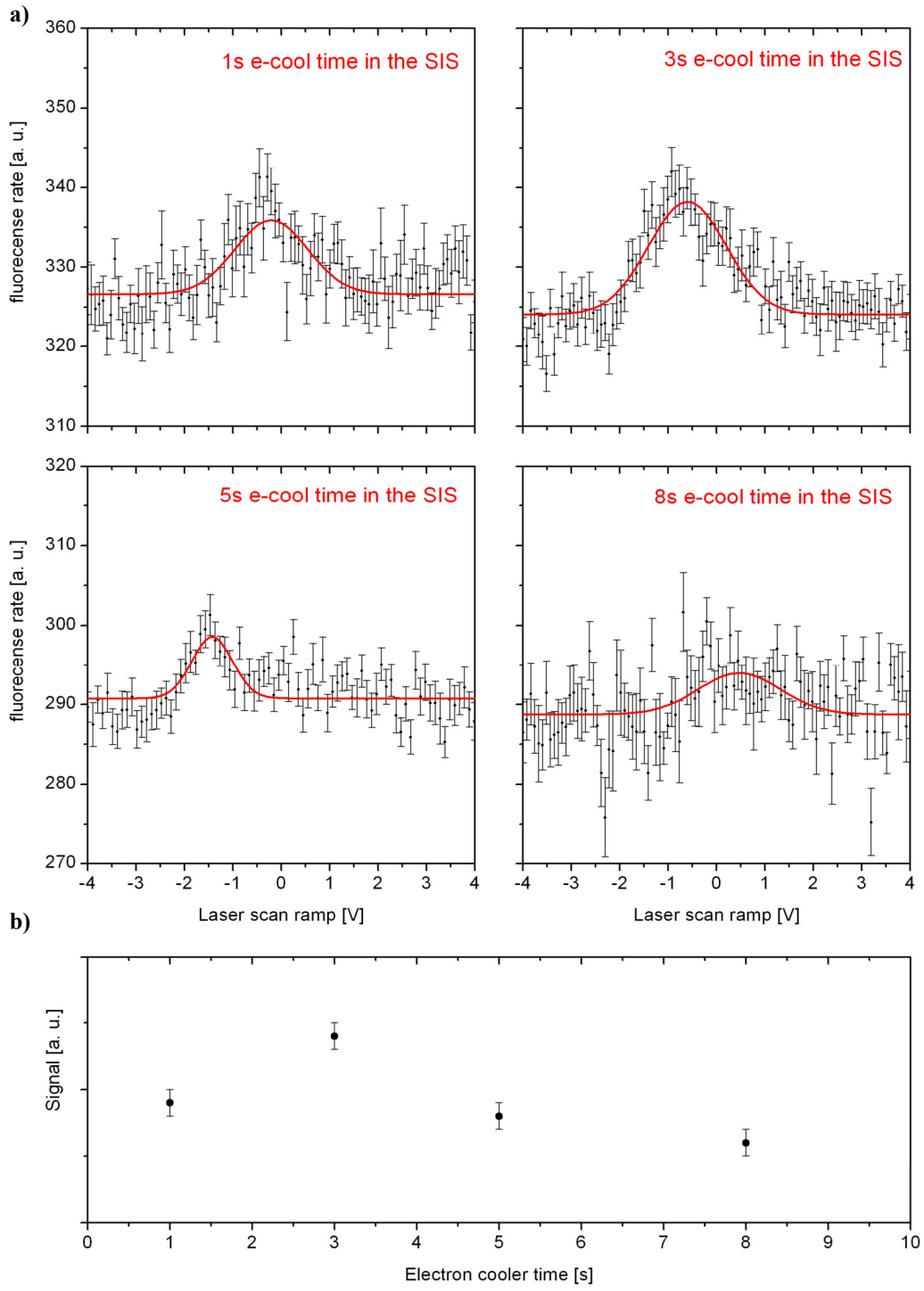

Figure 4.9: a) Doppler-broadened fluorescence signal of the metastable $^{7}Li^{+}$ ions in the ESR at four different electron cooler times in the SIS. The signals were recorded after 8 s additional electron cooling in the ESR. The red curves in the four upper diagrams present Gaussian fit of the data points. b) Plot of the measured fluorescence rate as a function of the electron cooling time in the SIS. For short SIS cooling times ($t < 3$ s) a small increase in the signal was measured that is due to the narrowing of the velocity distribution. At longer cooling times the decay of the metastable ions becomes the dominant process and lowers the rate in the ESR.

4.2.4 KINEMATICAL ION BEAM PROPERTIES IN THE ESR

The transmission efficiency from the SIS into the ESR is in the order of 5 %. This leads to an ion current of I_{DC} = 20 µA in average or a total number of singly charged particles of $N_{ions} = 1.3 \times 10^8$ ions in the ESR. The typical vacuum pressure in the experimental storage ring is better than 10^{-11} mbar. Such vacuum conditions allow for storage times of the ion beam of more than 100 seconds (see Figure 4.10). The lifetime of the ion beam is measured by recording the DC-Transformer signal after ion injection as a function of time. However, this lifetime characterises the entire ion beam, while for the test of time dilation, the lifetime of the metastable $^7Li^+$ fraction is the important factor. As will be seen later, this lifetime is considerably shorter[25].

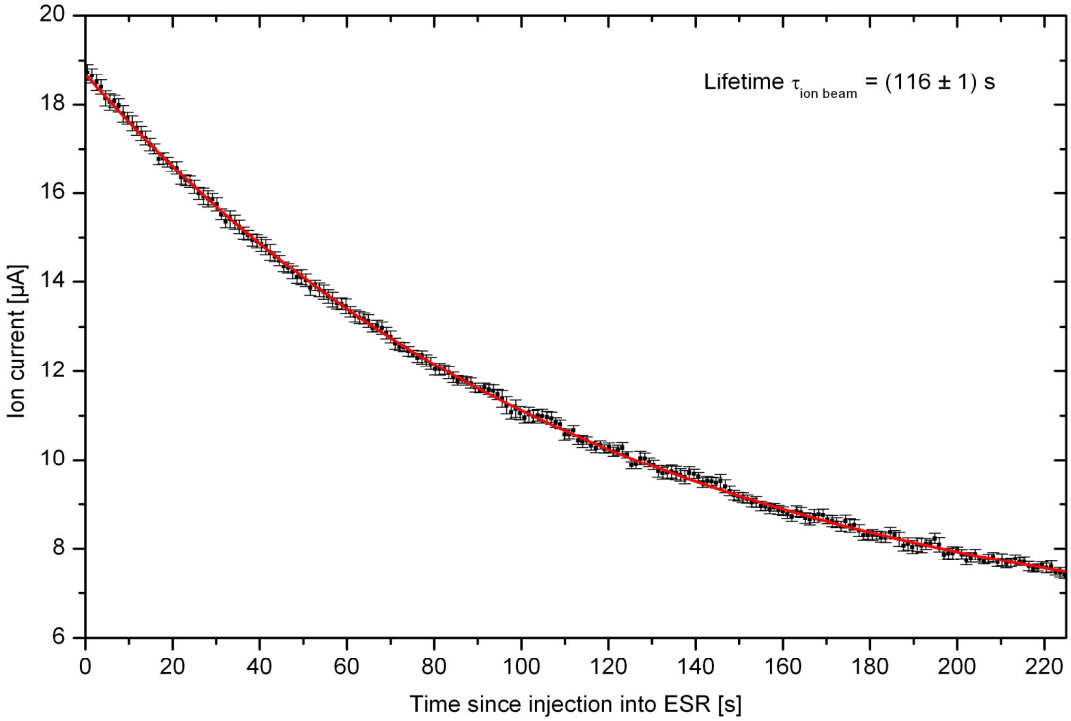

Figure 4.10: Lifetime of the ion beam, measured by recording the DC-Transformer signal over time. Red plot: exponential fit of the data. The calibration uncertainty of the ion current is ± 10 %.

[25] Beside the experiments at these excellent lifetimes, the vacuum was considerably worse at other beam times. Vacuum leaks in different sections of the storage ring decreased the residual gas pressure by two orders of magnitude to 10^{-9} mbar. Due to a strong correlation of the lifetime of an ion beam with the vacuum conditions in a storage ring, the lifetime dropped to 2 s which is insufficient for cooling and subsequent spectroscopic measurements. At a vacuum pressure of a few 10^{-10} mbar a lifetime of about 20 s was measured.

Concerning the storage time of an ion beam, one has to take into account that the DC-Transformer signal is not solely generated by lithium ions, but also by doubly charged nitrogen ions $^{14}N^{2+}$. Nitrogen emerges either from inclusions in the source material or of residual gas which remains after refilling the ion source (compare chapter 4.1). The mass-to-charge ratio of the two ion species is so similar that a $^{14}N^{2+}$ fraction can not be separated from $^{7}Li^{+}$ ions (see Table 4.1). In fact, resolving both ion fractions is possible only in the ESR.

Table 4.1: Comparison of the mass-to-chrage ratio of lithium and nitrogen [Audi03] (amu = atomic mass units)

	Mass-to-charge ratio [amu /q]		Mass difference [amu /q]
$^{7}Li^{+}$	7.016004	$\Rightarrow \Delta$	0.014467 or 0.2 %
$^{14}N^{2+}$	7.001537		

A Schottky analysis of the ion beam allows distinguishing between both isotopes and further offers the possibility to estimate their relative quantities. In Figure 4.11a, a time series of Schottky spectra from ion injection till clear separation of both ion fractions is shown. The Schottky frequency corresponds to the 61st harmonic of the revolution frequency of the ions. After injection into the ESR the momentum spread of the ions is very broad and both ion fractions can not be distinguished. After a few seconds, the momentum spread and thus the linewidths decrease so that the two particle species are resolved (Figure 4.7). Due to the higher mass-to-charge ratio of the $^{7}Li^{+}$ ions, their revolution frequency is lower than the one of $^{14}N^{2+}$ (see Table 4.2).

Table 4.2: Revolution circumference and frequency of both ion fractions in the ESR ($\Delta \equiv {}^{14}N^{2+} - {}^{7}Li^{+}$)

	ESR revolution frequency [kHz]	Ion revolution circumference [m]
^{7}Li	934.604	108.529
^{14}N	934.951	108.488
Δ	0.347	– 0.041

From Figure 4.11b, the relative amount of the ion fractions can be estimated. The peak area of the respective Schottky signal is proportional to the square of the charge state of the ion $n_{ion} \sim q^2$. Consequently, if both peaks have equal areas, the amount of singly charged lithium is four times larger than of doubly charged nitrogen. This means for a DC-Transformer signal of I_{DC} = 20 µA in the ESR a fraction of 9.8×10^7 particles are lithium ions and 3.2×10^7 are doubly charged nitrogen ions. However, no statement on the amount of lithium in the metastable ground state ($2s^3S_1$) can be given with this method. Only with laser spectroscopic techniques the singlet ground state $2s^1S_0$ can be distinguished from the metastable state.

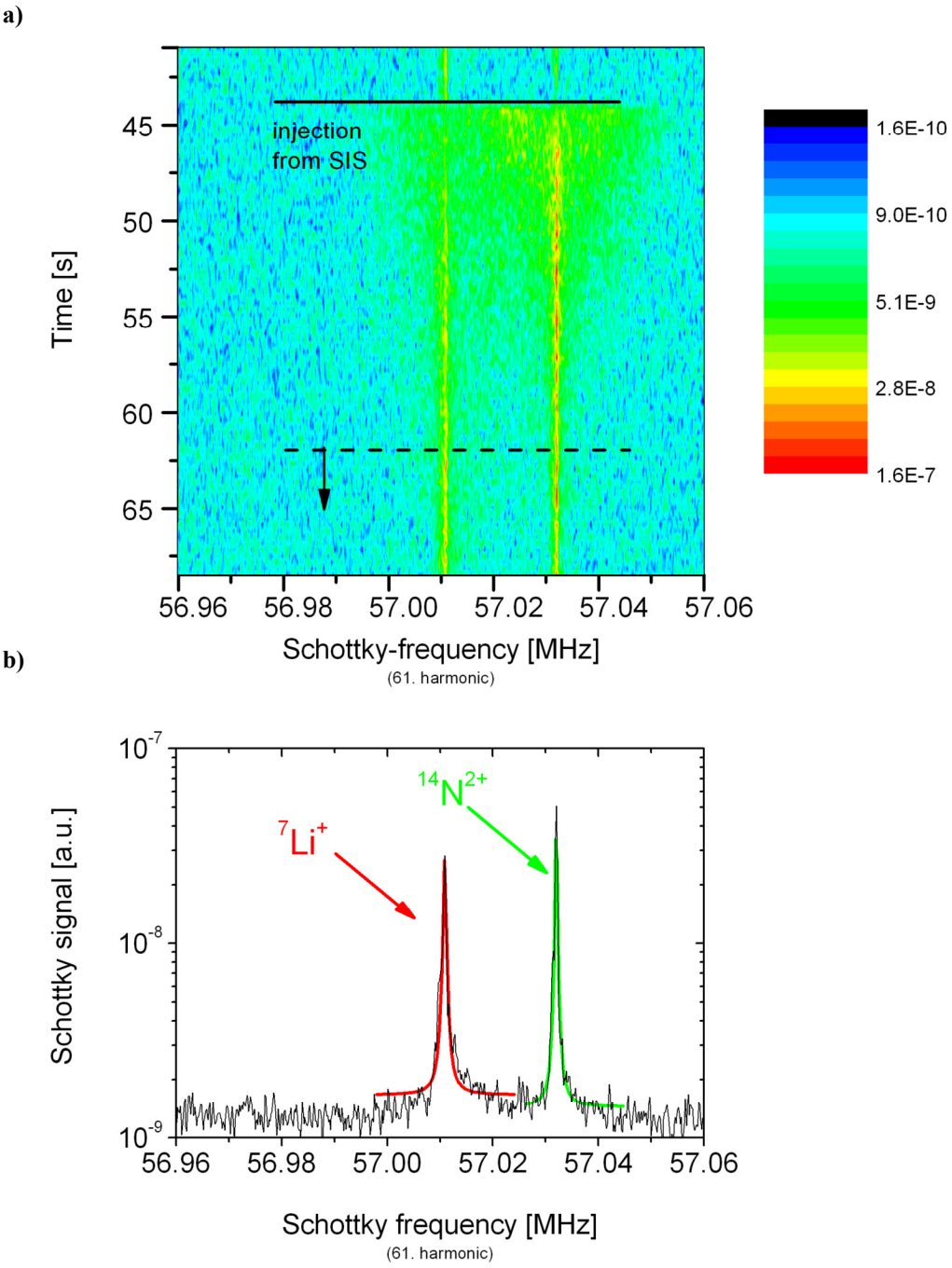

Figure 4.11: Schottky signals of both ion fractions in the storage ring. a) Time series of the ion beam after injection from the SIS. b) Spectrum after 20 s of electron cooling (averaged over 5 s). The dashed line in the upper diagram indicates the starting point for averaging in time.

From the linewidths of the Schottky signals in Figure 4.11b and equation (4.8) the momentum spread for each ion fraction can be determined. After 20 s of electron cooling the momentum spread of $^{7}Li^{+}$ is measured to be $\Delta p/p = (3.0 \pm 0.2)\times 10^{-5}$ and that of $^{14}N^{2+}$ $\Delta p/p = (1.4 \pm 0.1)\times 10^{-5}$. The value for the fraction of ions in the metastable $2s^3S_1$ ground state can be measured only by laser spectroscopy. In chapter 7.6 these measurements are described in detail and Figure 7.19 shows a typical Doppler-broadened spectrum for an ion beam at β = 33.8 %*c*. Compared to the Schottky measurements of all ground state ions, a slightly smaller momentum spread of $\Delta p/p = (8.4 \pm 0.6)\times 10^{-6}$ was found for the metastable lithium ions. These measurements were used to revise the settings of the electron cooler (typical values for an ion beam velocity of 33.8 %*c* were: U = 32.044 keV and I = 200 mA) with the accuracy of laser spectroscopy. The results fit within a two σ-error of the electron cooler uncertainty (compare chapter 7.6).

Out of these measurements the longitudinal temperature ΔT_{long} in the rest system of the ion beam can be estimated using

$$\Delta\nu_0 = \frac{\nu_0}{c}\sqrt{\frac{8\cdot k_B\cdot \Delta T_{\text{long}}\cdot \ln 2}{m}} \tag{4.10}$$

where k_B is the Boltzmann factor. From the measurement shown in Figure 7.19 a temperature of ΔT_{long} = 110 K for the velocity destribution is calculated. If one expresses naively the longitudinal kinetic energy of the ions (58 MeV/u) in terms of temperature $(E_{\text{kin}} \sim k_B \cdot T)$ one yields $T = 5\times 10^{12}$ K, what indicates a relative temperature stability of $\Delta T_{\text{long}}/T = 2\times 10^{-11}$ in the ion beam.

The lifetime of the metastable $^{7}Li^{+}$ $2s^3S_1$ ground state in the storage ring can be determined with fluorescence spectroscopy. The excitation laser is frequency tuned to resonance with the $2s^3S_1$ (F = $^5/_2$) → $2p^3P_2$ (F = $^7/_2$) transition for ions that are in the middle of the velocity distribution. The laser frequency is kept fix and the fluorescence signal is recorded as a function of time (e.g. for several minutes, till the signal converges to the background noise). The laser is introduced without waiting time for electron cooling of the ions. A rapid increase of the fluorescence rate at the beginning of each measurement is detected; this is due to the cooling which increases the number of ions in resonance (see Figure 4.12). Right after the injection the momentum spread of the ion beam is very broad (see chapter 4.2.1) and only a few ions are in the desired velocity class (small fluorescence rate). The electron cooling force narrows the distribution and the signal rises until the decay of the metastable state becomes the dominant process. Depending on the vacuum conditions in the ESR this point is reached after a few seconds up to half a minute. Then the signal $\hat{A}$ decreases exponentially

which can be explained by equation (4.11), where τ is the lifetime, t the time, A_0 the amplitude and ς the background noise.

$$\widehat{A} = A_0 \cdot e^{-\frac{t}{\tau}} + \varsigma \tag{4.11}$$

The amplitude is proportional to the number of metastable ions in the chosen velocity class. The background is due to thermal noise of the PMTs and remaining stray light of the lasers.

At excellent vacuum conditions ($p < 10^{-11}$ mbar), the lifetime of the metastable $^7Li^+$ ions was $\tau = (45 \pm 3)$ s, close to the natural one, while the storage time of the ion beam was more than two minutes. At a residual gas pressure of the order of $p \sim 10^{-10}$ mbar, the lifetime drops to $\tau = (27 \pm 3)$ s. The storage time of the entire ion beam in the ESR was even shorter (15 ± 1) s which can be understood if one remembers the composition of the ion beam. Beside the singly charged lithium ions, doubly charged nitrogen ions are present in the beam. The higher charge state of the nitrogen ions increases the probability of electron capture or coulomb interactions in the ring and therefore the losses increase. From the Schottky spectra a storage time of approximately 5 s was analysed, for the poorer vacuum conditions. This means that the decay of the doubly charged nitrogen shortens the measured storage time of the whole ion beam compared to a pure $^7Li^+$ beam.

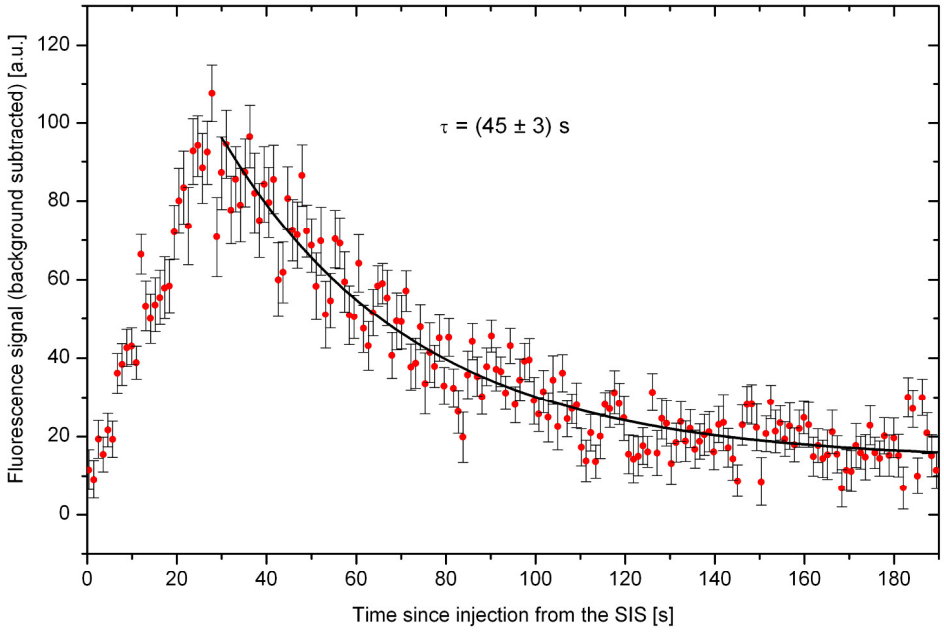

Figure 4.12: Lifetime of the metastable $2s^3S_1$ ground state of $^7Li^+$ in the ESR storage ring, measured by fluorescence (the background has been subtracted).

5 FIRST-ORDER DOPPLER-FREE SPECTROSCOPY TECHNIQUES

Although the momentum spread of an electron cooled ion beam is already narrow, the resulting Doppler-broadened fluorescence signal is not sufficient for a test of time dilation with higher precision than previous experiments. To achieve higher sensitivity first-order Doppler-free laser spectroscopy has to be performed. In such a kind of experiment fluorescence signals with sub-Doppler linewidths can be generated. This is possible by exciting particles simultaneously in and against their moving direction (equation (1.10)). With this technique a certain velocity class of ions is picked out of the velocity distribution and the fluorescence signal is narrowed by more than two orders of magnitude[26].

The hyperfine-structure splitting of the $2s^3S_1$ ground state and the $2p^3P_2$ state in $^7Li^+$ allows for three different kinds of first-order Doppler-free spectroscopy techniques by addressing different transitions. The three spectroscopy schemes are: V-spectroscopy, Λ-spectroscopy and saturation spectroscopy. These spectroscopy techniques need two laser beams to generate the desired fluorescence signal. One laser is kept on resonance with the chosen transition and a certain velocity class of ions; the other is frequency-tuned across the resonance. Considering the situation at storage rings, the alignment of these laser beams can be collinear-parallel or collinear-antiparallel with respect to each other and further with respect to the ion beam (see Figure 5.1). The main differences between the three alignment schemes are the different laser wavelengths that are needed to fulfil the resonance conditions for ions that travel with velocities approaching the speed of light (e.g. $\beta = 0.338$). For the signal generation it is irrelevant whether both lasers are aligned parallel or antiparallel with respect to each other (Figure 5.1a & b). Both cases allow for first-order Doppler-free spectroscopy. The advantage to perform measurements in the parallel laser-laser beam alignment is that both laser beams can travel through the same fibre and therefore uncertainties in the laser-laser overlap are minimised. This offers a good possibility to investigate the signal shape and the frequency position. At the ESR experiment only the collinear-antiparallel alignment was applied (Figure 5.1a) because the laser-background suppression in the fluorescence measurement is more efficient in than in the other regime. However, a test of time

[26] The Doppler-broadened signal has typically a FWHM in the GHz range. The first-order Doppler-free signal can have a linewidth in the range of the natural linewidth of the used transition [Reinhardt06].

dilation is only possible in a collinear-antiparallel laser-laser regime (Figure 5.1c). Only here the ion velocity cancels out and one is sensitive to time dilation.

All three spectroscopy schemes have advantages and drawbacks which are described in the following chapters, related to the time dilation experiment. For purposes of clarity the levels are labelled in the Dirac notation where $|g_n\rangle$ denotes a ground state n and $|e_m\rangle$ is the excited state m. Further the lasers that excite the transition from $|g_n\rangle$ to $|e_m\rangle$ are labelled $L_{(n+m)}$ and the respective transition is $\langle T_{n+m}\rangle$.

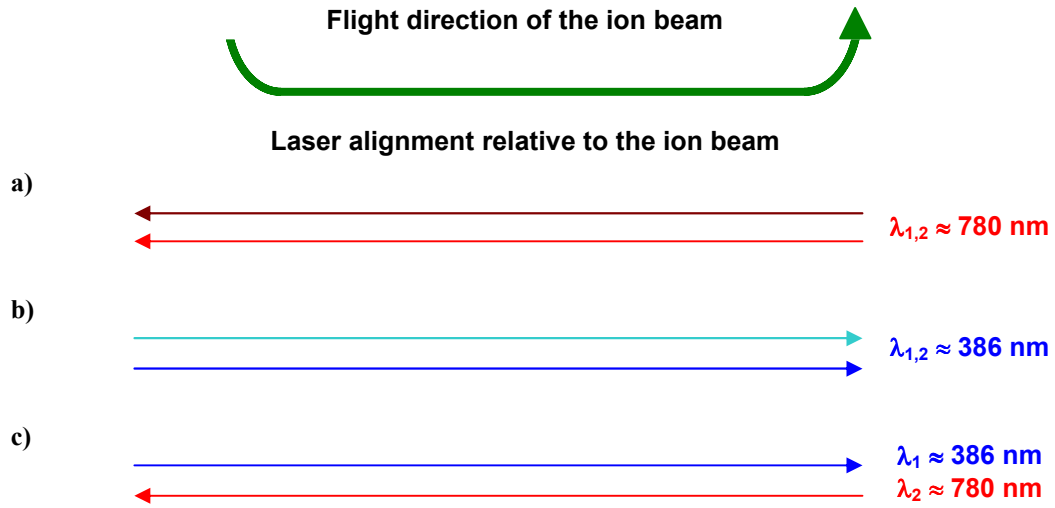

Figure 5.1: Three possible laser alignments for spectroscopy at a storage ring. a) the lasers are parallel and collinear-antiparallel to the ion beam, b) the laser are parallel and collinear-parallel to the ion beam, c) laser are antiparallel and collinear to the ion beam. The given wavelengths are for excitation of $^7Li^+$ ion with a velocity of $\beta = 0.338$.

5.1 V-SPECTROSCOPY

For V-type spectroscopy a three-level system with two excited states $|e_1\rangle$ and $|e_2\rangle$ that are coupled via one ground state $|g_0\rangle$ is needed (Figure 5.2 left). Further, an additional ground state $|g_1\rangle$ that is coupled to $|e_2\rangle$ and opens a loss channel from $|e_2\rangle$ is required. In the lithium ion this is given by the transitions $\langle T_1\rangle \equiv 2s^3S_1$ ($F = {}^5/_2$) $\rightarrow 2p^3P_2$ ($F = {}^7/_2$) and $\langle T_2\rangle \equiv 2s^3S_1$ ($F = {}^5/_2$) $\rightarrow 2p^3P_2$ ($F = {}^5/_2$), and the loss channel into the second ground state $|g_1\rangle \equiv 2s^3S_1$ ($F = {}^3/_2$).

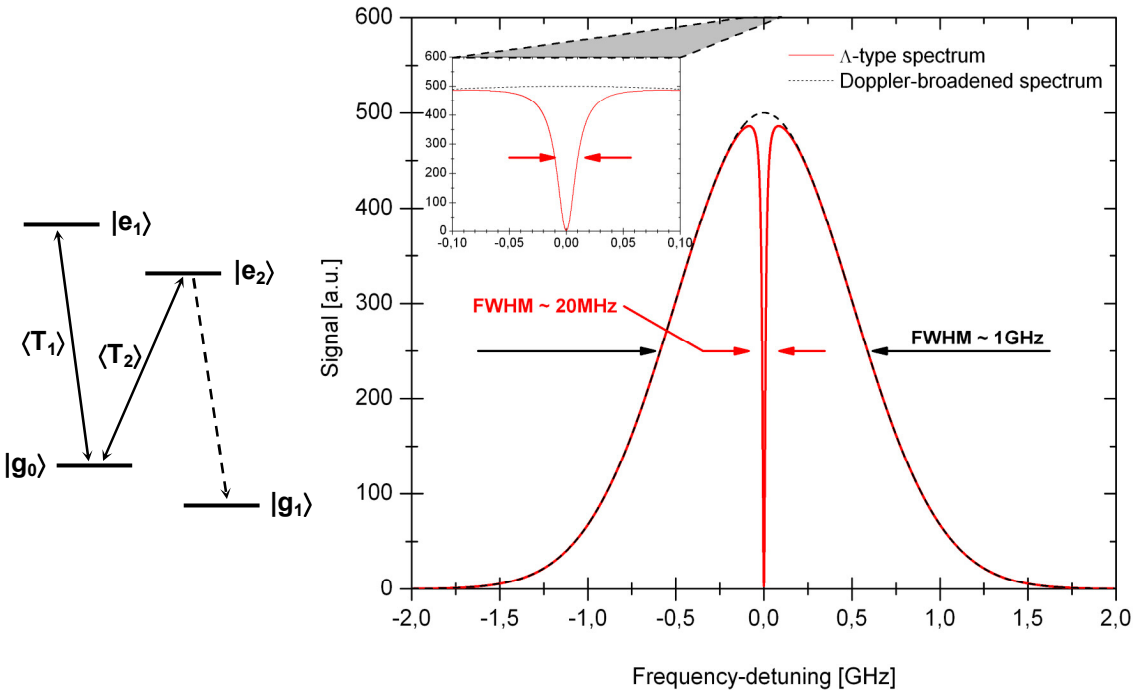

Figure 5.2: Left: Level scheme for a V-type spectroscopy where the lasers drive $\langle T_1\rangle$ and $\langle T_2\rangle$, respectively. The loss channel is indicated by the dashed arrow. Right: The dashed line indicates a Doppler-broadened fluorescence signal with a FWHM of 1 GHz (at $\langle T_1\rangle$). The red spectrum shows the influence of the second (frequency fixed) laser that is in resonance with $\langle T_2\rangle$. For the sake of clarity, the dip is overstated by a factor of ~ 4 of the natural linewidth.

Applying a laser L_1 that excites the closed two-level system $\langle T_1\rangle$ in the ion beam and tuning the frequency of this laser through the velocity distribution, one yields a Doppler-broadened spectrum that corresponds to the momentum spread of the beam (Figure 5.2, dashed line). Introducing a second laser L_2 that drives $\langle T_2\rangle$, a loss channel is opened because from $|e_2\rangle$ the electrons can decay into $|g_1\rangle$. Setting L_2 fix in frequency, resonant with a certain velocity class of the ions at $\langle T_2\rangle$, leads to a dip in the fluorescence spectrum (Figure 5.2, solid line). This is because all ions within the velocity class, L_2 is resonant with, are pumped into $|g_1\rangle$ and can not contribute to a fluorescence signal any more. Assuming the ions are not affected by velocity changing

forces, this dip width is in the range of the natural linewidth of the transition and the dip depth is at zero fluorescence. However, exactly those velocity changing effects (e.g. collisions in the electron cooler, intra-beam scattering) are present in a storage ring and cause a smearing of the dip.

5.2 Λ-SPECTROSCOPY

A closed three-level system, with two ground states $|g_0\rangle$ and $|g_1\rangle$ that are coupled via one excited state $|e_2\rangle$, is needed for Λ-type spectroscopy (Figure 5.3 left). In $^7Li^+$ two Λ-system are possible:

1. $2s^3S_1$ ($F = {}^5/_2$) → $2p^3P_2$ ($F = {}^5/_2$) and $2s^3S_1$ ($F = {}^3/_2$) → $2p^3P_2$ ($F = {}^5/_2$)
2. $2s^3S_1$ ($F = {}^1/_2$) → $2p^3P_2$ ($F = {}^1/_2$) and $2s^3S_1$ ($F = {}^3/_2$) → $2p^3P_2$ ($F = {}^1/_2$)

For storage ring experiments the first system is preferable, because of its larger hyperfine-splitting. Here $\langle T_2\rangle \equiv 2s^3S_1$ ($F = {}^5/_2$) → $2p^3P_2$ ($F = {}^5/_2$) and $\langle T_3\rangle \equiv 2s^3S_1$ ($F = {}^3/_2$) → $2p^3P_2$ ($F = {}^5/_2$).

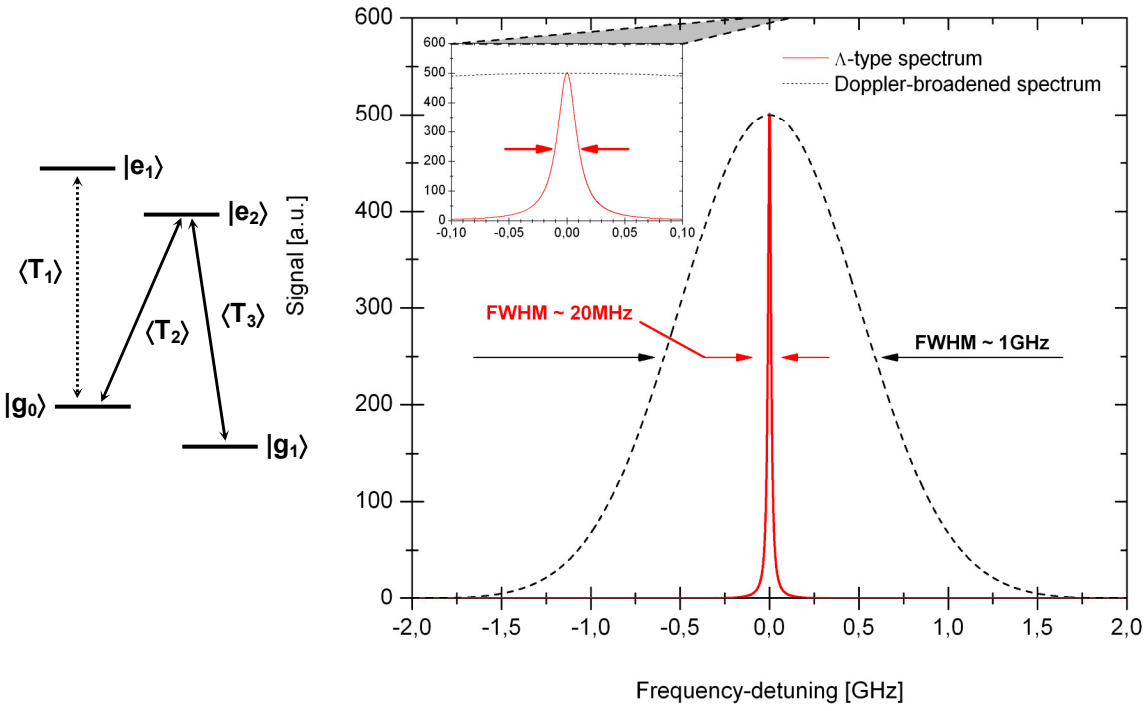

Figure 5.3: Left: Level scheme for a Λ-type spectroscopy. Right: The dashed line indicates a Doppler-broadened fluorescence signal with a FWHM of 1 GHz (at $\langle T_1\rangle \equiv (F = {}^5/_2) \rightarrow (F = {}^7/_2)$). The red curve shows the spectrum if one laser is in resonance with $\langle T_2\rangle$ and the second is tuned in frequency over $\langle T_3\rangle$. For the sake of clarity, the dip is overstated by a factor of ~ 4 of the natural linewidth.

Assuming an ideal ion beam[27] in a laser field L_1 that is in resonance with $\langle T_2 \rangle$ the electron in the excited state $|e_2\rangle$ can decay either into $|g_0\rangle$ or $|g_1\rangle$. When it decays into $|g_1\rangle$ it can only be excited again, if a second laser L_2 is in resonance with $\langle T_3 \rangle$. For L_1 these electrons are out of reach. Therefore the ground state distribution changes drastically when only L_1 is applied to the ions. Due to the continuous (stimulated) excitation of $|g_0\rangle$ and spontaneous emission into both ground states, $|g_0\rangle$ is depopulated within a short period. Hence, the equilibrium condition for ions in such a laser field is an empty $|g_0\rangle$ state, while all electrons are pumped into $|g_1\rangle$. For the detection of the fluorescence light this leads to a zero signal. If now the second laser is applied on resonance with $\langle T_3 \rangle$, the ions can be excited again. Establishing both lasers at resonance, a back and forth pumping of the electrons takes place and a stable fluorescence signal occurs.

Assuming a real ion beam[28] the velocity distribution of the ion beam has to be taken into account. However, the spectroscopy principle stays the same. If both lasers are in resonance with one transition of the Λ-scheme the electrons can be pumped back and forth. Hence, the resonance conditions have to be fulfilled for one velocity class of the ions. In the storage ring experiments L_1 is in resonance with $\langle T_2 \rangle$ for a certain velocity class of ions (typically, for a maximum of the signal, in the centre of the distribution) and fix in frequency. L_2 is tuned over $\langle T_3 \rangle$. A fluorescence signal appears only if both lasers are in resonance with ions of the same velocity class (Figure 5.3).

The theoretical linewidth of the signal should match the natural linewidth of the transition. However, the same mechanisms that smears out the signal of the V-type spectroscopy broadens the linewidth of the Λ-resonance to tens or hundreds of the natural one.

[27] Ideal means: without a velocity distribution in the ion beam.

[28] Real means: with a velocity distribution.

5.3 SATURATION-SPECTROSCOPY

Saturation spectroscopy can be performed only on a closed two-level transition $\langle T_1 \rangle$. Suitable levels in the lithium ion are the ground state $|g_0\rangle \equiv 2s^3S_1$ ($F = {}^5/_2$) and the excited state $|e_1\rangle \equiv 2p^3P_2$ ($F = {}^7/_2$) (compare Figure 5.4 left and Figure 2.2).

To describe the expected fluorescence signal of this spectroscopy type, the lasers are considered to interact separately with the ion beam at first. So, if one laser L_1 is frequency tuned over $\langle T_1 \rangle$, a Doppler-broadened fluorescence signal (orange plot in Figure 5.4 right) is generated. Assuming a second laser L_2 that is kept fix in frequency and in resonance with $\langle T_1 \rangle$, a fluorescence signal is gained, that is constant over time (indicated by the blue dotted line in Figure 5.4 right). If both lasers interact simultaneously with the ion beam, their fluorescence contributions are added which leads to a Gaussian spectrum that is lifted by a constant offset (black dashed line in Figure 5.4 right). But this statement is only valid if both lasers interact with ions of different velocity classes. When L_1 is tuned into resonance with the same class of ions that are already saturated by L_2, the fluorescence signal drops and a Lamp dip occurs (red plot in Figure 5.4 right). The width of the Lamb dip is only limited by the natural linewidth of the transition, the laser linewidth and saturation broadening effects.

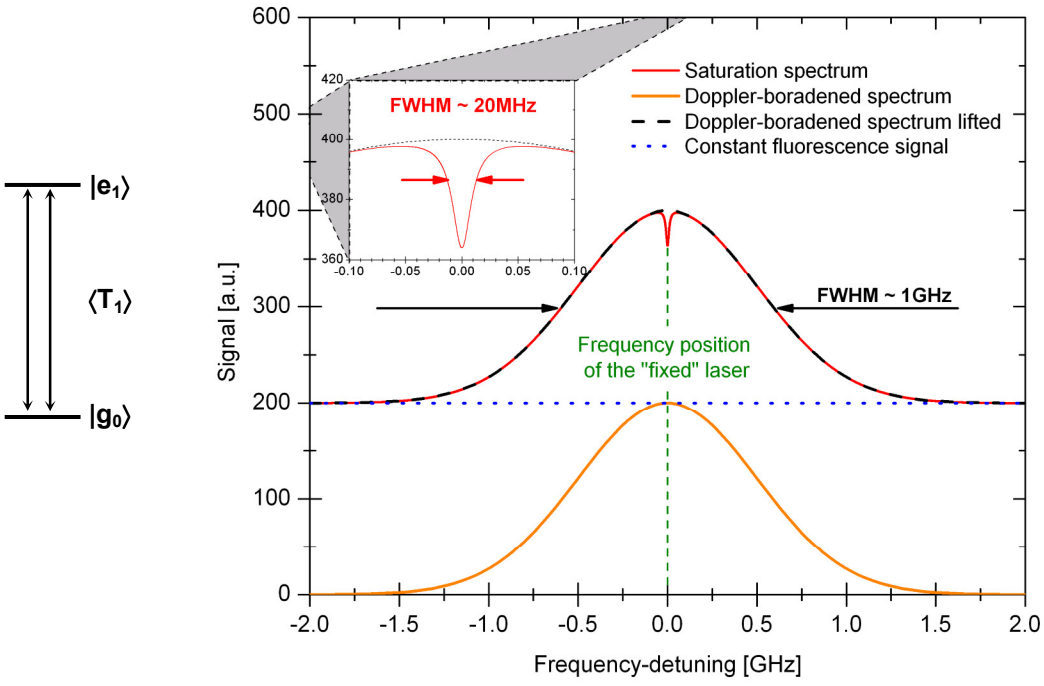

Figure 5.4: Left: Level scheme for saturation spectroscopy, both lasers excite the same transition $\langle T_1 \rangle$. Right: The orange line indicates a Doppler-broadened fluorescence signal with a FWHM of 1 GHz. The blue dotted line represents the fluorescence of the second (frequency fixed) laser. The dashed black plot combines both spectra, neglecting saturation effects. The red spectrum shows the Lamb dip that is induced by the saturation of the second laser. For the sake of clarity, the dip is overstated by a factor of ~ 4 of the natural linewidth.

6 THE LASER SETUP

For lithium ions at a velocity of 33.8 %c the Doppler effect shifts the excitation wavelength of the $2s^3S_1 \rightarrow 2p^3P_2$ transition from $\lambda_0 = 548.5$ nm at rest, to $\lambda_p = 386$ nm for a laser beam aligned parallel to the flight direction of the ion beam. For an antiparallel laser-ion beam excitation the shift results in a wavelength of $\lambda_a = 780$ nm. To perform first-order Doppler-free spectroscopy on fast lithium ions, two separate laser systems consisting of single mode lasers were installed: a frequency-doubled cw Ti:Sa[29] laser for generation of the 386 nm light and a diode laser or a Ti:Sa laser for the light at 780 nm (Figure 6.1) [30]. Both systems are controlled via frequency modulation saturation spectroscopy on I_2 molecules or Rb atoms. The absolute frequency was established by calibrating these resonances with a commercial frequency comb. Further a setup has been established (but not used in a beam time) where both lasers were directly and simultaneously controlled by the frequency comb. Additionally the lasers are controlled by Farby-Perot Interferometers (FPI) and wave meters. To get both laser beams to the ESR, where the fluorescence of the lithium ions is recorded, two different optical fibres are used..

A simplified overview of the laser spectroscopy system including the experimental section at the ESR is given in Figure 6.1. The light paths are colour coded: In bright green and red: laser light with a wavelength of 780 nm, orange: 772 nm, blue: 386 nm. The black lines/arrows indicate feedbacks from frequency control units to the respective lasers. The constituent parts of the system are described in the following chapters. A description of the measurement procedure and the interplay of the all components is given in chapter 7.6 (for Doppler-broadened spectroscopy) and in chapter 7.7 (for first-order Doppler-free spectroscopy).

[29] cw Ti:Sa = continuous wave titan:sapphire.

[30] For reasons explained in chapter 7.7 two diode lasers are implemented in the setup.

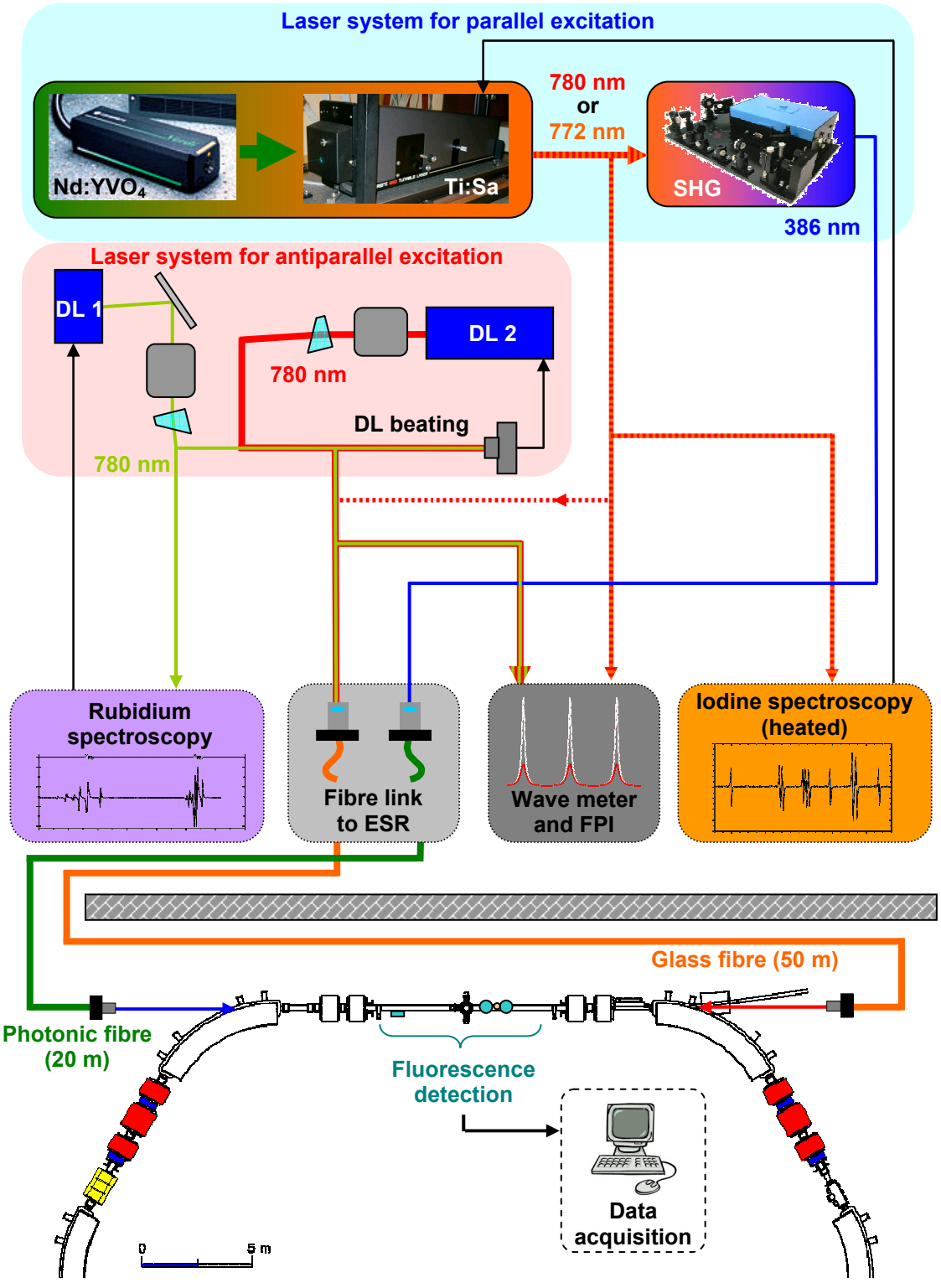

Figure 6.1: Overview screen of the laser setup for first-order Doppler-free spectroscopy of $^{7}Li^{+}$ at the ESR. The light paths are colour coded (for explanation see text). DL: diode laser, DL beating: frequency offset lock for the LDs, SHG: second harmonic generator, FPI: Fabry Perot interferometer.

6.1 LASER SETUP FOR PARALLEL EXCITATION

The laser light generation for ion excitation parallel to their moving direction a commercial tunable solid state ring laser (*coherent*, 899-21) with a titanium-sapphire crystal as the gain medium is used. This laser is pumped by a Nd:YVO_4 laser (*coherent*, Verdi) at 532 nm and the generated light (λ_{fp} = 772 nm) is afterwards frequency-doubled to the desired wavelength of λ_p = 386 nm.

A main feature of Ti:Sa crystal, as the laser medium, is its broad and homogenous gain profile that allows for emission wavelengths in the range of 700-1030 nm. A proper adjustment of the transmission frequency of the frequency selective elements in the ring cavity (etalons and birefringence filter) allows to tune the laser frequency over several tens of nm. A continuous tuning over the whole spectral range is limited by the reflection band of the mirrors. For the used laser this leads to a partition into three mirror-sets (700-825 nm, 790-930 nm and 925-1030 nm). A coarse wavelength tuning by arranging the birefringence filter and further frequency selection is done by changing the optical length of the cavity by tuning the thick and the thin etalon.

For short-term frequency stabilisation, the 899-21-system comprises a temperature stabilised reference cavity that consists of a Fabry-Perot interferometer (FPI) and a reference branch (Figure 6.2). Part of the laser light is split off by a beam splitter and guided to the FPI and the reference branch where the intensity of each beam is detected. The slope of the transmission peak of the FPI serves as a stable (not absolute) frequency reference. By generating the difference between the FPI transmission signal and the signal of the reference beam, a zero-crossing is produced on the slope, which determines the lock point of the stabilisation. In addition, the subtraction of the reference beam compensates for intensity fluctuations of the laser light. By feedback of the difference signal, which reflects the frequency deviation of the laser from the lock point, to a piezo crystal moving the output coupler, the laser frequency is stabilised by controlling the laser cavity length. With this technique the laser linewidth is kept of the order 1 MHz.

For remote tuning of the frequency, a glass plate is introduced in the reference cavity that can be tilted by an actuator. Applying a voltage of ± 5 V tilts the glass plate, changes the optical path length, and shifts the frequency of the transmission peaks. Since the laser is locked to one of the transmission peaks, it follows the frequency shifts. Mode-hop-free tuning ranges of more than 20 GHz are possible.

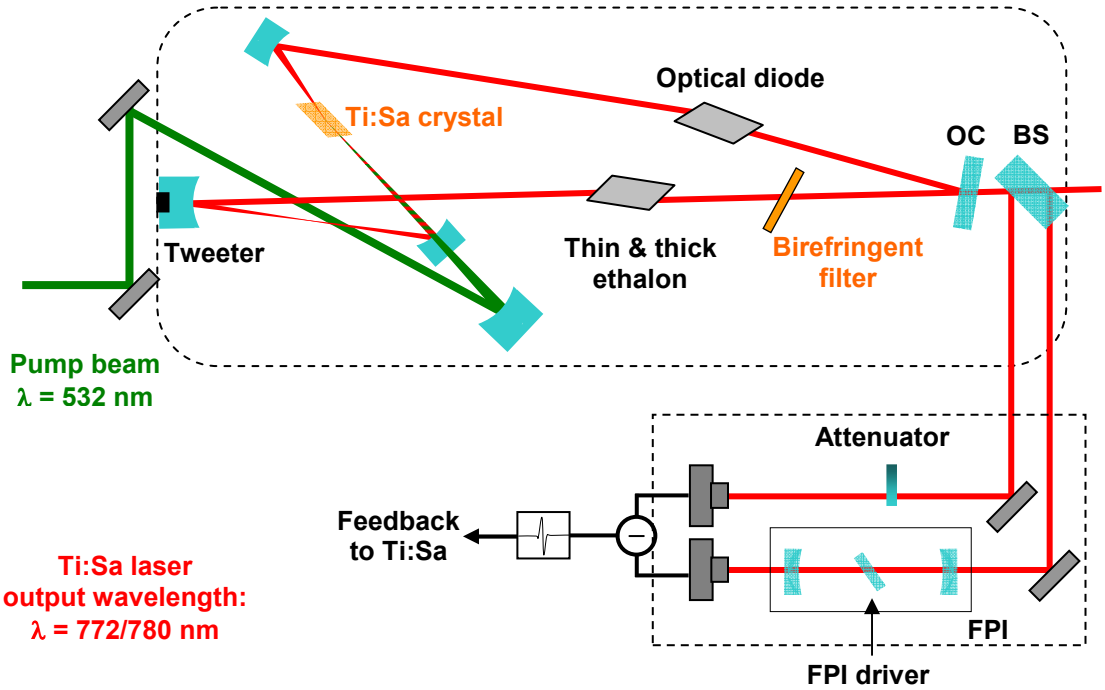

Figure 6.2: Schematic of the Coherent 899-21 cw Ti:Sa ring laser. OC: Out coupler, BS: Beam splitter for reference cavity, FPI: Fabry-Perot interferometer (explanation see text).

The broad and smooth tuning range and the high output power of the Ti:Sa laser (compared to the laser diode system) offers the possibility to use this system for the generation of the frequency for the antiparallel excitation (λ_a = 780 nm) as well as for the generation of the fundamental frequency for parallel excitation of the lithium ions. Both "red" wavelengths can be produced with the same set of mirrors. Only few adjustments of the frequency selecting parts are necessary. The conversion efficiency of the Ti:Sa laser saturates at a value of 19 % at a pump power of 13 W; 1.7 W of Ti:Sa laser light were available.

For ion excitation parallel to their flight direction, the Ti:Sa laser serves as the pump-source for a commercial frequency doubling system (*Tekhnoscan JS Company*, FD-SF-07). The conversion of the fundamental (λ_{fp} = 772 nm) to the second harmonic (λ_p = 386 nm) is done by a nonlinear optical BBO (beta-BaB_2O_4) crystal, aligned in a double Z-resonator (Figure 6.3). This resonator is frequency stabilised by the polarisation sensitive Hänsch-Couillaud technique [Hänsch80]. The birefringent BBO crystal is the optical element in the Z-resonator that generates the polarisation dependent error signal. Due to a phase shift between the parallel and the perpendicular fraction of the linear polarised light (caused by the imperfect alignment to the BBO crystal axis) the light that escapes the resonator is not anymore linear but elliptical polarised. Only if the cavity is in resonance[31], this phase shift disappears and the

[31] That means: $\delta = 2\pi \cdot m$, where δ = phase deviation; m = mode number {0… n}, n = integer number.

escaping light is linear polarised again. The light is guided through a λ/4 retarder, a polarisation beam splitter (PBS) and towards two photo diodes. Right before each photo diode another PBS is placed to attenuate the beam. The fast axis of the λ/4 retarder is tilted by 45° with respect to the doubling axis of the BBO crystal. Now, if the cavity is in resonance both photo diodes detect the same intensity and the signal difference is zero. Tuning the cavity length with a mirror, mounted on a piezo actuator, an error signal is generated with a zero-crossing when the cavity and the laser wavelength are in resonance. Or, vice versa, this signal is used to stabilise the cavity to the laser frequency.

The resulting power of the frequency-doubled light obeys $P(2\nu) = \Gamma \cdot L_K \cdot P^2(\nu) \cdot h(\delta,\xi)$ where Γ is a material parameter[32], L_K the length of the crystal along the laser beam, $P(\nu)$ the power of the fundamental and $h(\delta,\xi)$ a function of the mode matching[33]. A conversion efficiency up to 16.5 % has been achieved (see Figure 6.3). This results in a maximum output power of $P_p = 280$ mW.

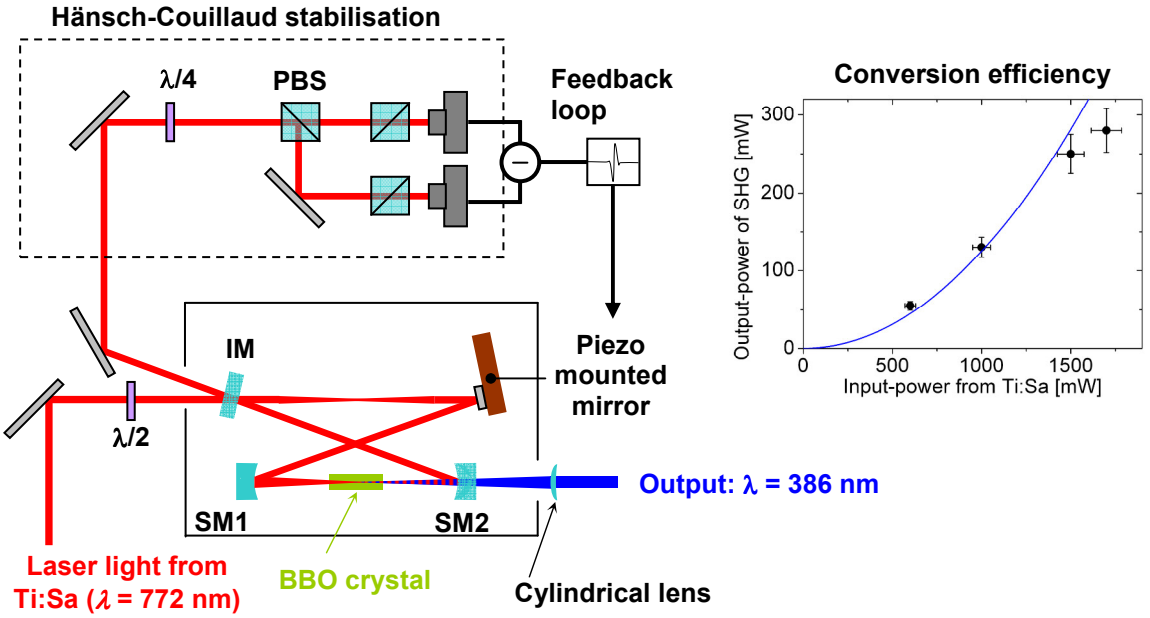

Figure 6.3: Schematic of the second harmonic generator FD-SF-07 with a Hänsch-Couillaud stabilisation. IM is the incoupling mirror; SM1 and SM2 are spherical mirrors that focus the fundamental into the frequency doubling BBO crystal. The conversion efficiency of the setup is shown in the lower right diagram. Black dots: measured data, blue line: square fit.

---

[32] $\Gamma = \dfrac{2 \cdot \left(\nu/2\pi\right)^3 \cdot d_{\text{eff}}^2}{\pi \cdot \varepsilon_0 \cdot n_1 \cdot n_2 \cdot c^4}$, where $d_{\text{eff}} \equiv$ effective thickness, n_1, $n_2 \equiv$ refraction index along the two crystal axis, $\varepsilon_0 \equiv$ dielectric constant.

[33] $h(\delta,\xi) = 1.068$ for optimal parameters [Boyd68].

6.2 LASER SETUP FOR ANTIPARALLEL EXCITATION

For antiparallel excitation of the ion beam either the system with the Ti:Sa laser or a setup with a laser diode is used. Due to the huge mode-hop-free scanning range the Ti:Sa laser is preferred for antiparallel Doppler-broadened spectroscopy. For first-order Doppler-free experiments laser diodes generate the light for antiparallel excitation These have a power maximum at 781 nm which can be detuned by 3 nm. They are implemented in a commercial laser head (*Toptica*, DL100) in Littrow configuration (Figure 6.4). The laser diode is placed behind a collimator lens and irradiates a reflection grating. The first-order diffraction of the desired wavelength is fed back into the laser diode to seed lasing at this frequency. The zero-order beam is coupled out via another mirror (that inhibits beam-walk during the tuning of the laser) and guided through an optical isolator (attenuation – 60 dB). After shaping by an anamorphic prism pair it is sent to the experiment. The temperature of the diode is controlled (to $\Delta T = \pm$ 0.1 °C) by a peltier element and kept at 16-21 °C, depending on the desired wavelength and laser diode type. To change the lasing frequency, the current of the laser diode or the piezo, which tilts the position of the grating, can be used. Tuning by current has the advantage of faster response (100 kHz to 500 MHz) while the mode-hop-free tuning range is comparatively small (tens of MHz). Due to the inertia of the grating in its mount the frequency changes performed with the piezo are not as fast as by the use of the current, but still suitable for lithium spectroscopy. Further the mode-hop-free tuning range by tilting the grid is larger (~ 10 GHz). The linewidth of the laser is 2 MHz and has a maximum power of 150 mW.

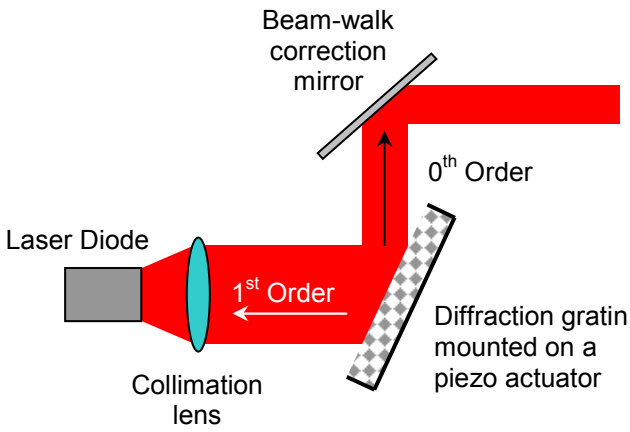

Figure 6.4: Schematic of the laser diode head in Littrow design. The first-order diffracted beam is fed back into the laser diode to seed the laser to this frequency. The zeroth-order light is guided (trough the beam-walk correction mirror) to the experiment.

6.3 FREQUENCY STANDARDS

The output frequency of a laser that is not stabilised to an external reference can vary over a huge frequency range in time (several GHz and more) due to temperature changes or power fluctuations. So, for precision spectroscopy it is indispensable either to stabilise the laser to a reference or to measure the frequency with respect to a frequency standard. In principle a frequency standard is a clock that produces a stable frequency with only small fluctuations over time combined with another oscillator that can be traced back to the frequency of a primary standard used to realise the SI[34] unit [Riehle04]. With such a device other references (e.g. atomic or molecular transitions) can be calibrated. For the test of the theory of special relativity at the ESR two different types of frequency references were used: direct optical frequency references based on atomic or molecular transitions; and rf references which were translated into the optical frequency domain using a frequency comb.

6.3.1 THE FREQUENCY COMB AS REFERENCE

A commercial frequency comb (*Menlo Systems*, FC1500), in combination with a rubidium radio frequency standard, has been used as a frequency reference. The comb structured light, with a peak wavelength of 1560 nm, is produced by an erbium doped fibre laser which is pumped by a diode laser. Its frequency is doubled to allow measurements in the near-infrared and visible region. The repetition rate of the frequency comb is around 100 MHz and the carrier envelope offset (CEO) frequency is stabilised to 20 MHz. The spectrum of the frequency-doubled output of the comb can be further broadened with a photonic crystal fibre. The accuracy of the frequency comb itself can reach $\Delta\nu/\nu < 10^{-14}$. This depends on the accuracy of the clock the comb is referenced to. In the presented thesis the external reference for the frequency comb is a rubidium radio frequency standard (*Stanford Research Systems*, FS725). The offset frequency and the repetition rate of the comb are compared to this standard. The Rb clock is specified to provide a relative accuracy of better than $\pm 5 \times 10^{-11}$ at the date of calibration and a yearly drift of less than 5×10^{-11}.

The frequency comb has been used either to beat the laser light directly with the comb mode (to stabilise the laser or maintain its frequency) or to calibrate molecular frequency references (see chapter 6.3.4).

---

[34] SI: Systéme International d'Unités which is French for International System of Units, the modern international standard version on the metric system.

LOCK TECHNOLOGY

To stabilise lasers on a frequency comb the monochromatic light of the laser and the comb structured light were merged by a PBS (see Figure 6.5). Here the polarisation of the overlapped beams are perpendicular to each other. To equalise the direction of polarisation, a λ/2 wave plate and another PBS are arranged in the beam path. The collinear beams are guided to a diffraction grating for wavelength separation. The laser beam and the closest mode of the frequency comb are matched on a fast photo diode to measure the beat frequency. This heterodyne radio frequency is compared with a preset value and an error signal is fed back to the laser. To achieve a good signal-to-noise ratio, the intensities of both beams are adapted via a λ/2 wave plate in front of the first PBS.

In the lithium experiment the desired wavelengths are 772 nm (for frequency-doubling to 386 nm) and 780 nm, respectively. Both wavelengths can be locked to the frequency comb simultaneously (Figure 6.5). This is achieved by overlapping both laser beams before merging them with the light from the frequency comb. The used grating reflects the two wavelengths at different angles so that the beat of both lasers with the comb can be guided to different photo diodes. The signals of both photo diodes are compared to the preset reference values and the resulting control signals are fed back to the corresponding laser.

For first-order Doppler-free fluorescence spectroscopy on $^{7}Li^{+}$ in the ESR, the Ti:Sa laser is stabilised to a certain comb mode at the fundamental wavelength λ_{pf} = 772 nm, all the time. The light of the laser diode is tuned by 100 MHz using an acousto-optic modulator (AOM, *Brimrose*, TEF-225-100-.780) in a double path arrangement. So the beat frequency of the laser light and the light of the frequency comb is changed by changing the rf frequency of the AOM. This beat signal is compared to a preset reference value, gaining a control signal which is fed back to the laser diode to compensate the shift of the AOM. Therewith the net effect is a tuning of the laser frequency. However, by tuning the frequency of the AOM the lateral position of the laser beam is changing too, although it is used in a double-path regime. This leads to intensity fluctuations in the beat signal and therefore to a weak feed back loop. To compensate this effect a mirror with piezo actuators is introduced into the optical path.

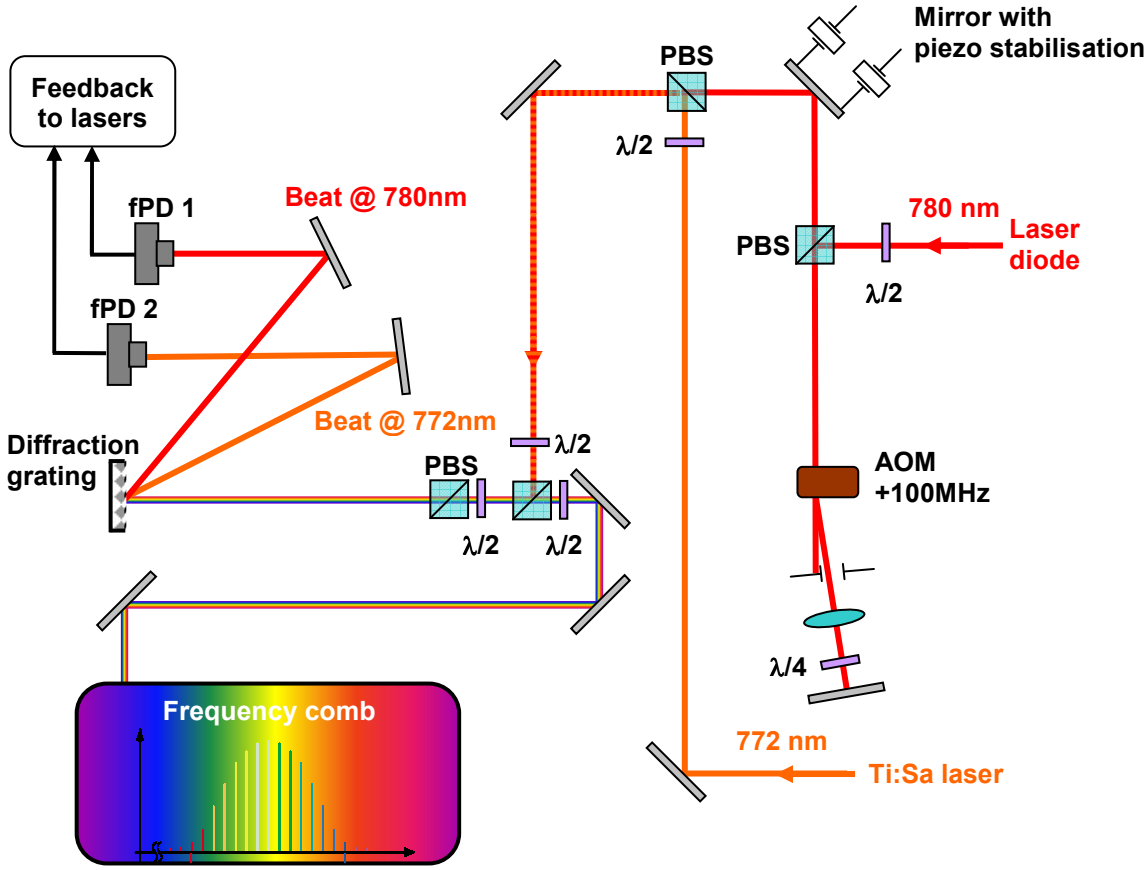

Figure 6.5: Setup to perform first-order Doppler-free fluorescence spectroscopy on $^{7}Li^{+}$ in the ESR (for explanation see text). AOM: acousto-optic modulator, fPD: fast photo diode, PBS: polarisation beam splitter.

6.3.2 ATOMIC AND MOLECULAR FREQUENCY REFERENCES

As described in the previous chapter the frequency comb is a powerful tool to control or maintain the frequency of lasers at highest precision. However, the frequency comb was shared with other experiments and therefore only limited available. For daily use a secondary reference was needed to control the laser frequencies. Furthermore, for a beam time at the ESR, secondary, robust, and independent frequency references are preferable to back up the frequency comb.

For the laser wavelength λ_a = 780 nm, ^{87}Rb is a well defined and commonly used atomic frequency reference [Banerjee03]. No secondary reference was realisable for the wavelength for parallel excitation λ_p = 386 nm. Even for the fundamental no candidate was available at standard conditions. But molecular iodine at high temperatures offers suitable transitions to which a laser can be referenced.

LOCK TECHNOLOGY

For laser stabilisation a narrow signal with an odd symmetry and a good signal-to-noise ratio is desirable. To obtain such a signal from molecular or atomic references, frequency modulation saturation spectroscopy is applied to particles in a gas cell. For the saturation spectroscopy two laser beams (one high power beam for saturation and one low power beam to probe) are aligned anti-collinear in the cell, frequency tuned over a resonance of the particle and the absorption of the probe laser is recorded as a function of the laser frequency. In contrast to the saturation spectroscopy performed at storage rings (chapter 5.3), both laser beams have the same frequency ν_1 (in the laboratory frame). Hence, these excite the particles from the ground level to the excited level that have a velocity υ, described by

$$\nu_1 = \nu_0 \cdot \gamma \cdot \left(1 \pm \frac{\upsilon}{c}\right) \tag{6.12}$$

where ν_0 is the rest frequency of the transition, c is the speed of light, and γ is the Lorentz factor[35]. Each laser burns a Bennett hole in the particle distribution of the ground state at $\pm\ \upsilon$ (see Figure 6.6). Only if the laser frequency is equal to the rest frequency both laser beams interact with particles of the same velocity group, namely $\upsilon = 0$. The modification of the population distribution of the probe beam is very low compared to the one induced by the saturation beam, which results in a lower absorption signal for the probe beam. In the absorption spectrum of the probe beam a dip (Lamb dip) appears when $\nu_1 = \nu_0$. The Lamb dip can be described by a Lorentz function with a linewidth $\gamma_S = \gamma_0 \cdot \left(1 + \sqrt{1+S}\right)$, where γ_0 is the natural linewidth without saturation and S is the saturation parameter, defined as the ratio of the used laser intensity divided by the saturation intensity I_s of the transition[36]. The power of the probe beam is usually by a factor of ten smaller compared to the saturation beam power.

[35] The ± sign denotes whether the laser is in resonance with particles which are moving in (+) or against (–) the propagation direction of the laser.

[36] [Svelto98]: $I_s = \frac{h \cdot \nu}{2 \cdot \sigma \cdot \tau}$, h is the Planck constant, σ is the absorption cross section, and τ is the lifetime.

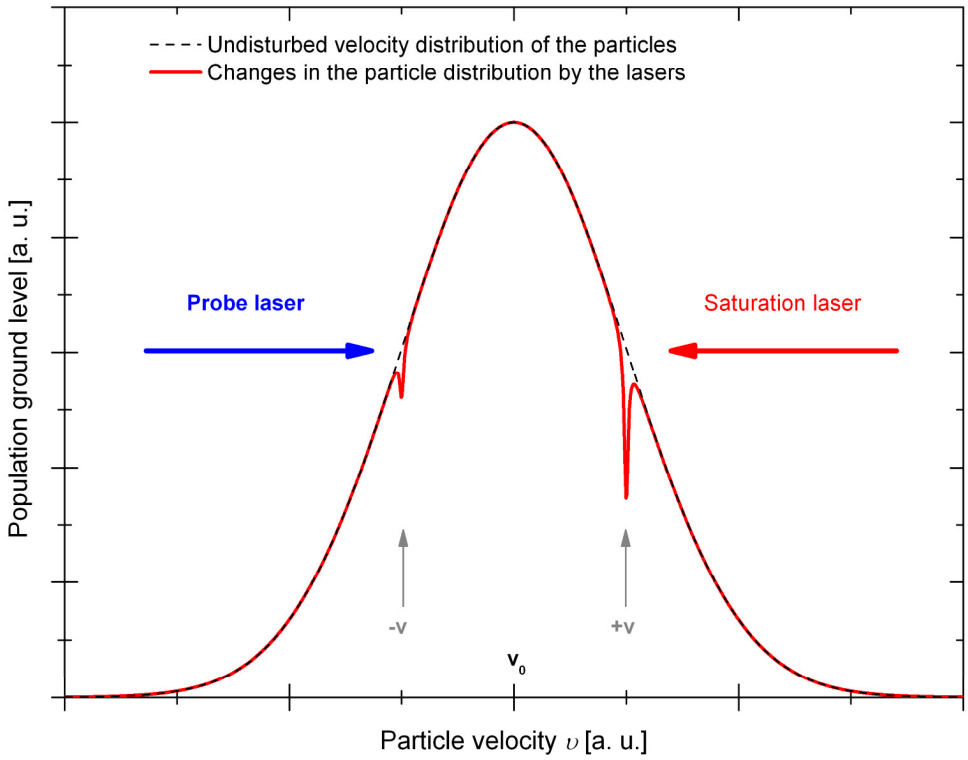

Figure 6.6: Hole-burning in the population distribution of the ground level with a strong saturation beam and a weak counter-propagating probe beam.

The sensitivity can be enhanced by frequency modulation spectroscopy. To this end, an electro-optic modulator (EOM, made by *Newfocus*, Model 4002 or a *self-made device* [Gabrysch94] were used) creates sidebands with a modulation frequency of $\pm\Omega$ (typically a few MHz) on the test beam. In principle this leads to two beat signals: The carrier frequency with a positive and a negative sideband ($I(\nu+\Omega)$ and $I(\nu-\Omega)$). Since the sidebands have opposite phases they compensate each other and a phase sensitive detector shows a zero signal at Ω. If the frequency of one sideband overlaps with a transition in the particle it is absorbed and a beat signal is detected. The heterodyne amplitude signal is measured by mixing the photo diode signal with the modulation frequency Ω of the EOM. With a phase shifter the absorption or the dispersion signal is selected and fed into a lock-in amplifier to suppress the remaining background noise. The reference frequency of the lock-in amplifier is the switching frequency of an AOM which chops the saturation beam. This odd signal is free of Doppler background and exhibits a good signal-to-noise ratio. It serves as the error signal for the PI-controller which holds the laser on the reference line. Besides chopping of the saturation beam the AOM shifts the frequency of the laser by $\Delta\nu_{12}$, which has to be small (compared to the width of the Doppler distribution) and that leads to the fact that the laser is not locked on the peak of the transition but to $\nu_{\text{Laser-lock}} = \nu_0 - \Delta\nu_{12}/2$.

The usual setup of the performed frequency modulation saturation spectroscopy is shown in Figure 6.7. A more detailed description of this technique is given in [Lock05].

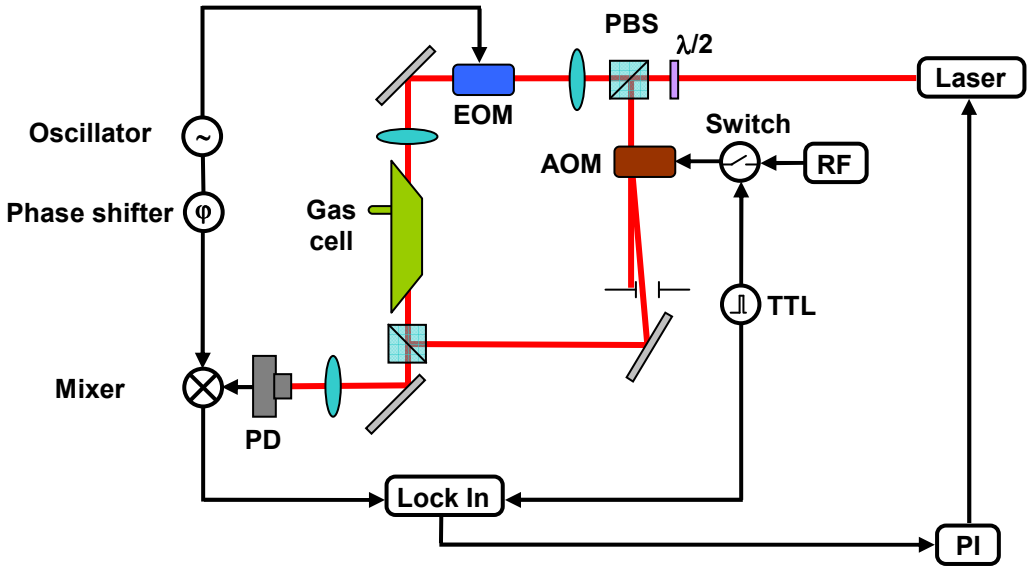

Figure 6.7: Basic sketch of a setup suitable for frequency modulation saturation spectroscopy (for explanation see text). RF is a radio frequency generator; TTL is a pulse generator which gives the chopping frequency. The intensities of the weak test and strong saturation beams are controlled by a λ/2-retarder and a PBS.

6.3.3 ATOMIC RUBIDIUM AS A FREQUENCY REFERENCE

For the lithium experiment at the ESR, atomic rubidium is a suitable candidate as a frequency reference for the laser light that is aligned against the flight direction of the ions. At the ion velocity of $\beta = 0.338$ the excitation frequency of the $2s^3S_1 \rightarrow 2p^3P_2$ transition in $^7Li^+$ is shifted to 780 nm, which is close to the strong D2 transitions of rubidium. In the used spectroscopic cell, the isotopes of the rubidium gas are composed according to their natural occurrence. Twenty nine Rb-isotopes are known while only two of them are quasi stabile. ^{87}Rb has a natural abundance of 27.835 % and a half-life of 4.88×10^{10} years. ^{85}Rb is a stabile isotope with an abundance of 72.168 % [CRC74-93]. The inner four electronic shells are filled and only one valence electron in the outer 5s shell determines the angular momentum configuration of the atom (J = 1/2). Therefore, the ground state is given by $5^2S_{1/2}$ with no fine-structure splitting. From this state two strong transitions to the first excited states ($5^2P_{1/2}$ and $5^2P_{3/2}$) are available. The splitting between both states is 7.123 THz [Sansonetti06] or in other words, for the excitation from $5^2S_{1/2} \rightarrow 5^2P_{1/2}$ (D1-line) a wavelength of 795 nm and for the second transition $5^2S_{1/2} \rightarrow 5^2P_{3/2}$ (D2-line) of 780 nm, is needed. The coupling of the nuclear spin of both isotopes ($I(^{85}Rb) = 5/2$ and $I(^{87}Rb) = 3/2$) with the angular momentum of

the electrons leads to the hyperfine splitting shown in Figure 6.8. Due to the selection rules for electric dipole transitions ($\Delta L = \pm 1$, $\Delta F = 0, \pm 1$) twelve transitions are allowed [Haken04]. These are distributed over a range of 7 GHz. These lines can be subdivided into four groups (Doppler-broadened spectrum) with a distance of 2-3 GHz between each group. In these groups three transitions are separated by tens of MHz and suitable for laser stabilisation. Addressing these transitions with saturation spectroscopy techniques additional crossover resonances appear (see Figure 6.9). These emerge if the probe beam is on resonance with one transition for a certain velocity class and the saturation beam is resonant with another transition for the same velocity class. The frequency of those crossover resonances (ν_{co}) is given by $\nu_{co} = (\nu_1 + \nu_2)/2$, where $\nu_{1,2}$ are the frequencies of the respective transitions. The additional line appears in the centre of both transition frequencies.

The absolute frequency of the crossover resonance $5^2S_{1/2} \rightarrow 5^2P_{3/2}$ (ν_1: (F = 2 → 3) and ν_2: (F = 2 → 2)) is known to (384 227 981 877.3 ± 5.5) kHz [Ye96]. It was determined by comparing this transition to the $5S_{1/2} \rightarrow 5D_{3/2}$ two photon transition in rubidium at 778 nm, a commonly used frequency reference [Nez93]. The hyperfine intervals of the D2 transition were measured in [Barwood91, Banerjee03, Bize99] to a sufficient accuracy in the kHz range. An overview of the physical and optical properties of ^{87}Rb is given in [Steck08].

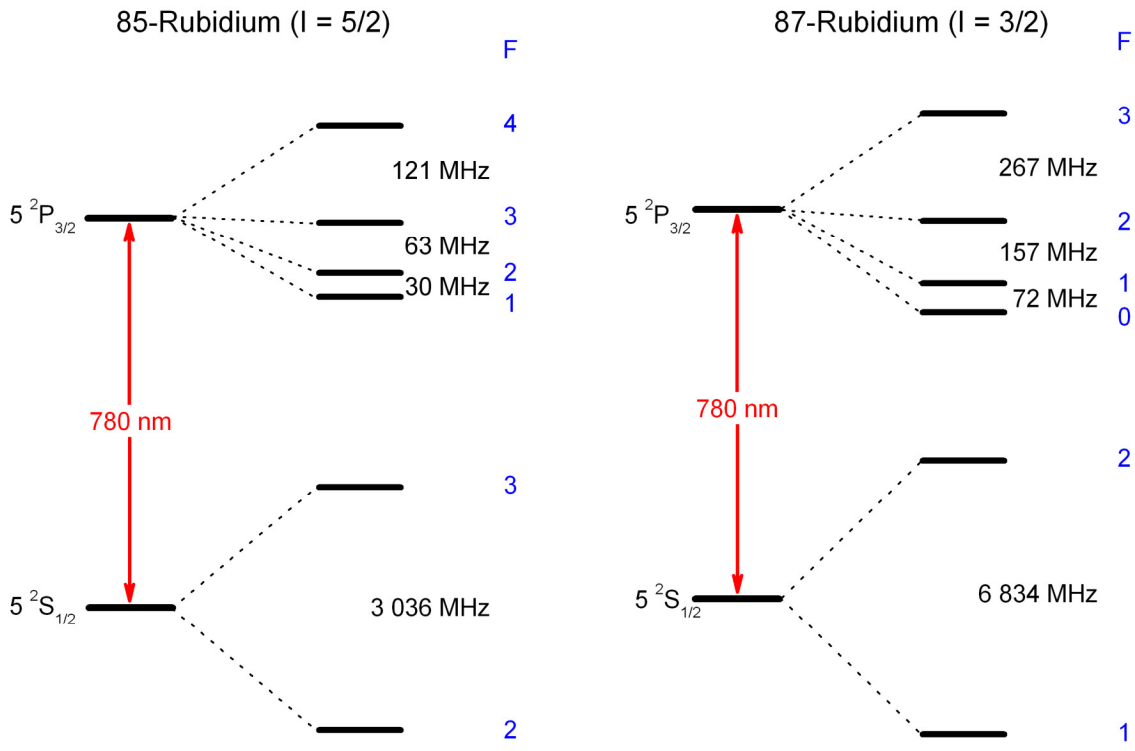

Figure 6.8: Hyperfine-structure splitting of the D2 transition for the two rubidium isotopes 85 and 87.

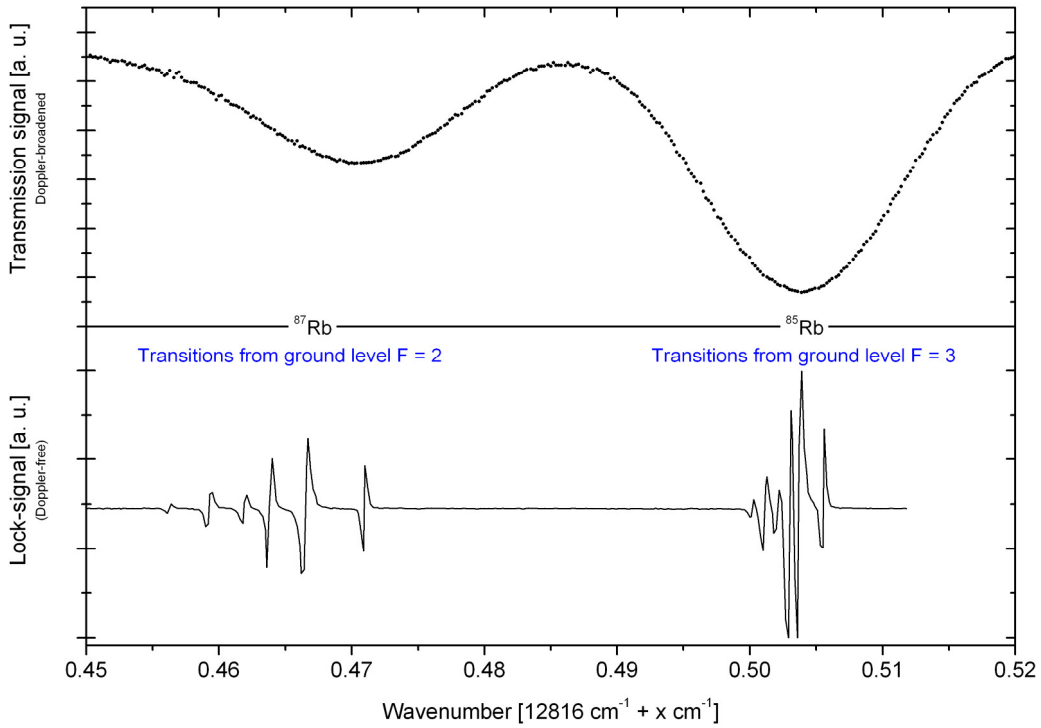

Figure 6.9: Upper panel: Doppler-broadened transmission spectrum of the D2 transitions from the ground level 5 $^2S_{1/2}$ (F = 2) for ^{87}Rb and the ground level 5 $^2S_{1/2}$ (F = 3) for ^{85}Rb. Lower panel: Spectrum gained by frequency modulation saturation spectroscopy and lock-in technique with the same D2 transitions.

6.3.4 MOLECULAR I_2 REFERENCE

Due to its rich and strong absorption spectra of the electronic $X^1\Sigma^+_g \rightarrow B^3\Pi^+_{0u}$ transition in the visible spectral range, the diatomic iodine molecule $^{127}I_2$ is often used as a frequency reference in laser spectroscopy [Lehmann78, Quinn03]. Iodine has a large nuclear quadrupole moment which leads to a strong hyperfine-structure splitting and natural linewidths of ~ 100 kHz [Bordé79]. Applying Doppler-free spectroscopy sharp lines can be recorded that are ideal for laser stabilisation, but also serve as frequency references at a high level of accuracy of a few part in 10^{-9} or better [Edwards99]. The small sensitivity to magnetic fields [Goncharov91&96] and the easy handling in glass cells make it favourable as a frequency reference and some I_2 lines are even recommended as wavelength standards by the Comité International des Poids et Measures (CIPM). These lines lie in the range of 532-640 nm and are measured with a sub-MHz uncertainty [Quinn03]. Theoretical values for the region from 667-776 nm have a relatively low accuracy of 30 MHz [Knöckel04] and so far the only high precision experiment in the "red" part of the visible I_2 spectrum was performed at 780 nm with an uncertainty of 36 kHz [Bodermann00]. To use molecular iodine as a frequency reference, for the test of special relativity, transitions in the region of interest

were calibrated to accuracies below 1 MHz by the help of a frequency comb. The rovibronic P(42)1-14 transition group is in the near-infrared region (λ = 772 nm), starting on a higher vibrational level of the electronic ground state. It has an even rotational quantum number for the ground state. Hence, the group consist of 15 hyperfine-structure lines due to the quantum statistical properties of a homonuclear diatomic molecule and the nuclear spin of the iodine atom. The iodine cell has to be heated to 550 °C to efficiently populate that level. At a cold finger temperature[37] of 25 °C three lines (a_1, a_{10}, a_{15}) are well resolved while the others are not (Figure 6.10). Each of these three lines can be used to stabilise the fundamental laser wavelength for parallel excitation.

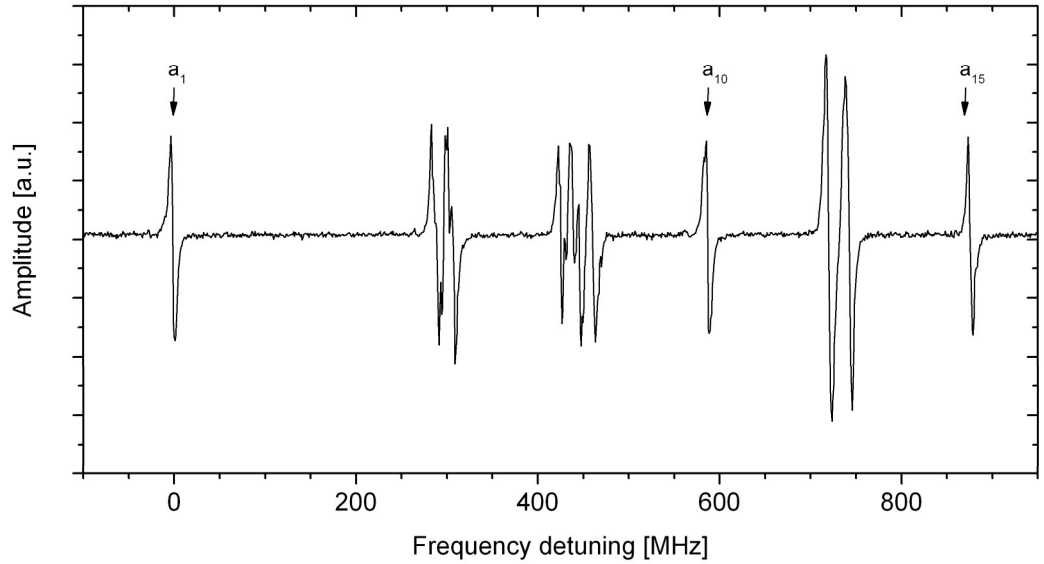

Figure 6.10: Hyperfine-structure pattern of the P(42)1-14 transition with the a_1 line used for absolute frequency calibration. The cell temperature was 550 °C; the cold finger temperature was 25 °C.

The transition group P(148)1-14 at 780 nm has been included in these measurements for comparison and to estimate the quality of the cell (e.g. to investigate influences of residual gases due to the manufacturing process). This transition was measured previously with an uncertainty of 36 kHz [Bodermann00] and due to the small uncertainty it acts as a second reference[38].

[37] The cold finger temperature determines the vapour pressure in the iodine cell.

[38] Further, lines from the transition group R(114)2-11 (735 nm) were measured [Reinhardt07b]. Those served as frequency reference for isotope shift measurements in lithium to determine the nuclear charge radii [Sánchez06].

For the calibration, the iodine cell is adjusted in a frequency modulation saturation spectroscopy setup that is described in principle in chapter 6.3.2. Further, part of the laser light is coupled into a polarisation maintaining single mode fibre (*Fibercore*, HB750) to transfer it to a wave meter (*Atos*, LM007)[39] and the frequency comb. In the experiment the repetition rate, the CEO frequency, and the heterodyne frequency between the laser and a comb mode (around 30 MHz) were measured. The reference of the frequency comb is a rubidium rf standard (*Stanford Research Systems*, FS725) that had a relative uncertainty of 6.3×10^{-10} at the date of the measurements.

In gas cells the energy levels of atoms or molecules are disturbed by collisions. This perturbation causes a shift of the spectral lines of the particle when absorbing or emitting light and thus a source for systematic errors. To investigate this effect in I_2 the absolute frequency ν of the a_1 line was measured as a function of the vapour pressure for both transitions. Here, the temperature of the cold finger was changed from 10 °C up to 40 °C. To convert the set temperature into the iodine vapour pressure, equation (6.13), according to [Gillespie36] is used

$$\log(p) = -\frac{3512.830}{T + 273.15} - 2.013 \cdot \log(T + 273.15) + 18.37971. \qquad (6.13)$$

p is the iodine vapour pressure in Pascal and T is the temperature of the cold finger given in degree Celsius instead of atmosphere and Kelvin as used in [Gillespie36]. The function for each transition is plotted in Figure 6.11. The slope dependence of the frequency is, (–5.0 ± 0.2) kHz/Pa for R(42)1-14 a_1 and (–5.5 ± 0.3) kHz/Pa for R(148)1-14 a_1. No significant difference in the derived slopes can be observed.

To determine the absolute frequency of the respective a_1 lines, the measurements, shown in Figure 6.11, were referred to the typical cold finger temperature (25 °C for P(42)1-14 and 20 °C for P(148)1-14). The results are plotted in Figure 6.12. Possible deviations in the cell temperature result in a frequency gradient of (0.1 ± 0.2) kHz/°C which is small compared to other uncertainties and therefore negligible. Regarding the uncertainties of the used spectroscopic setup (100 kHz), of the rubidium rf standard and the measured values, one obtains an uncertainty of ± 265 kHz for 772 nm and ± 263 kHz for 780 nm [Reinhardt07b]. For the 780 nm reference transition, a frequency that is (300 ± 266) kHz smaller than that reported in [Bodermann00] was obtained. Because the difference of 300 kHz is slightly higher than the given uncertainties, it is set as the overall uncertainty of the absolute frequency measurements for all transitions.

[39] The wave meter is used for a coarse control of the frequency ($\Delta\nu$ = 100 MHz) and to maintain the beat mode of the frequency comb.

In Table 6.1 the results are compared to the literature values. The agreement for the transition at 772 nm with the model prediction [Toptica02] is sufficient. This value can be used for a fine tuning of the model due to the, by two orders of magnitude, higher precision.

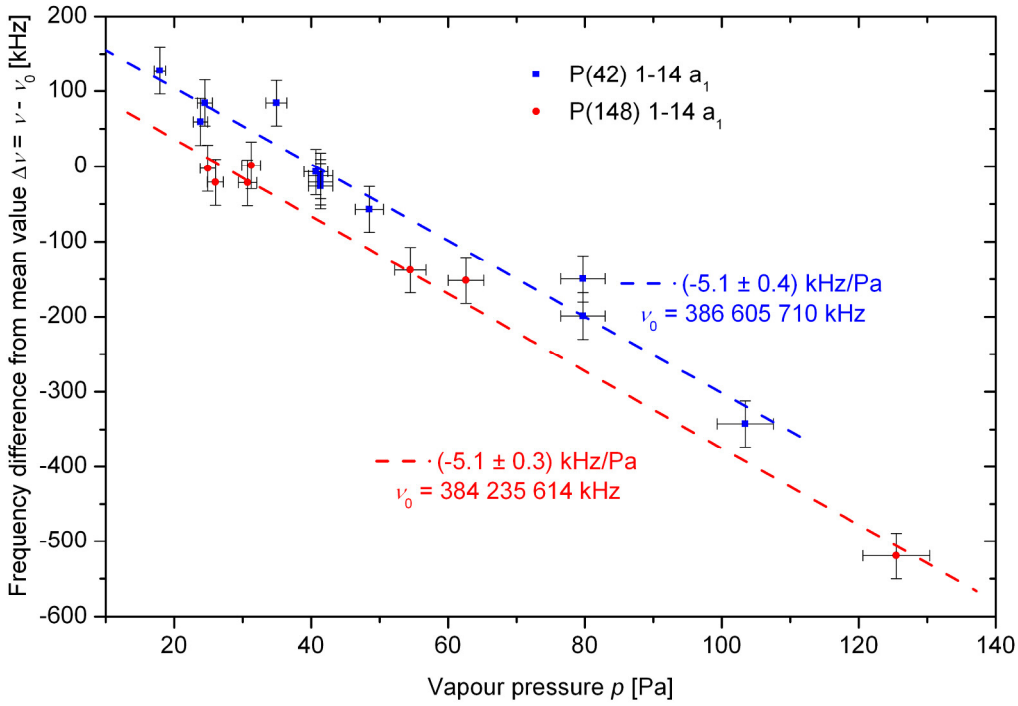

Figure 6.11: Frequency difference ($\Delta\nu = \nu - \nu_0$) of the measured frequency ν from the mean value ν_0 of the a_1 line as a function of the vapour pressure for the transition R(148)1-14 (red dots) and of the transition P(42)1-14 (blue squares).

Table 6.1: Comparison of the measured transition frequencies with the literature values: a) [Toptica02], b) [Bodermann00]

Transition	λ [nm]	T [°C]	Measured value [MHz]	Literature value [MHz]	Ref
P(42)1-14	772	25	388 605 083.71 (30)	388 605 094 (25)	a)
P(148)1-14	780	20	384 235 614.32 (30)	384 235 614.624 (36)	b)

Further, the hyperfine-structure splitting between the a_1, a_{10} and a_{15} lines was measured and the results are listed in Table 6.2. In this case the systematic uncertainty of the rubidium rf standard could be neglected, since the time differences between the measurements are around 15 min, where the rubidium standard provides a good short-term stability. The uncertainty of 100 kHz from the spectroscopic setup does not influence these measurements because all lines are measured with the same experimental settings. The reported uncertainty is the standard deviation for the

frequency difference of two single frequency measurements[40]. However, the data may provide an additional base for an improved modelling of the iodine spectrum in the region between 677 and 776 nm.

Table 6.2: Measured hyperfine-structure splitting for the a_{10} and a_{15} component in relation to the a_1 component

Transition	a_1 [kHz]	a_{10} [kHz]	a_{15} [kHz]
P(42)1-14	0	587 187 (42)	881 362 (42)

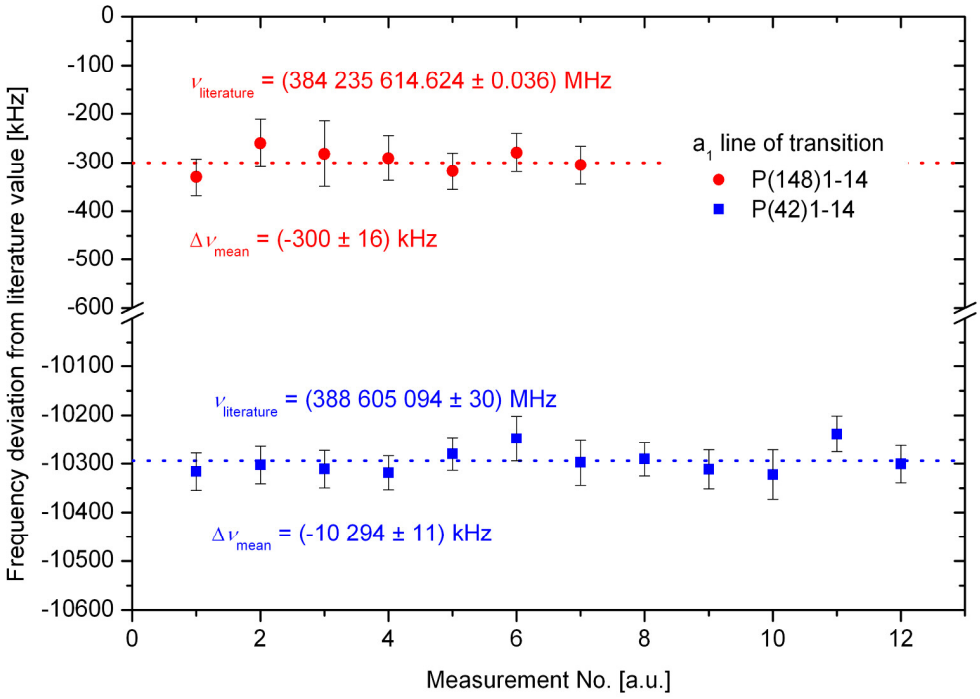

Figure 6.12: Measured frequencies of the a_1 line of the transition R(148)1-14 (red dots) and of the transition P(42)1-14 (blue squares). The given frequency values are the differences between the literature values (Table 6.1) and the measurement results.

[40] Other sources for uncertainties in the absolute frequency are impurities in the gas cells due to the manufacturing process. These lead in general to a red shift of the measured frequencies [Gill87]. To estimate this effect the used cell (manufactured from Institute of Scientific Instruments of the Academy of Science of Czech Republic) was compared to a second (manufactured by Opthos Inc, Maryland, USA). All transition frequencies measured with the latter cell were red shifted compared to the cell from Czech Republic and the reference values of the P(148)1-14 transition group. Consequently, the cell made in USA had more impurities and therefore was not used in the ESR experiment [Reinhardt07b].

7 THE EXPERIMENT AT THE ESR

The experimental setup for the lithium spectroscopy at the ESR can be separated in two parts: one to guide, control and manipulate the laser beams to/at the laser towers at the storage ring and another for the fluorescence detection. Both are described in detail in the two following chapters. Before coming to this, some general notes considering a beam time at the ESR are made.

Due to the safety regulations at the GSI, the access to the storage ring area is prohibited during operation. No changes or adjustments on the setup can be made by hand during a running experiment. Consequently, sensible parts (e.g. the laser-laser beam overlap) are monitored by cameras, and those parameters which have to be readjusted or changed during the experiment are remote controlled (e.g. lateral laser beam position). The arrangement of the setup along the field-free experimental section of the ESR is shown in Figure 7.1. The distance between both laser towers is 30 m. The overlap of the laser with the ion beam is given over a length of 20 m and is controlled with two scraper pairs[41] which are situated in the middle of the experimental section, 6.5 meters apart from each other. The system for fluorescence detection is in the middle of the interaction line.

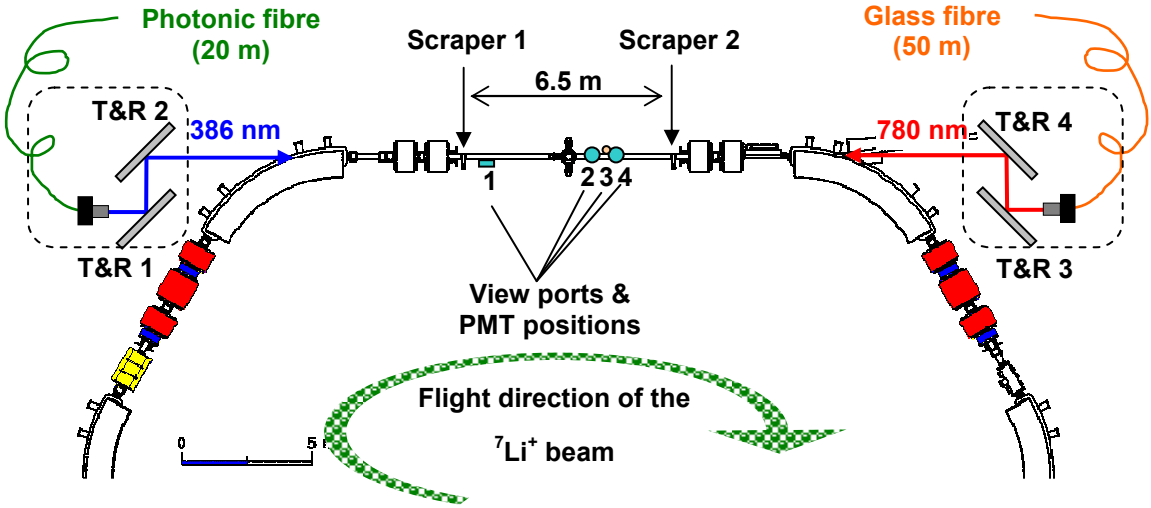

Figure 7.1: Schematic of the experimental section at the ESR. On each laser tower translation and rotation stages (T&R) are available to control the angle and the lateral position of the laser beam. In the middle of the field-free experimental section the PMT view ports and the scrapers are placed.

[41] A scraper pair consists of a metal-plate that can be introduced into the beam path in the *x*- and *y*-plane, respectively. The lateral reproducibility is ± 0.1 mm for each plane.

7.1 LASER BEAM TRANSPORT AND MANIPULATION

The laser towers for the incoupling of the laser beams into the ESR are situated on each end of the straight experimental section. The laser beams are transported via pm-sm[42] fibres from the laser laboratory to the towers. The light for parallel excitation of the lithium ions is guided by a 20 m long photonic fibre (*Crystal Fibre*, LMA PM5) to the incoupling tower. To reach the tower on the opposite side of the experimental section, the light for antiparallel excitation is guided through a glass fibre (*Fibercore*, HB750) with 50 m length. In principle, both towers are equipped similarly. Hence, only one is described and if there are differences between them they are stressed (see Figure 7.2). The fibres are mounted on a linear translation stage, in front of a microscope objective (10x). With this objective and a second lens ($f_{(\text{parallel})}$ = 1000 mm, $f_{(\text{antiparallel})}$ = 700 mm) the beam shape of the laser is adjusted. Further two apertures are introduced that block possible back reflections of surfaces. The laser light is reflected by two mirrors and guided towards the ESR. Each mirror is mounted on remote controlled motorised linear translation and rotation stages. These stages shift and tilt the laser beam in the horizontal and vertical plane. The accuracy of the used stages is 1.2 µm for the linear translation stage and 12.3 µrad (which corresponds to an uncertainty of $\Delta x = \pm$ 0.37 mm in a distance of 30 m ≡ position of the second tower) for the rotation stage.

Directly behind the microscope objective, a camera can be inserted into the beam path if (re-)adjustments of the incoupling of the laser light into the fibre are necessary. Additionally, before the laser enters the ESR, it passes a motorised aperture which is monitored from both sides by two cameras. This is done to control the overlap of the laser beams. Further at this position, a power meter can be introduced to monitor the laser power. It detects the power of the laser beam which has already passed through the storage ring. This is advantageous for spectroscopy techniques that require the light from only one side (e.g. Doppler-broadened spectroscopy). Here the laser power can be monitored online.

The incoupling windows at the ESR are made of fused silica and have a roughness of $\lambda/20$. To prevent straylight reflected by the windows from hitting the photomultipliers, the windows are mounted on rotatable bellows. With these the tilt of the window surface can be aligned.

[42] pm-sm = polarisation-maintaining single mode.

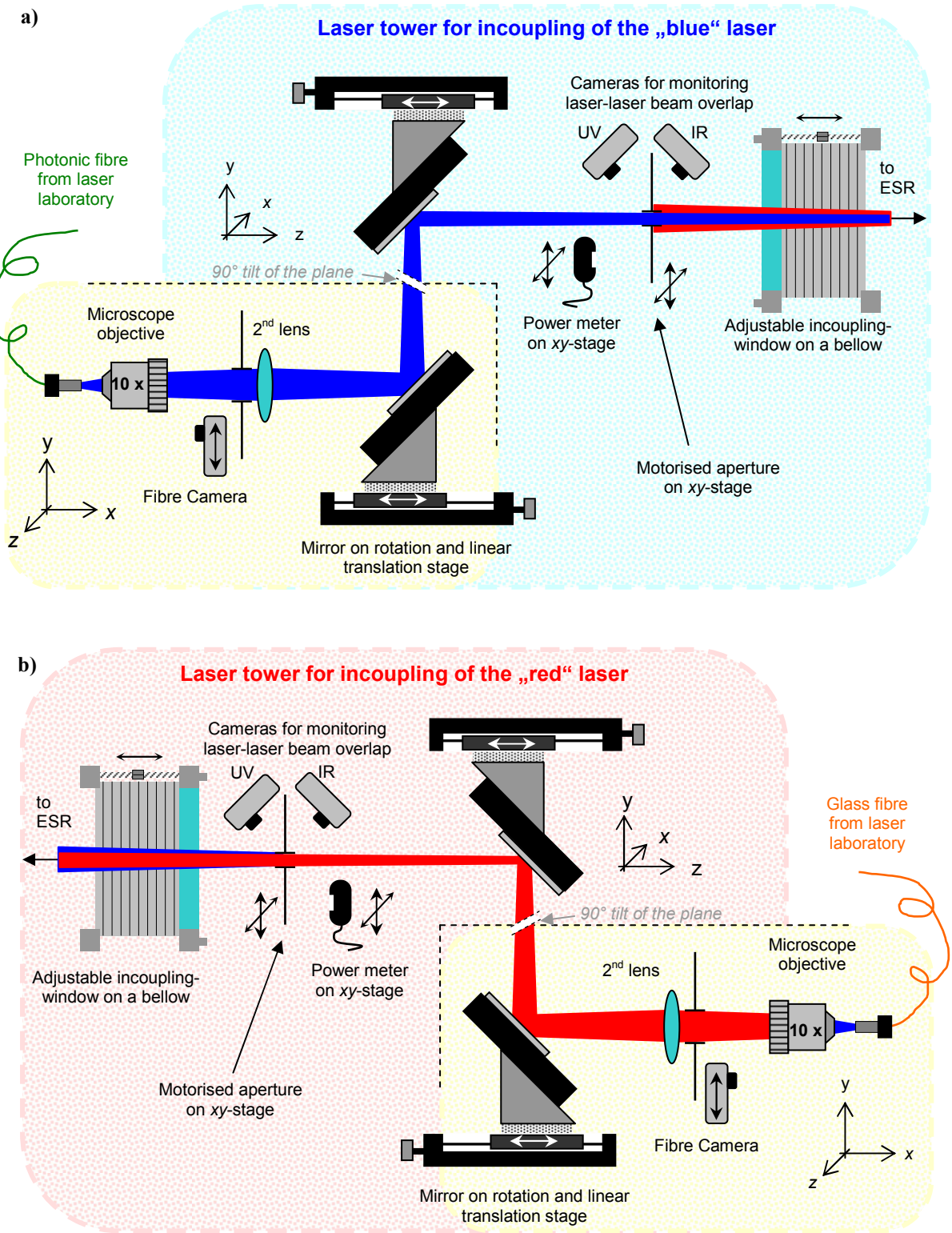

Figure 7.2: Laser towers for the incoupling of the laser light for excitation parallel a) and antiparallel b) to the flight direction of the ion beam (the ion beam is travelling parallel to the z-axis). The view in both figures is folded by 90°: yellow marked part: *xz*-plane, blue and red: *yz*-plane.

7.2 FLUORESCENCE DETECTION

The fluorescence signal is detected with three photomultipliers (PMTs) (two *Hamamatsu*, R2256P and one *Thorn EMI*, 9635QB). All PMTs are equipped with cooler housings to keep the temperature under 5 °C for thermal noise.

In principle, four viewports for spectroscopy purposes are available in the experimental section of the ESR. Since these are different in size, material and distance to the ion beam, for each viewport a particular detection system has been developed.

To increase the detection efficiency, light collector systems were introduced in front of the PMTs. These were adopted to the varying viewport environments and can be generally subdivided in two different systems. One consists of an acrylic light guide (Figure 7.3b) and the second of an arrangement of lenses (map the ion beam onto the PMT, Figure 7.3a). In the light guide system one side of the acrylic rod is coupled to the PMT surface via optical grease (*GC Technology*, BC-630) to minimise transfer losses. On the other side, filters (depending on the spectroscopy purposes) are placed that suppress the laser light. The coupling between the components is realised by optical grease too. The light guide has a transmittance of about 85% for an angle of incidence from 0 to 50° in the optical frequency band (Figure 7.4). The imaging system consists of two lenses that are adjusted in such a way that the first lens is one focal length away from the position of the ion beam path and the second lens is one focal length away from the PMT detection plane. Between both lenses, where the light propagation is assumed to be parallel, the filters for the suppression of the laser light are placed.

The dark rate[43] of the PMTs was 50-300 counts/s (depending on the type of PMT and the light collection system). For suppression of the 780 nm laser light a band gap filter (*Schott*, BG39) was used (see Figure D.1). At a power of 8 mW there is no influence on the counting rate of the PMTs. For the suppression of the laser light for parallel excitation interference filter were intended to use. With such filters the count rate could be kept at approximately 1000 counts/s at 0.5 mW of 386 nm laser light. But the available inference filters also reduce drastically the signal of the lithium spectroscopy. The alternative to these filters was a laminated plastic filter (*Schott*, KV407) which has an optical density of 4 (see Figure D.2) for 386 nm and is designed to produce only a small amount of fluorescence light (15.000 counts/s).

[43] Dark rate means: count rate of the PMT under beam time conditions without laser or ions in the ESR.

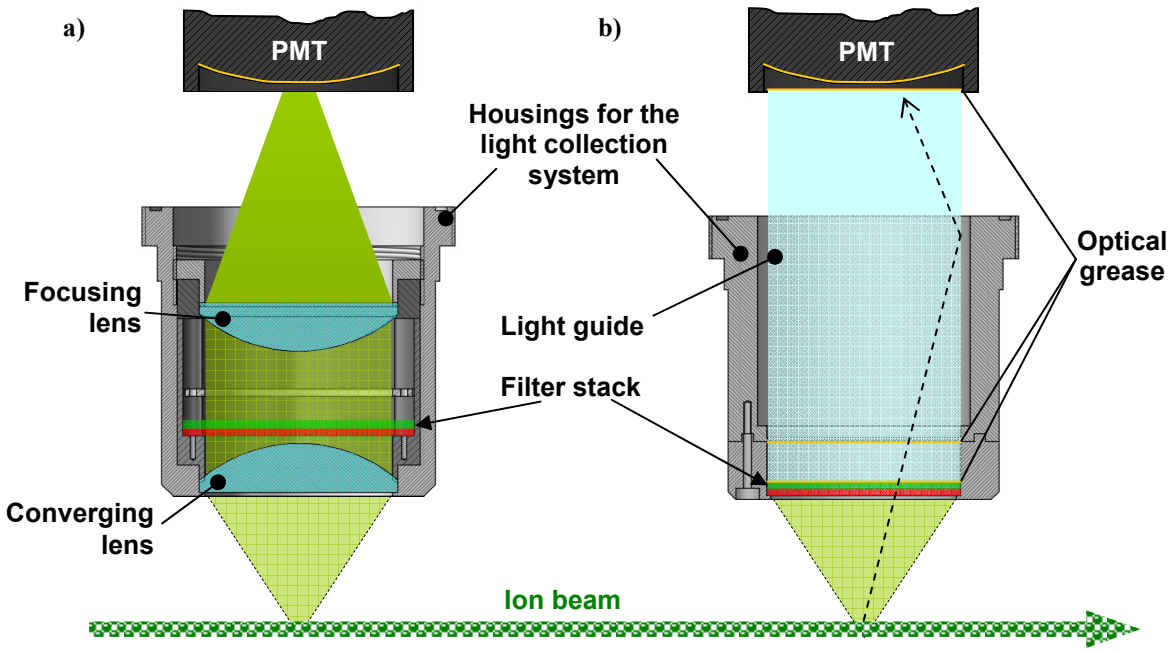

Figure 7.3: Illustration of the two light collection systems. a) The system of lenses that focuses the fluorescence light onto the PMT. The focal length of the first lens corresponds to the distance to the ion beam. b) The light guide collects the fluorescence and guides it, via total reflection on the walls, to the PMT. Optical grease is used to minimise transition losses.

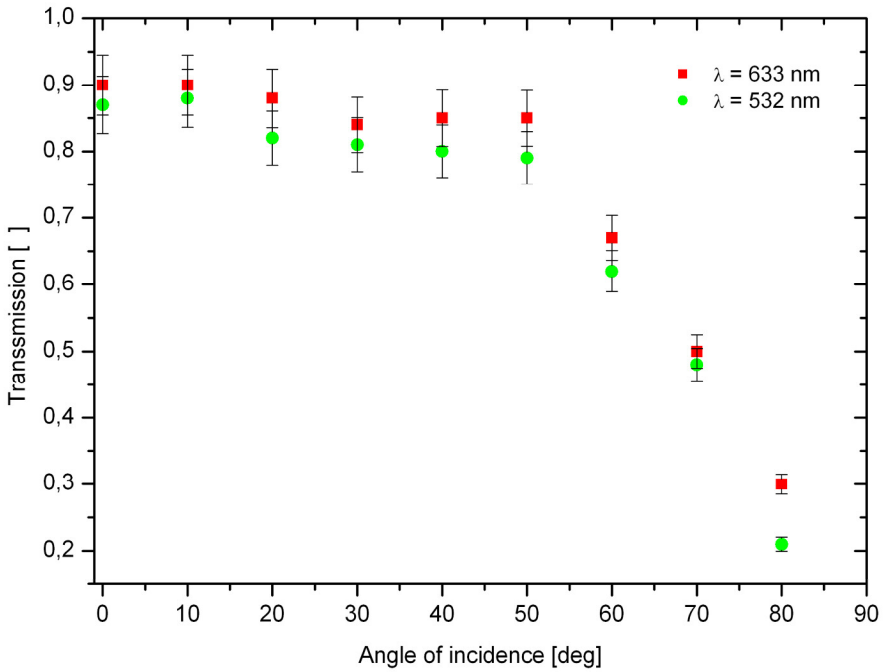

Figure 7.4: Transmission efficiency of the used light guide measured at two different laser wavelengths (a HeNe laser at 633 nm and a frequency-doubled Nd:YAG laser at 532 nm).

7.3 DOPPLER EFFECT AT STORAGE RINGS

The Doppler-shift in the emission and absorption frequency of fast moving lithium ions in the ESR depends on the angle of excitation or observation (equation (1.5)). For the used laser geometry, the frequencies for parallel and antiparallel excitation as a function of the ion velocity are shown in Figure 7.5. Further the frequency that is observed at an angle of 90°, in the laboratory rest frame, is depicted.

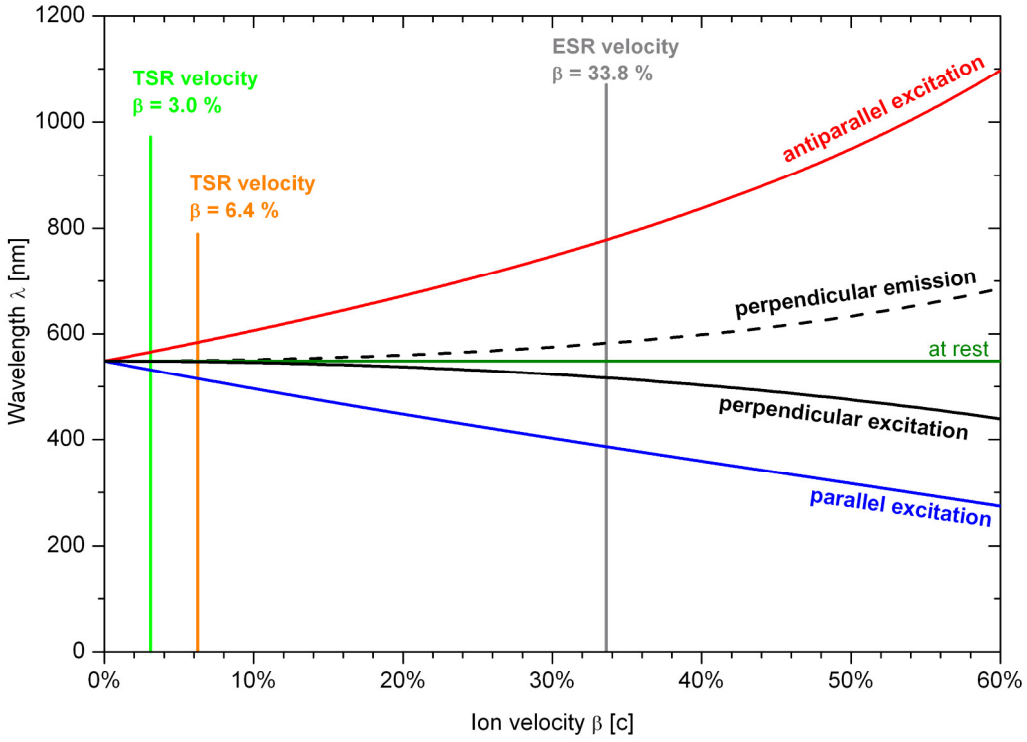

Figure 7.5: Changes in the excitation wavelength of the 2s $^3S_1 \rightarrow$ 2p $^3P_2$ transition (λ_0 = 548.5 nm), for parallel, antiparallel and perpendicular laser alignment, are plotted in solid lines as a function of the velocity. The dashed line indicates the wavelength that is detected by an observer, aligned perpendicular to the particles motion. Further the velocities of the storage ring experiments are denoted.

Considering the angle conversion (1.6), this frequency is not similar to that emitted at an angle of 90° in the ions' rest frame. This radiation appears at a detecting angle of 110° in the laboratory frame. The angle shift, observed in the laboratory system, relative to the one emitted in the ions' frame at a velocity of β = 33.8 % is shown in Figure 7.6a. According to this, frequency shifts for the angles in both frames are shown in Figure 7.6b. Basic values for the present ESR experiment are given in Table 7.1.

Table 7.1: Transformation values in terms of angle and wavelength for special geometries. θ_{ion} = angle in the ion frame, θ and λ are measured in the laboratory frame

Angle relation	θ_{ion} [deg]	θ [deg]	λ_l [nm]
in flight direction	0	0	385.8
perpendicular in the ion frame	90	70.2	516.2
perpendicular in the laboratory frame	110	90	583.0
against the flight direction	180	180	779.8

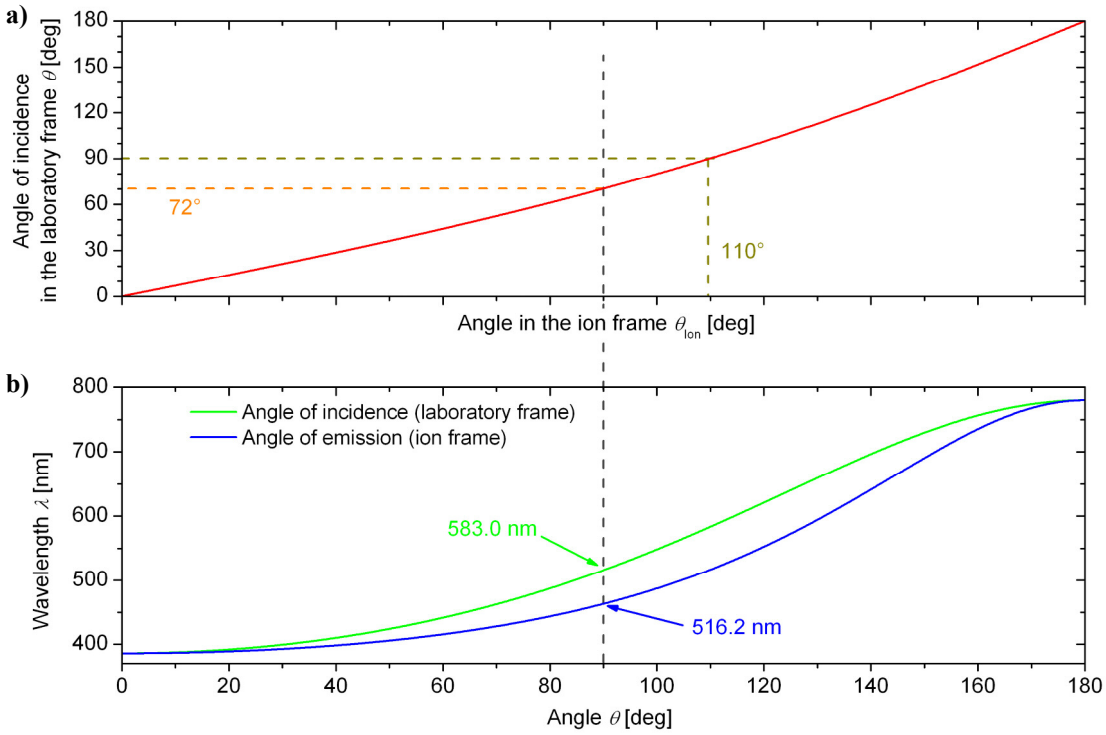

Figure 7.6: a) Conversion relation of the emission angle in the ion frame θ_{ion} into the observed angle of incidence θ in the laboratory frame. b) The observed wavelength, from the $2s^3S_1 \rightarrow 2p^3P_2$ transition in lithium, is shown as a function of the angle. The green line denotes the values for an angle of incidence that is measured in the laboratory frame. The blue line stays for the angle of emission in the ions' rest frame.

Beside the effect of Doppler-shifted radiation, a change of the emission characteristic appears in a laboratory frame from which the moving ion is observed. The radiation is not isotropic anymore but has a boost in flight direction. Three factors combine to produce these intensity changes: the change in the angular size of the emitting region, the Doppler change in the energy of the photons, and the change in the photon flux due to the combined effects of time dilation and the emitter's motion, which is an additional manifestation of the Doppler effect. In terms of the Doppler factor (equation (1.5)) these effects contribute to the change in intensity by factors of D^2, D and D, respectively, for a combined intensity change factor of D^4. In our experiment the photon flux ϕ is detected with photomultipliers and the flux changes by a factor of D^3, because the

energy change per photon is irrelevant [Trans07]. The angular distribution of the relative flux is given by

$$\frac{\phi_{\mathrm{ion}}(\theta_{\mathrm{ion}})}{\phi(\theta)} = D^3 = \frac{\left(\sqrt{1-\beta^2}\right)^3}{(1-\beta\cdot\cos\theta)^3} = \left(\frac{\lambda}{\lambda_{\mathrm{ion}}}\right)^3 \tag{7.1}$$

where the index "ion" denotes the parameters in rest frame of the moving ion. At a velocity of 33.8 %*c*, the photon intensity observed perpendicular to the flight direction of the ions is reduced by 17 % and in flight direction increased by a factor of 2.9. The whole angle behaviour is shown in Figure 7.7.

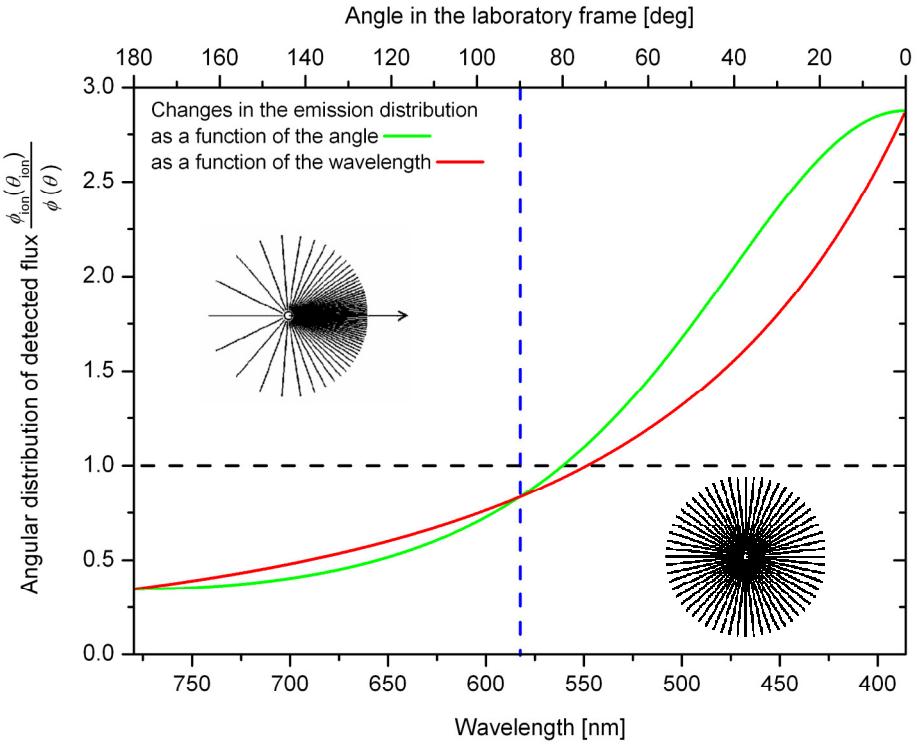

Figure 7.7: Intensity distribution, of a source that is moving with a velocity of 33.8 %*c*, seen by an observer at rest. The spherical emission characteristic in the rest frame of the moving particle (black dashed line) changes into a boost in flight direction in the laboratory frame.

7.4 SIGNAL ESTIMATION

For the estimation of the signal strength, a 1-D ion beam is assumed that is comparable with a chain of balls[44]. The ions are spread homogeneously along the z-axis, which is equivalent to the storage orbit in the ESR. On that path the ions are assumed to be separated by a distance Δz = 1 mm with respect to each other. From every ion 1801 photons are simulated that are displaced in angle by $\Delta\theta$ = 0.1° (Figure 7.8). To consider whether a photon contributes to the detector signal the light path is calculated for every photon. No reflections on the tube walls or other parts in the beam pipe are taken into account (viz, only the photons emitted by θ = 0°-180° can contribute).

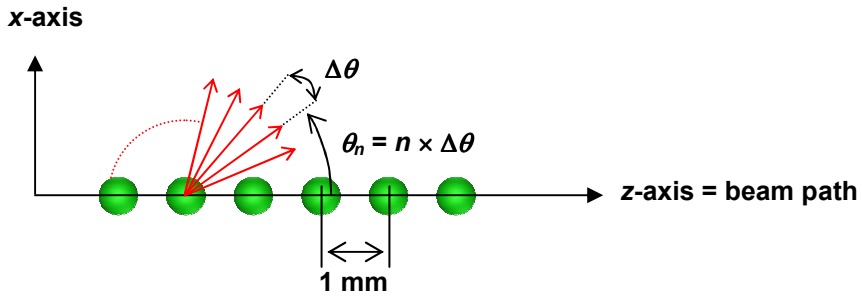

Figure 7.8: Simulation scheme for the estimation of the fluorescence signal at the ESR.

Further it is assumed that every photon that hits the detection plane is counted (no losses due to reflection or absorption). For a length of Δz = ± 500 mm around the detector, a vertical distance of the ion beam x = 80 mm and a velocity of β = 33.8 %, the distribution of the signal contribution as a function of the emission position is derived (see Figure 7.9). Photons which are emitted at z = – 17 mm are detected most efficiently (ε = 11%). This is due to the distorted angles by the angle conversion relation. Analysing the signal contribution in terms of the z-position, one finds that 89 % of the signal is generated in an area of Δz = ± 250 mm around z = 0. Furthermore, it has to be taken into account that the wavelength shift is a function of the angle of emission. Photons that are emitted more than 250 mm afar from the detector have a very small or very large angle of incidence. Thus, in the laboratory frame, the wavelengths of those photons are close to the used laser frequencies ($\lambda_a(z_+)$ = 768-780 nm and $\lambda_p(z_-)$ = 386-397 nm)[45]. Exactly these frequencies are strongly suppressed by filters to achieve low background. So, for the signal estimation the consideration of an area of

[44] In the ESR the electron cooled ion beam has a diameter of 1 mm. Thus the assumption of a 1-D chain is sufficient for the signal estimation.

[45] z_+ indicates the area of z > + 250 mm, z_- indicates the area of z < – 250 mm.

$\Delta z = \pm 250$ mm around the detector is sufficient. The distribution of the wavelength as a function of the position of emission is given in Figure 7.10. In this area an overall efficiency of 9 % is achieved. This range corresponds to a tenth of the distance excited $^{7}Li^{+}$ ions travel till (in average) half of them decay ($\tau = 43$ ns).

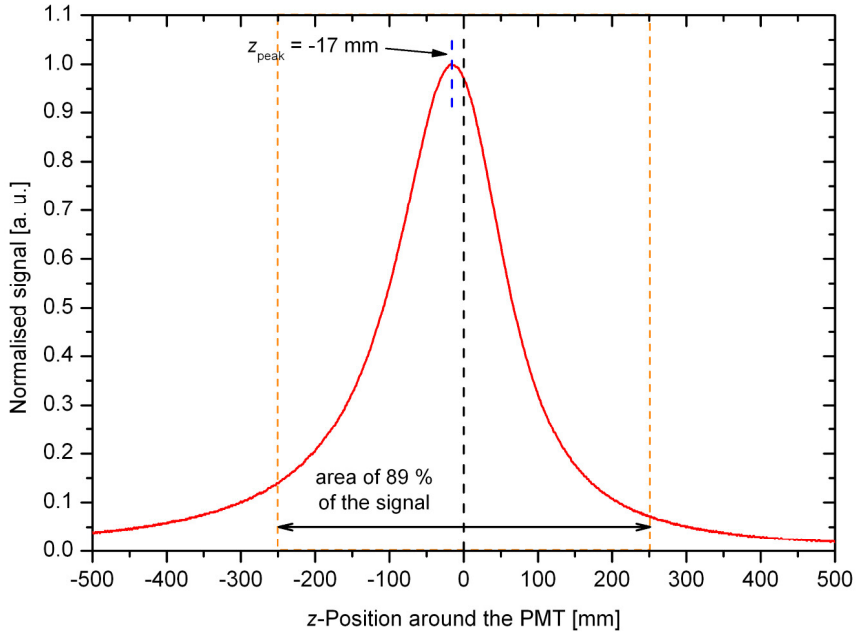

Figure 7.9: Normalised signal over the *z*-position around the detector. 89 % of the signal emerges in an area of ± 250 mm around the middle of the PMT. The maximum of the signal is at z = – 17 mm.

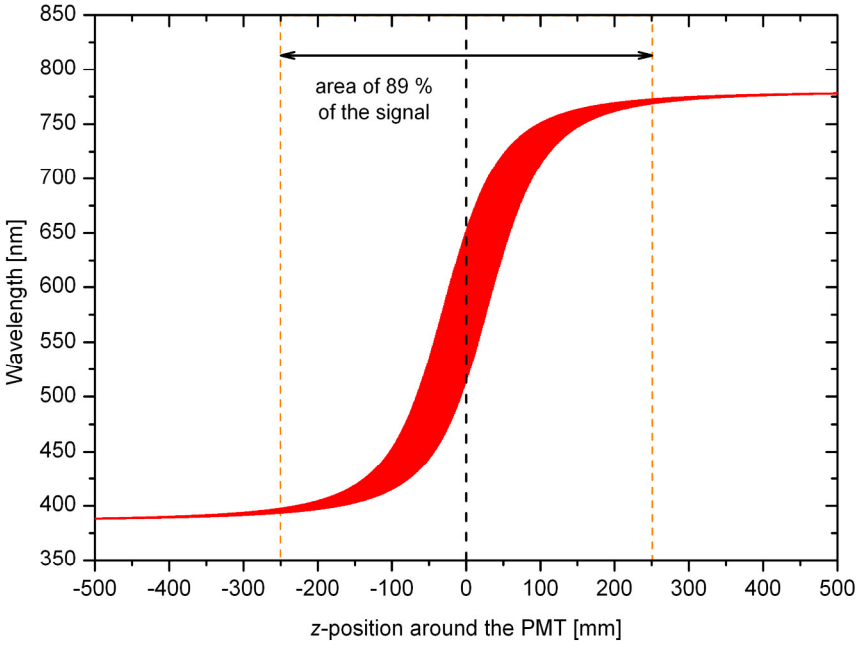

Figure 7.10: Signal contribution of a certain wavelength as a function of the *z*-position.

Regarding the full circular emittance of the ions this estimation has to be extended to a 3-D geometry. For this, photons emitted in the *yx*-plane have to be considered. Nevertheless, the photons emitted at angles of θ = 181°-359° in the *xz*-plane, still do not contribute to the signal. This leads to a reduction of efficiency by a factor 2. The total number of simulated photons $N(xyz)$ in 3-D is

$$N(xyz) = \frac{360° \cdot [N(xz) - 2]}{\Delta\theta}. \tag{7.2}$$

$N(xz)$ is the total number of simulated photons in the *xz*-plane and $\Delta\theta$ is the angle spacing between the angles of emission. To determine the number of photons which contribute to the signal, the change of the solid angle efficiency as a function of the position has to be considered. Furthermore the detector plane in the *xy*-dimension is not quadratic but circular, so the factor $\pi/4$ is introduced:

$$N_{\text{hits}}(xyz) = \sum_{-z}^{+z} N_z(xz) \cdot \frac{\Delta\theta_z}{\Delta\theta} \cdot \frac{\pi}{4}. \tag{7.3}$$

N_{hits} is the total number of photons hitting the circular detector plane and thus, contributing to the signal. N_z is the corresponding number in the *xz*-plane from the emission point z and $\Delta\theta_z$ is the corresponding solid angle. For the ESR viewport geometry ($\varnothing_{\text{detector}}$ = 60 mm, x = 80 mm), an efficiency of ε = 0.5 % is calculated. Beside this, a quantum efficiency of 10 % (averaged over the wavelength range) of the PMTs, the transmissions of the filters for lasers suppression of 50 % and of the waveguide of 85 % have to be considered. This leads to an overall detection efficiency of ε = 0.02 % for the range of Δz = ± 250 mm. In other words one in five thousand emitted photons contributes to the signal.

7.5 GEOMETRICAL UNCERTAINTIES

7.5.1 ANGLE-MISALIGNMENT

Regarding Doppler formula (1.5), an imperfect matching of the laser beam and the ion beam leads to an error in the measured frequency because the assumption of a purely longitudinal spectroscopy is not valid anymore and therefore the $\cos\theta$ term does not vanish. The consequences can be worked out by having a closer look to the formulas for both cases: perfectly aligned and misaligned. The first case leads to

$$\nu_1 = \nu_{\text{p}} \cdot \gamma \cdot (1 - \beta) \tag{7.4}$$

and

$$\nu_2 = \nu_{\text{a}} \cdot \gamma \cdot (1 + \beta). \tag{7.5}$$

$\nu_{1,2}$ are transition frequencies in the rest frame of the ion and $\nu_{a,p}$ the frequencies for parallel or antiparallel excitation. Assuming imperfect alignment (see Figure 7.11), described by the angle θ and ϕ, one obtains

$$\nu_1 = \nu'_p \cdot \gamma \cdot [1 - \beta \cdot \cos(180° - \theta)] \tag{7.6}$$

and

$$\nu_2 = \nu'_a \cdot \gamma \cdot [1 - \beta \cdot \cos\phi]. \tag{7.7}$$

Multiplying both sets of equations leads to

$$\nu_a = \frac{\nu_1 \cdot \nu_2}{\nu_p} \tag{7.8}$$

and

$$\nu'_a = \frac{\nu_1 \cdot \nu_2}{\nu'_p} \cdot \frac{1}{\gamma^2 \cdot (1 + \beta \cdot \cos\theta) \cdot (1 - \beta \cdot \cos\phi)}. \tag{7.9}$$

If the parallel laser frequency is fixed $\nu_p = \nu_p'$ and relation (7.8) for the case of perfectly aligned laser beams is used, the rest frequencies cancel out and one gets

$$\nu'_a = \nu_a \cdot \frac{1}{\gamma^2 \cdot (1 + \beta \cdot \cos\theta) \cdot (1 - \beta \cdot \cos\phi)}. \tag{7.10}$$

The deviation $\Delta\nu_a$ from the frequency at perfect alignment can be expressed as

$$\frac{\Delta\nu_a}{\nu_a} = \frac{1}{\gamma^2 \cdot (1 + \beta \cdot \cos\theta) \cdot (1 - \beta \cdot \cos\phi)} - 1 \tag{7.11}$$

where $\Delta\nu_a = \nu_a' - \nu_a$. Further, one can distinguish between the case of laser-laser beam misalignment (Figure 7.11a) and laser-ion beam misalignment (Figure 7.11b). If one laser beam is perfectly collinear to the ion beam and the second has an tilt to both ($\theta = 0$, $\phi \neq 0$), the deviation can be written as

$$\frac{\Delta\nu_a}{\nu_a} = \frac{1 - \beta^2}{(1 + \beta) \cdot (1 - \beta \cdot \cos\phi)} - 1. \tag{7.12}$$

For a perfect collinear alignment of the laser beams, but a small tilt with respect to the ion beam ($\theta = \phi \neq 0$), the frequency shift is given by

$$\frac{\Delta\nu_a}{\nu_a} = \frac{1 - \beta^2}{1 - \beta^2 \cdot \cos^2\theta} - 1. \tag{7.13}$$

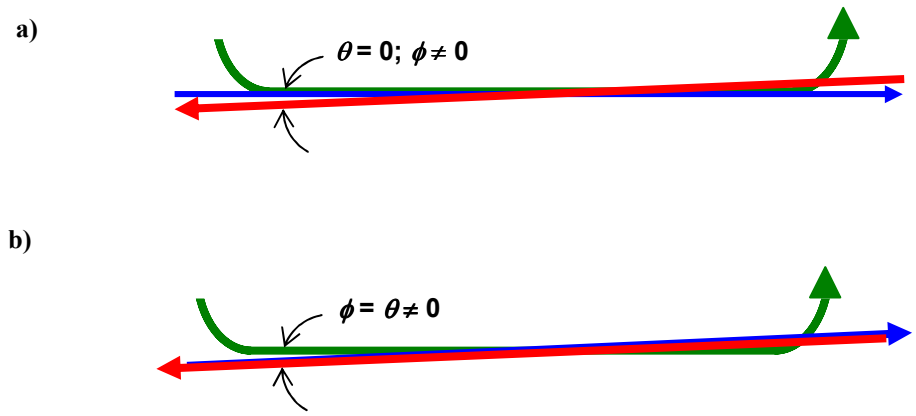

Figure 7.11: Two cases of misalignment a) Laser-laser tilt. b) Laser-ion angle misalignment.

At the ESR the overlap of both laser beams, is realised with the help of two iris apertures that are aligned on the laser towers and separated by a distance of 30 m. The *xy*-position of the laser beams can be controlled to $\Delta x_{\mathrm{Laser}} = \pm 0.5$ mm (at each iris). This leads to a frequency uncertainty ($\beta = 33.8$ %) of $\Delta \nu_{\mathrm{a\text{-}x}} = \pm 27$ kHz in one plane. Adding the uncertainties from the *x*- and the *y*- plane by Gaussian error propagation, a maximal uncertainty of $\Delta \nu_{\mathrm{a\text{-}xy}} = \pm 54$ kHz due to laser-laser beam alignment remains.

The determination of the laser-ion beam overlap is done with two scraper pairs. These are situated 6.5 m apart from each other, in the middle of the experimental section. The scraper can be introduced into the beam path with a reproducibility of better than 0.1 mm. A determination of the laser or the ion beam position to $\Delta x = \pm 0.5$ mm is possible, what leads to an uncertainty of $\Delta \nu_{\mathrm{a\text{-}x}} = \pm 293$ kHz in one plane and of $\Delta \nu_{\mathrm{a\text{-}xy}} = \pm 586$ kHz in both planes.

7.5.2 ION BEAM DIVERGENCE

Even if both (the laser and the ion) beams are aligned perfectly collinear, each ion has a small divergence due to the betatron oscillation around their mean orbit. This leads to a modification of the line shape although the mean angle of the ion beam is zero. To calculate the maximum divergence of an ion, stored in the ESR, the beta function and the beam diameter at one position has to be known. With this the behaviour along the whole storage orbit of the ions can be derived by equation (4.5). The typical beam diameter in the experimental section is 1 mm. The resulting envelope is shown in Figure 7.12. The corresponding values for the divergence as a function of the position are depicted in Figure 7.13. In the experimental section a maximum divergence of 40 µrad in the *x*-plane and 80 µrad in the *y*-plane is obtained.

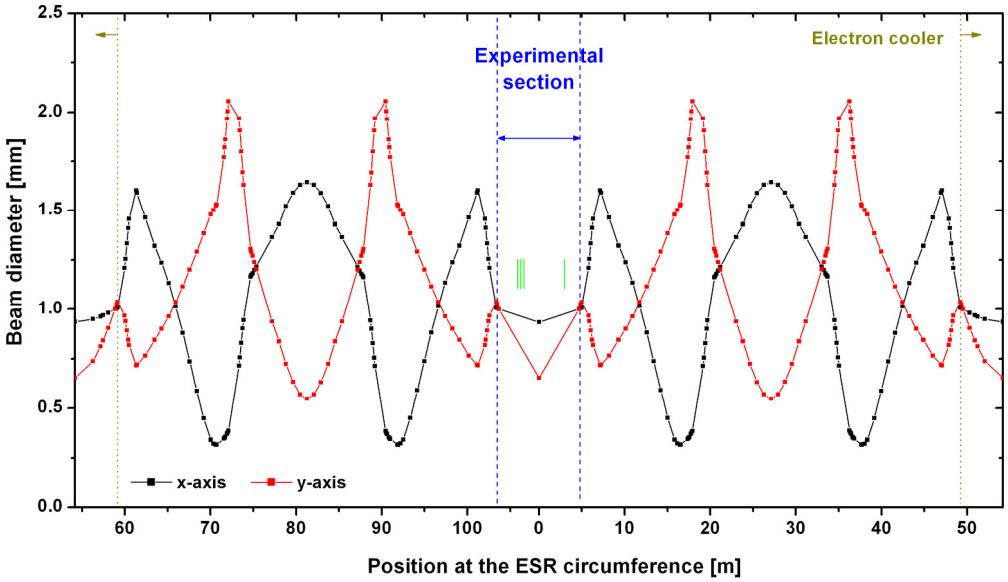

Figure 7.12: Evolution of the ion beam diameter along the ESR orbit in the *x*- (black curve) and the *y*-dimension (red curve). In the electron cooler and the experimental section the diameters of both axes are of the range 1 mm. The green lines indicate the PMT positions.

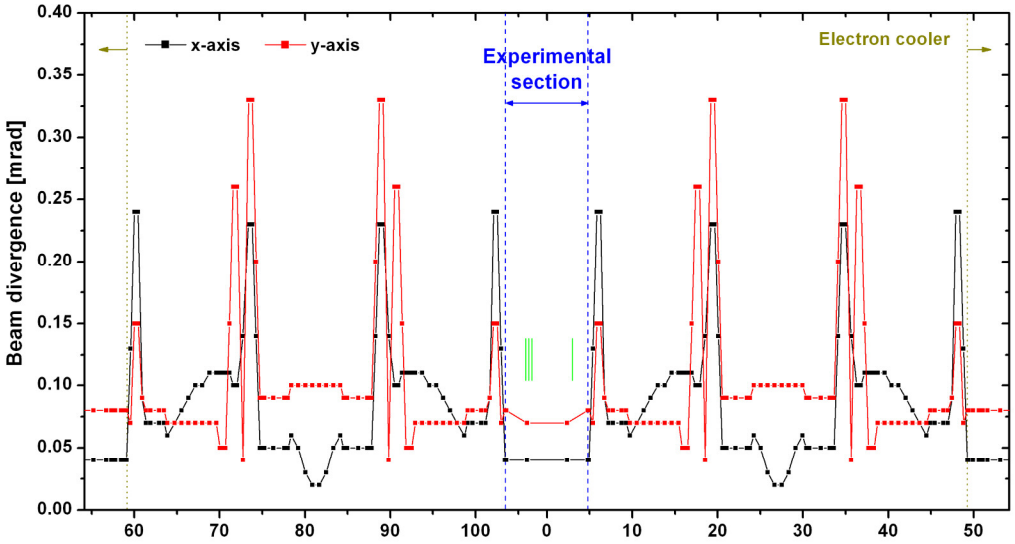

Figure 7.13: Evolution of the ion beam divergence in the *x*- (black curve) and the *y*-dimension (red curve). In the field-free experimental section the maximal divergences are 40 µrad for the *x*-axis and 80 µrad for the *y*-axis. The green lines indicate the PMT positions.

To estimate the influence of the ion beam divergence onto the line shape and the peak position, a Gaussian distribution of the angle divergence with the width σ_θ around $\theta = 0$ is assumed. This is folded with the Lorentzian distribution of the transition driven by the laser, with a resonance frequency ν_a for antiparallel alignment

$$f(\nu_a) = 2\int_0^{\pi/2} \underbrace{\frac{1}{\sigma_\theta \cdot \sqrt{2\pi}} e^{-\frac{\theta^2}{2\cdot\sigma_\theta^2}}}_{\text{Gaussian distribution}} \cdot \underbrace{\frac{\frac{\gamma_S^2}{4}}{\left(\nu_a - \nu'_a \cdot \frac{1-\beta^2}{1-\beta^2\cdot\cos^2(\theta)}\right)^2 + \frac{\gamma_S^2}{4}}}_{\text{Modification term due to ion divergence}} d\theta \,. \qquad (7.14)$$

γ_S is the linewidth of the transition, ν'_a is the frequency of the detuned laser. Hence it turns out that for an electron cooled ion beam the centre of the line is always shifted (e.g. by – 0.4 MHz at a divergence of 80 µrad) to smaller frequencies and the signal shape is slightly distorted compared to a plane beam. Nevertheless it can be approximated with sufficient accuracy[46] by the Lorentz function (Figure 7.14).

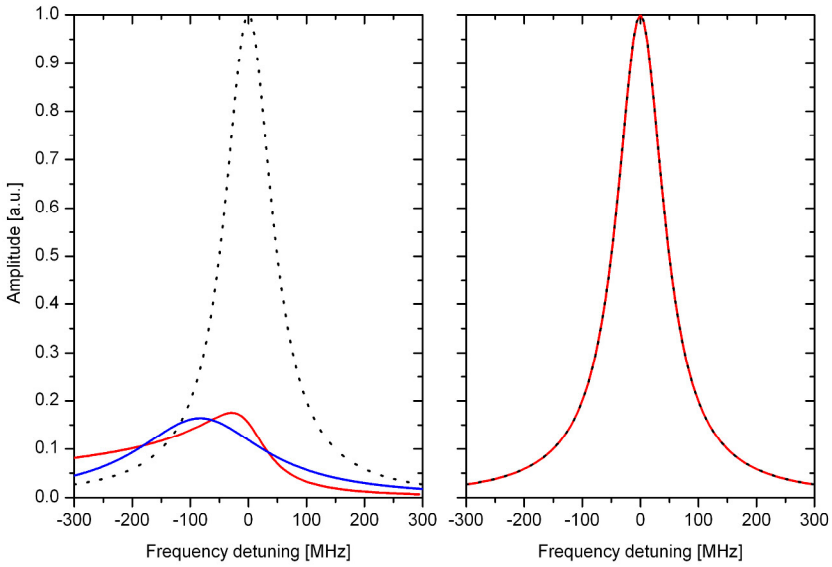

Figure 7.14: The differences between a Lorentzian function with a linewidth of $\Delta\nu_{FWHM}$ = 50 MHz and the distorted function (7.14) with the same linewidth (for two different beam divergences) is compared. Left panel: The red line indicates an ion beam with a divergence of 5 mrad (which corresponds to a "hot" ion beam extracted from the SIS). The line shape is heavily distorted compared to a Lorentzian shape (dashed line). If a Lorentzian function is fitted to the distorted line shape (blue line), the peak of the Lorentzian would differ by several tens of MHz from the real transition frequency. Right panel: A beam divergence of 80 µrad is assumed (ion beam after electron cooling). The line shape can be perfectly described by a Lorentzian function.

[46] The uncertainty in the Lorentzian fit is < 2 kHz.

7.5.3 GAUSSIAN BEAM

Up to now all effects are discussed assuming the laser beam to be a plane wave. But the power of such a plane wave would be infinite and can therefore not exist. To avoid this, the additional wave function $u(r,z)$ with $r^2 = x^2 + y^2$ has to be introduced:

$$E(r,z,t) = u(r,z) \cdot \exp\left[- j \cdot \frac{2 \cdot \pi}{\lambda} \cdot z \right] \cdot \exp[j \cdot 2 \cdot \pi \cdot \nu \cdot t]. \tag{7.15}$$

The propagation of a real laser beam[47] can be described sufficiently by a Gaussian beam. The field amplitude $u(r,z)$ for a wave, travelling in z-direction, is given by [Svelto98] to

$$u(r,z) = \frac{w_0}{w(z)} \cdot \exp\left[- \frac{r^2}{w^2} \right] \cdot \exp\left[- j \cdot \frac{\pi}{\lambda} \cdot \frac{r^2}{R(z)} \right] \cdot \exp[j \cdot \chi(z)] \tag{7.16}$$

with the beam waist w_0, the radius of curvature $R(z)$, a beam radius $w(z)$, and a phase deviation $\chi(z)$ from a plane wave where

$$R(z) = z \cdot \left[1 + \left(\frac{z_R}{z} \right)^2 \right], \tag{7.17}$$

$$w^2(z) = w_0^2 \cdot \left[1 + \left(\frac{z}{z_R} \right)^2 \right], \tag{7.18}$$

$$\chi(z) = \arctan\left(\frac{z}{z_R} \right), \tag{7.19}$$

and

$$z_R = \frac{\pi \cdot w_0^2}{\lambda}. \tag{7.20}$$

Here the Rayleigh range z_R is introduced that describes the distance from the beam focus to where the beam radius has increased by a factor $\sqrt{2}$. In equation (7.17), (7.18) and (7.19) one can see that $w(z)$, $R(z)$ and $\chi(z)$ (and hence the field distribution) depend only on w_0 (for given λ and z). This can be easily understood when one observes that, once w_0 is known, the field distribution at $z = 0$ is known. In fact we know its amplitude, since the field distribution is a Gaussian function with spot size w_0, and its phase, since it is assumed $R = \infty$ for $z = 0$ (≡ beam focus, see Figure 7.15). Once the field at $z = 0$ is

[47] A further assumption is that the laser beam is quasi monochromatic.

known, the corresponding field at $z \neq 0$ is uniquely established. Further z is defined to be positive in the direction of a divergent beam and negative in the direction of a convergent beam. Comparing the paraxial part of the Gaussian beam with a plane wave one sees that for $z < 0$, the phase front of the Gaussian beam is delayed (negative phase) and for $z > 0$ the wavefront is advanced (positive phase).

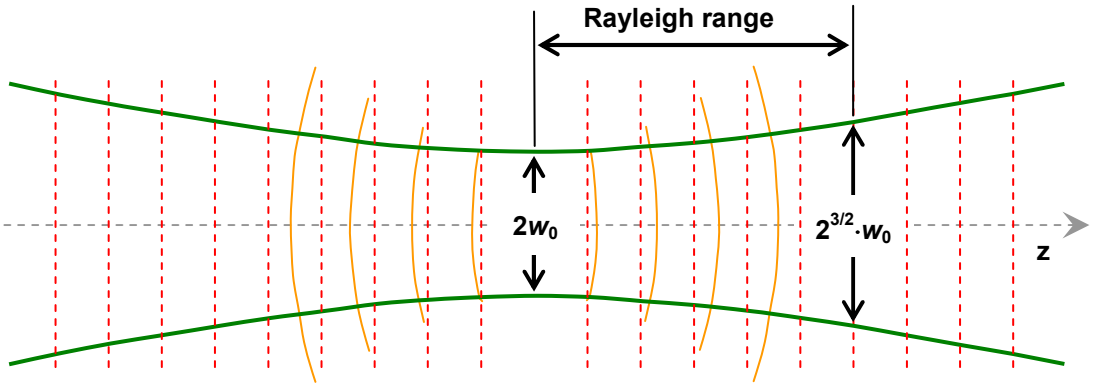

Figure 7.15: Longitudinal intensity profile of a Gaussian beam (solid orange lines). The corresponding wavefronts of a plane wave of the same frequency are depicted by the dashed red lines.

In the frame of an ion, moving along the z-axis, this Gaussian shape leads to a shift in the frequency experienced by the ion. Furthermore, if the ion beam is slightly tilted with respect to the propagation axis of the laser beam, the frequency shift becomes a function of the position. This frequency ν' is determined, up to first-order velocity terms in β, by the total derivative of the phase φ, of the Gaussian beam, with respect to time t

$$\nu' = \frac{1}{2 \cdot \pi} \cdot \frac{d\varphi}{dt}, \tag{7.21}$$

$$\varphi(r,z,t) = \underbrace{2 \cdot \pi \cdot \nu \cdot t - \frac{2 \cdot \pi}{\lambda} \cdot z}_{\text{Plane wave}} \underbrace{- \frac{r^2}{w^2} - \frac{\pi}{\lambda} \cdot \frac{r^2}{R(z)} + \arctan\left(\frac{z}{z_R}\right)}_{\text{Gaussian beam}}. \tag{7.22}$$

Further the movement of the particles has to be considered. This leads to the fact that z and r become time dependent and change the total time derivative to a convective derivative

$$\nu' = \frac{1}{2 \cdot \pi} \cdot \left(\frac{\partial \varphi}{\partial t} + \frac{\partial \varphi \cdot \partial z}{\partial z \cdot \partial t} + \frac{\partial \varphi \cdot \partial r}{\partial r \cdot \partial t} \right). \tag{7.23}$$

Assuming the ions pass trough the focal point, i.e. $z = 0$, r = 0, a (small) angle ϕ with respect to the z-axis, and the propagation direction of the laser beam is the same as the moving direction of the ions ($\rightarrow$ parallel excitation scheme), one finds

$$\nu' = \nu_p \cdot \left(1 - \beta \cdot \left[\frac{r \cdot |z| \cdot \phi}{z^2 + z_R^2} + \left(1 - \frac{\phi^2}{2}\right) \cdot \left(1 - \frac{w_0^2}{2 \cdot \left(z^2 + z_R^2\right)} - \frac{r^2 \cdot \left(z^2 - z_R^2\right)}{2 \cdot \left(z^2 + z_R^2\right)^2}\right)\right]\right) \cdot \gamma \cdot \qquad (7.24)$$

For the calculation the approximations $v \cdot \cos\phi \approx v \cdot \left(1 - \phi^2/2\right)$ and $\pm v \cdot \sin\phi \approx \pm v \cdot \phi$ were used (the (–) sign stays for $z < 0$ and (+) sign for $z > 0$). Equation (7.24) reduces to the known Doppler-shift formula (equation (1.5)) for parallel laser excitation with slight angular misalignment if one assumes $|z|$ and/or $z_R >> 0$. For perfect alignment ($\phi = 0$) an additional velocity proportional term remains that is related to the Gaussian wave function. The formula for antiparallel laser excitation can be derived by changing $\beta \rightarrow -\beta$ and $\phi \rightarrow -\theta$ in equation (7.24)

$$\nu' = \nu_a \cdot \left(1 + \beta \cdot \left[-\frac{r \cdot |z| \cdot \phi}{z^2 + z_R^2} + \left(1 - \frac{\phi^2}{2}\right) \cdot \left(1 - \frac{w_0^2}{2 \cdot \left(z^2 + z_R^2\right)} - \frac{r^2 \cdot \left(z^2 - z_R^2\right)}{2 \cdot \left(z^2 + z_R^2\right)^2}\right)\right]\right) \cdot \gamma \cdot \qquad (7.25)$$

In Figure 7.16 the formulas (7.24) and (7.25) are plotted for typical laser beam waists as a function of the distance from the focus. Both laser beams are assumed being perfectly aligned ($r = \phi = 0$) to figure out the size of the effect due to the Gaussian waveform. The velocity is $\beta = 0.338$ and the wavelength corresponds to the $2s^3S_1 \rightarrow 2p^3P_2$ transition in lithium. One finds that the frequency deviation of the Gaussian beam, in comparison to a plane wave, becomes smaller the further one gets away from the focal point.

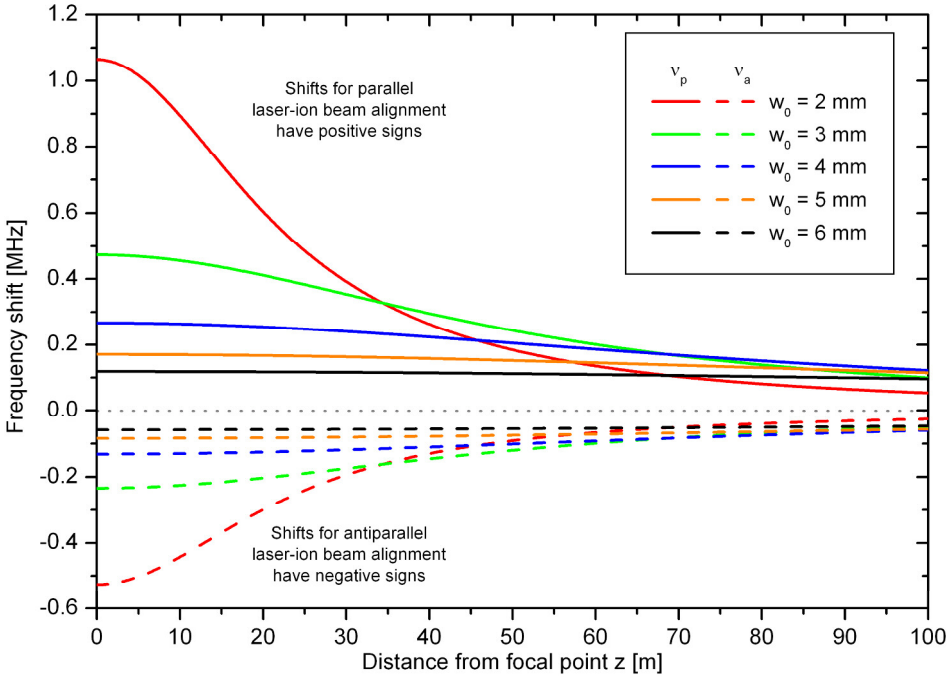

Figure 7.16: Correction curves for measured transition frequencies concerning different laser beam diameters ($2 \cdot w_0$). These curves are plotted as a function of the distance of the focal point to the interaction zone.

The focal points of the lasers in the ESR experiment were aligned to a distance of 20 m apart from the laser-ion interaction zone with a diameter of $2 \cdot w_0 = 10$ mm. This leads to frequency shifts of 170 kHz for the parallel and of 83 kHz for the antiparallel laser beam. The relation of both shifts corresponds to the relation of the two laser frequencies

$$\frac{\nu_\mathrm{p}}{\nu_\mathrm{a}} = \frac{\Delta\nu_\mathrm{p}}{\Delta\nu_\mathrm{a}} = 2.023\,. \tag{7.26}$$

By fixing two laser parameters (w_0 = 5 mm, z = 20 m), one can investigate the frequency shift as a function of the tilt and a lateral shift of the laser beams in relation to the ion beam travelling axis. The results are plotted in Figure 7.17. For the chosen worst case scenario (ϕ = 400 µrad, r = 20 mm) the frequency shift is 24 MHz. With the setup, applied at the ESR, an angle uncertainty of $\Delta\phi$ < 100 µrad is feasible. Here, the frequency shifts are below 1 MHz and therefore under sufficient control for the experiment.

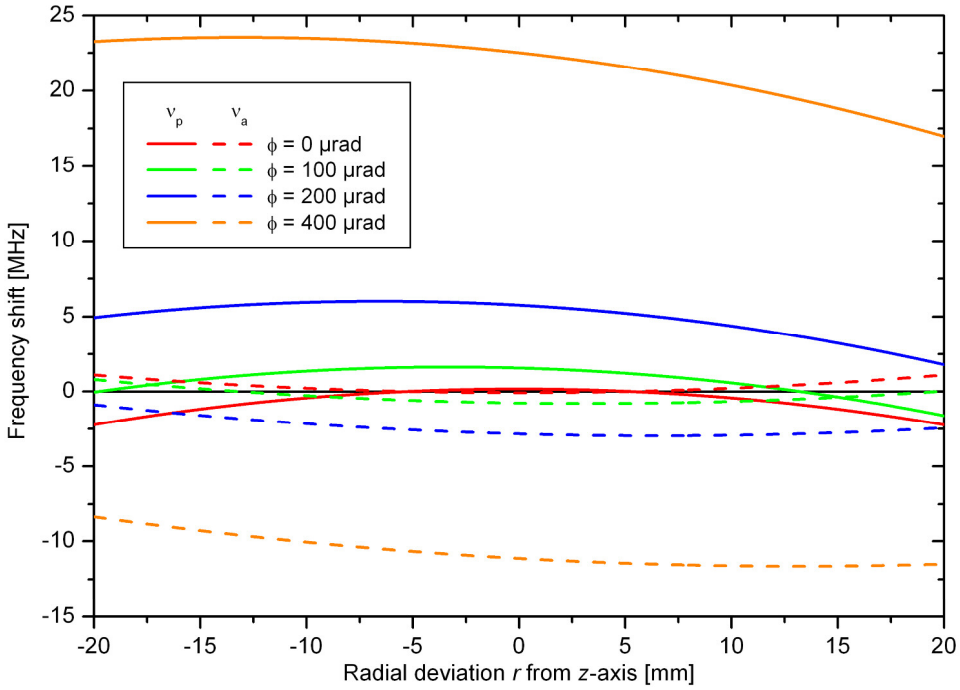

Figure 7.17: Frequency shift due to imperfect alignment of laser and ion beam concerning a Gaussian beam as a function of radial deviation of the laser from the ion beam. ϕ = 0 implies a perfect alignment. However, the frequency is shifted anyhow.

7.6 DOPPLER-BROADENED SPECTROSCOPY

In the Doppler-broadened spectroscopy experiments a laser system, which consists of a Nd:YVO_4 pumped cw Ti:Sa laser, was used to generate the laser light for ion excitation antiparallel to their moving direction (Figure 7.18). The laser frequency was maintained by a wave meter (*ATOS*, LM 007), to a sufficient accuracy of 100 MHz. A mode-hop-free fine detuning ($\Delta\nu_{Laser} \leq 15$ GHz) can be done software controlled via an ADC[48] card with 5 V output. The laser light was guided through the switch AOM and the sm-pm fibre to the ESR laser tower ($P \sim 20$ mW). The laser beam was aligned to stay convergent in the laser-ion beam interacting zone with a diameter in the range of maximal 8 mm. The focal point of the laser beam was adjusted approximately 5 m behind the out coupling window of the ESR.

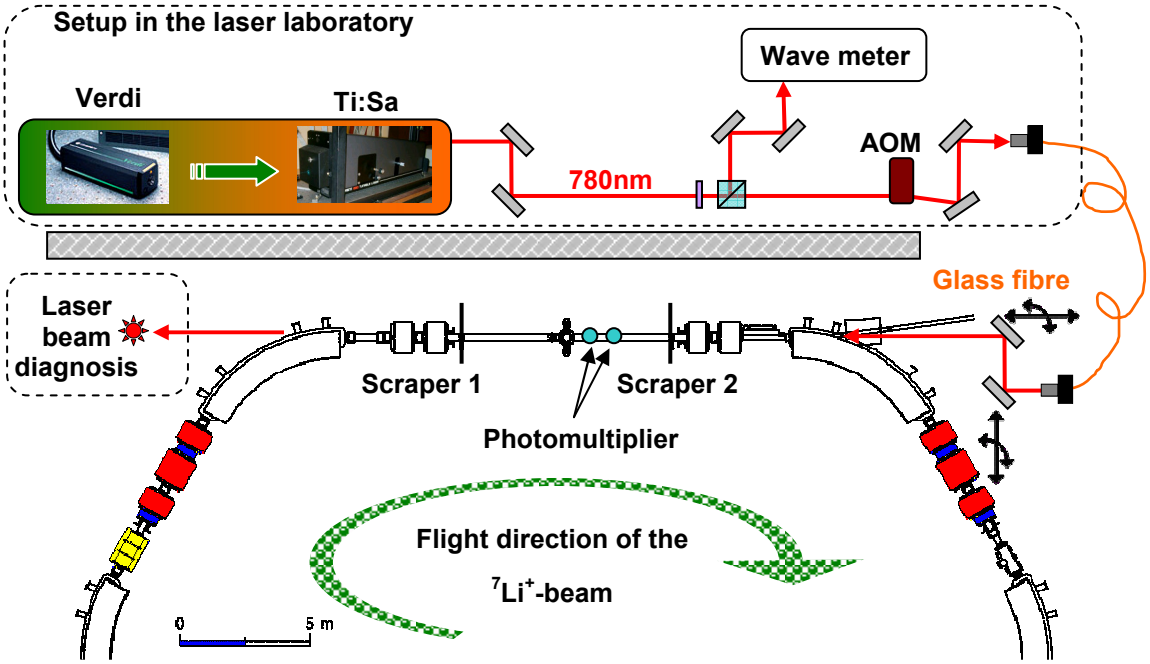

Figure 7.18: Schematic of the laser setup used for Doppler-broadened spectroscopy in the antiparallel excitation regime. Further the equipment needed at the experimental section at the ESR is shown.

The fluorescence light of the metastable ions is detected with PMTs aligned between two scrapers. The scrapers are used to verify the overlap of the ion beam with the laser beam. All PMTs are equipped with photon collecting optics described in chapter 7.2. To suppress background noise from the excitation laser, a band gap filter (*Schott*, BG39) is placed before the photomultiplier tube. It attenuates the laser wavelength (λ_a = 780 nm)

[48] ADC = analogue digital converter.

by five orders of magnitude while its transmittance in the visible is in the range of 80 % (see Figure D.1 in the appendix).

To investigate the velocity distribution, the frequency of the $2s^3S_1$ ($F = {}^5/_2$) $\rightarrow$ $2p^3P_2$ ($F = {}^7/_2$) transition is addressed by laser light that is tuned several GHz across the resonance. For the velocity β = 33.8 %c and a laser beam aligned antiparallel to the flight direction of the ions the excitation frequency shifts from 546 466 918.8 MHz to 384 236 572.3 MHz. During one frequency scan the frequency range is sub-divided into 100 points with a dwell time of 0.1 s (so the overall measuring time of a single scan is ~ 10 s). The first 5 s after ion injection, the beam is merely electron cooled with the laser beam blocked. A typical spectrum of the Doppler-broadened signal is shown in Figure 7.19. The linewidth of this signal is (1.09 ± 0.08) GHz which corresponds to a momentum spread of $\Delta p/p = (8.4 \pm 0.6) \times 10^{-6}$. This value is slightly smaller than the momentum spreads of $^7Li^+$ and $^{14}N^{2+}$ which are determined by analysis of Schottky signals (see chapter 4.2.4).

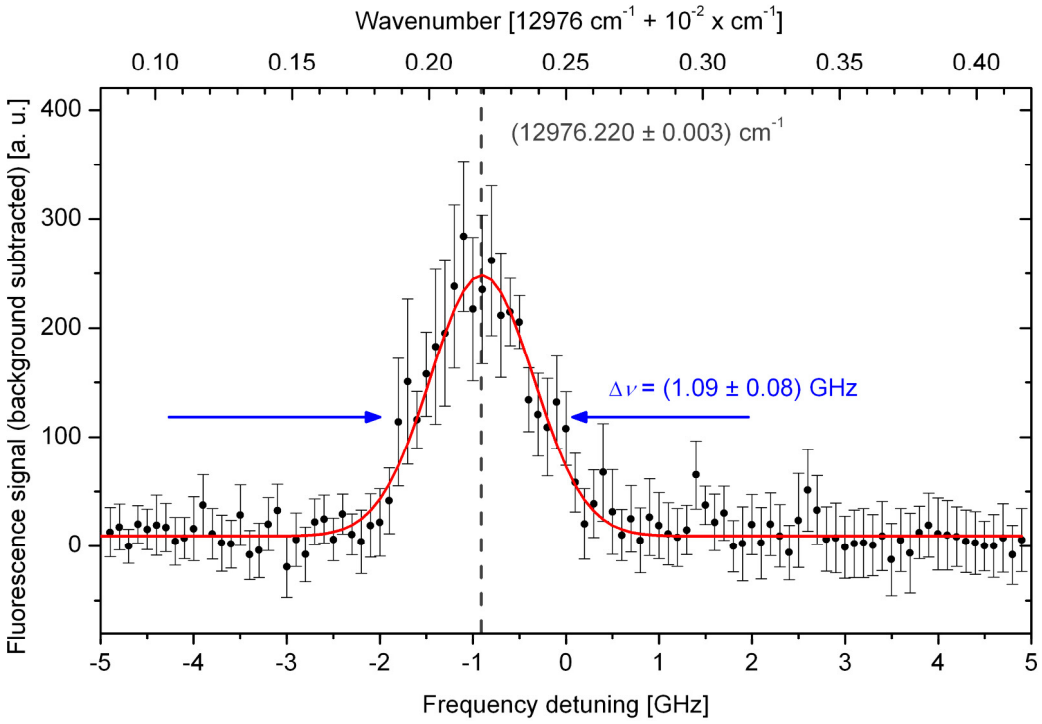

Figure 7.19: Doppler-broadened spectrum with a linewidth of $\Delta\nu \approx 1$ GHz. The frequency of the Ti:Sa laser was tuned ± 5 GHz with a laser power of 20 mW. The upper scale shows the spectrum in absolute wave numbers. Red line: Gaussian fit on the data points.

Taking all Doppler-broadened measurements into account, an averaged linewidth of (1.04 ± 0.14) GHz was found (see Figure 7.20). To transform these signals into the ions' rest frame one use

$$\Delta\nu_0 = \gamma \cdot (1+\beta) \cdot \Delta\nu_a \tag{7.27}$$

which yields a distribution width of $\Delta\nu_0$ = (1.48 ± 0.22) GHz in the ion frame.

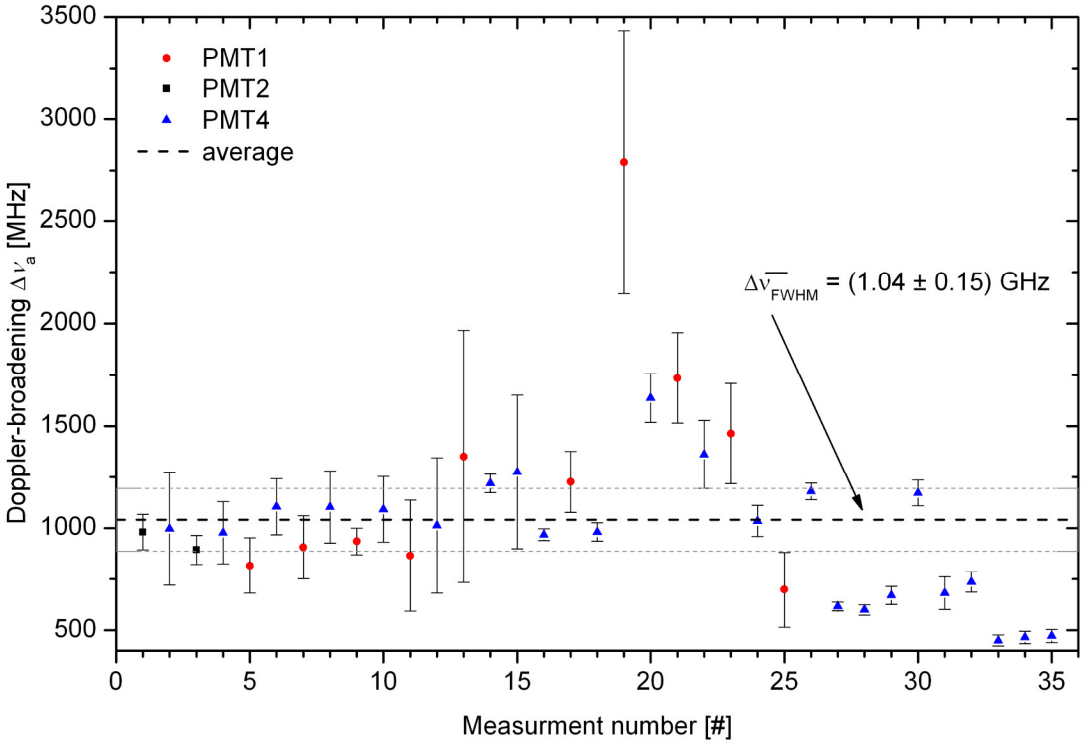

Figure 7.20: Comparison of the Doppler-broadened linewidths taken in different measurements with different PMTs.

Out of these measurements, the absolute frequency of the transition in the laboratory frame can be determined with an accuracy of 100 MHz (e.g. ν_a = (383 621.0 ± 0.1) GHz for the spectrum shown in Figure 7.19). So, together with the rest frame frequency, which is known to 73 kHz, the centre of mass of the velocity distribution can be calculated and compared with the parameters of the electron cooler (U = 32.355 keV, I = 200 mA). In fact a calibration of the electron cooler with unique accuracy is possible. The electrons of the cooler can have a maximum energy of 300 keV. A very precise measurement of the absolute voltage is difficult. Usually special potentiometers are used to calibrate electron coolers (e.g. available at PTB Braunschweig with an accuracy of 10^{-5}) by comparing it to standardised resistors. For daily operation, an accuracy of 2×10^{-4} can be realised. The limiting parameters are the creepage current and the aging of the components. Further, for the precise determination of the ion beam

energy, corrections due to the space charge effects of the cooler electrons have to be considered. These induce a potential gradient over the width of the ion beam, which leads to a difference of more than 100 V (at 1 A electron current) in the potential between the drift tube surface of the cooler and the centre of the beam. For the ESR 1 mA is equal to a change of 0.3 V of the electrode voltage[49]. Furthermore, the ionisation of residual gas to positively charged ions can lead to a partial compensation of space charge of the electrons. However, at the ESR those residual ions are removed rapidly. Thus, this effect is negligible. Taking the relative uncertainty of 2×10^{-4} at a voltage of 32 kV into account, this leads to an uncertainty of $\Delta U = \pm$ 6.4 V. For converting this in terms of laser frequency uncertainty for the parallel excitation of the $2s^3S_1$ ($F = {}^5/_2$) $\rightarrow$ $2p^3P_2$ ($F = {}^7/_2$) transition, following relations apply

$$\beta = \sqrt{1 - \frac{1}{\left(1 + \frac{E_{\mathrm{kin}}}{E_0}\right)^2}} \quad \rightarrow \quad \Delta\beta = \frac{1 - \frac{\left(E_{\mathrm{kin}} \cdot \left(E_{\mathrm{kin}} + 2 \cdot E_0\right)\right)}{\left(E_{\mathrm{kin}} + E_0\right)^2}}{\sqrt{E_{\mathrm{kin}} \cdot \left(E_{\mathrm{kin}} + 2 \cdot E_0\right)}} \cdot \Delta E_{\mathrm{kin}} \tag{7.28}$$

and $$\nu_{\mathrm{a}} = \gamma \cdot \nu_0 \cdot \left(1 - \beta\right) \quad \rightarrow \quad \Delta\nu_{\mathrm{a}} = \gamma \cdot \nu_0 \cdot \left(\frac{\beta}{1 - \beta^2} - 1\right) \cdot \Delta\beta \tag{7.29}$$

and $$\beta = \frac{\nu_0^2 - \nu_{\mathrm{a}}^2}{\nu_0^2 + \nu_{\mathrm{a}}^2} \quad \rightarrow \quad \Delta\beta = \left| -\frac{4 \cdot \nu_0^2 \cdot \nu_{\mathrm{a}}}{\left(\nu_0^2 + \nu_{\mathrm{a}}^2\right)^2} \cdot \Delta\nu_{\mathrm{a}} \right| \tag{7.30}$$

where E_0 is the electron energy at rest and E_{kin} is the kinetic energy of the electrons in the electron cooler ($E_{\mathrm{kin}} = U \cdot q$). This leads to an uncertainty of $\pm$ 27 GHz for the frequency position of the laser or, vice versa, with the knowledge of the laser frequency in the sub-GHz range a calibration of the absolute electron cooler velocity in the order of $\Delta\beta \sim 10^{-6}$ is possible. This value is two orders of magnitude more precise than the one achieved by the electronic setup. Comparing all Doppler-broadened measurements, a mean fluctuation of 1.3 GHz in the laser position and furthermore, an offset of 54.3 GHz ($\equiv 2\sigma$ error) compared to the expected values were found (see Figure 7.21).

[49] This is valid for an electron energy E_{kin} = 32 keV and a current I = 0.1-0.2 mA [Steck06].

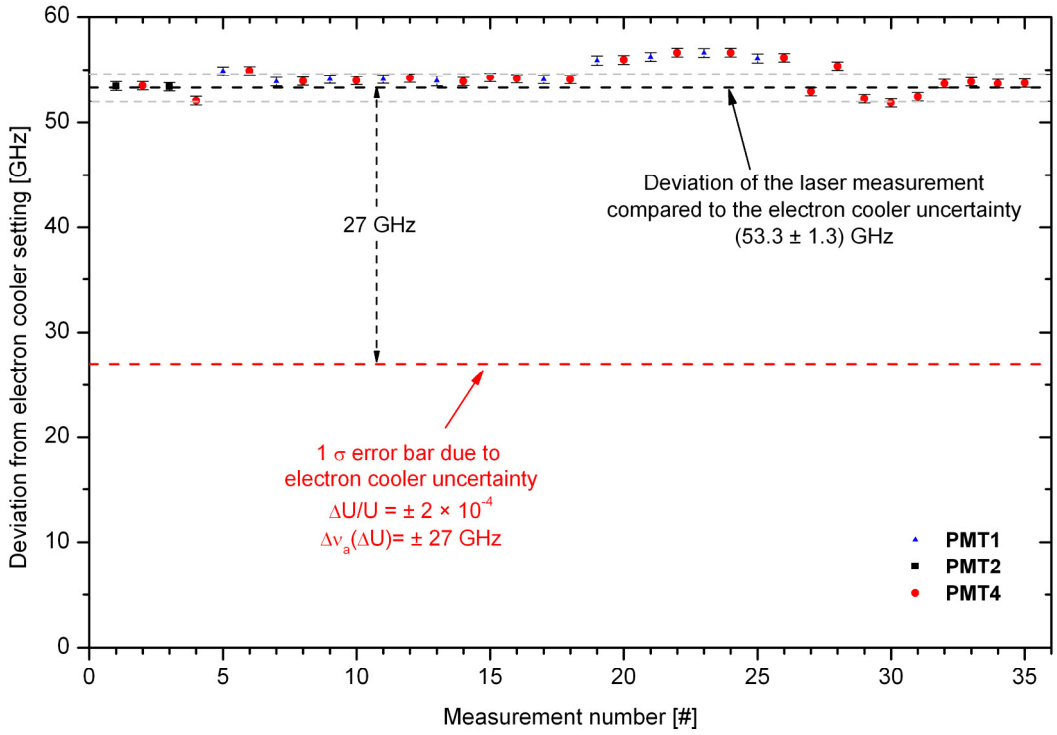

Figure 7.21: Deviation of the antiparallel frequency expected by the settings of the electron cooler, compared to the measured laser frequency.

7.6.1 ESTIMATION OF THE METASTABLE FRACTION

At an ion current of I_{DC} = 20 µA, a number of approximately $N_{ions} \approx 10^8$ ions are stored in the ESR. This leads to an ion per meter density of 1.85 × 10^6 ions/m, assuming the ions to be homogeneously distributed along the orbit in the ring. So, in the detection region (± 250 mm around the PMT) on average 9.3 × 10^5 ions are present. These ions are affected by laser light of a power of $P_{Laser} \approx$ 20 mW that is distributed over a diameter of $\varnothing_{laser\text{-}beam}$ = 8 mm of the Gaussian laser beam. These settings lead to a saturation parameter of S_0 = 5.9. For a two-level system, the population of the excited state is given by [Demtröder00] to

$$N\left(^3S_1\right) = \frac{S_0}{2 \cdot \left(1 + S_0 + 4 \cdot \tau_{ph}^2 \cdot \delta^2\right)} \tag{7.31}$$

where δ describes the frequency detuning (here δ = 0) from resonance and τ_{ph} the lifetime of the upper state (43 ns). In case all ions were in the triplet spectrum, the population of the excited state would be $N(^3S_1)$ = 43 %. Thus 4 × 10^5 excited ions would be present in the detection range which, due to the lifetime of the upper state, would generate a signal of 9 × 10^{12} photons/s. Considering the efficiency of the PMT system

with ε = 0.02 %, a signal of A_ε = 1.9 × 10^9 photons/s is expected, if a velocity distribution of the ions, narrower than the laser linewidth, is assumed. In fact it is the other way around, the laser linewidth ($\Delta\nu_{\text{Laser}} \approx 1$ MHz) covers only a thousandth part of the velocity distribution ($\Delta\nu_{\text{Doppler}}$ = 1 GHz in terms of laser frequency) and thus is affecting only a certain fraction of the whole beam. Considering the signal in the middle of the Gaussian distribution the amplitude can be taken to be constant and after

$$A = \frac{A_\varepsilon}{\sqrt{2 \cdot \pi} \cdot \Delta\nu_{\text{Doppler}}} \cdot \Delta\nu_{\text{Laser}} \tag{7.32}$$

a signal of A = 7 × 10^5 photons/s would be expected. Comparing this value with the measured one (see Figure 7.19), where the tip-signal of the Doppler-broadened spectrum is 250 counts/s (after subtraction of the background), one finds that a fraction of 0.04 % of the whole ion beam consists of $^7Li^+$ ions in the metastable state.

7.7 FIRST-ORDER DOPPLER-FREE SPECTROSCOPY

To perform spectroscopy with sub-Doppler linewidths on particles with high velocities an extended laser system, compared to the Doppler-broadened spectroscopy, is indispensable. Typically two lasers are needed that excite either the same transition (saturation spectroscopy) or two different ones (V- and Λ-spectroscopy)[50]. For the second case, the transitions have to be coupled by sharing one (upper or lower) state. These transitions were addressed by laser light that is in resonance with particles at the desired velocity. Further, the frequency of the laser light has to be maintained with high accuracy. As explained in chapter 6.3, atomic or molecular references or a frequency comb were used for this task. The setup that fulfils these requirements is sketched in Figure 7.22. Since in the present experiment at the ESR saturation spectroscopy was not yet applied, the further discussion is restricted to the V- and Λ-spectroscopy schemes. Nevertheless, saturation spectroscopy can be performed with the same setup.

For the antiparallel excitation, a system of two diode lasers with a wave meter for coarse and an atomic rubidium standard for fine monitoring of the frequency was build up. Both diode lasers are external cavity lasers in the Littrow configuration, irradiating at a wavelength of 780 nm with a linewidth of 2 MHz and are mode-hop-free tunable over 8 GHz. In the following, one diode (*sharp*, GH0781JA2C, $P_{\text{out}} \approx 80$ mW) is called low power laser diode (LP-LD, green path in Figure 7.22). The other (*Toptica*, LD-

[50] One can also think of a two photon excitation scheme where only one laser beam is needed but this is out of the scope of this work.

0780-P250-1, $P_{out} \approx 150$ mW) is the high power laser diode (HP-LD, red path). The LP-LD is locked to a rubidium transition and therefore acts as the frequency reference. The HP-LD is used for lithium spectroscopy in the ESR, while its frequency is controlled by a frequency offset lock to the LP-LD. Small parts of the laser light of both diodes are split off, merged and guided to a 25 GHz photo diode (*New Focus*, VIS-IR 1434) to compare the beat signal of the merged lasers with the reference frequency of a signal generator. The resulting signal is fed-back to the HP-LD to stabilise its laser frequency (relative to the locked LP-LD). With this stabilisation technique, the HP-LD can be detuned by changing the reference frequency without loosing accuracy. Additionally, both lasers are coupled into a wave meter for coarse control and adjustment of the wavelength. The major part of the light from the HP-LD is coupled into the sm-pm fibre that guides the light to the ESR. In front of the glass fibre incoupling, an AOM (*Crystal Technology*, 3200-121) is placed. It is used for switching the laser beams on and off, adjusting the intensity and shifting the wavelength by – 200 MHz. For test measurements, the major part of the LP-LD light is also guided to the glass fibre, but via a different beam path. It goes through another AOM (*Crystal Technology*, 3200-121) which shifts the wavelength by + 200 MHz and allows for intensity adjustments and switching, respectively, independent of the other laser beam. It is merged with the HP-LD beam with two PBS in order to ensure that both laser beams have the same polarisation orientation at the ESR.

The laser light for the parallel excitation ($\lambda_p = 386$ nm) is generated by the frequency-doubled Ti:Sa laser (blue path in Figure 7.22). A small part of the fundamental ($\lambda_{fp} = 772$ nm, orange path) is split off and guided to a second wave meter and the saturation spectroscopy setup with heated iodine molecules, to monitor the frequency. The frequency doubled laser light is beam shaped by two cylindrical silica lenses ($f_1 = + 200$ mm, $f_2 = + 500$ mm) and focused, by a spherical lens ($f = + 2000$ mm), into an 85-MHz AOM (*Brimrose*, TEM-85-2-.386) for switching and intensity correction. The first-order diffracted light is guided to the ESR via the sm-pm photonic fibre with a transmission efficiency of 40 %. In this setup a flip mirror is introduced that allows for switching the beam path of the Ti:Sa laser light between the SHG setup and the glass fibre. This is a sufficient solution for having a simple possibility to use the Ti:Sa at its fundamental wavelength for Doppler-broadened spectroscopy.

For spectroscopy with sub-Doppler linewidths a bunched ion beam has to be used, to suppress particle velocity changes caused by fluctuations in the voltage of the electron cooler ($\Delta U/U \sim 10^{-5}$). These lead to a random shifting of the velocity classes and thus to a smearing of the spectroscopy signal. In bunches the ion velocity is kept more stabile and even the momentum spread is narrowed (see appendix C). The bunch frequency corresponds to the 10^{th} harmonic of the revolution frequency of the ions.

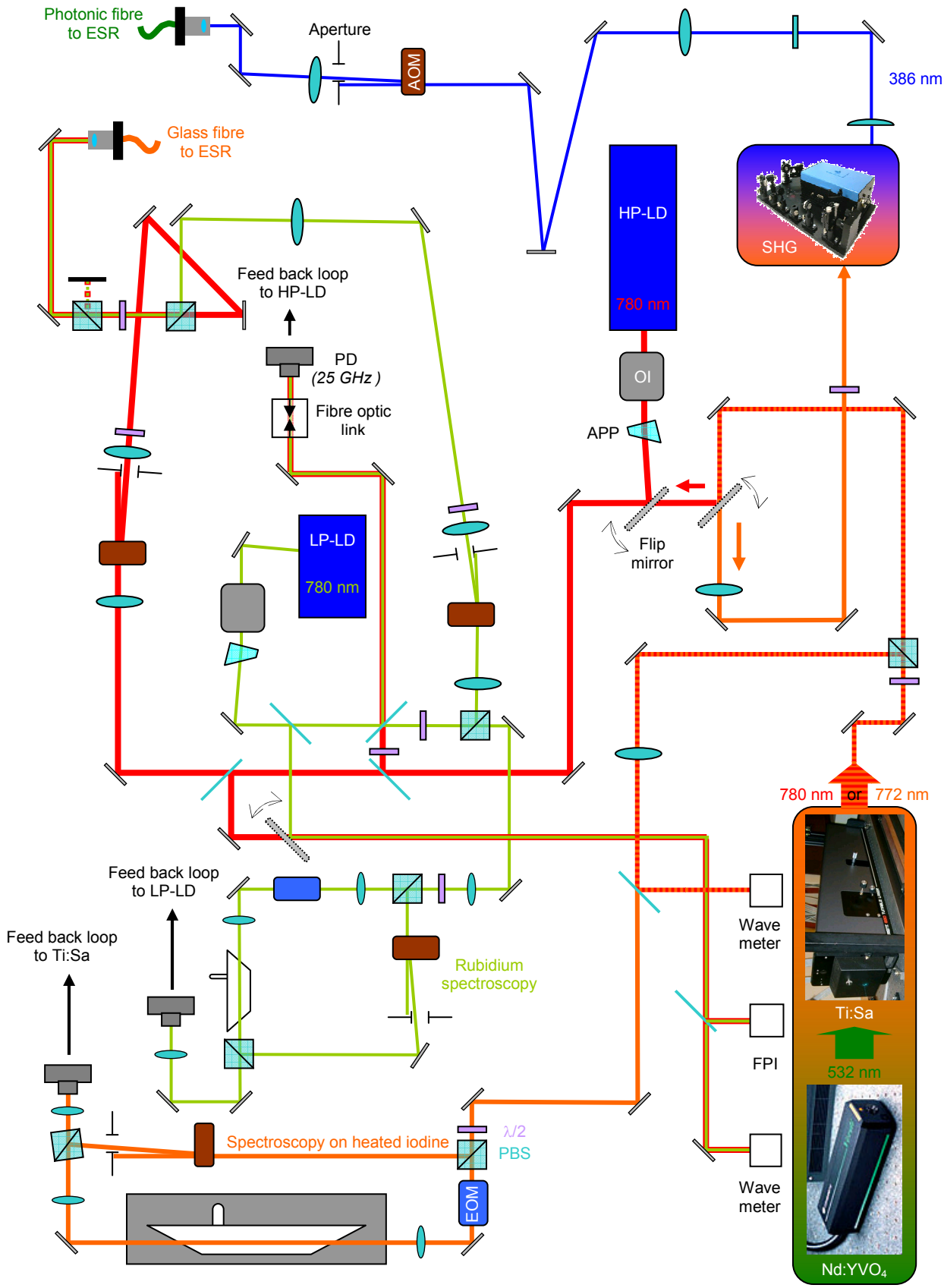

Figure 7.22: Laser setup for first-order Doppler-free spectroscopy of $^{7}Li^{+}$ in the ESR. For explanation see text. APP: anamorphic prism pair, PD: photo diode, OI: optical isolator.

7.7.1 IR V-SPECTROSCOPY

The V-type spectroscopy is performed with two laser beams whose frequencies are in resonance with two transitions which are coupled via one ground state (see chapter 5.1) and are aligned collinear-antiparallel with respect to the flight direction of the ions. This scheme has the advantage that uncertainties due to laser-laser overlap are not present because both laser beams can be guided through the same optical fibre and therefore propagate the same way after out coupling. The background noise, induced by laser stray light, is comparably low (~ 300 counts/s), due to a low detection efficiency of the PMT at $\lambda = 780$ nm and a sufficient suppression by the BG-39 filter.

In this spectroscopy scheme the LP-LD was used as the fixed frequency laser. It is stabilised to the D2 transition (F = 2) $\rightarrow$ (F = 3) in ^{85}Rb at a frequency of $\nu_1 = 384\,228\,116$ MHz. The ion velocity was tuned in such a way that the Doppler-shifted frequency for the excitation of the $2s^3S_1$ (F = $^5/_2$) $\rightarrow$ $2p^3P_2$ (F = $^5/_2$) transition is equal to ν_1. The second transition in the V-spectroscopy scheme, was driven by the Ti:Sa laser. The frequency of this laser was tuned across the $2s^3S_1$ (F = $^5/_2$) $\rightarrow$ $2p^3P_2$ (F = $^7/_2$) transition of the same velocity class of ions. The hyperfine-structure splitting of the $2s^3P_2$ (F = $^5/_2$) $\leftrightarrow$ (F = $^7/_2$) states is 12 GHz in the ion frame and 8 GHz in the laboratory frame, respectively. Hence, the frequency of the Ti:Sa laser can be observed by maintaining the beat frequency between both lasers.

Introducing only the Ti:Sa laser in the ESR, Doppler-broadened spectroscopy on a closed two-level system is performed. Applying additionally the LP-LD, the closed two-level scheme is changed to an open three-level system with a decay channel into the $2s^3S_1$ (F = $^3/_2$) ground state. The Doppler-shifted hyperfine splitting of the $2s^3S_1$ metastable ground state for (F = $^5/_2$) $\leftrightarrow$ (F = $^3/_2$), at an ion velocity of $\beta = 33.8$ %, is $\Delta\nu_{hfs}$ = 14 GHz. To excite those electrons that have decayed into the (F = $^3/_2$) state, either a laser has to be tuned by 14 GHz for repumping or the ion velocity has to be changed. However, neither can this frequency gap be bridged by the ion velocity changing processes in the ESR nor are the lasers tuned to this frequency; consequently, if an electron decays into the $2s^3S_1$ (F = $^3/_2$) state it is not excited anymore. The $2s^3S_1$ (F = $^5/_2$) state gets depopulated and the fluorescence signal drops down. For the V-spectroscopy scheme, where the LP-LD laser is kept fixed in frequency and the Ti:Sa laser is tuned across resonance, this results in a hole in the Doppler-broadened signal. By theory, the depth of the hole in the distribution should be 100 % and the width in the range of the natural linewidth[51] of this transition.

[51] Saturation effects are neglected here.

In the measurements at the ESR, it turned out that instead of a hole emerging in the fluorescence signal, the fluorescence vanishes completely (Figure 7.23). The smearing of the hole is due to the velocity changing forces in the ring. These are not strong enough to mix the hyperfine split states but powerful enough to mix the ion velocity classes in the Doppler-broadened spectrum. They randomly shift all velocity classes of the ions in resonance with the LP-LD laser frequency, leading to a depopulation of all velocity classes instead of only a narrow one.

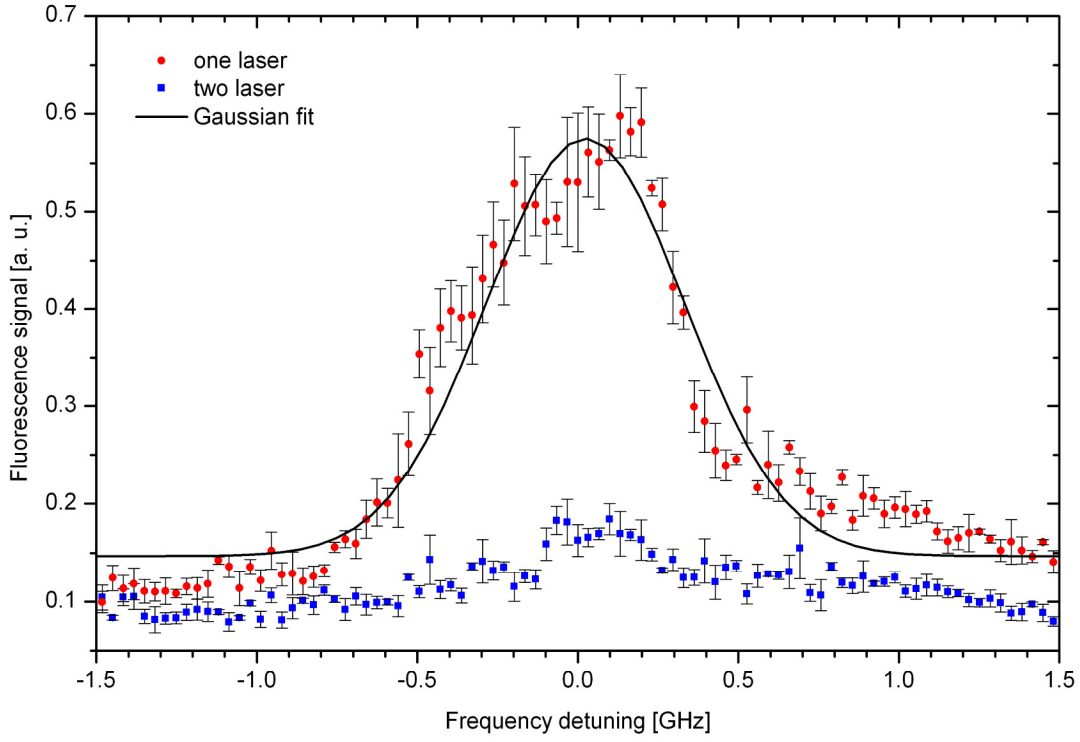

Figure 7.23: Fluorescence signal of the V-type spectroscopy (blue squares) with two lasers aligned antiparallel to the flight direction of the ions. The red dots show the Doppler-broadened signal, if only one laser (on the ($F = {}^5/_2$) → ($F = {}^7/_2$) transition) is interacting with the ions.

7.7.2 IR Λ-SPECTROSCOPY

In principle, changing the spectroscopy scheme from V-spectroscopy to Λ-spectroscopy requires a change of the frequency of the tuning laser from the two-level system $2s^3S_1$ ($F = {}^5/_2$) → $2p^3P_2$ ($F = {}^7/_2$) to the $2s^3S_1$ ($F = {}^3/_2$) → $2p^3P_2$ ($F = {}^5/_2$) transition. The fixed laser remains at the $2s^3S_1$ ($F = {}^5/_2$) → $2p^3P_2$ ($F = {}^5/_2$) transition. In this scheme a fluorescence signal appears if both lasers are in resonance with the same velocity class of ions. Only then, a back and forth pumping of the electrons, from one metastable ground state to the other, is possible. If the lasers interact with ions of different velocity classes, the affected states are depopulated in a short period and the fluorescence signal

disappears. The advantages of this scheme are the same as in the V-spectroscopy (no uncertainty in the laser-laser alignment, small background noise). It is used to investigate the shape and the size of the first-order Doppler-free Λ-fluorescence signal. Here we do not prevent ground state correlations in the beam velocity due to the laser light force.

The LP-LD was locked to the (F = 2) → (F = 3) transition of ^{85}Rb, while the ion velocity was tuned in such a way that the Doppler-shifted excitation frequency for the $2s^3S_1$ (F = $^5/_2$) → $2p^3P_2$ (F = $^5/_2$) transition was at the same frequency. The Ti:Sa laser was tuned across $2s^3S_1$ (F = $^3/_2$) → $2p^3P_2$ (F = $^5/_2$) transition. The addressed metastable ground states have a hyperfine-structure splitting of 20 GHz in the ions' rest frame and 14 GHz in the laboratory frame. The beat frequency of the laser beams was recorded with the 25 GHz photo diode. This made it possible to control the absolute frequency of the tuned laser in the sub-MHz range. The intensity of the lasers was maintained online by a power meter at the ESR. The measured spectra can be described by a Lorentzian profile (Figure 7.24). The linewidth yielded is 10-15 times the natural linewidth but also a factor of ten narrower compared to the Doppler-broadened signal. This line broadening was already studied in the TSR experiments [Saathoff02] and could be related to memory effects imposed on the revolving ions. Ion velocity changes that arise over several to many roundtrips of the ions in the storage ring are the reason for the broadening. Λ-spectroscopy is very susceptible to such velocity changes as nothing requires the two lasers to be in resonance simultaneously, i.e. the back and forth pumping between the two ground states can occur over many roundtrips in the ring. If during that time the ion velocity changes by collisions the resonance signal smears out. Ions that are only resonant with one laser should stay dark for the rest of the measurement. However, velocity changes can bring these ions into resonance with the other laser. Sources for velocity changes are intra-beam scattering and collisions in the electron cooler or with rest gas atoms. The signal linewidth is (70 ± 2) MHz at laser intensities of $P \sim 2$ mW and increases to a maximum width of (140 ± 10) MHz at $P \sim 14$ mW.

A reduction of the signal linewidth can be achieved by applying a proper switching procedure between the lasers. In [Saathoff02] it was found that, if the measurement is performed in a switching scheme where the fluorescence signal is recorded when first one laser, then the other, then both simultaneously and in the final step no laser interacts with the ions, the FWHM can be reduced to less than 30 MHz. Taking the difference in the fluorescence signals recorded with the lasers introduced separately, from the signal recorded when both lasers are in the ring simultaneously, the fluorescence rate related to velocity changing effects can be isolated. The difference signal contains not only the "true" Λ-signal stemming from photons scattered in one passage through the interaction

region. Additionally, fluorescence from ions that perform several roundtrips according to the duration of one time window contributes to the difference signal. Velocity changes, that occur on this time scale lead to a broadening of the difference signal. The present Doppler-free ESR measurements were performed with a switching frequency of 50 kHz. Systematic investigations at different switching rates could not been done yet. However, regarding the revolution frequency (~ 1 MHz) of the $^{7}Li^{+}$ ions in the ESR, a narrower signal is expected to be found at switching rates in the range of 1 MHz.

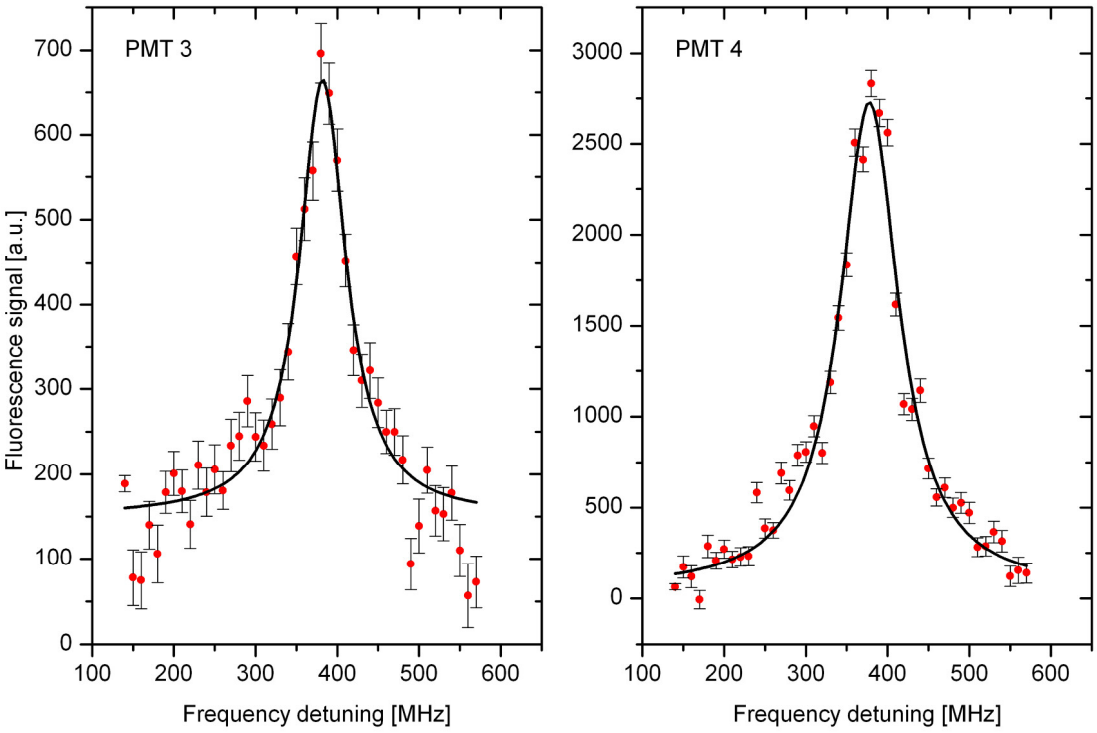

Figure 7.24: Fluorescence signals achieved by IR Λ-type spectroscopy. Both laser beams are aligned antiparallel with respect to the ion beam. Left panel: PMT 3 signal with a linewidth of (70 ± 5) MHz. Right panel: PMT 4 signal with (87 ± 2) MHz recorded at 1.6 mW laser power.

In Figure 7.25 the fluorescence rate as a function of the overall laser power (1.7-14 mW) for two different PMTs is shown. All data points (of the respective PMT) can be fit with a straight line. No saturation behaviour can be found in this diagram.

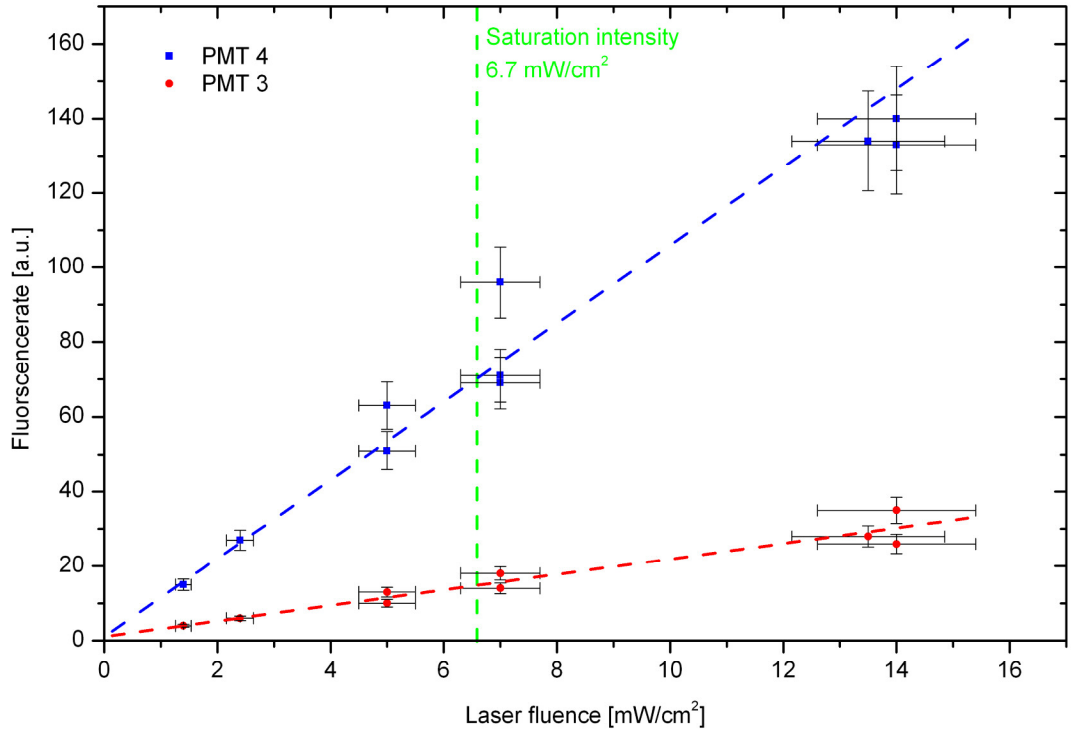

Figure 7.25: Fluorescence rate as a function of the laser power for two PMT positions with IR Λ-type spectroscopy. The dashed lines are linear fits of the data points of the respective PMT.

7.7.3 UV/IR Λ-SPECTROSCOPY

A test of time dilation following the principle of Ives and Stilwell requires a Λ-spectroscopy with one laser aligned in- and one against the ion flight direction. Only then the ion velocity cancels out. The transitions, used for this measurement, are the same as for the IR Λ-spectroscopy (described in the previous chapter). The ion velocity is tuned in such a way that the Doppler-shifted excitation frequency of the $2s^3S_1$ ($F = {}^5/_2$) $\rightarrow$ $2p^3P_2$ ($F = {}^5/_2$) transition (ν_1 = 546 455 144.75 MHz at rest) is equal to the ($F = 2$) $\rightarrow$ ($F = 3$) transition frequency in ^{85}Rb at rest. In these measurements the LP-LD was not stabilised to the rubidium transition, but the transmission signals of the saturation spectroscopy were recorded. This becomes necessary after the HP-LD broke down during the experiments and the intended frequency offset lock was not applicable anymore. The light for excitation parallel to the movement of the ions, was generated by the frequency-doubled Ti:Sa laser. It was set in resonance with the $2s^3S_1$ ($F = {}^5/_2$) $\rightarrow$ $2p^3P_2$ ($F = {}^3/_2$) transition (ν_2 = 546 474 962.65 MHz at rest). For the used ion velocity $\beta = 0.338$ this means a frequency of ν_p = 777 204 798 MHz (or λ_p = 386 nm) in the laboratory frame. A further consequence of the damage of the HP-LD was that no

reference transition in the iodine molecule was available for this spectroscopy scheme[52]. So, the available frequency accuracy was reduced to the uncertainty of the wave meter (± 100 MHz).

Applying the frequency-doubled laser light for the parallel spectroscopy, an additional filter has to be introduced in the PMT system to suppress the laser stray light. Photons with a wavelength of 386 nm already induce a considerably higher amount of fluorescence in standard colour glass filters, so that a special filter has to be used. A laminated plastic filter (*Schott*, KV407), which is characterised for producing only a small amount of fluorescence, turned out to be the best choice. This filter lowers the laser intensity by four orders of magnitude at 386 nm and has an average transmittance of ~ 80 % in the optical region (see Figure D.2 in the appendix). To suppress the laser light at 780 nm the BG 39 filter is used. However, the suppression of this filter combination for the 386 nm laser in not perfect. Another PMT (without filters) is used to measure the temporal evolution of the laser background that can be subtracted afterwards. The fluctuations are due to changes of the range of 10 % of the total laser power.

The power of the laser was (1.7 ± 0.2) mW for the parallel excitation and (10 ± 1) mW for antiparallel excitation. The measured fluorescence spectrum is shown in Figure 7.26 in comparison with the simultaneously recorded rubidium spectrum. A linewidth of $\Delta\nu_a$ = (79 ± 25) MHz in the laboratory frame is measured. Compared with the theoretical one (5.2 MHz, equation (2.5)) this is a broadening of more than a factor of ten. Transforming this into the ions' rest frame with

$$\Delta\nu_1 = \gamma\cdot(1+\beta)\cdot\Delta\nu_a - \Delta\nu_2$$

the linewidth becomes $\Delta\nu_1$ = (109 ± 32) MHz.

The position of the peak can be determined to an accuracy of ± 7.1 MHz. It is found 120.5 MHz from the (F = 2) → (F = 3) rubidium reference (Figure 7.26). This leads to an absolute frequency of $\nu_a^{exp} = (384\ 228\ 269.8 \pm 8.4)$ MHz for the antiparallel excitation frequency. To measure the frequency for the parallel excitation the fundamental of the Ti:Sa laser was monitored by the wave meter $\nu_{fp}^{exp} = (388\ 602\ 295 \pm 100)$ MHz. This leads to $\nu_{fp}^{exp} = (777\ 204\ 676 \pm 200)$ MHz

[52] It was planned to set the ion velocity in such a way that the $2s^3S_1$ (F = $^5/_2$) → $2p^3P_2$ (F = $^3/_2$), driven by the Ti:Sa laser, is in resonance. Here calibrated reference lines (compare chapter 6.3.4) in the iodine molecule are available. The difference between the excitation frequency for the $2s^3S_1$ (F = $^5/_2$) → $2p^3P_2$ (F = $^5/_2$) transition and the Rb-reference should be bridged by a frequency offset lock technique where the beat frequency of the HP-LD with the LP-LD is measured.

for the frequency-doubled laser light (comprising all frequency shifts by AOMs). Assuming no deviation from special relativity, the frequency for the excitation of the $2s^3S_1$ ($F = {}^5/_2$) $\rightarrow$ $2p^3P_2$ ($F = {}^5/_2$) transition is $\nu_a^{theo} = (384\ 228\ 330 \pm 99)$ MHz. Comparing this value with the measured one a difference of $\delta\nu_a = \nu_a^{exp} - \nu_a^{theo} = (60 \pm 99)$ MHz between the expected and the measured value, which is well inside the uncertainty, remains. Since the uncertainty of the wave meter is (at least) a factor 10 larger than all uncertainties, caused by laser-laser beam, laser-ion beam alignments or by electro-optic components, only this has to be considered. The relevant frequencies and their uncertainties are summarised in Table 7.2.

Table 7.2: Frequencies and uncertainties of the UV/IR Λ-type spectroscopy for the test of time dilation

Lithium transitions			[MHz]		[MHz]
$2s^3S_1$ ($F = {}^5/_2$) $\rightarrow$ $2p^3P_2$ ($F = {}^5/_2$)	ν_1	=	546 455 144.75	±	0.08
$2s^3S_1$ ($F = {}^3/_2$) $\rightarrow$ $2p^3P_2$ ($F = {}^5/_2$)	ν_2	=	546 474 962.65	±	0.08
Laser for antiparallel excitation	ν_a^{exp}	=	384 228 269.8	±	8.4
Laser for parallel excitation	ν_p^{exp}	=	777 204 676	±	200
	ν_a^{theo}	=	384 228 330	±	99
	$\delta\nu_a$	=	60	±	99

In the next chapter these results are interpreted in terms of test theories.

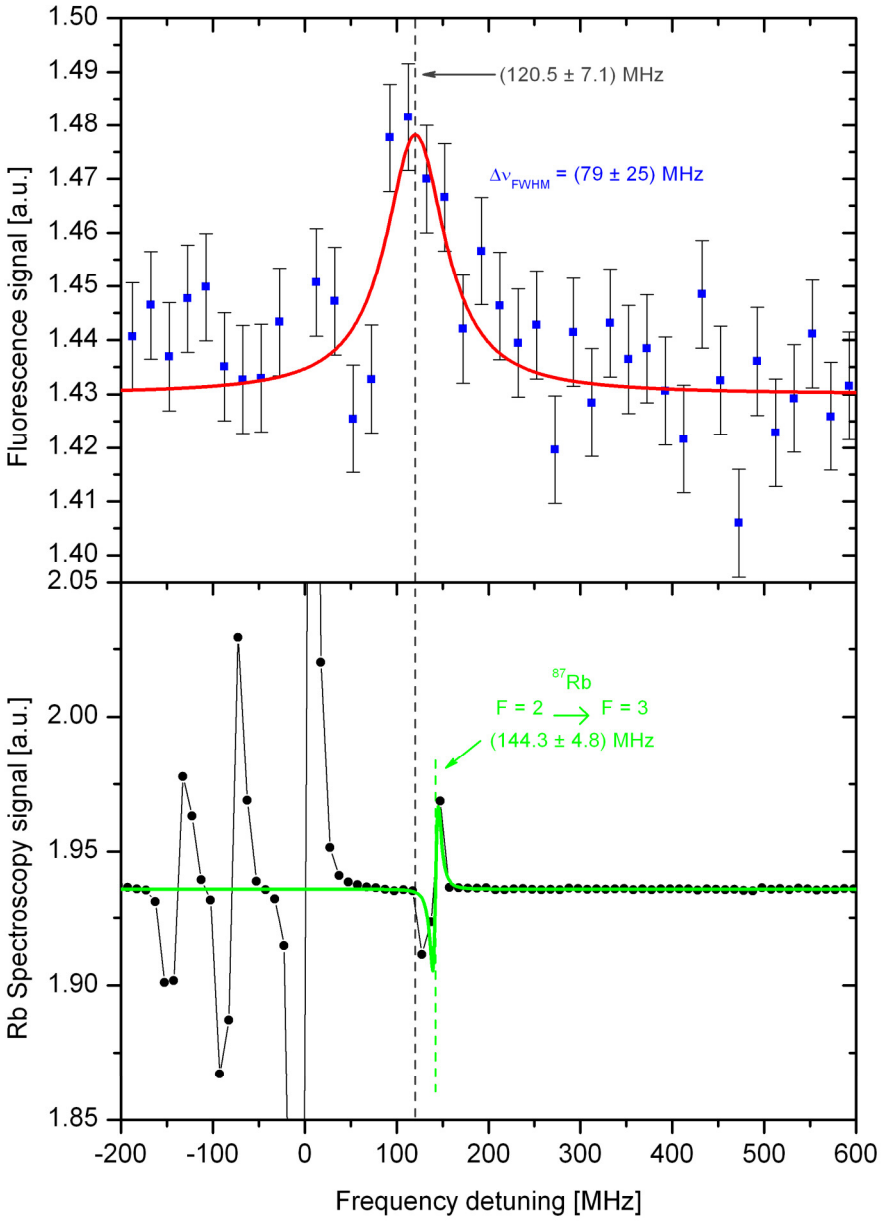

Figure 7.26: Upper panel: Fluorescence signal from the UV/IR Λ-type spectroscopy. The spectrum was measured with a power of 1.7 mW of the "blue" laser and 10 mW of the "red" laser. Red line: Lorentzian fit on the data points. From this, a linewidth of (75 ± 25) MHz was found in the laboratory frame. Lower panel: Signal from spectroscopy on rubidium which was recorded simultaneously as a frequency reference. The position of the lithium signal has been determined to 8 MHz.

7.8 BOUNDARIES FOR SPECIAL RELATIVITY

From the resonance frequencies measured by the UV/IR Λ-spectroscopy technique on the metastable $^7Li^+$ ions, a new limit for the second-order test parameter in the Mansouri-Sexl test theory can be derived. According to equation (1.35) one starts with

$$\frac{\nu_a \cdot \nu_p}{\nu_1 \cdot \nu_2} = \left[\frac{\alpha(\vec{u}^2)}{\alpha(\vec{w}^2)} \right]^2 \tag{7.33}$$

which can be transformed into

$$\frac{\nu_a \cdot \nu_p}{\nu_1 \cdot \nu_2} - 1 = \varepsilon(\vec{\beta}). \tag{7.34}$$

Using the measured data (Table 7.2) an upper bound for hypothetical deviations from special relativity at the ESR can be given to $\varepsilon(\vec{\beta}) = (-1.6 \pm 2.6) \times 10^{-7}$. Comparing (7.34) and (1.39) one can identify $\varepsilon(\vec{\beta})$ with

$$\varepsilon(\vec{\beta}) = 2 \cdot \alpha \cdot \beta^2 + (\alpha + 2 \cdot \alpha_2) \cdot \beta^4 . \tag{7.35}$$

Since the MS test parameters α, α_2 are velocity-independent, the recent upper limit measured in the TSR experiment to $\alpha = (-4.8 \pm 8.4) \times 10^{-8}$ [Reinhardt07a] can be used to fix α_2 by

$$\alpha_2 = \frac{\varepsilon(\vec{\beta})}{2 \cdot \beta^4} - \alpha \cdot \left(\frac{1}{\beta^2} + \frac{1}{2} \right) \tag{7.36}$$

to $$\alpha_2 = (-5.6 \pm 9.8) \times 10^{-6} .$$

This result is an improvement of a factor 28 compared to the so far best value from the angle-tuned spectroscopy on hydrogen at β = 0.84 (compare chapter 3.3 and [MacArthur86a]).

Neglecting contributions of higher-orders than β^2, an upper limit for the first-order deviations can be derived to

$$\alpha = \frac{1}{2 \cdot \beta^2} \cdot \left(\frac{\nu_a \cdot \nu_p}{\nu_1 \cdot \nu_2} - 1 \right) = (-6.7 \pm 11.2) \times 10^{-7} . \tag{7.37}$$

Comparing the uncertainty contributions in the ESR experiment, the moderate knowledge of the Ti:Sa laser is the dominating one. This is due to the uncertainty of the wave meter and limits the sensitivity to hypothetical deviations from the predictions of

special relativity. The first-order test parameter is a factor of 13 weaker than the current upper bound of α [Reinhardt07a]. Nevertheless, this value offers the perspective to increase the limit in accuracy to hypothetical first-order deviations by applying the first-order Doppler-free spectroscopy with full frequency resolution.

7.8.1 COMPARISON OF EXPERIMENTS TESTING TIME DILATION

An overview on the evolution of the test parameter α, from the original Ives-Stilwell experiment to the expected upper limit from the ESR measurement is given in Figure 7.27. The muon decay and the angle-tuned hydrogen experiments are inserted in the diagram, although one has to be careful when interpreting only the first-order test parameter α. This is only a naive comparison, thus the particle velocities of both experiments do not allow a reduction of the MS test function $a(\upsilon)$ to the lowest-order term (compare Figure 1.5). Further, experiments that are sensitive on the sidereal term are included and labelled in green. A solid base for a comparison of the high relativistic experiments with other time dilation measurements is given by Robertson's test theory and the velocity depended test function g_0. The conversion between the MS formalism and g_0 is given by [MacArthur86a] to

$$a(\upsilon) = \frac{1}{\gamma \cdot g_0} \tag{7.38}$$

which is related, for the ESR experiment, to the test parameter α by

$$g_0 \approx \frac{1}{1+\alpha \cdot \beta^2}. \tag{7.39}$$

If special relativity holds $g_0 = 1$. For the sake of clarity, the limit in terms of Robertson's test theory is given as $\Delta g_0 = g_0 - 1$. An upper limit for deviations in terms of Robertson's' test theory can be given by the ESR experiment to $\Delta g_0 < 1.3 \times 10^{-7}$ (see Figure 7.28).

A test theory independent base to compare the results of the different time dilation measurements is the assumption that a hypothetical deviation manifests in a change of the Lorentz factor. Without loss of generality one can postulate

$$\gamma_{\mathrm{EXP}} = \gamma_{\mathrm{SRT}} \cdot \left[1 + \varepsilon\left(\vec{\beta}\right)\right] \tag{7.40}$$

where γ_{EXP} is the combination of γ_{SRT} (the Lorentz factor predicted by special relativity) and $\varepsilon(\vec{\beta})$ which expresses hypothetical deviations from the Lorentz factor. To point out the sensitivity related to the specific particle energy $\xi(\vec{\beta})$ is introduced

$$\xi\left(\vec{\beta}\right)=\frac{\gamma_{\mathrm{EXP}}-\gamma_{\mathrm{SRT}}}{\gamma_{\mathrm{SRT}}-1}. \tag{7.41}$$

In Figure 7.29 the sensitivity on $\xi(\vec{\beta})$ of time dilation experiments are compared. The ESR experiment bridges the gap between the TSR test at 6.4 %c and the measurements on hydrogen beams at 84 %c and lead to a limit of $|\xi(\vec{\beta})| < 2.2 \times 10^{-6}$.

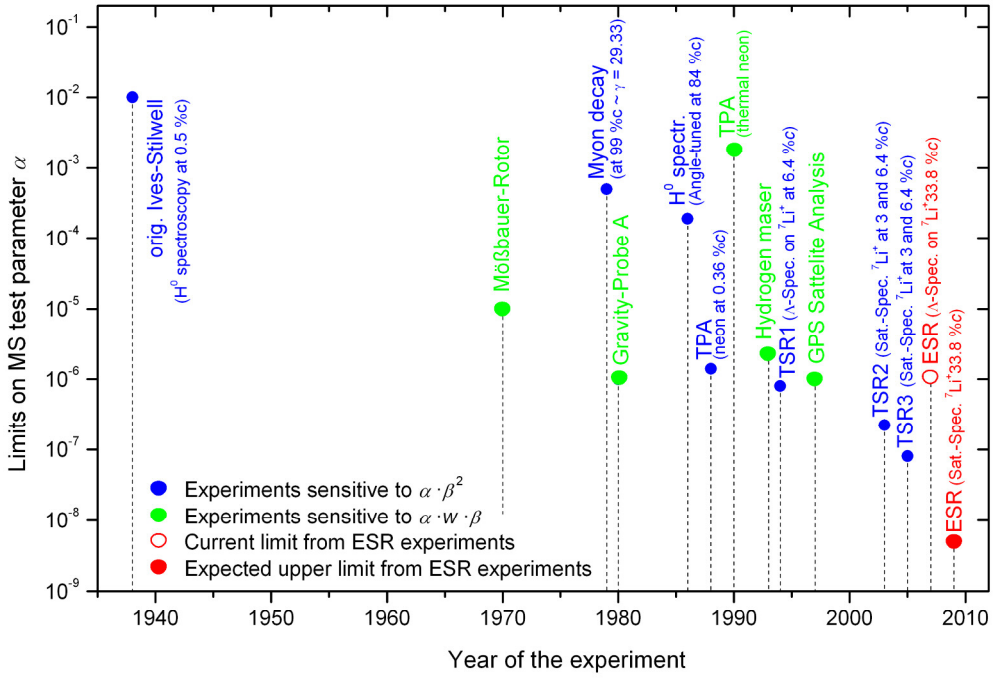

Figure 7.27: Evolution of the test parameter α from the first Ives-Stilwell-type experiments to date. Blue points: experiments with fast particles ($\vec{\beta} >> \vec{w}$: sidereal term is neglected). Green points: experiments probing for sidereal deviations due to $\vec{w}$. The red circle indicates the current value for the ESR experiment, the red point the expected upper limit. The experiments are described in chapters 1.3.2 to 3.5 and appendix A, respectively.

A further comparison of time dilation experiments can be found in [MacArthur86a] or [Zhang97]. A detailed discussion in terms of the MS test theory is reported in [Will92, Gwinner05].

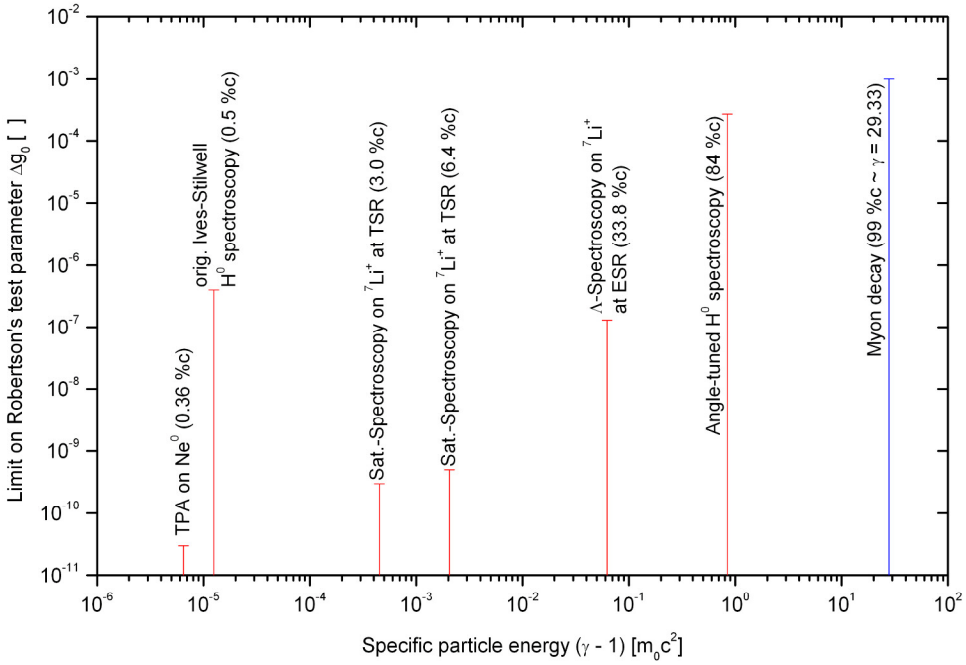

Figure 7.28: Overview of experiments that measure the transverse Doppler effect at different velocities in the formalism of the test theory of Robertson (red). For comparison one experiment with $\gamma >> 1$ is included that measures the lifetime of muons (blue). For the sake of clarity $\Delta g_0 = g_0 - 1$, so the deviation from zero is shown.

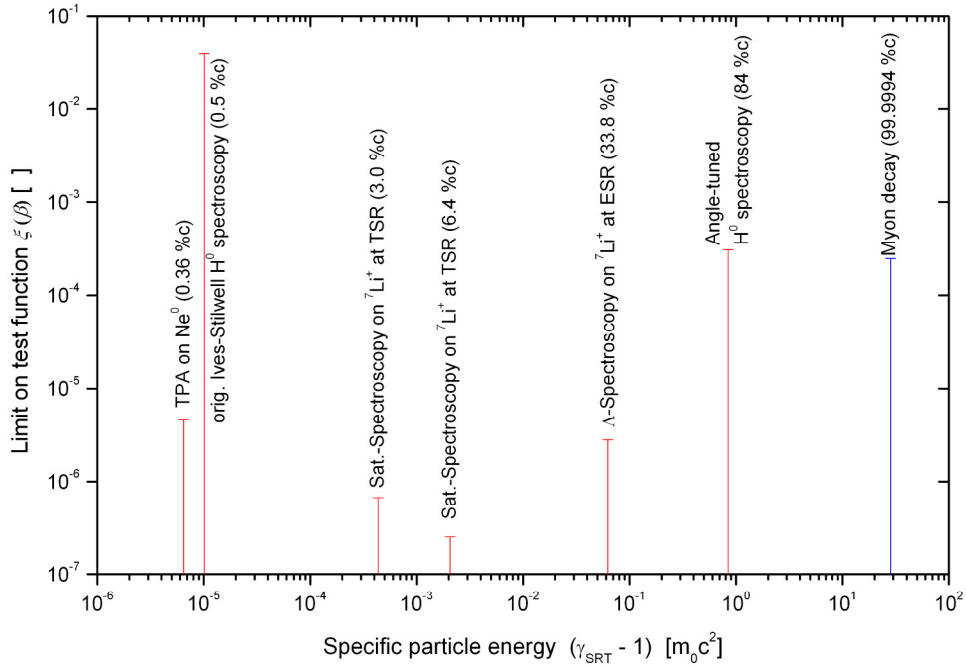

Figure 7.29: Upper limit for hypothetical deviations from the Lorentz factor γ_{SRT}, predicted by the theory of special relativity. Experiments that measure the transverse Doppler effect at different velocities directly are marked by red points. For comparison one experiment with $\gamma >> 1$ is included, which tests special relativity by measuring the lifetime of muons (blue). The experiments are described in chapter 7.8.1.

8 CONCLUSION & OUTLOOK

8.1 CONCLUSION

In this thesis an experiment is presented where, for the first time, the technique of first-order Doppler-free spectroscopy on ions stored in a ring at high velocity (β = 0.338) was applied. The experiment combines the advantages of precision spectroscopy on high energy ion beams with the superb beam quality at a storage ring for a test of time dilation.

In principle, the challenges that have been overcome can be categorised in separate tasks:

- development of laser systems for parallel and antiparallel excitation of $^7Li^+$ ions at a particle velocity of 33.8 %*c*,
- development and implementation of adequate frequency references for both laser systems,
- realisation and characterisation of the quality of the production, acceleration and storage of $^7Li^+$ ions in the $2s^3S_1$ metastable ground state at GSI,
- investigations on the ion beam quality in the ESR.

In the following the most relevant items of each task and the outcome of the measurements concerning the test of time dilation are given.

TEST OF SPECIAL RELATIVITY

Our modern version of the Ives-Stilwell experiment pushes the limit for hypothetical second-order deviations in terms of the MS test theory to $\alpha_2 = (-5.6 \pm 9.8) \times 10^{-6}$ which means an improvement by a factor of 28, compared to previous experiments. Despite of the moderate frequency accuracy it is only 13 times less sensitive to the test parameter $|\alpha|$ compared to the current best value. Hence, the perspective to increase the upper bound of the first-order parameter at the ESR has been demonstrated. The upper limits for $|\alpha|$ and $|\alpha_2|$ can reach a level of 10^{-9} and 10^{-7}, respectively, when the tested frequency references are applied and systematic studies on the geometric uncertainties

at the ESR have been performed. For comparison the recent upper bounds of the test parameter in the MS test theory are given in Table 8.1.

Table 8.1: Recent limits on the Lorentz violating test parameter in the notation of MS

Experiment type Tested parameter(s) Reference	IS α	KT $(\alpha - \hat{\beta}_1)$	MM $(\hat{\beta}_1 + \hat{\delta})$
[Reinhardt07a]	$(-4.8 \pm 8.4) \times 10^{-8}$		
[Wolf04]		$(1.6 \pm 3.0) \times 10^{-7}$	
[Antonini05]			$(-0.5 \pm 3 \pm 0.7) \times 10^{-10}$
[Stanwix05]			$(-0.9 \pm 2.0) \times 10^{-10}$

In terms of Robertson's test theory we bridged the gap in the measurements of hypothetical deviations from Lorentz invariance at different velocities between the TSR experiment at $\beta = 0.064$ and the angle-tuned hydrogen spectroscopy at $\beta = 0.84$. Here we confirmed special relativity to $\Delta g_0 < 1.3 \times 10^{-7}$.

ION BEAM QUALITY

It has been demonstrated that ions in the $2s^3S_1$ metastable ground state are generated in the ECR ion source and survive the whole acceleration process (to 58 MeV/u).

The electron cooled and bunched ion beam in the ESR was found to have an excellent momentum spread of $\Delta p/p \sim 10^{-6}$ or, in other words, the Doppler-broadened ion distribution has a linewidth of $\Delta\nu = 1.4$ GHz in terms of frequency in the ions' rest frame. With these measurements the settings of the electron cooler can be verified to an accuracy of $\Delta\beta = 10^{-6}$ (at $\beta = 0.338$). The fraction of metastable $^7Li^+$ ions in the ion beam was found to be below 0.1 % of a total amount of 10^8 stored ions. The lifetime of the metastable $^7Li^+$ ions in the ESR can reach 50 s.

LASER DEVELOPMENT

The laser equipment required for first-order Doppler-free spectroscopy has been built up and tested successfully. Both systems include an atomic or molecular frequency reference to stabilise or monitor the laser frequency. Further the laser systems were locked simultaneously to a frequency comb that was referenced to a rubidium clock. With the help of this frequency standard the used lines from the molecular I_2 references were calibrated to better than 0.3 MHz[53]. So these can be used as a stable and reliable back up reference for the frequency comb.

[53] The atomic reference is rubidium. The D2 transitions were already measured to an accuracy of ± 5 kHz that is sufficient for our experiment.

8.2 OUTLOOK

The next step in the scope of a test of time dilation at the ESR is to perform Λ-type spectroscopy with full frequency resolution and investigate systematic effects on the MHz scale. All applied frequency references provide a control of the frequency to better than 1 MHz making systematic investigations of the alignment of the lasers with respect to the ion beam indispensable. Further uncertainties due to the focal position of both lasers become important.

To reach this level of accuracy a further narrowing of the signal linewidth is desirable. The use of a measurement scheme, where the lasers can be switched on and off with a frequency that is comparable to the revolution frequency (~ 1 MHz) of the ions in the storage ring, can fulfil this task. With this, the line broadening caused by velocity changing effects (that are accumulated during several revolutions in the ring) is expected to be suppressed [Saathoff02].

Another possibility to gain a narrow signal is to change the spectroscopy type from the Λ-scheme to saturation spectroscopy. Such a spectroscopy system, combined with the fast laser switching technique, allows for linewidths close to the natural one [Reinhardt06]. However, for saturation spectroscopy the signal-to-noise ratio has to be at least improved by a factor of 10 (compared to the present one). Beside the implementation of filters with higher suppression (to reduce the laser background) an increase of the signal is desirable. For instance, this is possible by adding sidebands to both excitation laser beams by electro-optic modulators (Figure 8.1). These sidebands can be understood as additional lasers which interact simultaneous with ions in different velocity classes of the ion beam. The signal of all sidebands can be summarised which in the end leads to an increase in the fluorescence signal (compare [Kramer80]).

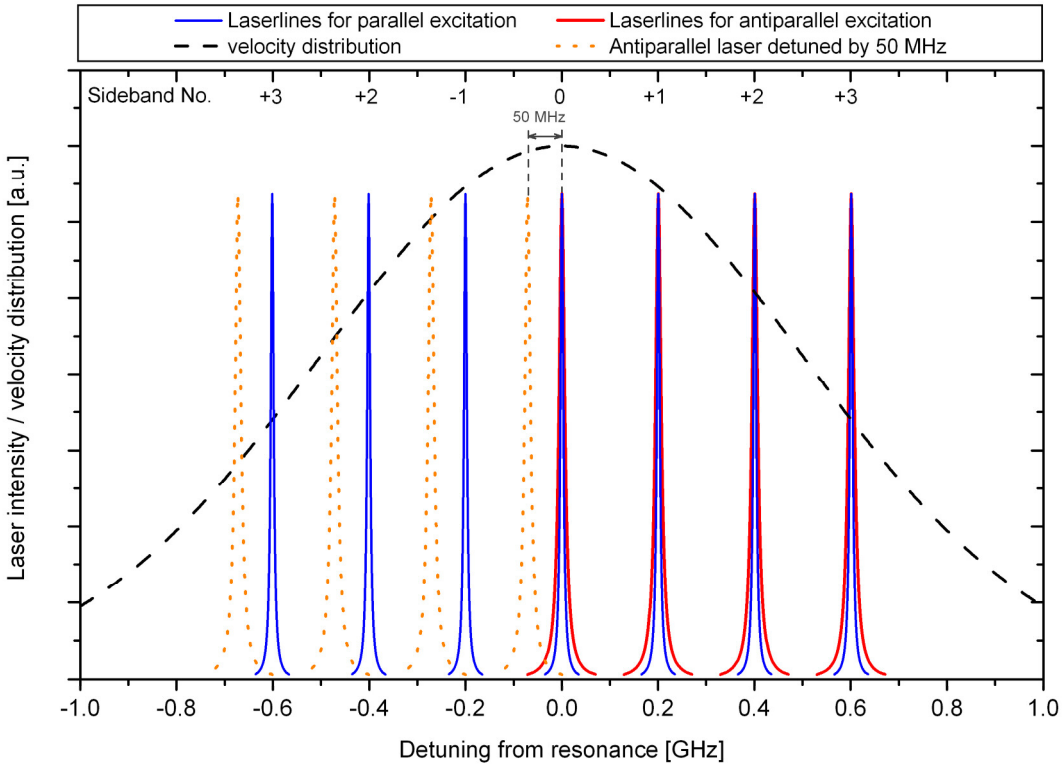

Figure 8.1: Comb-structured laser light for the ion excitation. The dashed black plot indicates the velocity distribution of the ion beam ($\Delta\nu = 1$ GHz). The solid and the dotted plots show laser lines in the ions' rest frame ($\Delta\nu_{\text{laser}} = 10$ MHz). On the positive axis both lasers (red and blue lines) are in resonance with the same ions. On the negative axis the laser for antiparallel excitation is detuned by 50 MHz. The sideband spacing for the antiparallel laser is 141 MHz and 285 MHz for the parallel laser in the laboratory frame. In the rest frame of the ions these result in a spacing of 200 MHz.

APPENDIX

A TESTS FOR SIDEREAL IMPACT ON TIME DILATION

Time dilation tests can be distinguished in experiments looking for sidereal deviations from special relativity and in experiments that are sensitive to non-sidereal deviations. Experiments looking for non-sidereal effects are described in chapter 3. Here, an overview on experiments is given that are sensitive on the sidereal term. A further measurement which was performed in such a way being sensitive for both the sidereal and non-sidereal term, is the TPA experiment. The principle of this experiment is already described in chapter 3.4.

A.1 MÖSSBAUER ROTOR EXPERIMENTS

For testing time dilation with Mössbauer rotor experiments gamma ray sources and resonant absorbers are used. Due to the resonant and recoil-free emission and absorption of gamma rays by bound atoms in a solid form a precise measurement of hypothetical frequency shifts (because of sidereal changes) is possible. Emitter and absorber are either mounted to opposite tips of a fast rotor (compare [Champeney63] and Figure A.1), the emitter is placed on the rim of the rotating disk and the absorber is placed at the centre [Turner64] or viz versa [Champeney65]. In all arrangements a detector is used to quantify the transmission of the gamma rays through the absorber as a function of the laboratory/earth orientation. For special relativity the absorber frequency ν_{ab} is equal to the emission frequency ν_{em} (if the absorber and the emitter have the same composition). In the formalism of the MS test theory for double-tip arrangement[54] one obtains

$$\nu_{ab} = \nu_{em} \cdot \left(1 + 4 \cdot \alpha \cdot \vec{\beta} \cdot \vec{w}\right)$$

where $\vec{\beta}$ is the velocity of the source with respect to the laboratory frame and $\vec{w}$ the velocity of the laboratory relative to the hypothetical preferred system. Assuming the

[54] For the arrangement at tip and centre the factor 4 is by replaced by 2.

cosmic microwave background (CMB) to be the preferred frame ($\vec{w}$ = 350 km/s) an upper limit for α is given by [Champeney63] to $|\alpha| < 1\times10^{-5}$.

In 1970, a Mössbauer rotor experiment with a hundredfold improvement of α is claimed by [Isaak70]. However, no data or details of the experiment were ever published.

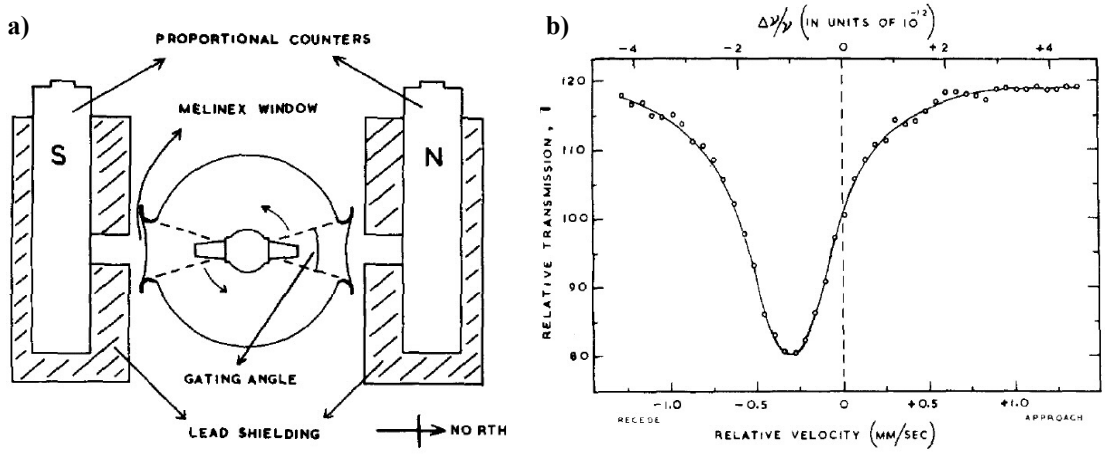

Figure A.1: a) Top view on the setup of the Mössbauer rotor experiment of Champeney et al. where the absorber and the emitter are placed on opposite tips on the rim of a disk. Two xenon proportional counters are placed with their windows respectively north and south of the rotor, so that the apparatus is sensitive to a component of aether drift in an east-west direction. b) Spectrum for a Co^{57} in copper source versus stainless steel absorber enriched in Fe^{57}. Due to the use of different materials for the emitter and the absorber the spectrum is shifted from zero. The transmission of the 14.4 keV gamma rays is shown as a function of the relative velocity between source and absorber [Champeney63].

A.2 GRAVITY PROBE A MISSION

The Gravity Probe A mission was intended as a space-based experiment to test Einstein's theory of general relativity, more precisely the gravitational redshift [Vessot79]. But it turned out to be sensitive to special relativity as well. In the experiment a Scout-D rocket carrying a hydrogen maser clock was launched to an altitude of 10 000 km (Figure A.2). A second identical hydrogen maser was located on Earth (Merrit Island, Florida). This was used to compare the frequency of the earth-based maser with the one in space. Therefore a round-trip signal was sent from the ground maser to the rocket and back, while a one-way signal was sent by the maser on the rocket to Earth. As discussed in [Will92], this allows the separation of first-order Doppler effect on one hand and gravitational and second-order Doppler-shift on the other. A limit of $|\alpha| < 1\times10^{-6}$ can be derived due to the absence of second-order Doppler-shift variations correlated with an angle between the rocket's velocity vector and the moving direction of the Earth with respect to the CMB.

a)

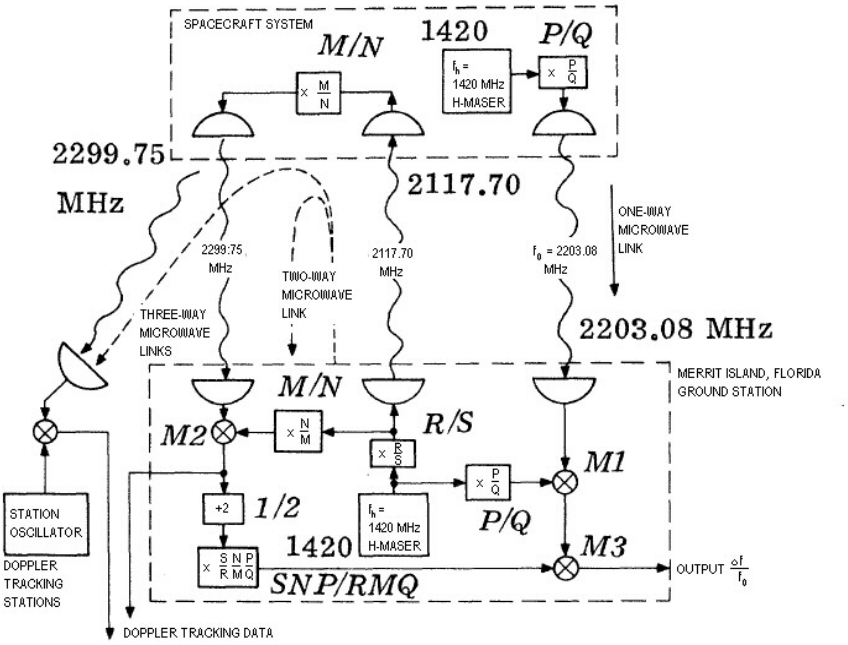

b)

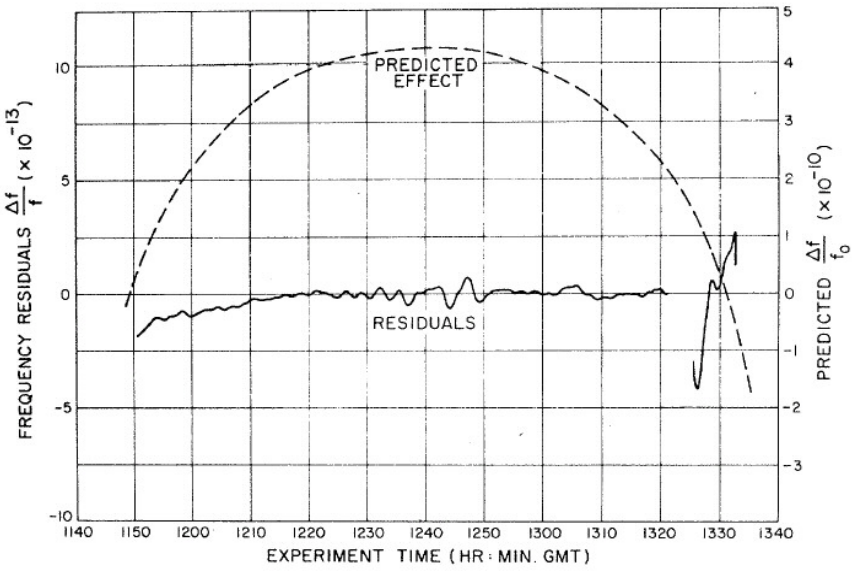

Figure A.2: a) Measuring scheme provided one-way and two-way Doppler information by simultaneous transmission of three microwave signals. For detailed description see [Vessot79]. b) Measured frequency residuals $\Delta f/f$ (after corrections and smoothing) and predicted frequency shifts $\Delta f/f_0$ (due to relativistic gravity and special relativity) during the Gravity Probe A mission [Vessot79].

A.3 HYDROGEN MASER COMPARISON

This experiment was performed at the NASA Deep Space Network by Krisher at al. in 1988 [Krisher90]. The phases of two hydrogen maser oscillators, separated by a base line of 21 km, were compared by propagating a laser carrier signal along a fibre optic link connecting them (Figure A.3). According to [Will92], deviations in the phase ϕ of both masers can be described in the MS formalism by

$$\frac{\Delta\phi}{\phi} = 2 \cdot \alpha \cdot \vec{w}$$

where higher-order contributions of $\vec{w}$ (350 km/s) are not considered. An upper limit for α was found to $|\alpha| < 1.8 \times 10^{-4}$.

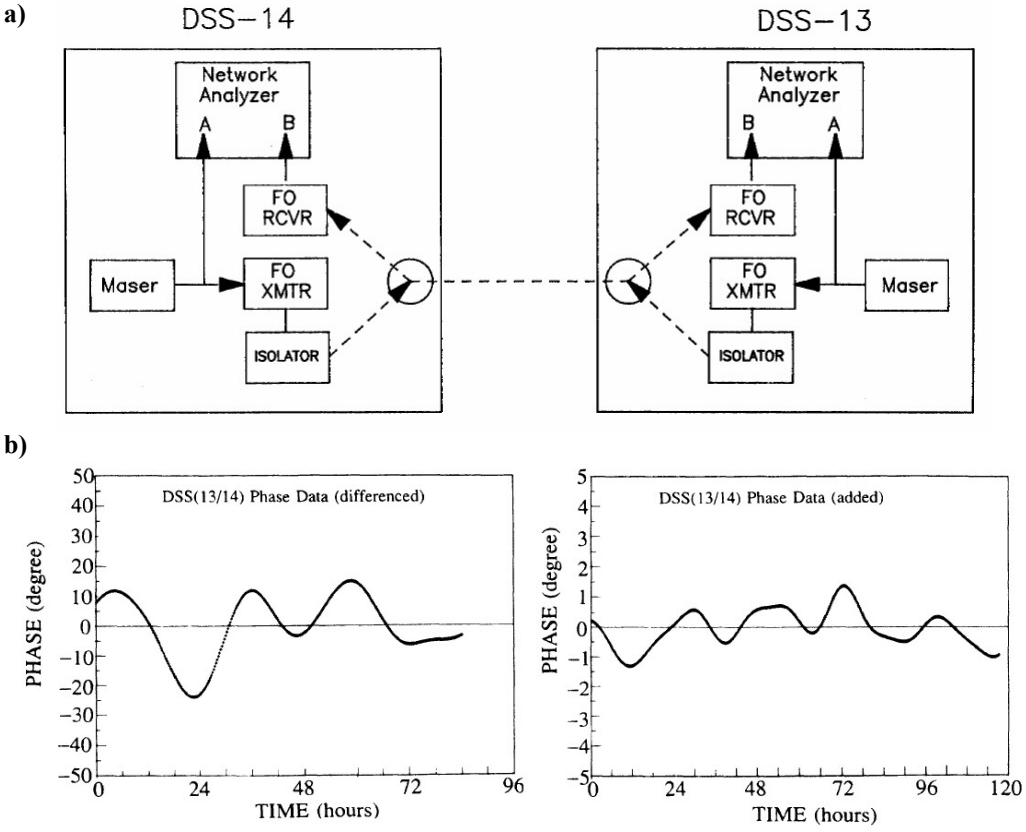

Figure A.3: a) Schematic of the instrumentation that was used to perform the phase measurements (DSS: Deep Space Station). The 100 MHz output frequency of the masers was split into two signals. One signal was fed directly into one channel of a Network Analyser. The other signal was fed into a fibre optics laser transmitter (FO XMTR), which used the signal to modulate the optical carrier along the fibre. This modulation was detected at the far end of the fibre with the fibre optics receiver (FO RCVR), the output of which was fed into the second channel of the network analyser at that end. The network analysers measured the relative signal phase between the two channels. b) Differenced and added phase records after low-pass filtering [Krisher90].

A.4 GPS SATELLITE ANALYSIS

In [Wolf97], a test of special relativity was performed by analysing the data of clock comparisons between hydrogen maser clocks on the ground and caesium and rubidium clocks on board of global positioning system (GPS) satellites (Figure A.4). The clocks were compared via carrier phase measurements of the GPS signal using geodetic receivers at eight stations of the International GPS Service for Geodynamics spread world wide. The frequency stability of the clock's on-orbit was stated of the order 10^{-13} for integration times of one day. Other uncertainties (e.g. satellite ephemerides or estimations on tropospheric delay) were considerably smaller. They found an upper limit for the isotropy of the speed of light of $\partial c/c = 2 \times 10^{-9}$ which is transferred in the MS test theory formalism[55] by $\partial c/c = (1 + 2 \cdot \alpha) \cdot \upsilon/c$ where υ is the velocity of the Earth with respect to the CMB. An upper bound for first-order deviations α can be given to $|\alpha| < 1 \times 10^{-6}$.

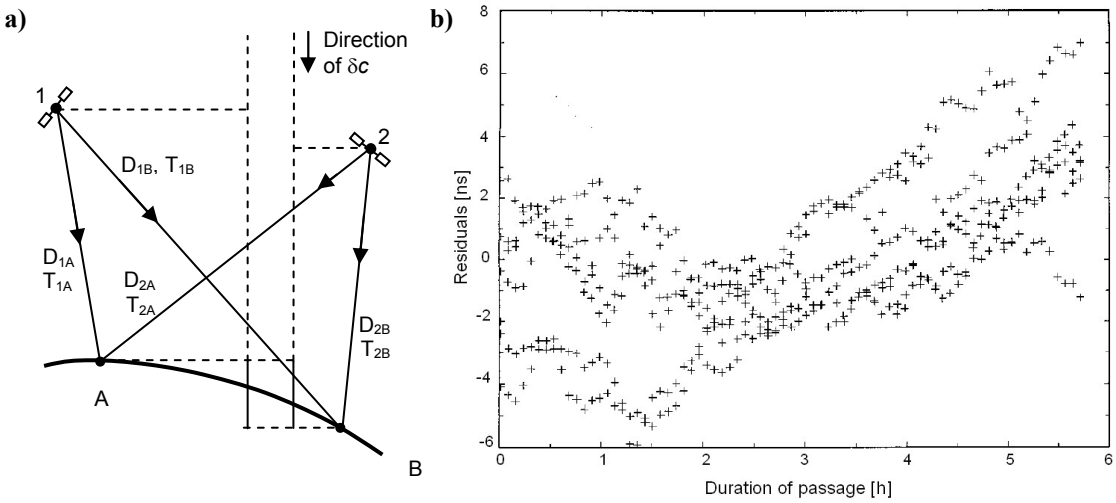

Figure A.4: a) Experimental procedure of the GPS experiment. The emission time of a signal as measured by the on-board clock τ_e (at satellite 1 or 2) and its reception time as measured by the ground-clock τ_r (at A and B) are recorded. The difference $T_{ij} = \tau_r - \tau_e$ represents the transmission time of the signal plus some initial phase difference. Defining D as the distance along a straight line from the satellite (at the moment of emission) to the ground station (at the moment of reception) in geocentric, non-rotating coordinate system, one can write $T - D/c = \Delta$, where Δ is a constant characterising the initial phase difference of the two clocks. Special relativity requires that Δ should remain constant (after correction of for the relative rate of the two clocks due to the gravitational redshift, second-order Doppler-shift and the intrinsic frequency difference of the clocks). For reasons explained in [Wolf97] the double difference for a pair of stations and satellites has been considered. b) Residuals of $(T - D/c)$ after filtering and adjustment of an offset per passage. The graph shows six passages of a GPS satellite vehicle over Brussels shifted onto the same day.

[55] Here is assumed that in special relativity $\alpha = 1/2$.

B ECR SOURCE TEST

The structure of the GSI facility does not allow generating metastable $^7Li^+$ ions in a similar process as in the experiments performed at the test storage ring at the Max Planck-Institute für Kernphysik in Heidelberg. There one starts with negatively charged lithium ions that are produced by a metal ionised sputtering source (MISS) close to ground potential of a tandem van de Graaf accelerator. These $^7Li^-$ ions are than accelerated towards the positively charged high-voltage terminal of the tandem, where they are guided through a thin nitrogen gas target to strip off electrons by collisions. The positively charged lithium ions are then further accelerated by the high-voltage to full kinetic energy and separated from other charge states by a bending magnet. During the electron stripping, 10 % of the $^7Li^+$ ions remain in the metastable ground state.

At GSI, the acceleration is accomplished by rf accelerators which do not involve electron stripping processes. Thus the production method for $^7Li^+$ in the metastable 2^3S_1 ground state is done by excitation with $^7Li^+$ from the 1^1S_0 state in a 14.5 GHz ECR source. In this source the evaporated raw material is ionised by the electrons in the plasma and extracted by a voltage of 15 keV. To optimise the yield of lithium ions in the metastable ground state, tests with different source materials were realised. Due to modifications of the former ECR test stand to work at higher rf fields, no similar offline tests source is available at the GSI. The operation grade of the online ECR source is close to 100 % so tests or improvements can only be made during regular beam times. Further an identification of the metastable state is only possible by laser spectroscopic means in the ESR. No analytical tool of the GSI can distinguish between the metastable 2^3S_1 and the stable 1^1S_0 ground state and none can be introduced before the ESR.

However, these tests could be realised at the University of Giessen in the group of Alfred Müller. There a comparable ECR ion source is attached to a test stand where metastable $^7Li^+$ ions can be quantified (see Figure B.1). It is not possible to deduce absolute parameters for the online ECR source at the GSI by these experiments because both sources are only roughly comparable but in particular not similar (e.g. different radio frequency and ion beam current ($I_{\text{Giessen}} \sim$ nA $\leftrightarrow$ $I_{\text{GSI}} \sim$ 100 μA), respectively). However a relative comparison between different materials is possible.

A detailed description of the setup and the experiments is given in [Titte06]. Here only a few properties, relevant for the ESR experiment, are sketched. At the test stand the source material is evaporated in an oven and exposed to 10 GHz radio frequency for ionisation. The ions are accelerated with a voltage of 20 kV, separated after charge-to-mass ratio by an analysing magnet, and overlapped with an electron beam. The energy of the beam can be tuned in a range from 0 eV to 1000 eV which allows a further

ionisation of the particles. The doubly charged lithium ions are guided through a second magnet to be separated from the remaining beam. The intensity of the doubly charged ions is detected as a function of the electron energy. The energetic difference of $^7Li^+$ in the 1^1S_0 ground state to the metastable 2^3S_1 state is 59 eV, which can be resolved by this setup. So a differentiation between both lithium states can be made. A further separation of the singlet 2^1S_1 from the triplet 2^3S_1 (ΔE = 1.9 eV) is not possible.

Three different lithium materials were tested: pure metallic lithium[56], lithium fluoride (LiF) and lithium carbonate (Li_2CO_3). It turned out that a yield of 7-9 % of lithium ions in the metastable ground state can be obtained with pure metallic lithium as source material. Li_2CO_3 leads to a fraction of 2-3 % and from lithium fluoride no significant amount of metastable ions has been detected (the detection limit was at a level of 1%). So Li_2CO_3 seems to be the right choice, but the handling of this material in the oven appears to be very complicated. A large amount of gas that consists of various carbon-compounds and water due to hygroscopic properties of the carbide, respectively, emerges during the evaporation.

In ESR beam times Li_2CO_3 and LiF were tested with the result that the total amount of metastable $^7Li^+$ ions stored in the ESR is comparable for both source materials. However, a significant difference in the lifetime of the source was observed. While LiF has a smooth lifetime of 4 days on average, for Li_2CO_3 only hours could be measured. Furthermore a smooth continuous operation of the oven was not possible. Lumps of the source material were evaporated which resulted in a hardly controllable environment in the ECR source. So, LiF had to be chosen due to the good working experiences at the GSI and the possibility of a yield of metastable close to 1%.

[56] Due to safety regulations concerning the cancer therapy program at the GSI, the introduction of metallic lithium is not allowed. This material was tested for comparison.

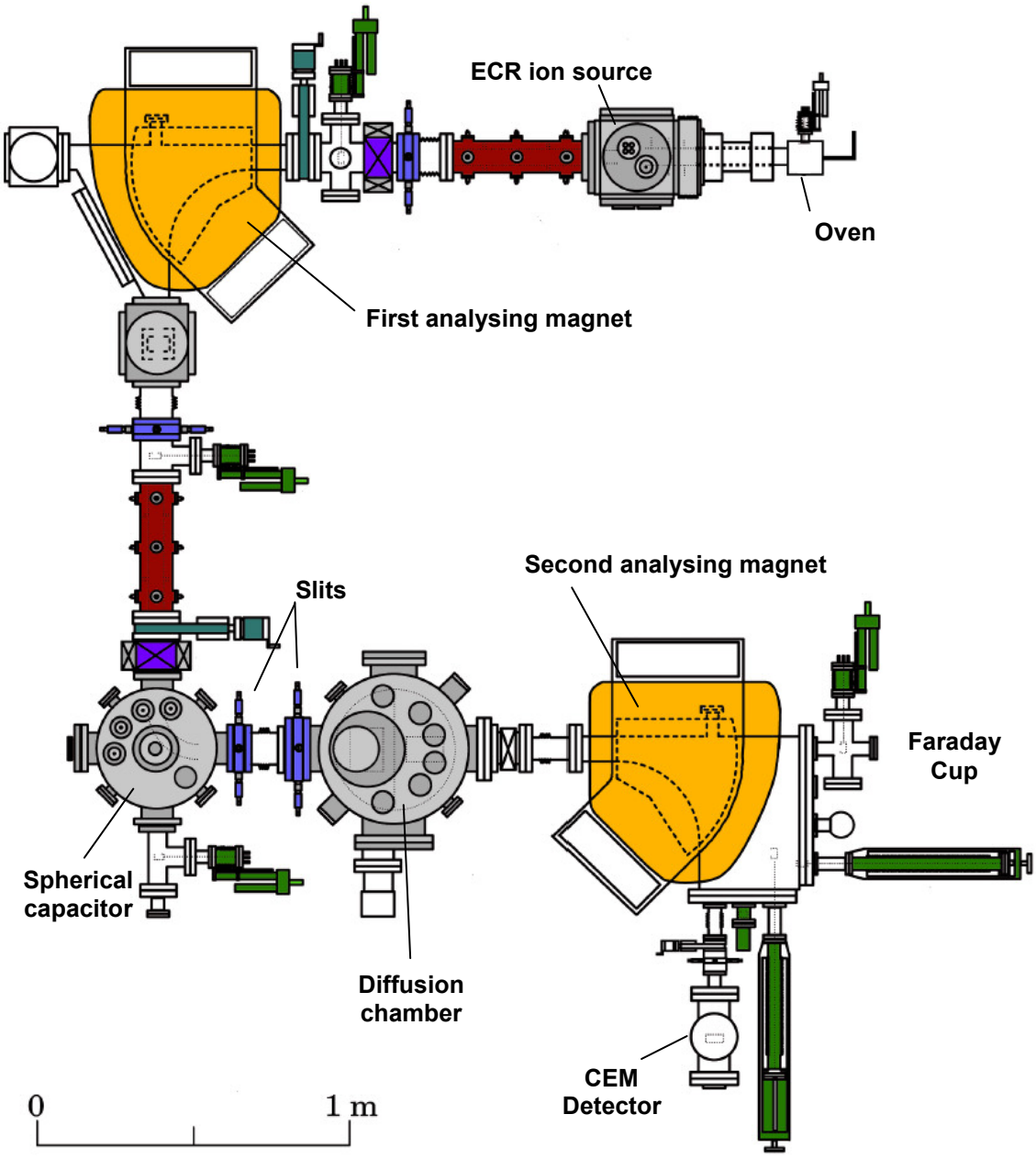

Figure B.1: Experimental setup to measure the production rate of lithium ions in the metastabile ground state from an ECR ion source. The solid source material is evaporated in the oven and ionised in the ECR plasma chamber. The ion cloud is extracted towards the first analysing magnet where it is mass-to-charge separated by a magnet field to the desired ratio of 1:7. These ions are guided towards a spherical capacitor which focuses and bends the ion beam into the diffusion chamber. In front of this chamber two slits can be used to collimate the beam. In the diffusion chamber the ions cross an electron beam which is tuned in energy to remove a further electron from those lithium ions that are in the metastable ground state. The doubly charged lithium is separated from the primary beam by a second analysing magnet and guided to a CEM[57] detector. The singly charged lithium beam is led towards a faraday cup [Titte06].

[57] CEM: Channel electron multiplier.

C ION BEAM BUNCHING

From the Λ-spectroscopy it turned out that it is essential to apply the technique of beam bunching to the ions, which are stored in the ESR. Without beam bunching the voltage fluctuations of the electron cooler induce velocity fluctuations in the ion beam which perturb the first-order Doppler-free measurements.

C.1 OVERVIEW

The electron cooled ion beam at the ESR suffers from a remaining jitter of the longitudinal ion velocity. This jitter emerges due to instabilities in the electron cooler energy as well as of the magnetic fields of the ESR magnets and cause small transverse beam displacements that are translated into velocity fluctuations. These lead to shifts in the order of a few widths of the velocity distribution. To damp these changes the ion beam is bunched. To this end, a force produced by an electric field with radio frequency is applied to the ions by using two metal plates[58] (Figure C.1). The frequency of this field is a multiple of the revolution frequency of the ions in the ESR and because the plates are on the same potential, no transversal force acts on the ion beam.

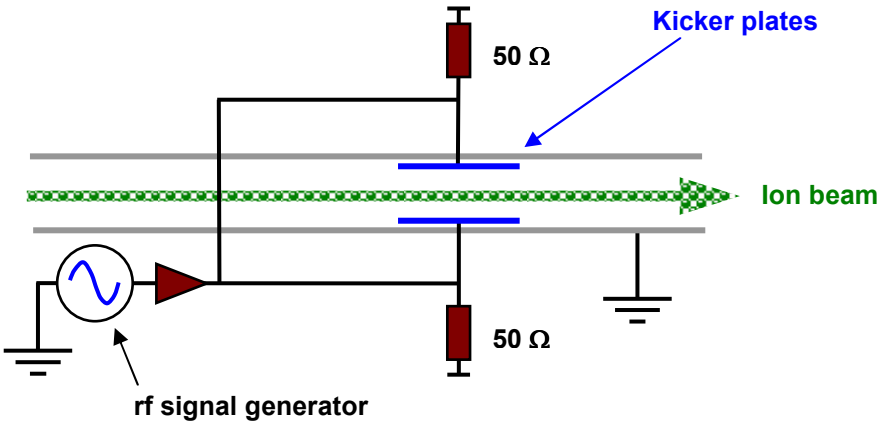

Figure C.1: Setup of the buncher for energy stabilisation of the ion beam.

Ions that enter the oscillating electric field at a time t see the voltage $U(t)$. But when they leave, they see $U(t+\Delta t)$ where Δt is the time the ions needed to fly through the plates and L_{kp} is the length of the plates

[58] In laser cooling experiments these plates are used to apply the counterforce to the laser force on the ion beam [Bussmann07].

$$\Delta t = \frac{L_{\mathrm{kp}}}{v_{\mathrm{ion}}}.$$

Thus, the ions experience a net potential difference of

$$\Delta U(t) = U(t) - U(t + \Delta t).$$

Since the passing through time Δt is much smaller than the applied rf period, one can approximate

$$\Delta U(t) \approx \frac{\partial U(t)}{\partial t} \cdot \Delta t = \dot{U}(t) \cdot \Delta t\,.$$

The force averaged over one ring circumference L_{ESR} is

$$F(t) = \frac{q}{L_{\mathrm{ESR}}} \cdot \dot{U}(t) \cdot \Delta t$$

where q stands for the charge state of the ion beam. The oscillation in the voltage can be described by a cosine function with the amplitude U_0 and the radio frequency ν_{Bunch} to

$$U(t) = U_0 \cdot \cos(2 \cdot \pi \cdot \nu_{\mathrm{Bunch}} \cdot t).$$

This leads to

$$\begin{aligned} \dot{U}(t) &= -2 \cdot \pi \cdot \nu_{\mathrm{Bunch}} \cdot U_0 \cdot \sin(2 \cdot \pi \cdot \nu_{\mathrm{Bunch}} \cdot t) \\ &= -2 \cdot \pi \cdot \nu_{\mathrm{Bunch}} \cdot U_0 \cdot \sin(\varphi) \end{aligned}$$

with the phase φ. Considering that the ion beam has a velocity distribution $\Delta\upsilon$ around υ_{ion}, this can be described by a phase deviation $\Delta\varphi$ with [Eisenbarth98]

$$\Delta\varphi = 2 \cdot \pi \cdot h \cdot \gamma^2 \cdot \eta \cdot \frac{\Delta\upsilon}{\upsilon_{\mathrm{ion}}}.$$

Here, h is the harmonic of ν_{Bunch} with respect to the revolution frequency of the ions in the ring, γ is the relativistic dilation and η the slip-factor. Setting the reference phase to zero ($\varphi = \Delta\varphi$), the force can be given as a function of the velocity distribution

$$F(\Delta v) = -\frac{2 \cdot \pi \cdot U_0 \cdot q \cdot L_{\mathrm{P}} \cdot \nu_{\mathrm{Bunch}}}{L_{\mathrm{ESR}} \cdot \upsilon_{\mathrm{ion}}} \cdot \sin\left(2 \cdot \pi \cdot h \cdot \gamma^2 \cdot \eta \cdot \frac{\Delta\upsilon}{\upsilon_{\mathrm{ion}}}\right).$$

Therefore, the spatial structure of the bunched ion beam reflects the harmonic of the radio frequency.

C.2 COMPARISON OF BUNCHED AND NON-BUNCHED ION BEAMS

The use of a bunched ion beam minimises velocity changing effects which are due to fluctuations in the voltage of the electron cooler. This is done by affecting the ion beam with a radio frequency, which corresponds to the 10^{th} harmonic of the revolution frequency of the ions. The effect of beam bunching can be also visualised in the Schottky spectrum of the ions (see Figure C.2 and Figure C.3). Compared to non-bunched signals the distribution is narrower and directly after the injection side-fringes emerge where the ions are accumulated. Without electron cooling the envelope of the momentum spread matches a Gaussian distribution. After 15 s of electron cooling the signal is in a Lorentzian shape.

Without beam bunching the ion classes are strongly mixed (within their Doppler-broadened distribution) which leads to multiple random signals in a frequency range of 1.6 GHz around the resonance (see Figure C.4a). In principle each peak corresponds to a first-order Doppler-free spectrum. Nevertheless, these signals can not be related to a certain velocity and so, not be used for precision measurement. Covering the ions in beam bunches, this velocity mixing is suppressed to fluctuations in the range of 100 MHz of the laser frequency that corresponds to the of the Λ-type spectroscopy signal (see Figure C.4b and chapter 7.7.2).

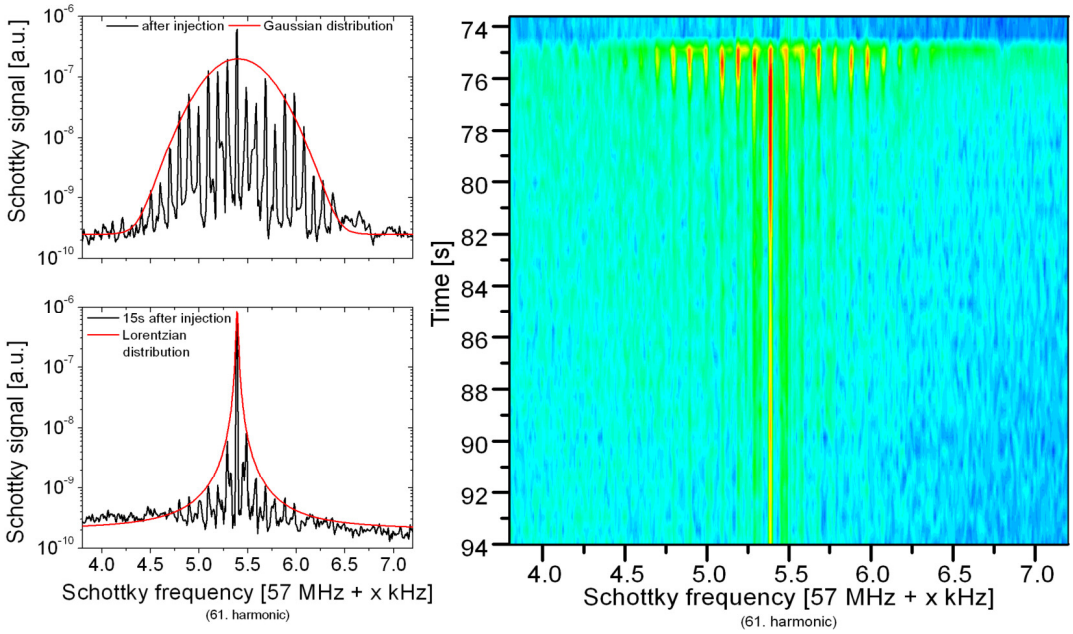

Figure C.2: Comparison of a bunched "hot" ion beam, measured directly after injection from the SIS (upper left diagram). This beam shows a Gaussian distribution with a modulated substructure. After 15 s of electron cooling the beam distribution becomes Lorentzian shaped. In the right diagram the time evolution of a bunched ion beam is given. Only the fraction of lithium ions is shown here.

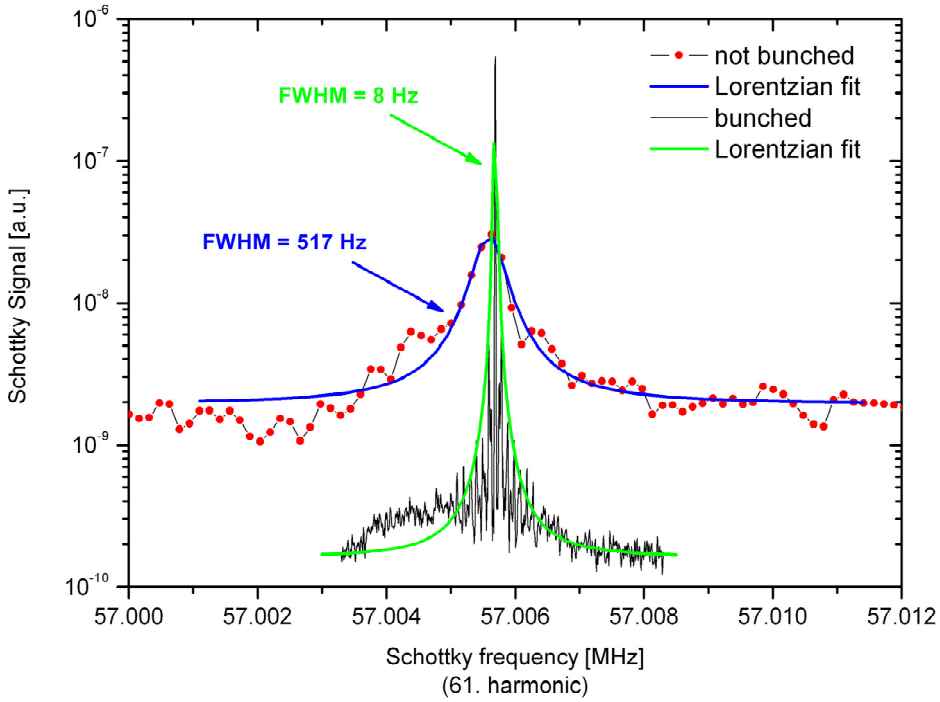

Figure C.3: Schottky signal of a bunched (black line) and a non-bunched (red dots) lithium ion beam. Both spectra are taken after 15 s of electron cooling and can be fitted by a Lorentzian peak.

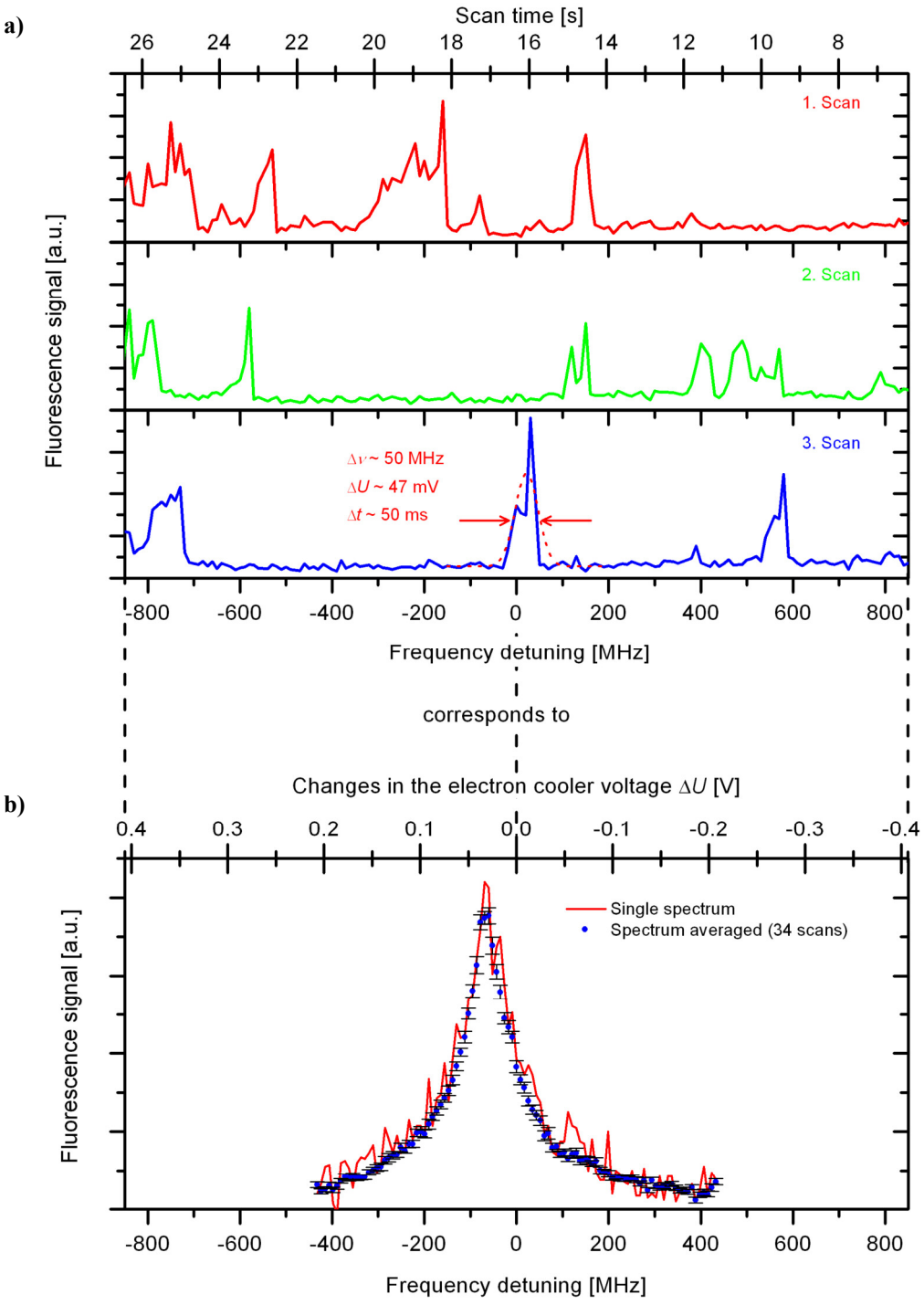

Figure C.4: a) Fluorescence signals from Λ-type spectroscopy without ion beam bunching. Three scans are shown where signals with sub-Doppler width appear randomly. The scans are started after 5 s of electron cooling. b) First-order Doppler-free signal from Λ-type spectroscopy with ion beam bunching. The red curve indicates a single scan (span = ± 400 MHz). The blue dotes are a spectrum averaged over 34 scans.

D TRANSMISSION SPECTRA OF THE USED FILTER

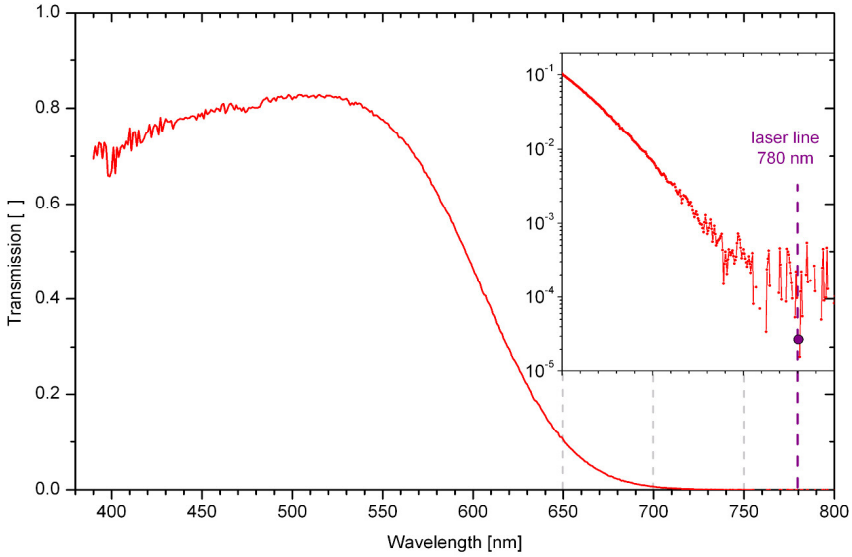

Figure D.1: Transmission spectrum of the band-gap filter BG39. The spectrum was measured with an optical spectrum analyser (*ANDO*, AQ 6315-A) and a white light source (*ANDO*, AQ 40038) with an uncertainty of 1%. Additionally, the suppression at 780 nm was determined to be better than 3×10^{-5} by using the diode laser and a power meter (*Coherent*, OP-2-VIS).

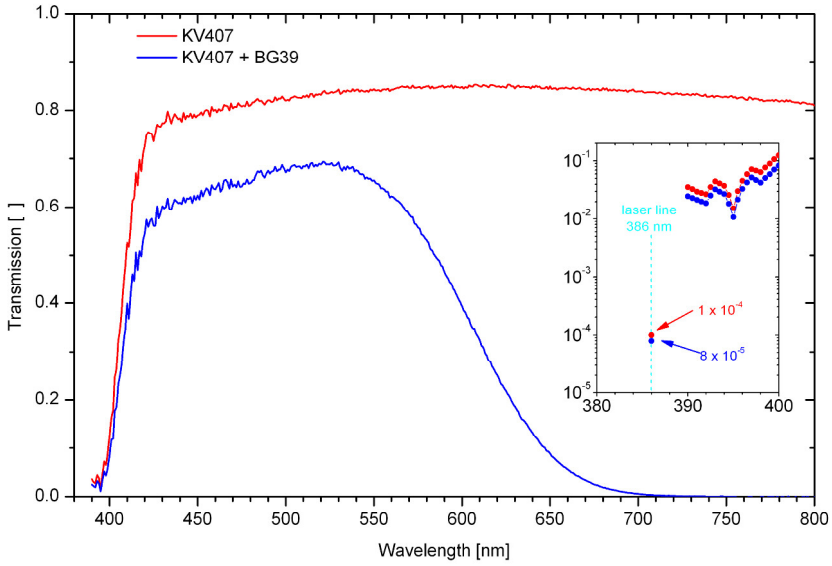

Figure D.2: Transmission spectra of the bare laminated plastic filter KV407 and in combination with BG39. The spectrum was measured with an optical spectrum analyser (*ANDO*, AQ 6315-A) and a white light source (*ANDO*, AQ 40038) with an uncertainty of 1%. Additionally, the suppression at 386 nm was determined to be better than 10^{-4} by using the SHG and a power meter (*Coherent*, OP-2-UV).

REFERENCES

[Antonini05] Antonini, P., Okhapkin, M., Göklü, E., Schiller, S.: "Test of constancy of speed of light with rotating cryogenic optical resonators". *Physical Review A* **71** (2005), S. 050101/1-4.

[Audi03] Audi, G., Wapstra, A. H., Thibault, C.: "The AME2003 atomic mass evaluation". *Nuclear Physics A* **279** (2003), 337-676.

[Bailey77] Bailey, J., Borer, K., Combley, F., Drumm, H., Krienen, F., Lange, F., Picasso, E., von Rüden, W., Farley, F. J. M., Field, J. H., Flegel, W., Hattersley, P.: "Measurements of relativistic time dilation for positive and negative muons in a circular orbit". *Nature* **268** (1977), 301-305.

[Bailey79] Bailey, J., Borer, K., Combley, F., Drumm, H., Eck, C., Farley, F. J. M., Field, J. H., Flegel, W., Hattersley, P. M., Krienen, F., Lange, F., Lebée, G., McMillan, E., Petrucci, G., Picasso, E., Rúnolfsson, O., von Rüden, W., Williams, R. W., Wojcicki, S.: "Final report on the CERN moun storage ring including the anomalous magnetic moment and the electric dipole moment of the moun, and a direct test of relativistic time dilation". *Nuclear Physics B* **150** (1979), 1-75.

[Banerjee03] Banerjee, A., Das, D., Natarajan, V.: "Precise frequency measurement of atomic transitions by use of a Rb-stabilized resonator". *Optics Letters* **28** (2003), 1579-1581.

[Barwood91] Barwood, G. P., Gill, P. and Rowley, W. R. C.: "Frequency Measurements on Optically Narrowed Rb-Stabilised Laser Diodes at 780 nm and 795 nm". *Applied Physics B* **53** (1991), 142-147.

[Bize99] Bize, S., Sortais, Y., Santos, M. S., Mandache, C., Clairon, A. and Salomon, C.: "High-accuracy measurement of the ^{87}Rb ground-state hyperfine splitting in an atomic fountain". *Europhysics Letters* **45** (1999), 558-564.

[Bluhm06] Bluhm, R.: "Overview of the Standard Model Extension: Implications and Phenomenology of Lorentz Violation". *Lecture Notes in Physics* **702** (2006), 191-226.

[Bluhm98/99] Bluhm, R., Kostelecký, V. A., Russel, N.: "CPT and Lorentz tests in Penning traps". *Physical Review D* **57** (1998), 3932-3943.
and
Bluhm, R., Kostelecký, V. A., Russel, N.: "CPT and Lorentz Tests in Hydrogen and Antihydrogen". *Physical Review Letters* **82** (1999), 2254-2257.

[Bodermann00] Bodermann, B., Klug, M. Winkelhoff, U., Knöckel, H. and Tiemann, E.: "Precise frequency measurements of I_2 lines in the near infrared by Rb reference lines". *The European Physics Journal D* **11** (2000), 213-225.

[Bordé79] Bordé, C. J., Camy, G. and Decomps, B.: "Measurement of recoil shift of saturation resonances of $^{127}I_2$ at 5145 Å: A test of accuracy for high-resolution saturation spectroscopy". *Physical Review A* **20** (1979), 254-268.

[Boussard85] Boussard, D.: *Advanced Accelerator Physics*. (1985), CERN Accelerator School.

[Boyd68] Boyd, G. D., Kleinman, D. A.: "Parametric interaction of focused Gaussian light beams". *Journal on Applied Physics*, **39** (1968), 3597-3639.

[Budker76] Budker, G. I.: "An effective method of damping particle oscillations in proton and antiproton storage rings". *Atomnaya Energiya* **22** (1976), 346-448 (translated title).
and
Budker, G. I., Dikansky, N., Kudelainen, V. I., Meshkov, I.,Parchomchuk, V. V., Pestrikov, D., Skrinsky, A. N., and Sukhina, B. N.: "Experimental studies of electron cooling". *Particle Accelerators* **7** (1976).

[Bussmann07] Bussmann, M., Schramm, U., Habs, D., Steck, M., Kühl, T., Beckert, K., Beller, P., Franzke, B., Nörtershäuser, W., Geppert, C., Novotny, C., Kluge, H.-J., Nolden, F., Stöhlker, T., Kozhuharov, C., Reinhardt, S., Saathoff, G., Karpuk, S.: "The Dynamics of Bunched Laser-Cooled Ion Beams at Relativistic Energies". *Journal of Physics: Conference Series* **88** (2007), 012043/1-6.

[Carroll90] Carroll, S. M., Field, G. B., Jackiw, R.: "Limits on a Lorentz- and parity-violating modification of electrodynamics". *Physical Review D* **41** (1990), 1231-1240.

[Champeney63] Champeney, D. C., Isaak, G. R., Khan, A. M.: "An 'aether drift' experiment based on the Mössbauer effect". *Physics Letters* **7** (1963), 241-243.

[Champeney63] Champeney, D. C., Isaac, G. R., Kahn, A. M.: "An 'aether drift' experiment based on the Mössbauer effect". *Physics Letters* **7** (1963), 241-243.

[Champeney65] Champeney, D. C., Isaak, G. R., Khan, A. M.: "A time dilation experiment based on the Mössbauer effect". *Proceedings of the Physical Society* **85** (1965), 583-593.

[Clarke03] Clarke, J. J., Wijngaarden, W. A.: "Hyperfine and fine-structure measurements of $^{6,7}Li^{+}$ 1s2s ^{3}S and 1s2p ^{3}P states". *Physical Review A* **67** (2003), 012506/1-5.

[Colladay97^{s}] Colladay, D., Kostelecký, V. A.: "CPT violation and the standard model". *Physical Review D* **55** (1997), 6760-6774.
and
Colladay, D., Kostelecký, V. A.: "Lorentz-violating extension of the standard model". *Physical Review D* **58** (1998), 116002/1-23.
and
Kostelecký, V. A., Mewes, M.: "Signals for Lorentz Violation in Electrodynamics". *Physical Review D* **66** (2002), 056005/1-24.

[CRC74-93] Lide D.R. (Ed.): *CRC Handbook of Chemistry and Physics, 74th Edition* (1993), CRC Press, Boca Raton Florida, ISBN 0849304741 / 9780849304743.

[Demtröder00] Demtröder, W.: *Laserspektroskopie – Grundlagen und Techniken* (2000), 4. Aufl. Springer-Verlag, Berlin Heidelberg NewYork, ISBN 3-540-64219-6.

[Edwards99] Edwards, C. S., Barwood, G. P., Gill, P. and Rowley, W. R.: "A 633 nm iodine-stabilized diode-laser frequency standard". *Metrologia* **36** (1999), 41-45.

[Einstein05] Einstein, A.: "Zur Elektrodynamik bewegter Körper". *Annalen der Physik* **17** (1905), 891-921.

[Einstein07] Einstein, A.: "Über die Möglichkeit einer neuen Prüfung des Relativitätsprinzips". *Annalen der Physik* **328** (1907), 197-198.

[Einstein15&16] Einstein, A.: "Die Feldgleichungen der allgemeinen Relativitätstheorie". *Sitzungsberichte der Preussischen Akademie der Wissenschaften zu Berlin* (1915), 844-847.
and
Einstein, A.: "Die Grundlage der allgemeinen Relativitätstheorie". *Annalen der Physik* **49** (1916), 770-822.

[Eisenbarth01] Eisenbarth, U.: Laser Cooling of fast stored ion beams to extreme phase-space densities (2001), Dissertation, University Heidelberg.

[Eisenbarth98] Eisenbarth, U.: Kühlung hochenergetischer Ionenstrahlen am Speicherring TSR: neuartige Bunchformen und Raumladungseffekte. (1998), Diploma theses, University Heidelberg.

[Frantzke87] Franzke, B.: "The heavy ion storage and cooler ring project ESR at GSI". *Nuclear Instruments and Methods in Physics Research B* **24-25** (1987), 18-25.

[Gabrysch94] Gabrysch, M.: Chirpkomensation durch elektrooptische Phasenmodulation bei gepulsten Farbstofflaserverstärkern. (1994), Diploma theses, University Heidelberg.

[Geissel92] Geissel, H., Armbruster, P., Behr, K. H. and Brünle A: "The GSI projectile fragment separator (FRS): a versatile magnetic system for relativistic heavy ions". *Nuclear Instruments and Methods in Physics Research B* **70** (1992), 286-297.

[Gemmel06] Gemmel, C.: Voruntersuchungen zu Lorentzinvarianz-Tests mit Hilfe eines ^{3}He-Magnetometers. (2006), Diploma theses, University Mainz.

[Gill87] Gill, P. and Thompson, R.C.: "The Preparation and Analysis of Iodine Cells". *Metrologia* **23** (1986/87) 161-166.

[Gillespie36] Gillespie, L. J. and Fraser, L. H. D.: "The Normal Vapor Pressure of Crystalline Iodine". *Journal of the American Chemical Society* **58** (1936), 2260-2263. Original equation in atmosphere and Kelvin:
$$log(p) = -\frac{3512.830}{F} - 2.013 \cdot log(T) + 13.37400$$

[Goncharov91&96] Goncharov, A. N., Gateva-Kosteva, S. V., Skvortsov, M. N. and Chebotayev, V. P.: "Direct Obersvation of the Anomalous Zeeman Effect at the X $\rightarrow$ B Transition of Melecular Iodine by the Method of Nonlinear Laser Spectroscopy". *Applied Physics B* **52** (1991), 311-314.
and
Goncharov, A. N., Nevsky, A. Yu., Skvortsov, M. N.: "Second-order Zeeman effect of the X-B transition in molecular iodine". *Applied Physics B* **62** (1996), 427-430.

[Grieser94] Grieser, R., Klein, R., Huber, G., Dickopf, S., Klaft, I., Knobloch, P., Merz, P., Albrecht, F., Grieser, M., Habs, D., Schwalm, D., Kühl, T.: "A test of special relativity with stored lithium ions". *Applied Physcis B* **59** (1994), 127-133.

[GSI08] Official internet presentation of GSI (13.05.2008), http://www.gsi.de/forschung/einfuehrung_e.html.

[Gwinner05] Gwinner, G.: "Experimental Tests of Time Dilation in Special Relativity". *Modern Physics Letters A* **20** (2005), 791-805.

[Haken04] Haken, H., Wolf, H. C.: *Atom- und Quantenphysik* (2004), 8. Aufl., Springer-Verlag, Berlin Heidelberg New York, ISBN 3-540-02621-5.

[Hangst91] Hangst, J., Kristensen, M., Nielsen, J., Poulsen, O., Schiffer, O. and Shi, P.: "Laser Cooling of a fast Stored Ion Beam to 1 mK". *Physical Review Letters* **67** (1991), 1238-1241.

[Hänsch80] Hänsch, T. W. and Couillaud, B.: "Laser frequency stabilization by polarisation spectroscopy of a reflecting reference cavity". *Optics Communication* **35** (1980), 441-444.

[Hasselkamp79] Hasselkamp, D., Mondry, E. and Scharmann, A.: "Direct Observation of the Transversal Doppler-Shift", *Zeitschrift für Physik A* **289** (1979), 151-155.

[Herrmann06] Herrmann, S., Senger, A., Kovalchuk, E., Müller, H. and Peters, A.: "Test of Lorentz Invariance Using a Continuously Rotating Optical Resonator". *Lecture Notes in Physics* **702** (2006), 385-400.

[Hogan07] Hogan, J.: "Behind the hunt for the Higgs boson". *Nature*-News **424** (2007), 239.

[Hohensee07] Hohensee, M., Glenday, A., Li, C.-H., Tobar, M. E. and Wolf, P.: "Erratum: New methods of testing Lorentz violation in electrodynamics". *Physical Review D* **71** (2007), 025004/1.

[Huber88] Huber, G., Schmidt, N., Schröder, S., Wendt, K., Dutta, M., Kühl, T., Marx, D., Orth, H.: "Laser spectroscopy with stored relativistic $^7Li^+$ ions". Proposal for an Experiment at the ESR, GSI-ESR-111 (1988); Henning, W.: *Nuclear Physics News* **1** (1990), 13.

[Hvelplund76] Hvelplund, P.: "Electron capture and loss by ground-state and metastable Li^+ in helium and argon targets". *Journal of Physics B* **9** (1976), 1555-1565.

[IS38] Ives, H. E. and Stilwell, G. R.: "An experimental study of the rate of a moving clock". *Journal of Optical Society of America* **28** (1938), 215-226.

[IS41] Ives, H. E. and Stilwell, G. R.: "An experimental study of the rate of a moving clock. II", *Journal of Optical Society of America* **31** (1941), 369-374.

[Isaak70] Isaak, G. R.: "Application to relativity". *Physics Bulletin* **31** (1970), 255-257.

[Kaivola85] Kaivola, M., Poulsen, O., Riis, E.: "Measurement of the Relativistic Doppler Shift in Neon". *Physical Review Letters* **54** (1985), 255-258.

[Klein91] Klein, R., Grieser, R., Hoog, I., Huber, G., Klaft, I., Merz, P., Kühl, T., Schröder, S., Grieser, M., Habs, D., Petrich, W., Schwalm, D.: "Measurement of the transverse Doppler shift using a stored relativistic $^7Li^+$ ion beam". *Zeitschrift für Physik A* **342** (1992), 455-461.
and
Klein, R.: Präzisionsspektroskopie an gekühlten Li^+ Ionen im Schwerionen-speicherring als experimenteller Test der speziellen Relativitätstheorie (1991), Dissertation, University Mainz.

[Knöckel04] Knöckel, H., Bodermann, B. and Tiemann, E.: "High precision description of the rovibronic structure of the I_2 B-X spectrum". *The European Physics Journal D* **28** (2004), 199-209.

[Kostelecký08] Kostelecký, V. A. and Russel, N.: "Data Tables for Lorentz and CPT Violations". *arXiv* 0801.0287v1 [hep-ph] (2008), 1-12 .

[Kostelecký89^s] Kostelecký, V. A., Stuart S.: "Spontaneous breaking of Lorentz symmetry in string theory". *Physical Review D* **39** (1989), 683-685.
and
Kostelecký, V. A. and Potting, R.: "CPT and Strings". *Nuclear Physics B* **359** (1991), 545-570.

[Kostelecký99] Kostelecký, V. A. and Lane, C. D.: "Constraints on Lorentz violation from clock-comparison experiments". *Physical Review D* **60** (1999), 116010/1-17.

[Kowalski83] Kowalski, J., Neumann, R., Noethe, S., Suhr, H., zu Putlitz, G. and Herman, R.: "Triplet-Singlet Interaction in the $1s2s\,^3S_1$ Hyperfine Splitting of He-Like Li^{+}". *Zeitschrift für Physik A* **313** (1983), 147-150.

[Kramer80] Kramer, G., Ghosh, R. D. N., Hlemcke, J., Spieweck, F.: "Saturation spectroscopy with multiple-frequency excitation". *Applied Physics Letters* **37** (1980), 354-356.

[Kretzschmar92] Kretzschmar, M.: “Doppler spectroscopy on relativistic particle beams in the light of a test theory of special relativity”. *Zeitschrift für Physik A* **342** (1992), 463-469.

[Krisher90] Krisher, T. P., Maleki, L., Lutes, G. F., Primas, L. E., Logan, R. T., Anderson, J. D., Will, C. M.: “Test of the isotropy of the one-way speed of light using hydrogen-maser frequency standards”. *Physical Review D* **42** (1990), 731-734.
and
Krisher, T.P., Maleki, L., Primas, L. E., Logan, R. T., Lutes, G. F., Anderson, J. D., Will, C. M.: “Results of a new test of relativity”. *Proceedings of the Twentieth Annual Precise Time and Time Interval (PTTI) Applications and Planning Meeting*, (1988), 251-259.

[Lämmerzahl06] Lämmerzahl, C.: “Test Theories for Lorentz Invariance”. *Lecture Notes in Physics* **702** (2006), 349-384.

[Lane05] Lane, C. D.: “Probing Lorentz violation with Doppler-shift experiments”. *Physical Review D* **72** (2005), 016005/1-9.

[Lehmann78] Lehmann, J. C.: “Iodine, a test molecule in modern spectroscopy”. *Contemporary Physics* **19** (1978), 449-467.

[Lehnert08] priv. comm. Ralf Lehnert (2008).
and
Carroll, S. M., Field, G. B., Jackiw, R.: “Limits on a Lorentz- and parity-violating modification of electrodynamics”. *Physical Review D* **41** (1990), 1231-1240.
and
Kostelecký, V. A. and Mewes, M.: “Cosmological Constraints on Lorentz Violation in Electrodynamics”. *Physical Review Letters* **87** (2001), 251304/1-4.

[Lock05] Arie, A., Byer, R. L.: ”Laser heterodyne spectroscopy of $^{127}I_2$ hyperfine structure near 532 nm”. *Journal of the Optical Society America B* **10** (1993), 1990-1997.
and
Cordinale, P., Galzerano, G., Schnatz, H.: “International comparison of two iodine-stabilized frequency-doubled Nd:YAG lasers at $\lambda = 532$ nm”. *Metrologia* **37** (2000), 177-182.
and
Hall, J. L., Hollberg, L., Baer, T., Robinson, H. G.: “Optical heterodyne saturation spectroscopy”. *Applied Physics Letters* **39** (1981), 680-682.
and
Reinhardt, S.: Measurement of Time Dilation by Lasers Spectroscopy on Fast Stored Lithium Ions. (2005), Dissertation, University Heidelberg.

[MacArther86b] MacArthur, D. W., Butterfield, K. B., Clark, D. A., Donahue, J. B., Gram, P. A. M.: “Test of the Special-Relativistic Doppler Formula at $\beta = 0.84$”. *Physical Review Letters* **56** (1986), 282-285.

[MacArthur86a] MacArthur, D.W.: “Special relativity: Understanding experimental tests and formulations”. *Physical Review A* **33** (1986), 1-5.

[Mattingly05] Mattingly, D.: “Modern Tests of Lorentz Invariance”. *Living Reviews in Relativity* **8** (2005), 5. URL (cited on 20.03.2008): http://www.livingreviews.org/lrr-2005-5.

[McGowan93] McGowan, R. W., Giltner, D. M., Sternberg, S. J., Lee, S. A.: “New Measurement of the relativistic Doppler Shift in Neon”. *Physical Review Letter* **70** (1993), 251-254.

[MS77a] Mansouri, R., Sexl, R. U.: “A Test Theory of Special Relativity: I. Simultaneity and Clock Synchronization”. *General Relativity and Gravitation* **8** (1977), 497-513.

[MS77b] Mansouri, R., Sexl, R. U.: "A Test Theory of Special Relativity: II. First Order Tests". *General Relativity and Gravitation* **8** (1977), 515-524.

[MS77c] Mansouri, R., Sexl, R. U.: "A Test Theory of Special Relativity: III. Second-Order Tests". *General Relativity and Gravitation* **8** (1977), 809-814.

[NASA08] NASA/WMAP Science Team, March 2008, http://www.nasa.gov /topics/universe/features/wmap_five.html, Picture: CMB.

[NASA72] NASA Apollo 17 Mission, 07.12.1972, http://nssdc.gsfc.nasa.gov/ imgcat/html/object_page/a17_h_148_22727.html, Picture: Earth.

[Nez93] Nez, F., Biraben, F., Felder, R. and Millerioux, Y.: "Optical frequency determination of the hyperfine components of the 5 $S_{1/2}$ – $5D_{3/2}$ two-photon transitions in rubidium". *Optics Communications* **102** (1993), 432-438.

[Poth90] Poth, H.: "Electron cooling: Theory, experiment, application". *Physics Reports* **196** (1990), 135-297.

[Quinn03] Quinn, T. J.: "Practical realization of the definition of the metre, including recommended radiations of other optical frequency standards". *Metrologia* **40** (2003), 103-133.

[Reinhardt05] Reinhardt, S.: Measurement of Time Dilation by Lasers Spectroscopy on Fast Stored Lithium Ions. (2005), Dissertation, University Heidelberg.

[Reinhardt06] Reinhardt, S., Saathoff, G., Karpuk, S., Novotny, C., Huber, G., Zimmermann, M., Holzwarth, R., Udem, Th., Hänsch, T. W., Gwinner, G.: "Iodine hyperfine structure and absolute frequency measurements at 565, 576, and 585 nm". *Optics Communications* **261** (2006), 282-290.

[Reinhardt07a] Reinhardt, S., Saathoff, G., Buhr, H., Carlson, L. A., Wolf, A., Schwalm, D., Karpuk, S., Novotny, C., Huber, G., Zimmerman, M., Holzwarth, R., Udem, T., Hänsch, T. W., and Gwinner, G.: "Test of relativistic time dilation with fast optical clocks at different velocities". *Nature Physics* **3** (2007), 861-864.

[Reinhardt07b] Reinhardt, S., Bernhardt, B., Geppert, C., Holzwarth, R., Huber, G., Karpuk, S., Miski-Oglu, N., Nörtershäuser, W., Novotny, C., Udem, T.: "Absolute frequency measurements and comparisons in iodine at 735 nm and 772 nm". *Optics Communications* **274** (2007), 354-360.

[Riehle04] Riehle, F.: *Frequency Standards: Basics and Applications* (2004), WILEY-VCH Verlag GmbH & Co. KGaA, Weinheim, ISBN 3-527-40230-6.

[Riis88] Riis, E., Andersen, L.-U. A., Bjerre, N., Poulsen, O.: "Test of the Isotropy of the Speed of Light Using Fast-Beam Laser Spectroscopy". *Physical Review Letters* **60** (1988), 81-84.

[Riis94] Riis, E., Sinclair, A. G., Poulsen, O., Drake, G. W. F., Rowley, W. R. C. and Levick, A. P.: "Lamb shifts and hyperfine structure in $^6Li^+$ and $^7Li^+$: Theory and experiment". *Physical Review A* **49** (1994), 207-220.

[Robertson49] Robertson, H. P.: "Postulate versus Observation in the Special Theory of Relativity." *Review of Modern Physics* **21** (1949), 378-382.

[Rong98] Rong, H., Grafström, S., Kowalski, J., Neumann, R. and zu Putlitz, G.: "A new precise value of the absolute 2^3S_1, F=5/2 – 2^3P_2, F=7/2 transition frequency in $^7Li^+$". *European Physics Journal D* **3** (1998), 217-222.

[Saathoff02] Saathoff, G.: Experimental Test of Relativistic Time Dilation by Laser Spectroscopy of Fast Ions. (2002), Dissertation, University Heidelberg.

[Saathoff03] Saathoff, G., Karpuk, S., Eisenbarth, U., Huber, G., Krohn, S., Muñoz Horta, R., Reinhardt, S., Schwalm, D., Wolf, A. and Gwinner, G.: "Improved Test of Time Dilation in Special Relativity". *Physical Review Letters* **91** (2003), 190403/1-4.

[Saghiri99] Saghiri, A. A.: Hochauflösende Messung zur dielektronischen Rekombination von metastabilen und Grundzustands-Li^+-Ionen (1999), Dissertation, University Heidelberg.

[Sánchez06] Ewald, G., Nörtershäuser, W., Dax, A., Götte, S., Kirchner, R., Kluge, H.-J., Kühl, T., Sánchez, R., Wojtaszek, A., Bushaw, B. A., Drake, G. W. F., Yan, Z.-C., Zimmermann, C.: "Nuclear Charge Radii of ^{8,9}Li Determined by Laser Spectroscopy". *Physical Review Letters* **93** (2004), 113002/1-4 and "Erratum" *Physical Review Letters* **94** (2005), 039901/1.
and
Sánchez, R., Nörtershäuser, W., Ewald, G., Albers, D., Behr, J., Bricault, P., Bushaw, B. A., Dax, A., Dilling, J., Dombsky, M., Drake, G. W. F., Götte, S., Kirchner, R., Kluge, H.-J., Kühl, T., Lassen, J., Levy, C. D. P., Pearson, M. R., Prime, E. J., Ryjkov, V., Wojtaszek, A., Yan, Z.-C., Zimmermann, C.: "Nuclear Charge Radii of ^{9,11}Li: The Influence of Halo Neutrons". *Physical Review Letters* **96** (2006), 033002/1-4.

[Sansonetti06] Sansonetti, J.E.: "Wavelengths, Transition Probabilities, and Energy Levels for the Spectra of Rubidium (Rb I through Rb XXXVII)". *Journal of Physical and Chemical Reference Data* **35** (2006), 301-421.

[Schröder90] Schröder, S., Klein, R., Boos, N., Gerhard, M., Grieser, R., Huber, G., Karafillidis, A., Krieg, M., Schmidt, N., Kühl, T., Neumann, R., Balykin, V., Grieser, M., Habs, D., Jaeschke, E., Krämer, D., Kristensen, M., Music, M., Petrich, W., Schwalm, D., Sigray, P., Steck, M., Wanner, B. and Wolf, A.: "First Laser Cooling of Relativistic Ions in a Storage Ring". *Physical Review Letters* **64** (1990), 2901-2904.

[Schröder94] Schröder, U. E.: *Spezielle Relativitätstheorie* (1994), 3. überarb. und erw. Auflage, Verlag Harri Deutsch, Frankfurt am Main Thun, ISBN 3-8171-1367-6.

[Stanwix05] Stanwix, P. L., Tobar, M. E., Wolf, P., Susli, M., Locke, C. R., Ivanov, E. N., Winterflood, J., van Kann, F.: "Test of the Lorentz Invariance in Electrodynamics Using Rotating Cryogenic Sapphire Microwave Oscillators". *Physical Review Letters* **95** (2005), 040404/1-4.

[Steck04] Steck, M., Beller, P., Beckert, K., Franzke, B., Nolden, F.: "Electron cooling experiments at the ESR". *Nuclear Instruments & Methods in Physical Research A* **532** (2004), 357-365.
and
Franzke, B.: "The heavy ion storage and cooler ring project ESR at GSI". *Nuclear Instruments & Methods in Physical Research B* **24/25** (1987), 18-25.

[Steck06] priv. comm. Markus Steck.

[Steck08] Steck, D.A.: *Rubidium 87 D Line Data (2008)*, online at http://steck.us/alkalidata/

[Svelto98] Svelto, O.: *Principles of Lasers – Fourth Edition* (1998), Plenum Press, New York, ISBN 0-306-45748-2.

[Tinschert08] priv. comm. Klaus Tinschert. (In 1997 an experiment with a $^7Li^+$ ion beam was performed at the UNILAC. The ions were produced in the ECR ion source with LiF as source material. Out of this experiment, however, no statement on the production of the metastable lithium state and its behaviour during acceleration and storage can be made.)

[Titte06] Titte, A.: Elektronenstoßionisation von heliumähnlichen metastabilen Lithium-Ionen (2006), Diploma theses, University Giessen.

[Tobar05] Tobar, M. E., Wolf, P., Fowler, A., Hartnett, J. G.: "New methods of testing Lorentz violation in electrodynamics". *Physical Review D* **71** (2005), 025004/1-15.

[Toptica02] Iodine Spec, *Iodine Spectrum Calculating Software*, Version 4.0 (11.04.2002), Toptica.

[Trans07] McKinley, J. M.: "Relativistic transformations of light power". *American Journal of Physics* **47** (1979), 602-605.
and
Savage, C. M., Searle, A. and McCalman, L.: "Real Time Relativity: Exploratory learning of special relativity". *American Journal of Physics* **75** (2007), 791-798.
and
Weiskopf, D., Kraus, U. and Ruder, H.: "Searchlight and Doppler Effects in the Visualization of Special Relativity: A Corrected Derivation of the Transformation of Radiance". *ACM Transactions on Graphics* **18** (1999), 1-14.

[Turner64] Turner, K. C., Hill, H. A.: "New Experimental Limit on Velocity-Dependent Interactions of Clocks and Distant Matter". *Physical Review* **134** (1964), B252-B256.

[Vessot79] Vessot, R. F. C., Levine, M. W., Mattison, E. M., Blomberg, E. L., Hoffman, T. E., Nystrom, G. U., Farrel, B. F., Decher, R., Eby, P. B., Baugher, C. R., Watts, J. W., Teuber, D. L., Wills, F. D.: "Test of Relativistic Gravitation with a Space-Borne Hydrogen Maser". *Physical Review Letters* **45** (1980), 2081-2085.
and
Vessot, R. F. C., Levine, M. W.: "A Test of the Equivalence Principle Using a Space-Born Clock". *General Relativity and Gravitation* **10** (1979), 181-204.

[Wanner98] Wanner, B., Grimm, R., Gruber, A., Habs, D., Miesner, H.-J., Nielsen, J. S. and Schwalm, D.: "Rapid adiabatic passage in laser cooling of fast stored ion beams". *Physical Review A* **58** (1998), 2242-2251.

[Will92] Will, C. M.: "Clock synchronization and isotropy of the one-way-speed of light". *Physical Review D* **45** (1992), 403-411.

[Wille96] Wille, K.: *Physik der Teilchenbeschleuniger und Synchrotronstrahlungs-quellen. Eine Einführung* (1996), 2. überarb. und erw. Aufl., Teubner Studienbücher, Stuttgart, ISBN 3-519-13087-4.

[Wolf04] Wolf, P., Tobar, M. E., Bize, S., Clairon, A., Luiten, A. N., Santarelli, G.: "Whispering Gallery Resonators and Tests of Lorentz Invariance". *General Relativity and Gravitation* **36** (2004), 2351-2372.

[Wolf97] Wolf, P., Petit, G.: "Satellite test of special relativity using the global positioning system". *Physical Review A* **56** (1997), 4405-4409.

[Ye96] Ye, J., Swartz, S., Jungner, P. and Hall, J. L.: "Hyperfine structure and absolute frequency of the ^{87}Rb 5P3/2 state". *Optics Letters* **21** (1996), 1280-1282.

[Zhang97] Zhang, Y. Z.: *Special Relativity and its experimental foundations* (1997), World Scientific, (Advanced Series on Theoretical Science).